Impact of the chromatin remodeller SMARCAD1 on murine intestinal intraepithelial lymphocyte and white adipose tissue biology.

Keith Michael Porter

The Babraham Institute

Homerton College

September 2016

This dissertation is submitted for the degree of
Doctor of Philosophy

Declaration

This research the result of my own work and includes nothing which is the outcome of work done in collaboration except as declared in the Preface and specified in the text.

It is not substantially the same as any that I have submitted, or, is being concurrently submitted for a degree or diploma or other qualification at the University of Cambridge or any other University or similar institution except as declared in the Preface or specified in the text. I further state that no substantial part of my dissertation has already been submitted, or, is being concurrently submitted for any such degree, diploma or other qualification at the University of Cambridge or any other University or similar institution except as declared in the Preface or specified in the text.

It does not exceed the prescribed word limit for the Biological Sciences Degree Committee.

Keith Michael Porter

Impact of the chromatin remodeller SMARCAD1 on murine intestinal intraepithelial lymphocyte and white adipose tissue biology.

Chromatin remodelling factors use the energy of ATP hydrolysis to drive the movement of and/or affect molecular changes to the nucleosome. One such factor, SMARCAD1 (SWI/SNF-related matrix-associated actin-dependent regulator of chromatin subfamily A containing DEAD/H box 1), has been previously shown to restore heterochromatin at the replication fork *in vitro*. This project aimed to assess the impact of SMARCAD1 on mammalian biology, utilising an animal model in which the catalytic ATPase domain of murine SMARCAD1 had been deleted using Cre/lox technology.

Preliminary results had implicated SMARCAD1 in adaptive-immunity and white adipose tissue biology, and SMARCAD1 expression in these tissues/cells was confirmed by tissue-panel western blot. This project therefore aimed to build on these results to understand better the impact of SMARCAD1 on adaptive immune development and white adipose tissue biology. In addition, fewer than expected viable *Smarcad1*$^{-/-}$ homozygous offspring were produced during *Smarcad1*$^{+/-}$ x $^{+/-}$ matings, which both confirmed the observation from a previous knockout model of *Smarcad1*, and limited the number of knockout animals available for this study.

Investigation of systemic B- and T-cells in the bone marrow, thymus and spleen had previously suggested there was no significant defect in adaptive immune development in *Smarcad1*$^{-/-}$ mice, however a tissue-specific and age-related loss of intra-epithelial (IEL) T-lymphocytes was found in the small intestine by flow cytometry. Analysis by qPCR of duodenal RNA suggested that differentiation rather than inflammation may underpin any loss-of-IEL phenotype, although further examination of cell-proliferation and crypt/villus anatomy by EdU incorporation and immunofluorescence revealed no overt cell-anatomical or proliferative difference in the knockout mice. The requirement for large numbers of aged mice made further investigation of the intestinal IEL phenotype logistically prohibitive.

The reduction of epididymal white adipose tissue (eWAT) size had also been observed in male *Smarcad1*$^{-/-}$ mice, and serum from these mice showed elevated triglyceride (TG) and free fatty acids (FFA) levels. Transcriptomic analysis by RNA-seq of whole-WAT revealed an elevation in macrophage-related markers in knockout mice, which was confirmed by flow cytometry. As a number of reports have implicated SMARCAD1 in stem cell biology, putative adipose stem cells were isolated from +/+ and -/- mice by FACS and used for adipogenic differentiation assays *ex-vivo* In parallel, mouse embryonic fibroblasts from +/- and -/- mice were also assayed for adipogenic differentiation. While no significant differences in adipogenesis were observed, *Smarcad1*$^{-/-}$ mice challenged with a (60%) high fat diet did show increased weight gain over +/+ mice, and measurements of adipocyte size and cell cycle/cell proliferation analysis suggested hyperplasia rather than defects in adipogenesis may drive any WAT-related pathology in these mice.

Keith Michael Porter

Table of acknowledgement of assistance received during course of thesis.

1) Initial training in techniques and laboratory practice and subsequent mentoring: Louise Matheson, Rachel Walker and Marc Veldhoen – FACS and IEL preparation for FACS Animal handling and dissection – Marc Veldhoen and Dan Bolland.
2) Data obtained from a technical service provider (e.g. DNA sequencing, illustrations, simple bioinformatics information etc) Kristina Tabbada – Illumina platform RNA-sequencing Simon Andrews – RNA-seq results genomic alignment Rachel Walker/Arthur Davis/Lynzi Waugh/Rebecca Roberts - Cell Sorting Keith Burling (Core Biochemistry Assay Laboratory Addenbrookes hospital) – serum assays Anne Segonds-Pichon – statistical methods.
3) Data produced jointly (e.g. where it was necessary or desirable to have two pairs of hands) Irem Kiris (visiting student) – Tissue Panel Western Blots and culture of mouse embryonic fibroblasts.
4) Data/materials provided by someone else (e.g. one-off analysis, bioinformatics analysis, where parallel data or technical provision in a very different area is needed to provide a connected account in the thesis) Keith Burling (Core Biochemistry Assay Laboratory Addenbrookes hospital) – serum assays

Acknowledgements.

I would like to thank Dr. Patrick Varga-Weisz not just for the opportunity to pursue a PhD, but for allowing me through the looking glass of research savoir-faire.

The down-to-earth perspective of Professor Anne Ferguson-Smith FRS was invaluable and gave exactly the taste of scientific cut-and-thrust this student desired, while never sparing of support when needed. Similarly the endless patience of Dr Anne Corcoran allowed me to mentally explore without reproach or suffocation, and whose leadership and success provide inspiration for many.

No pivotal moment of my life would be right without mention of my late friend, Richard Dhamesin. Moments of struggle are always grounded by his memory, and I'm certain that he's somewhere chortling that I managed to pull this one off ☺ I'll be raising a glass to you, but keeping the PhD to myself thank you very much ;)

The biggest dedications have to go to family and friends. My parents have never pressured me in whatever I do, but instead always have an ear and supportive words to encourage me along the way. My partner Carol Edwards thought it would be a good idea to apply to the Babraham Institute, and has always offered scientific and non-scientific advice – but most importantly has always been there. We also shared possibly the most expensive and life-changing bottle of Rosé wine in Carpentras in 2013, for which we will forever be picking up the tab –x-

There aren't the words to describe the gratitude I have for the entry of Alicia Erin Porter into my life. So rather than try and fail, I'll just say that moments after she was born she opened her eyes and looked me up and down, which made it clear we were equals from the get-go; nothing more, nothing less. More than any seminar, the reality of biology unfolding before my eyes is the greatest influence and celebration of the subject I try and articulate over the next couple of hundred pages –x-

Contents

List of figures.

List of Tables.

Chapter 1 - General Introduction

1.1 Chromatin, nucleosomes and DNA compaction

The mammalian cell contains around 2 metres of genomic DNA, which must be packaged tightly within the 3-dimensional constraints of the cell. The primary DNA sequence harbours functional and non-functional sequences, both of which must become accessible during processes such as replication. However, outside of replication many stretches of DNA are not required for cell-specific functions, and are repressed *via* compaction. Genes that are required for cell-specific function must remain accessible, along with binding sites for transcription factors and other sequences involved in gene regulation (e.g. repressors and non-[protein]-coding RNA). The ability to access the appropriate functional regions of DNA is key to cell-specific function.

Compaction of DNA is achieved by the wrapping of DNA around a core of histone proteins in the form of the 'nucleosome,' and multiple nucleosomes package together to produce a chromatin fibre (Figure 1.1). The nucleosome is the unit of packaged DNA comprising of 147 base-pairs of DNA helix wound around an octet of histone proteins to form the nucleosome core, with an additional stretch of around 80 base-pairs of DNA linking to the next nucleosome core (Luger, Mä, Richmond, Sargent, & Richmond, 1997). These higher order structures of chromatin structure form regions of open and accessible DNA, or conversely inaccessible compacted DNA sequences.

Access to functional DNA sequences requires the ability to de-compact the chromatin structure and is achieved by two types of protein complex, (i) covalent histone modifying enzymes, which attach specific covalent groups to/from histone proteins, thereby creating a binding site for accessory factors or affecting the strength of DNA/histone interaction (ii) ATP-dependant chromatin remodelling complexes, which use the energy of ATP hydrolysis to drive the movement of and/or affect molecular changes to the nucleosome, affecting the overall shape of chromatin.

1.2 Histone modification and the histone code.

The presence of covalent modifications to core histone proteins was first described in 1964 (Allfrey, Faulkner, & Mirksy, 1964) and underpins the "histone code" – the association of specific modifications with specific chromatin states or structures. The presence of these covalently attached groups can create a binding site for accessory factors, or aid in the opening of the nucleosome due to alteration of the electrostatic interaction between e.g. positively charged lysine amino acids on histones and the negatively charged phosphate backbone of DNA (Figure 1.2). Studies over the previous

55 years have unveiled the association between many histone-modifications and chromatin states. These covalent modifications exist dynamically and are enzymatically attached to (or removed from) amino acids on the exposed tails of histone core proteins (Bannister & Kouzarides, 2011). For example, acetylation of histone H3 on lysine residue number 4 (abbreviated to H3K4Ac) is associated with open chromatin and transcription.

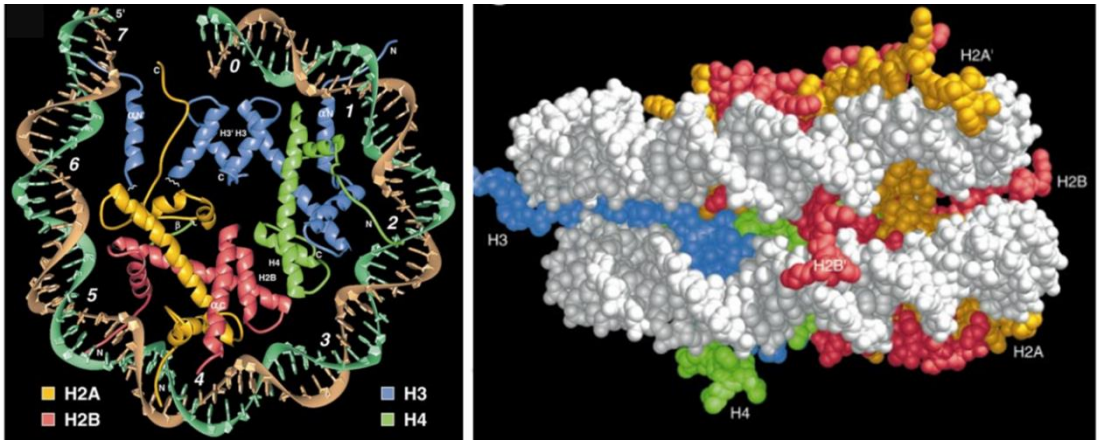

Figure 1.1. Structure of the nucleosome core structure at 2.8Å resolution. DNA (in the classic double-helix form) is wrapped around a core of 8 histone proteins (two each of H2A, H2B, H3 and H4 histone proteins), with 147 bases of DNA completing 1.67 turns of the core particle. Histone tails protrude from the central nucleosome particle, providing sites for covalent modification and the creation of binding sites for factors involved in the control of DNA function. From Luger et al., 1997.

There are two main effects of covalent modifications to histones: changing the electrostatic forces between core histone proteins and the DNA backbone, and the creation or ablation of binding sites for histone-binding proteins. The presence of positively-charged lysine residues within histone proteins increases the electrostatic attraction between the negatively charged DNA backbone and the histone core. Modification of these lysine resides by addition of an acetyl or phophoryl group effectively neutralises the positive charge, weakening this attraction. Given the number of lysine residues within the histone tails (e.g. H3K4, H3K9, H3K14, H3K18, H4K5, H4K8 and H4K12 (Kouzarides, 2007), a potentially large number of target sites exist for modification which can significantly impact chromatin structure.

The addition of acetyl residues to histone is catalysed by the histone acetyltransferase (HAT) enzymes, of which type A HATs can acetylate multiple lysine residues within the N-terminal tail of histones, whereas type B HATs primarily acetylate newly synthesized H4 histones at residues K4 and K12 in the cytoplasm (i.e. before histone deposition into the nucleosome - these marks being removed shortly after deposition (Sterner & Berger, 2000)). By contrast to HATs, the histone deacetylase (HDAC) enzymes remove acetyl residues from histones, and are associated with chromatin compaction and gene repression. There are four families of HDACs, and - unlike HAT-type-B enzymes (which can specifically target H4) - many have low substrate specificity and are able to deacetylate multiple residues (Bannister & Kouzarides, 2011).

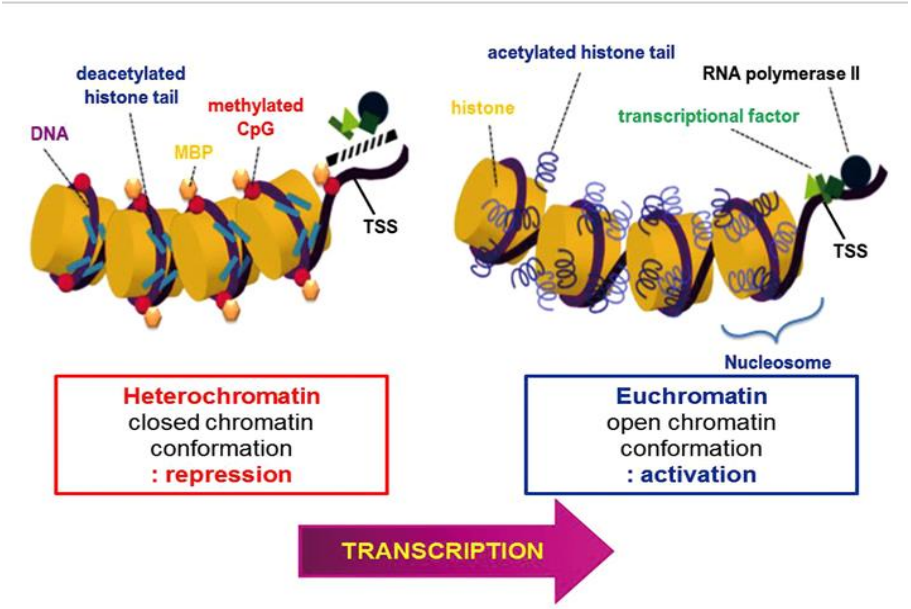

Figure 1.2. Nucleosomes assemble into chromatin fibres, which are condensed in regions of transcriptional repression (heterochromatin) and associated with methylated (CpG) DNA. Covalent attachment of positive-charged acetyl groups to histone proteins introduces electrostatic repulsion between histones and the negatively charged phosphate back-bone of DNA, driving and aiding a relaxed chromatin structure accessible to transcription factors and other functional elements. From Y. Z. Kim, 2014.

Of the other histone modifications studied to date, methylation of histone residues has been the focus of much study. Unlike acetylation, histone methylation does not affect electrostatic charges around the nucleosome, but rather creates sites for other chromatin-binding proteins. Both lysine and arginine residues in particular have been shown to become methylated, and multiple (mono- di- or tri-) methyl groups can be

added to residues. In one example, tri-methylation of H3K9 (H3K9me3) creates a binding site for heterochromatin protein 1 (HP1), which binds to H3K9me3 through its chromodomain. The remaining chromoshadow-domain of HP1 is able to dimerise with other H3K9me3-bound HP1 proteins, forming the closed heterochromatin structure (Thiru et al., 2004). In this way histone modification directs higher order chromatin structure.

The addition of methyl groups to histone residues is catalysed by histone methyltransferase enzymes, which perform addition of methyl groups *via* their SET domain and are often target specific. For example, the methyltransferase Suv39H1 trimethylates histone H3K9 (Chiba et al., 2015), whereas SET7/9 mono-methylates histone H3K4 (B. Xiao et al., 2003). Similarly, histone demethylases are functionally restrained to demethylate only certain residues. As such, enzymes such as LSD2 (lysine demethylase 2) specifically demethylate histone H3K4me1 and H3K4me2, whereas JMJD5 (JmjC-domain-containing histone demethylase 5) demethylates H3K36me2 (Kooistra & Helin, 2012). Of the many histone demethylases now detailed, the majority contain a Jumonji C domain which catalyses the removal of mono- di- and tri- methyl groups from lysine residues (Klose, Kallin, & Zhang, 2006). In contrast, the original histone demethylase discovered (LSD1) is only able to remove mono- or di-methyl groups from lysine (Shi et al., 2004). The presence of multiple histone methyltransferases and demethylases adds flexibility and complexity to the histone code.

While histone acetylation and methylation are two particularly well studied examples of covalent histone modification, many other covalent modifications exist (Table 1). Phosphorylation of threonine residues (H2A-Thr120, H3-Thr3) for example, is associated with mitosis (Aihara et al., 2004), whereas ubiquitination of H2A-K119 is a mark associated with gene silencing and spermatogenesis (H. Wang et al., 2004). In addition, sumoylation of H2B-K6 or K7 is associated with transcriptional repression, (Nathan et al., 2006), while by contrast citrullination of histone is linked to decondensed chromatin and pluripotency (Christophorou et al., 2014). More recently, covalently histone modifications derived from short-chain fatty acids linked to potential metabolic stress (such as lysine-crotonylate or lysine-hydroxybutyrate) have been described (Sabari, Zhang, Allis, & Zhao, 2016). It would seem likely that more modifications will be discovered in future, and the functional impact of these and currently known modifications will continue to be detailed.

Residue	Modification	Functions
Histone H2A		
Ser1	Phosphorylation	Mitosis
Lys5	Acetylation	Transcriptional activation
Lys119	Ubiquitylation	Spermatogenesis
Thr120	Phosphorylation	Mitosis
Histone H2AX		
Ser139	Phosphorylation	DNA Damage repair, apoptosis
Tyr142	Phosphorylation	Regulation of DNA damage foci formation
Histone H2B		
Lys5	Acetylation	Transcriptional activation
Lys12	Acetylation	Transcriptional activation
Ser14	Phosphorylation	Apoptosis
Lys15	Acetylation	Transcriptional activation
Lys20	Acetylation	Transcriptional activation
Lys120	Ubiquitylation	Transcription (elongation?)

Residue	Modification	Functions
Histone H4		
Ser1	Phosphorylation	Transcriptional activation
Arg3	Methylation	Transcriptional activation
Lys5	Acetylation	Histone deposition, transcriptional activation
Lys8	Acetylation	Transcriptional activation
Lys12	Acetylation	Histone deposition, transcriptional activation
Lys16	Acetylation	Transcriptional activation
Lys20	Methylation	Transcriptional silencing, heterochromatin
Lys91	Acetylation	Histone deposition, DNA damage repair

Residue	Modification	Functions
Histone H3		
Arg2	Methylation	Transcriptional activation
Thr3	Phosphorylation	Mitosis
Lys4	Acetylation	Transcriptional activation
Lys4	Methylation	Euchromatin, transcriptional activation
Thr6	Phosphorylation	Transcriptional activation
Arg8	Methylation	Transcriptional activation
Lys9	Acetylation	Histone deposition, Transcriptional activation
Lys9	Methylation	Transcriptional silencing, heterochromatin
Ser10	Phosphorylation	Mitosis, immediate early gene activation
Thr11	Phosphorylation	Mitosis; DNA damage induced transcription
Lys14	Acetylation	Transcriptional activation
Arg17	Methylation	Transcriptional activation
Lys18	Acetylation	Transcriptional activation
Lys23	Acetylation	Transcriptional activation
Arg26	Methylation	Transcriptional activation
Lys27	Methylation	Transcriptional silencing
Ser28	Phosphorylation	Mitosis
Lys36	Acetylation	Transcription activation
Lys36	Methylation	Transcription elongation
Thr45	Phosphorylation	DNA replication, apoptosis
Lys56	Acetylation	DNA damage repair, chromatin assembly
Lys79	Methylation	Transcriptional activation

Table 1.1. The histone code. Histone residues can be subject to post-translational covalent modification, and a large number have so far been characterised in the context of the functional or biological impact of the modification. Processes associated with specific histone modifications include gene expression, DNA repair and replication, to give an example. Table recreated from http://www.activemotif.com/documents/1815.pdf.

1.3 Chromatin remodelling and chromatin remodeller families.

A further level of control is imparted onto chromatin by protein complexes that move nucleosomes with respect to the underlying DNA. Chromatin remodellers are multi-unit complexes that use the energy of ATP hydrolysis to move nucleosomes, and can be subdivided into four families based on sequence of the DNA-dependent ATPase domains (and adjacent domains): the SWI/SNF (switching defective/sucrose non-fermenting) family of remodelers, ISW1 (Imitation switch 1), CHD (Chromodomain, helicase, DNA binding) and INO80 (Inositol Requiring 80) (Figure 1.3). The ATPase domain of each protein contains two RecA-like folds, a DEAD-like helicases superfamily domain (DExx) and helicase superfamily c-terminus (HELICc) domain. The domains flanking this ATPase domain determine the differences in function between the families and peptides, with the ATPase domain itself being split in the INO80 family of remodellers (Längst & Manelyte, 2015).

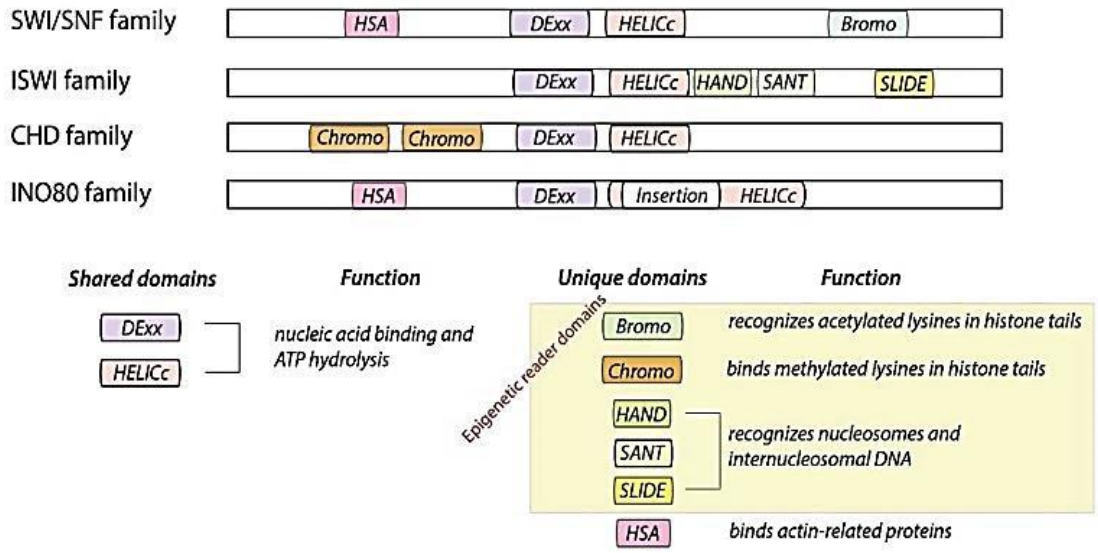

Figure 1.3. There are four families of chromatin remodellers based on sequence of the ATPase (DExx/HELICc) domain and the presence of associated functional domains (HSS,Bromo, HAND/SANT/SLIDE and Chromo): SWI/SNF family remodellers bind acetylated histones *via* the bromodomain and actin *via* the HSA domain, ISWI family remodellers bind the linker DNA between nucleosomes *via* the HAND-SANT-SLIDE domain, CHD remodellers bind methylated histones *via* the chromodomain, and INO80 proteins which can also bind actin *via* the HSA domain. From Längst and Manelyte, 2015.

1.3.1. Chromatin remodelling families.

Members of the **SWI/SNF family** are involved in the sliding of nucleosomes to create space and e.g. the accessibility of DNA, and bind actin/actin-related proteins *via* the Helicase-SANT Associated (HSA) domain (allowing increased DNA translocation/nucleosome ejection) (Clapier et al., 2016). These can also bind acetylated histones *via* the bromodomain (Filippakopoulos & Knapp, 2012); indeed, many SWI/SNF family members were originally associated with active transcription (Kadam & Emerson, 2003), however - more recently – SWI/SNF family remodellers have been associated with DNA repair (Smith-Roe et al., 2015, Costelloe et al., 2012), and transcriptional repression (discussed later) (Rowbotham et al., 2011b).

By contrast to the SWI/SNF family, members of the **ISWI family** of remodellers play a role in nucleosome assembly and the regular spacing of nucleosomes e.g. during DNA replication (Ito et al., 1999). In addition to the ATPase domain, ISWI family remodellers also contain a HAND-SANT-SLIDE (HSS) domain that binds unmodified histone tails (Boyer, Latek, & Peterson, 2004) and the stretch of 'linker' DNA that extends away from the nucleosome (Dang & Bartholomew, 2007). While many ISWI remodellers have been linked to transcriptional repression (e.g. Strohner et al., 2004) one ISWI complex (NURF) has been shown conversely to promote transcription (H. Xiao et al., 2001). As with the seemingly opposing functions of the SWI/SNF member *SMARCAD1* in transcriptional activation/repression, these seemingly opposing functions reported for ISWI family members may reflect the influence of accessory subunits on the complex.

While SWI/SNF and ISWI proteins perform (in the majority of cases) distinct activities, the functions of the **CHD family** remodellers are more heterogeneous. These proteins are characterised by the presence of two chromodomains, (which bind methylated histone H3), and have been shown to assemble regularly spaced nucleosomes (Lusser, Urwin, & Kadonaga, 2005) to facilitate the opening of chromatin during transcription (Murawska & Brehm, 2011) and catalyse histone exchange (such as the incorporation of histone variant H3.3 in the Drosophila embryos, (Konev et al., 2007)). By contrast, other members of the CHD family function in repression, such as CHD3/CHD4, which are components of the NURD (Nucleosome and Remodelling Deacetylase) complex along with histone deacetylases (HDAC1/2) and methyl CpG-binding domain (MBD) proteins (Denslow & Wade, 2007). Some members of the CHD family (e.g. CHD1 and CHD2 in higher eukaryotes) possess SANT and SLIDE domains which serve as DNA binding domains (DBD), and preferentially bind to AT-rich DNA sequences (Stokes & Perry,

1995, Ryan, Sundaramoorthy, Martin, Singh, & Owen-Hughes, 2011). Interestingly, mutations in the CHD family member *CHD7* have been found in patients with CHARGE syndrome (Coloboma of the eye, Heart defects, Atresia of the choanae, Retardation of growth and/or development, Genital and/or urinary abnormalities, and Ear abnormalities), in which haploinsuffiency of *CHD7* (frequently due to mutation of one allele) leads to a spectrum of developmental anomalies (Lalani et al., 2006)

The **INO80 family** of chromatin remodellers differs from the other 3 families in the ATPase domain due to the presence of an insertion between the DExx and HELICc domains, which is larger in higher organisms (~1000 amino acids in mammals) than in yeast (~250 amino acids). This inserted domain can bind the Ruv-like proteins RVB1 and RVB2 (providing helicase activity to INO80 proteins (Huen et al., 2010)) in addition to binding an actin related protein (ARP) (Y. Bao & Shen, 2007). Indeed, INO80 complexes bind to specialised DNA structures *in vitro* (e.g. structures similar to Holliday junctions) and are implicated in homologous recombination and DNA repair (S. Wu et al., 2007), in addition to transcriptional activation (through interaction with factors such as YY1, (Cai et al., 2007)). Furthermore, a number of studies have highlighted the role of INO80 members in nucleosome editing: the SWR1C, p400 and SRCAP (Snf2-related CBP activator) complexes are able to replace the histone H2A with the H2A.Z variant, while conversely the INO80C complex catalyses the reverse H2A.Z to H2A movement (Papamichos-Chronakis, Watanabe, Rando, & Peterson, 2011). In addition to H2A.Z replacement, INO80C also harbours the ability to remove the histone H2 variant γH2A.X from the vicinity of DNA double-strand breaks (van Attikum, Fritsch, & Gasser, 2007), and has been shown to regulate nucleosome spacing (Udugama, Sabri, & Bartholomew, 2011). Another important editing function is the replacement of histone H3.1 with variant H3.3 in promoter regions during gene activation by E1A binding protein p400 (EP400), which is done in combination with H2A.Z deposition (mentioned above, (Pradhan et al., 2016)). Together, these studies have highlighted the role of INO80 family remodellers in DNA repair, transcriptional activation and nucleosome editing. An overview of how these chromatin remodelling families impact chromatin is given in Figure 1.4.

1.3.2. Impact of chromatin remodellers on development.

Building on the knowledge of how chromatin remodellers interact with DNA, mammalian models have furthered the understanding of these factors during development. Rodent knockout models lacking functional subunits of remodelling

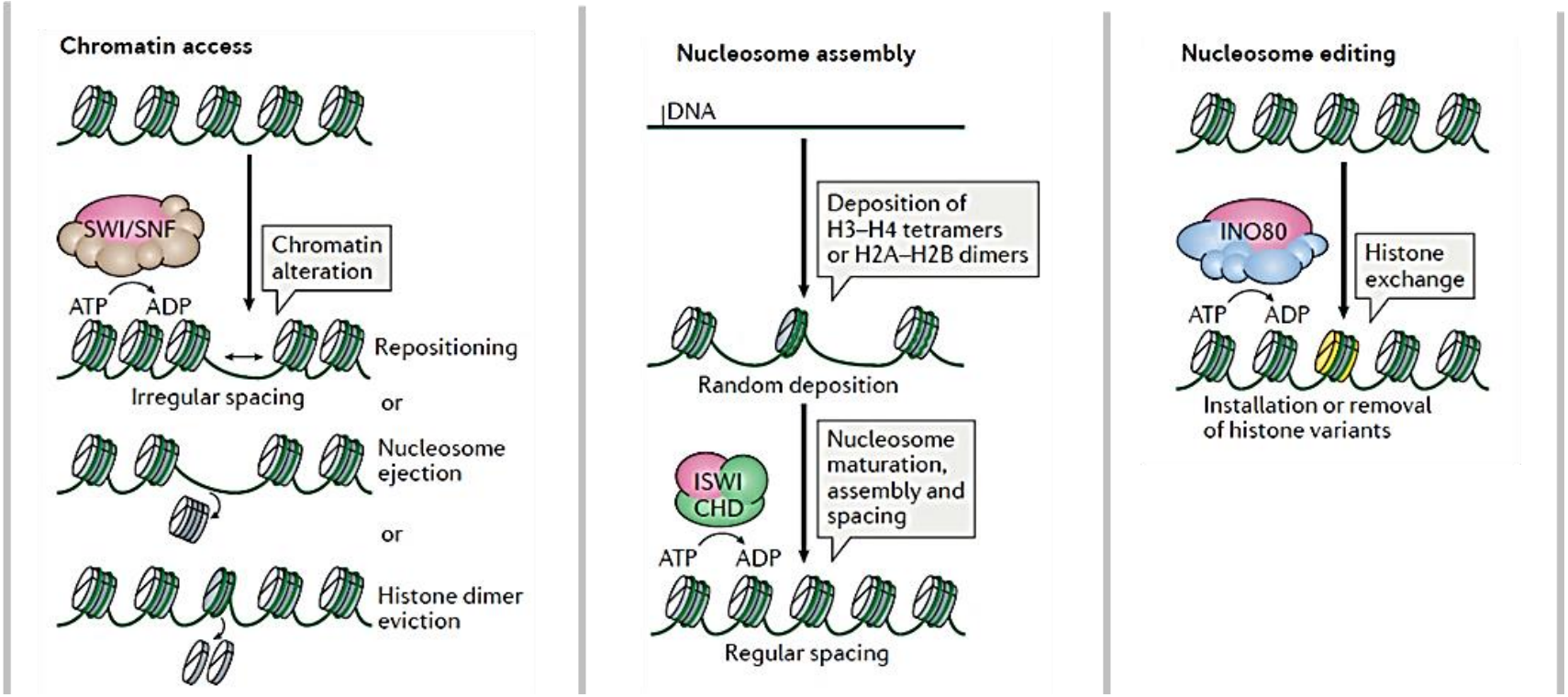

Figure 1.4. Chromatin remodellers classified by impact on nucleosome structure. Remodellers are capable of increasing chromatin access by nucleosome sliding (repositioning), ejection or histone eviction; nucleosome assembly (e.g during DNA replication); or nucleosome editing (the exchange of histone variants within the nucleosome core). Reproduced from Clapier et al 2017.

complexes present with developmental anomalies of varying severity, from prenatal lethality to more subtle later-onset phenotypes. However, many of the original remodelling complexes were discovered in yeast, and related proteins later identified in higher organisms. In each case chromatin remodellers typically function as part of a multi-subunit complex, and recruitment to specific genomic loci of the complex can be directed by other (non-remodeller) members of the complex (Hota & Bruneau, 2016).

The importance of these complexes during development was highlighted by studies of the SWI/SNF Brahma complex in Drosophila (Marenda, Zraly, Feng, Egan, & Dingwall, 2003), and the Brahma-related gene 1 (BRG1) complex factor during the peri-implantation stage in mouse (Bultman et al., 2000). During development, the BAF complexes (BRG1 or hBRM Associated Factors) direct essential transcriptional programs and apply the changes to chromatin required for differentiation. In particular, the BAF complex was shown to direct early lineage specification in the mouse embryo (Panamarova et al., 2016). Furthermore, the ability of these complexes to control self-renewal and pluripotency of embryonic stem cells has been linked to their binding to promoter sequences of key pluripotency genes (Kidder, Palmer, & Knott, 2009, (Ho, Jothi, et al., 2009), such as the esBAF complex (embryonic stem cell BAF, containing BAF155, and BAF60A). Interestingly, esBAF complexes differ in their composition between human and mouse, as the BAF170 subunit is present in human but absent from the mouse complex (Ho, Ronan, et al., 2009). Furthermore, the mouse/human esBAF complex contains the SWI/SNF member SMARCAD1 (discussed later).

Later stages of development are also influenced by chromatin remodelling complexes. During neural development, BRG1 and BAF155 are required for neural tube closure in a dose-dependent manner. Indeed, heterozygous BRG1/BAF155+/- mutants show neural tube closure defects and exencephaly (Marathe et al., 2013). Other neural differentiation events need functional remodelling complexes: the differentiation of glial cells into functional myelin-producing oligodendrocytes requires BRG1 (Yu et al., 2013). In addition, the differentiation of neural progenitors to mature neurons requires the exchange of specific subunits within the BAF complex (Lessard et al., 2007), demonstrating the flexibility conferred by multi-subunit complexes. Upon terminal differentiation, the influence of chromatin remodelling is still evident as the BAF53B complex is required in post-mitotic neurons for dentrite growth and branching (J. I. Wu et al., 2007). Together these highlight the scope of chromatin remodelling impact throughout development.

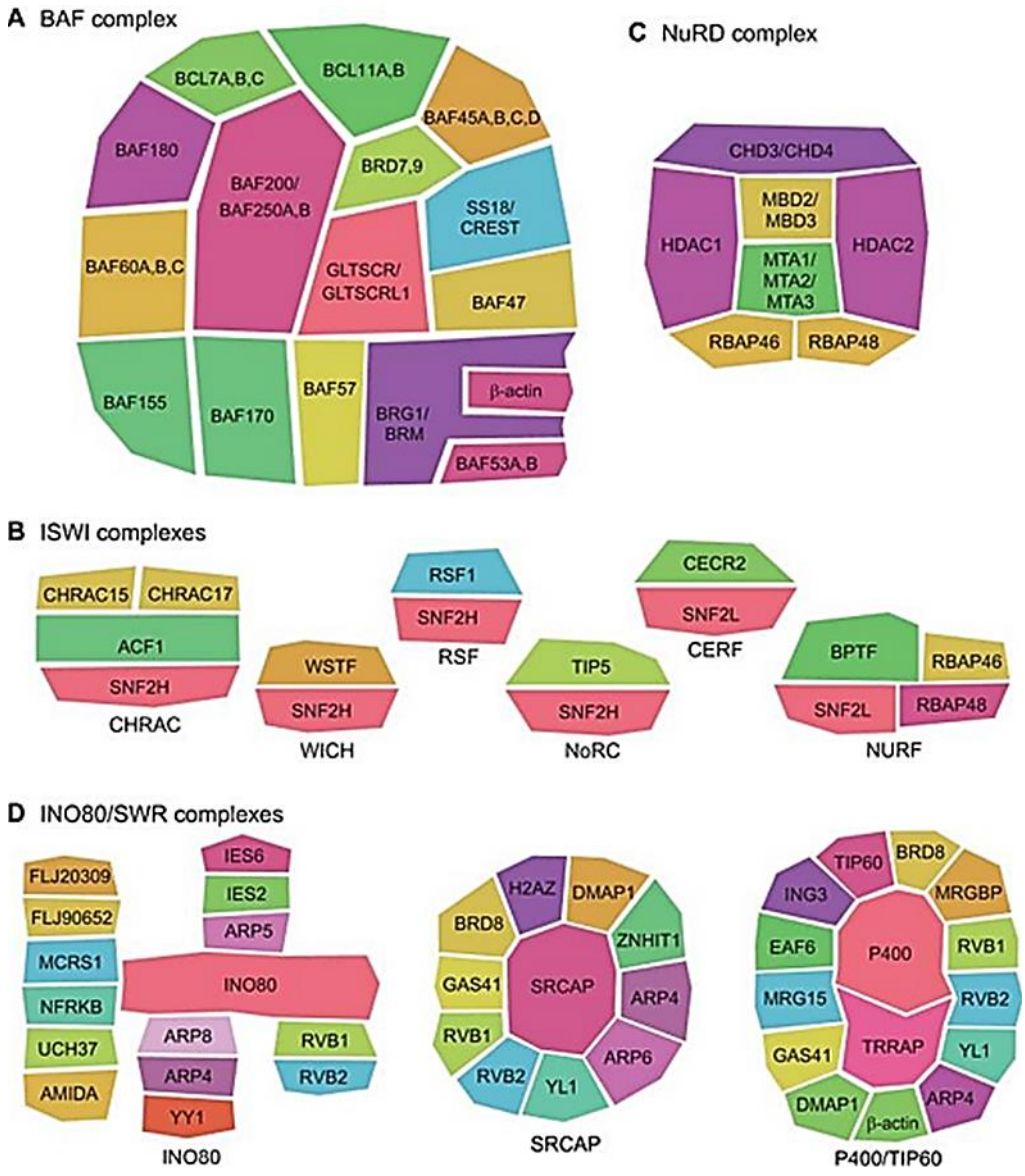

Figure 1.5. Chromatin remodelling enzymes function within complexes. The BAF complex (A) includes BRG1/BRM remodeller subunit along with e.g. subunits BAF45A, BAF155, BAF170 in neural progenitor cells, although the BAF170 subunit is replaced by a second BAF155 subunit in embryonic stem cells. Similar subunit exchanges reflect functional differences within the NuRD complex (C). whereby the MTA2 subunit has been shown to be replaced by MTA1 in metastatic breast cancers. Subunit derivation of other remodelling complexes (WICH/RSF/NoRC/CERF/NURF/INO80/SRCAP/P400) are shown in (B) and (D). From Hota et al., 2016.

Other tissues and organs have also been studied with respect to remodelling complex function. Regeneration of cell types in the epidermis is directed by BAF complexes, and expression of the BAF53A subunit of BAF is required to maintain keratinocyte progenitors in an undifferentiated state (X. Bao et al., 2013) Furthermore, terminal differentiation of keratinocytes requires expression of SMARCAD4 (BRG1) and SMARCA2 (BRM), as conditional deletion of BRG1 leads to defects in the skin permeability barrier, which is exacerbated in SMARCA2 mutant mice (Indra et al., 2005).

During heart development in mouse and zebrafish, BRG1 is required in a dosage sensitive manner. Animals heterozygous for BRG1 show morphological defects and cardiac gene expression dysregulation due to an allelic imbalance between BRG1 and the cardiac transcription factors Tbx5, Tbx20 and Nkx2-5 (Takeuchi et al., 2011). Prior to this, the differentiation of mesoderm cells into cardiac progenitors coincides with the expression of Smarcd3 (also known as Baf60c) (Devine, Wythe, George, Koshiba-Takeuchi, & Bruneau, 2014). Indeed, the interaction of Smarcd3 with Tbx5 (and another transcription factor, GATA4) drives the production of cardiomyocytes from mouse mesoderm (Takeuchi & Bruneau, 2009).

The development of the various cells and lineages of the immune system is controlled by the actions of chromatin remodellers. The conditional deletion of BAF53a was shown to impair proliferation of haematopoietic stem cells and formation of downstream lineages, while also reducing the survival of progenitors – leading to aplastic anaemia and rapid mortality (Krasteva et al., 2012). During B-cell development, which involves multiple stages within the bone marrow, the BRG1 and BAF155 subunits are required for successful formation of common lymphoid progenitors and development of pro-B cells, due to a loss of expression of the key transcription factors EBF1 and IL7ra and their downstream targets (Choi et al., 2012).

In T-cell development, immature thymocytes express both CD4 and CD8 co-receptors before lineage specification and the expression of either CD4 or CD8. The choice of co-receptor is reflected in the interplay between BRG1 and BAF57 remodelling complexes, whereby BRG1 is required for CD8 expression, but both BRG1 and BAF57 are required for the silencing of CD4. Reflecting this, BRG1 mutants produce fewer CD8+ T cells, whereas both BRG1 BAF57 mutants produce CD4+ at an inappropriate early stage (Chi et al., 2002, Chi et al., 2003). Indeed, binding of the transcriptional repressor RUNX1 to a 434bp region proximal to the CD4 gene is increased by the actions of BRG1 and BAF57, reducing the content of the H1 linker histone and thereby increasing accessibility (Wan

et al., 2009). A summary of some of the initial chromatin remodeller knockout mice and then range of phenotypic effects is given in Table 2, emphasizing the importance of these factors in mammalian development.

Targeted subunit	Genetic defect	Phenotype	References
SWI/SNF family			
BRG1	Gene inactivation	Homozygotes die at peri-implantation stage; heterozygotes are predisposed to exencephaly and tumours, and CD8 levels in thymocytes are suppressed	14,20
	Hypomorphic mutations	Lethality at ~E11.5–E14.5 due to erythropoietic defects, including failure to activate β-globin gene expression	18
	T-cell specific gene inactivation	Blockage in T-cell development, thymic abnormalities, CD4 derepression and CD8 inactivation	19–21
BRM	Gene inactivation	Increased cellular proliferation	13
INI1/SNF5	Gene inactivation	Peri-implantation lethality; loss of heterozygosity associated with tumours of the head, neck and nervous system	15–17
	Liver-specific gene inactivation	Neonatal death due to severe hypoglycaemia, impaired glycogen storage and energy metabolism; increased cell proliferation	25
BAF57	T-cell specific transgenic expression of dominant-negative alleles	CD4 levels derepressed and CD8 levels suppressed	20
BAF60C	Gene inactivation	Lethality at E10–E11 due to abnormal cardiac and skeletal muscle development	26
BAF155/SRG3	Gene inactivation	Homozygotes die at peri-implantation stage; heterozygotes show exencephaly and defects in neural development	24
	T-cell specific transgenic overexpression	Increased sensitivity of peripheral T-cells to glucocoricoid- and stress-induced apoptosis	22
BAF180	Gene inactivation	Lethality at E12.2–E15.5 due to cardiac and placental defects	27
ISWI family			
SNF2H	Gene inactivation	Homozygotes die at peri-implantation stage	40
CHD family			
CHD4	T-cell specific gene inactivation	Inhibition of thymocyte differentiation, repression of CD4, decrease in thymocyte cell division	23
MBD3	Gene inactivation	Lethality at or before E8.5	133
HDAC1	Gene inactivation	Lethality at E10.5 due to global decrease in cell proliferation and overall growth retardation	134

BAF, BRG-associated factor; BRG, bramha-like 1; BRM, brahma; E, embryonic day; CHD, chromodomain helicase DNA-binding protein; HDAC1, histone deacetylase 1; INI1, integrase interactor 1; MBD3, methyl CpG binding domain 3.

Table 1.2. Initial murine knockout models of chromatin remodellers unveiled the importance of these factors in mammalian development. In some models the inactivation of such factors lead to embryonic lethality (e.g. BRG1) or less severe symptoms when tissue-specific knockout was employed (such as abnormalities of T-cell development with T-cell specific depletion of BRG1). From de la Serna, Ohkawa, & Imbalzano, 2006.

1.3.3. SWI/SNF Chromatin remodellers.

The SWI/SNF family of chromatin remodellers is a family of complexes of around 10 proteins initially discovered in yeast, where mutants fail to undergo the mating type "switch" (SWI) and instead become "sucrose non-fermenters" (SNF). Like other chromatin remodelling families, the SWI/SNF complexes are conserved across higher eukaryotes, and use the energy of ATP hydrolysis to reposition nucleosomes and alter the accessibility of chromatin to activating or repressive factors. Such changes can have a profound impact on processes such as cellular differentiation, and are often accompanied by changes in gene expression (J. I. Wu, 2012).

SWI/SNF remodelling complexes are formed from 8-11 components, within which the ATPase subunit (e.g. BRM/BRG1/hBRM) alone is sufficient to catalyse partial chromatin remodelling alone. The other subunits aid in complex assembly and function specificity (e.g. promoter targeting), and allow for cell or tissue-specific complex function. For example, SNR1 subunit has been shown to block BRM activity and associates with gene repression during Drosophila wing/vein and inter-vein cell development, in a histone deacetylase (HDAC) dependent manner (Marenda et al., 2003). The interplay between multiple units determines the molecular and biological impact, and sequence comparison of the ATPse domain reveals the evolutionary relationship between SWI/SNF family members (Figure 1.6).

Interactions between SWI/SNF and other factors are important in human disease. As an example, the polycomb group repressor complex PRC2 often functions in an antagonistic manner to SWI/SNF complexes by promoting transcriptional repression (Kadoch, Copeland, & Keilhack, 2016). Mutation in either SWI/SNF or PRC complexes can lead to human malignancy, driven by a loss in the normal balance of SWI/SNF versus PRC action. Indeed, mutation in *SMARCB1* is associated with malignant rhabdoid tumours, mutations in *SMARCA2* and *SMARCA4* with breast and lung cancer (Kadoch et al., 2016), whereas loss of function mutations in PRC2 complex subunit *EZH2* or *EED* lead to T-cell acute lymphoblastic leukaemia (T-ALL) (K. H. Kim & Roberts, 2016).

Initial tissue and organ development is also dependent on the action of SWI/SNF remodellers. As an example, normal cardiogenic development is driven by the transcription factors TBX5, GATA-4, and these have been shown to interact with the SWI/SNF complex subunit BAF60c (Bevilacqua, Willis, & Bultman, 2014). In addition,

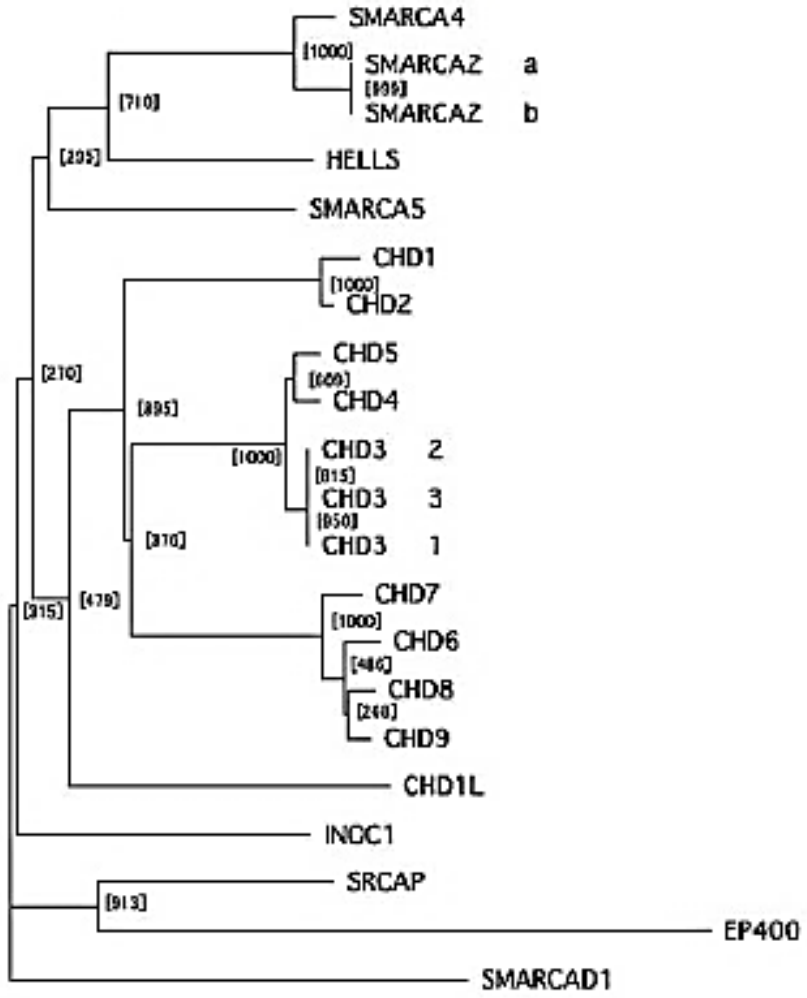

Figure 1.6. Phylogenetic tree of SWI/SNF chromatin remodelling family members, based on comparison of 10 different conserved regions. *SMARCA4* and *SMARCA2* (top) are the mammalian homologues of Drosophila *BRG1* and *BRM* respectively. *SMARCAD1* is most closely related to Snf2 related *CREBBP* activator protein (*SRCAP*) and E1A binding protein p400 (*EP400*) based on these sequence comparisons. From Okazaki et al., 2008.

cellular responses to environmental cues are also influenced by SWI/SNF remodellers – for example in the context of metabolism. SWI/SNF complexes containing BAF60a activate the transcription of fatty acid oxidation genes during fasting, whereas complexes containing BAF60c activate lipogenic genes in response to insulin, forming the lipoBAF complex that promotes lipogenesis and increased triglyceride levels (Zhang, Li, Bao, & Huang, 2016). In these examples, the role of SWI/SNF remodellers in cellular and physiological homeostasis has been made apparent.

1.3.4. The SWI/SNF family chromatin remodeller SMARCAD1.

SMARCAD1 (SWI/SNF-related, matrix-associated actin-dependent regulator of chromatin subfamily a, containing DEAD/H box 1, also known as ETL1/HEL1) is a SWI/SNF nucleosome remodeling enzyme that hydrolyses ATP driving histone/DNA structural compaction (Rowbotham et al., 2011). It is a member of the SWI2/SNF2 family of nucleic acid dependent helicase/ATPases, which are implicated in cell cycle control, mitotic chromosome segregation, DNA repair and transcriptional control (Costelloe et al., 2012). *SMARCAD1* orthologues are found across eukaryotic species from the budding yeast *S. Cerivisiae* (*Fun30*), to *Drosophila* (*CG5899*) to human and mouse (*SMARCAD1*/*Etl1*) (Neves-Costa, Will, Vetter, Miller, & Varga-Weisz, 2009) and contain conserved ATPase, helicase and CUE (coupling of ubiquitin to ER-degradation) domains (Figure 1.12, Section 1.3.9).

1.3.5. Identification of mammalian *SMARCAD1*/*ETL1* and initial studies.

Smarcad1/*Etl1* (Enhancer Trap Locus 1) was originally identified by Soininen et al in mouse (Soininen et al., 1992) as a gene highly expressed throughout development (especially in epidermal tissue and the central nervous system) with sequence similarity to the Drosophila gene *Brahma* and the (then) newly identified yeast transcriptional activator proteins SNF2/SNF2. A subsequent study using a mouse knockout model implicated *Smarcad1*/*Etl1* in skeletal development, growth and fertility, with decreased peri- and postnatal survival (Schoor, Schuster-Gossler, Roopenian, & Gossler, 1999). This study also confirmed the expression of SMARCAD1 from the two-cell stage of development, and in other embryonic tissues including the inner cell mass and (later in development) the central nervous system, epithelia and thymus. Postnatally SMARCAD1/ETL1 was shown to be ubiquitously expressed in mouse tissues, and knockout mice were reported to have a decrease in body weight of up to 25% by 5

weeks of age (Figure 1.7), along with skeletal dysplasias and reproductive problems (Schoor et al 1999).

1.3.6. SMARCAD1 is required for pluripotency in stem cells.

Following the observations that *Smarcad1* is expressed prenatally in embryonic and developing tissues, a study using cultured mouse embryonic stem cells (ESCs) showed that a number of highly expressed factors in cultured mouse embryonic stem cells were chromatin binding proteins, and upon differentiation (induced by removal of leukaemia inhibitory factor (LIF) from the culture media) this expression declines (Kurisaki et al., 2005). Furthermore, the authors then focussed on one of the factors identified (TIF1β) and showed that phosphorylated TIF1β forms a complex with the pluripotency-specific transcription factor OCT3/4 along with SMARCAD1, inhibiting differentiation (Seki et al., 2010). The maintenance of pluripotency was not driven by SMARCAD1 alone, as *Smarcad1* overexpression did not maintain the undifferentiated state, but rather the complex including SMARCAD1, TIF1β, OCT3/4 and other chromatin associated factors (BRG-1 and BAF155) were required to retain pluripotency.

Stage	*Etl1*$^{+/+}$ (%)	*Etl1*$^{-/+}$ (%)	*Etl1*$^{-/-}$ (%)	
Mixed (BL6/SV129) background				
D18 p.c.	**22**	**58**	**20**	
Newborns	**24**	**51**	**24**	
Adults	**29**	**59**	**13**	*
SV129 background				
Newborns	**27**	**48**	**27**	
Adults	**30**	**59**	**11**	*

(a)

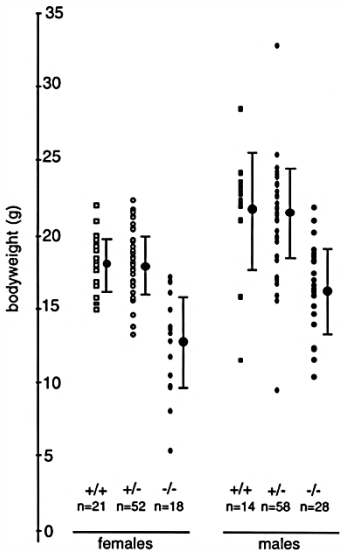

(b)

Figure 1.7. The original *Smarcad1*/*Etl1* knockout mice showed (a) increased postnatal mortality (*as denoted by the lower than expected 25% ratio of -/- adult mice) and reduced body weight by 5 weeks old (median body weight shown by black down to the right of data points, with error bars). From Schoor et al., 1999.

In agreement with this work, studies of gene expression patterns during the spontaneous differentiation of mouse embryonic stem (mES) cells into embryoid bodies revealed *Smarcad1* as one factor expressed in the undifferentiated mES cells but not in embryoid bodies (Hong et al., 2009). To validate this finding, expression of *Smarcad1* was knocked-down (i.e. expression was reduced using short-hairpin RNA transfection) in mES cells, and the loss of pluripotency was confirmed by the change in cell morphology and loss of alkaline phosphatase staining. Furthermore, analysis of a marker of differentiation (FGF5) using quantitative PCR (qPCR) revealed an elevation of FGF5 expression in mES cells four days after *Smarcad1* knock-down (Figure 1.8). These results confirmed that expression of *Smarcad1* is linked to pluripotency in mES cells.

Using a different cell type, a more recent study established a link between *Smarcad1* and the pluripotency factor *Sox-2* (SRY [sex determining region Y]-box 2). *Smarcad1* had been previously shown to be a downstream target of SOX2 in embryonic stem cells (Boyer et al., 2005), and indeed SOX-2 was subsequently shown to be one of four key transcription factors required for induction of pluripotency (Takahashi & Yamanaka, 2006). However, the role of SOX-2 and SMARCAD1 in tissue-resident precursor cells such as mesenchymal stem cells had not previously been elucidated. Osteoblasts and preadipocytes are both lineage-committed precursors derived from mesenchymal stem cells (which contribute to the production of bone, fat, muscle or cartilage). In this set of experiments, the deletion of *Sox-2* in osteoblasts was shown to deplete the ability to self-renew, and this loss was accompanied by the loss of *Smarcad1* expression (alongside other markers of pluripotency) (Seo, Basu-Roy, Zavadil, Basilico, & Mansukhani, 2011).

The molecular function and interactions of *Smarcad1* during pluripotency have recently been investigated using pre- and post-implantation embryos in human and mouse. In this study, particular focus was given to histone modifications that are associated with SMARCAD1 at this early stage of development. Ten histone modifications were examined for potential genomic co-localisation with SMARCAD1, of which two demonstrated such genomic overlap; H3K27-acetyl and H3K27-citrullinate. To further infer the role of these modifications in stem cell biology, the genomic binding sites of SMARCAD1 were compared with the pluripotency transcription factor OCT-4, and indeed enrichment of both SMARCAD1 and OCT-4 was found at sites of H3K27 citrullination (Figure 1.9). Interestingly, loss of SMARCAD1 in these stem cells was associated with an increase in H3K9me3 marks, implying that SMARCAD1 functions to

oppose formation of repressive chromatin in this particular cell type (S. Xiao et al., 2017).

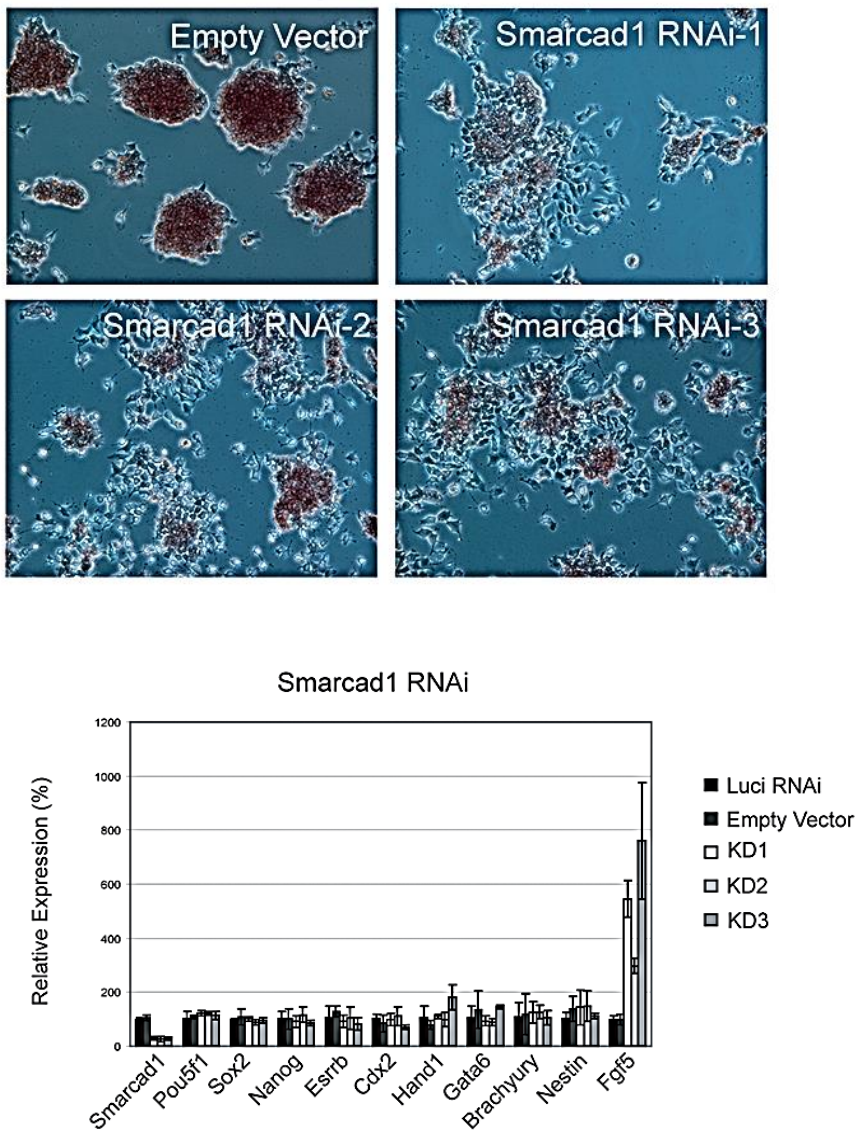

Figure 1.8. SMARCAD1 is required for maintenance of pluripotency in mES cells (from Hong et al 2009). Knock-down of SMARCAD1 expression (a) results in altered morphology and reduced alkaline phosphatase staining (panels RNAi-1, RNAi-2, RNAi-3 above left) alongside increased expression of the differentiation marker FGF5 (above right). From Hong et al., 2009.

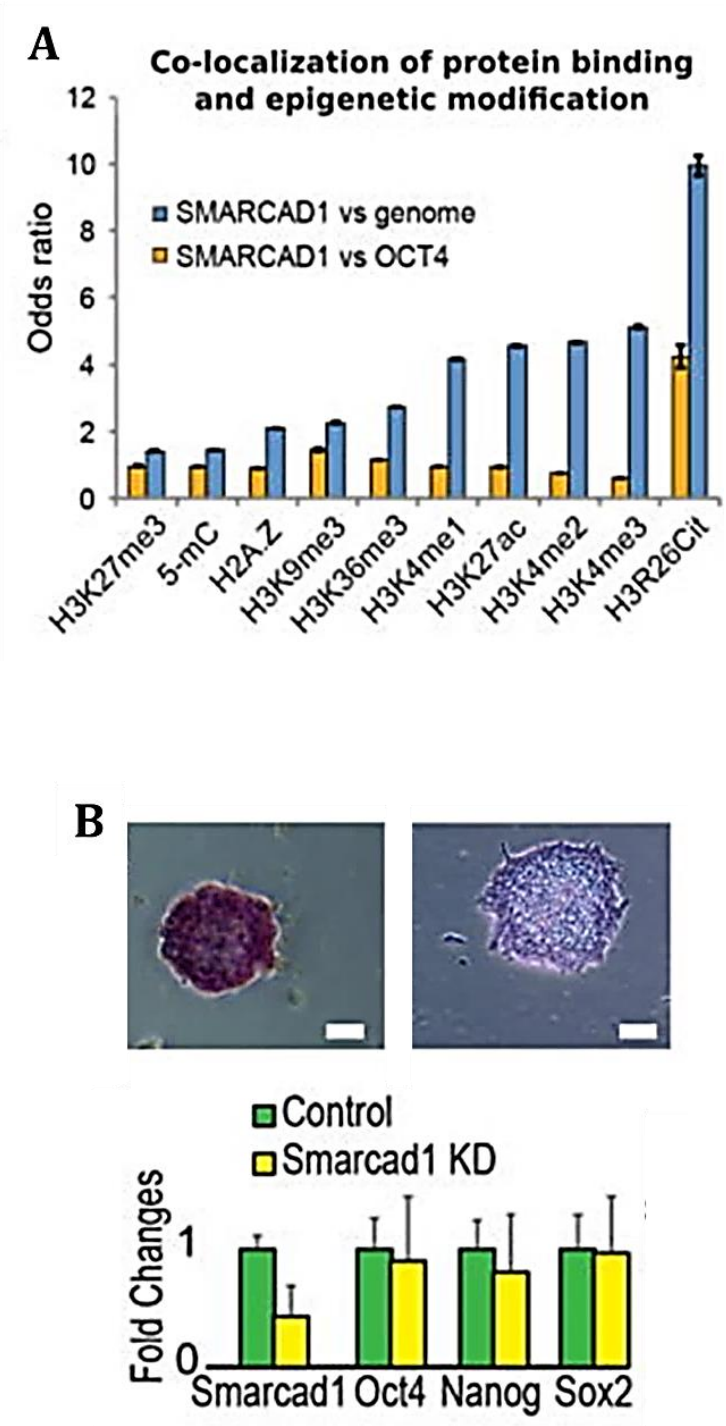

Figure 1.9. (a) SMARCAD1 associates with citrullinated histone H3-K26-Ci in mouse embryonic stem cells (top). (b) *Smarcad1*-depleted mESCs show a reduction in maintenance of pluripotency (shown be the drop in alkaline phosphatase staining between the two images in yet without significant reduction in expression of the pluripotency transcription factors OCT4, NANOG or SOX-2 (bottom). From Xiao et al., 2017.

1.3.7. SMARCAD1 and transcription.

In addition to the work on mES cells, work in Drosophila and human cells has provided insight into the impact of SMARCAD1 on gene expression. Using nuclear extracts from the Drosophila S2 cell line, the ATP-dependent acetylation of histone H2A was shown to be driven by SMARCAD1 and CREB-binding protein (CBP) and associated with up-regulation of a number of target genes (Doiguchi et al., 2016). Furthermore, acetylation of H2A-K5 and H2A-K8 was a result of CBP action, and enhanced by SMARCAD1 - thereby suggesting SMARCAD1 was an accessory factor in histone modification. Subsequent chromatin immunoprecipitation (ChIP) analysis localised CBP and SMARCAD1 to the promoter region of a number of genes, and interestingly the initial CBP recruitment was required for subsequent presence of SMARCAD1 at these sites (Doiguchi et al., 2016).

A previous study using human cancer cell lines described the binding of SMARCAD1 to the vicinity of the transcriptional start site (TSS) of 69 genes. Using a novel anti-SMARCAD1 antibody (generated against 175 C-terminal amino acids of SMARCAD1) for chromatin-immunoprecipitation, genomic DNA bound to SMARCAD1 could be mapped back to the genome using DNA microarrays. Results from these experiments identified the region of -350 to -250 bases from the TSS as strongest for SMARCAD1 binding, with the region between -450 and +350 bases implicated in SMARCAD1 binding (Okazaki et al., 2008). Furthermore, this study revealed the association of SMARCAD1 with the transcriptional repressor KAP1 (TRIM-28) at these loci; however, any changes in specific gene expression in the absence of SMARCAD1 was not explored (Okazaki et al., 2008).

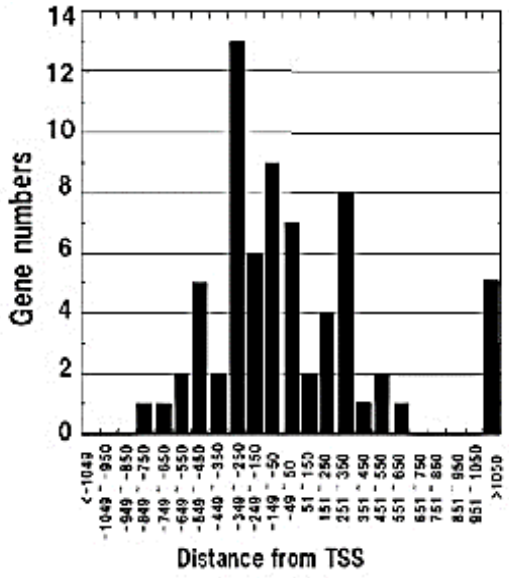

Figure 1.10. Binding of SMARCAD1 to the vicinity of the transcription start site of 69 candidate genes, revealed by ChIP-on high-resolution tiling arrays. Each peak corresponds to the array signal produced from SMARCAD1-associated DNA binding to (mapped) probes on the array. The probes on the array are approximately 100bp in length, and tile across regions +/- 1kb of Transcriptional Start Sites (TSS). From Okazaki et al., 2008.

1.3.8. SMARCAD1 facilitates DNA repair after double-strand breaks.

A number of studies have linked SMARCAD1 to DNA repair mechanisms. One group investigated both the mammalian and the yeast homologue (*Fun30*) and showed that SMARCAD1 is required for long range resection of DNA immediately after double-strand breaks (Costelloe et al., 2012). Further to this, a study investigating the mechanisms of DNA repair pathway choice demonstrated that the switch from the (resection-inhibiting) 53BP1 repair pathway is driven by the ubiquitin ligase activity of the BRCA1-BARD1 complex acting on histone H2A. Ligation of ubiquitin to H2A subsequently allows the binding of SMARCAD1, driving resection and homologous recombination with the remodelling of chromatin and repositioning of 53BP1. Indeed, the resistance to drug induced DNA damage (after e.g. olaparib or camptothecin treatment) facilitated by

SMARCAD1 can also be brought about by 53BP1 loss, enhancing selection of the BARD1-BRCA1 repair pathway (Densham et al., 2016).

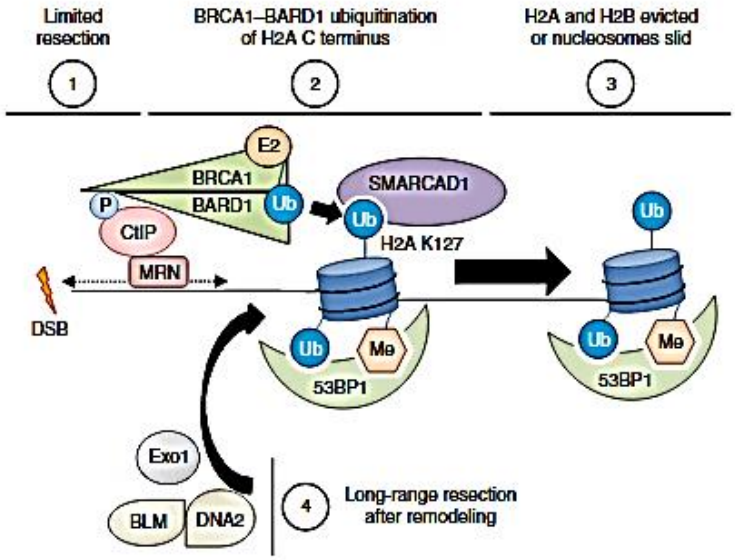

Figure 1.11. Proposed model for the role of SMARCAD1 in DNA double-strand break repair. Initial DNA resection (i.e. production of a long single-stranded 3' overhang for homologous recombination events) proceeds at a limited rate by the CTIP and MRN proteins. Ubiquitination of histone H2A by the BRCA1/BARD1 complex allows the binding of SMARCAD1 to H2A, and increased resection (facilitated by nucleosome sliding) with inhibition of the 53B1 mediated resection-block. From Densham et al., 2016.

1.3.9. SMARCAD1 and chromatin compaction.

Further to the work linking SMARCAD1 to transcription and DNA repair, one study identified the role of SMARCAD1 in restoration of heterochromatin after DNA replication (Rowbotham et al., 2011). Mass spectrometry of purified (flag-tagged) SMARCAD1 and subsequent immunoprecipitation experiments identify a complex containing SMARCAD1, the transcriptional repressor KAP1, the histone deacetylases HDAC1/2, the histone methyltransferase G9a/GLP, heterochromatin protein 1 (HP1α), and proliferating cell nuclear antigen (PCNA), thus localizing this complex to the replication fork (Figure 1.13a). (Rowbotham et al., 2011). These data suggest that SMARCAD1 influences known marks linked to epigenetic repression, and maintains these after cells divide (Mermoud, Rowbotham, & Varga-Weisz, 2011).

While these associations link SMARCAD1 function to cell division, in the same study the loss of SMARCAD1 *in vitro* was shown to have no gross effect on either cell cycle progression or DNA synthesis (Figure 1.13b). Synchronized control of SMARCAD1-depleted cells analyzed over a 24 hour time-course showed no significant difference in the proportion of cells present in each phase of the cell cycle at each time point, and studies of DNA synthesis using EdU incorporation again revealed no significant difference between control and SMARCAD1-depleted cells. However, a global increase in histone H3 acetylation and decrease in HP1α and histone H3-Lysine 9 (H3K9) tri-methylation, was observed, suggesting SMARCAD1 loss also drives a global decrease in heterochromatin. Together these data indicate that loss of SMARCAD1 does not impact progression of the cell cycle itself, although global differences in markers of heterochromatin are found (Figure 1.14) (Rowbotham et al., 2011).

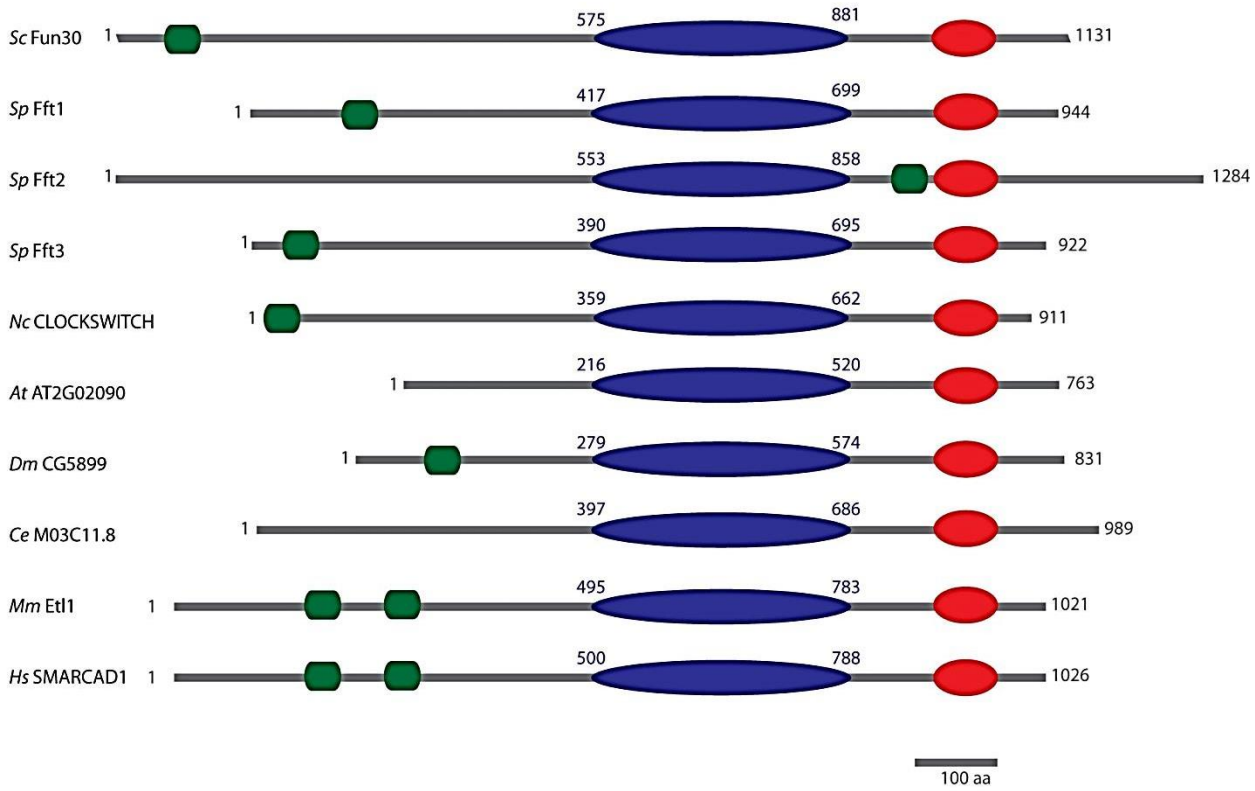

Figure 1.12. Schematic domain alignment of SNF2-factor family members showing ATPase domains (blue), helicase domains (red) and CUE motifs (green). Top to bottom (species/homologue) *Saccharomyces cerevisiae* (*Sc*) Fun30, *Schizosaccharomyces pombe* (*Sp*) Fft1, Fft2, Fft3, *Neurospora crassa (Nc)* CLOCKSWITCH, *Arabidopsis thaliana (At)* AT2G02090, *Drosophila melanogaster (Dm)* CG5899, *Caenorhabditis elegans (Ce)* M03C11.8, Human /mouse (*Hs, Mm*) *SMARCAD1*/ETL1 From Neves-Costa et al., 2009.

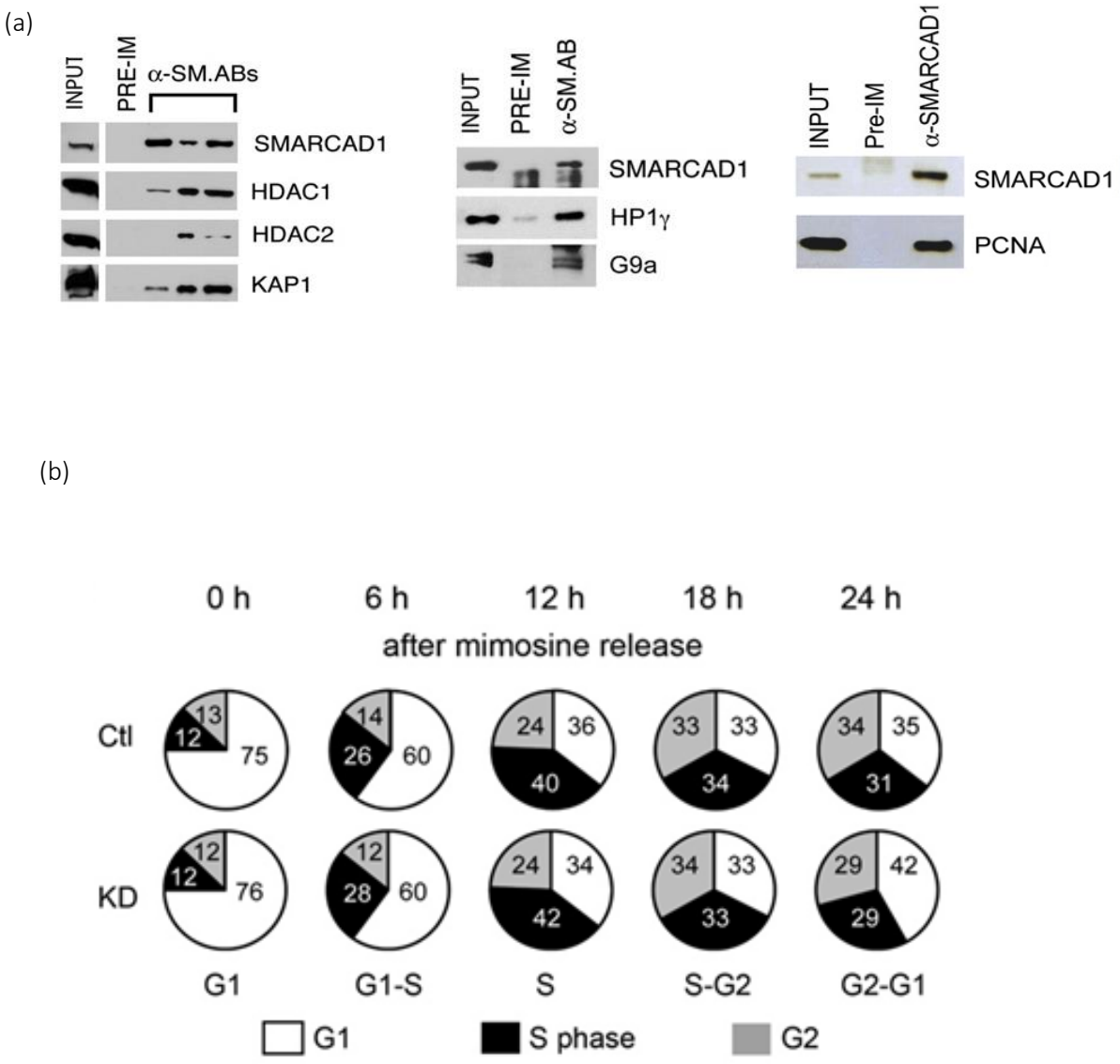

Figure 1.13. (a) Immunoprecipitation of *SMARCAD1* reveals bound interaction partners associated with compact chromatin marks such as histone deacetylaces 1 and 2 (HDAC1/2) and histone methyltransferase G9a, the transcriptional repressor KAP1, heterochromatin protein 1 α (HP1α) and proliferating cell nuclear antigen (PCNA). (b) Proportion of cells in each phase of the cell cycle after synchronization with mimosine at time points up to 24 hours in control (ctl) HeLa cells and *SMARCAD1* knock-down (KD) HeLa cells. No significant difference is seen at each time point. From Rowbotham et al., 2011.

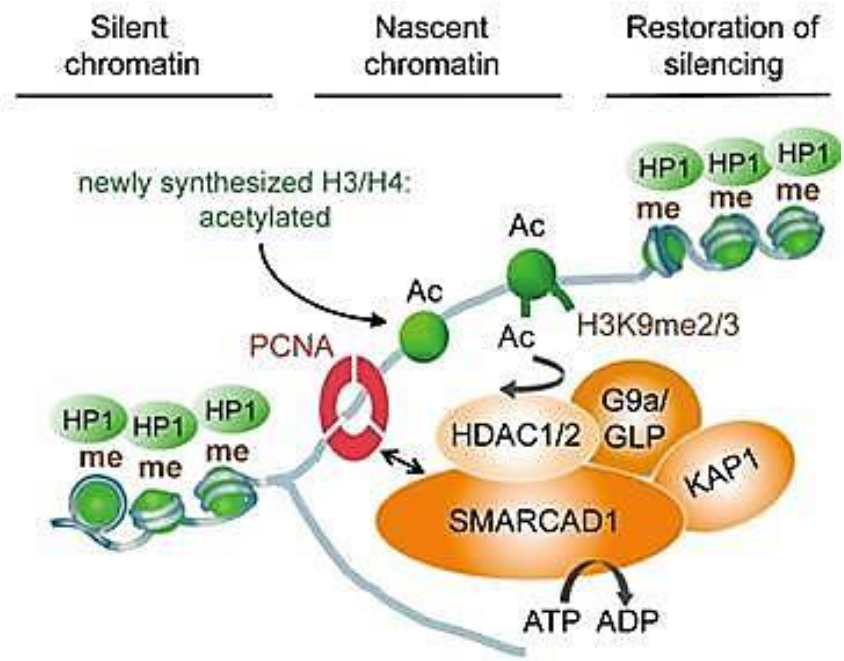

Figure 1.14. Model of the action and interactions of *SMARCAD1* behind the replication fork, restoring markers of heterochromatin (e.g. H3K9me3) during DNA replication. *SMARCAD1* forms a complex with histone deacetylases 1 and 2 (HDAC1/2), the histone methyltransferase G9a/GLP and the KAP1 transcriptional corepressor protein, along with Proliferating Cell Nuclear Antigen (PCNA), placing the complex in the proximity of the replication fork. From Rowbotham et al., 2011.

1.3.10 SMARCAD1 in human disease.

Shortly after the description of the *Smarcad1*/*Etl1* knockout mouse, the human *SMARCAD1* gene was described and mapped to chromosome 4q22 – a region associated with genome instability and human diseases (in particular hepatocellular carcinoma / hematologic malignancies) (Adra et al., 2000). More recently, a screen of head and neck cancers identified this same genomic region as one frequently deleted in these cancers (Cetin et al., 2008), and furthermore increased survival time in bladder cancer has been associated with *SMARCAD1* expression (Tapak, Saidijam, Sadeghifar, Poorolajal, & Mahjub, 2015). Further to these observations, a missense mutation of *SMARCAD1* was shown to increase sensitivity to the oral 5-fluorouracil (5-FU) prodrug capecitibine (O'Donnell et al., 2012). This may be no surprise given the mechanism of action of capecitibine (DNA damage) and the role of SMARCAD1 in DNA repair.

While it is likely that the direct interaction of SMARCAD1 with chromatin directly underpins these disease associations, one study implicated SMARCAD1 as an important factor in breast cancer migration, invasion and metastasis. Using the invasive breast cancer cell line MDA-MB-231, knock-down of *SMARCAD1* was shown to increase cell-cell adhesion with decreased cell migration, invasion, and metastasis. This effect was shown to be linked to the inhibition of the transcription factor STAT3 phosphorylation, which may reflect the impact that chromatin interactions have on downstream cell biological events (Al Kubaisy, Arafat, De Wever, Hassan, & Attoub, 2016).

In addition to these associations with cancer, a meta-analysis of 3 genome wide association studies (GWAS) - covering 931 individuals with testicular germ cell tumours (TGCT) and 1975 unaffected controls - identified the region containing *SMARCAD1* (4q22.2) as one of four genomic loci associated with TGCT (C. C. Chung et al., 2013). Interestingly, a reduction in expression of *SMARCAD1* has also been reported in the sperm of infertile men (Bansal, Gupta, Sankhwar, & Rajender, 2015). RNA expression array analysis of spermatozoa from normal (fertile), normozoospermic (infertile but normal motility) and asthenozoospermic (infertile and impaired motility) men revealed a down-regulation of *SMARCAD1* specifically in the asthenozoospermic group. This may be unsurprising given the reduced fertility reported in the original mouse *Smarcad1*/*Etl1* knockout model (Schoor et al 1999).

Two phenotypically overlapping diseases linked to epidermal differentiation have been associated with *SMARCAD1* mutations. The inability to develop fingerprints is the

hallmark of human adermatoglyphia. A recent study of Autosomal-Dominant Adermatoglyphia (ADA) in humans identified a short isoform of *SMARCAD1* - containing an alternative transcription start site, whose expression is required for the development of epidermal ridges in human fingerprints (Nousbeck et al., 2011). Tissue expression of this shorter isoform of *SMARCAD1* was shown to be greatest in skin fibroblasts (compared to the longer isoform), and also present in keratinocytes and the esophagus. Loss of expression of the short isoform was reported in a family who lacked fingerprints and hence experienced repeated problems when trying to enter foreign countries during global travel (and hence the alternative name 'immigration delay disease'). Linkage analysis and subsequent sequencing of *SMARCAD1* identified a point mutation which ablated expression of the short isoform, leading to loss of fingerprints (Figure 1.15).

A second disease linked to epidermal differentiation has also been associated with mutations in *SMARCAD1*. Symptoms of Basan syndrome are more severe then ADA, with widespread blistering, lack of sweating and palmoplantar epidermal ridges (i.e. lacking from the soles of the feet and palms of the hand) and thickening of the skin. A heterozygous splicing variant of the short isoform of *SMARCAD1* was associated with Basan syndrome across a 3-generation pedigree (Marks, Banks, Cunningham, Witman, & Herman, 2014) in an American family, and variants at the same base were also reported across 8 individuals of a 4-generation pedigree in China (M. Li et al., 2016). Together, these associations of *SMARCAD1* with numerous cancers and disorders of epidermal differentiation highlight the importance of this chromatin remodeler in differentiation and proliferation.

While the short isoform of *SMARCAD1* has to date been described in human, it is worth noting that the first exon of the alternative isoform is conserved and in-frame across a number of species (Figure 1.16). While expression of this short isoform is yet to be confirmed in mouse, the sequence conservation across multiple genomes lends weight to the possibility that short isoform expression is also conserved. Importantly, while the previously reported *Smarcad1*/*Etl1* knockout mouse model introduced a frameshift mutation in the first exon of (canonical) *Smarcad1* (ablating expression of the full length transcript), it is possible that these mice still expressed the short isoform of (Schoor et al 1999). Targeting of the ATPase domain in exons 12 to 14 as described in this thesis thereby targets both short and long (canonical) isoforms of *Smarcad1*.

(a)

(b)

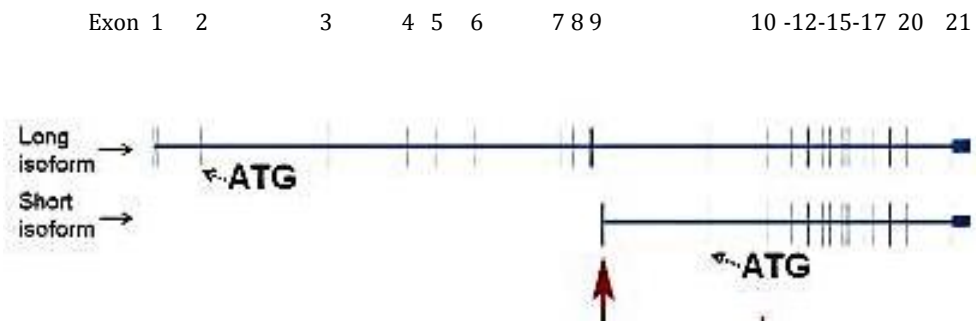

Figure 1.15 (a) Loss of epidermal ridges (fingerprints) visible in a patient with adermatoglyphia (b) presence of an alternative start site for *SMARCAD1* producing a short isoform (red arrow) which is lost in adermatoglyphia. Previous *Smarcad1*/*Etl1* knockout models introducing a nonsense 1.1 mutation proximal to the canonical transcription start site would have retained this isoform. From Nousebeck et al., 2011.

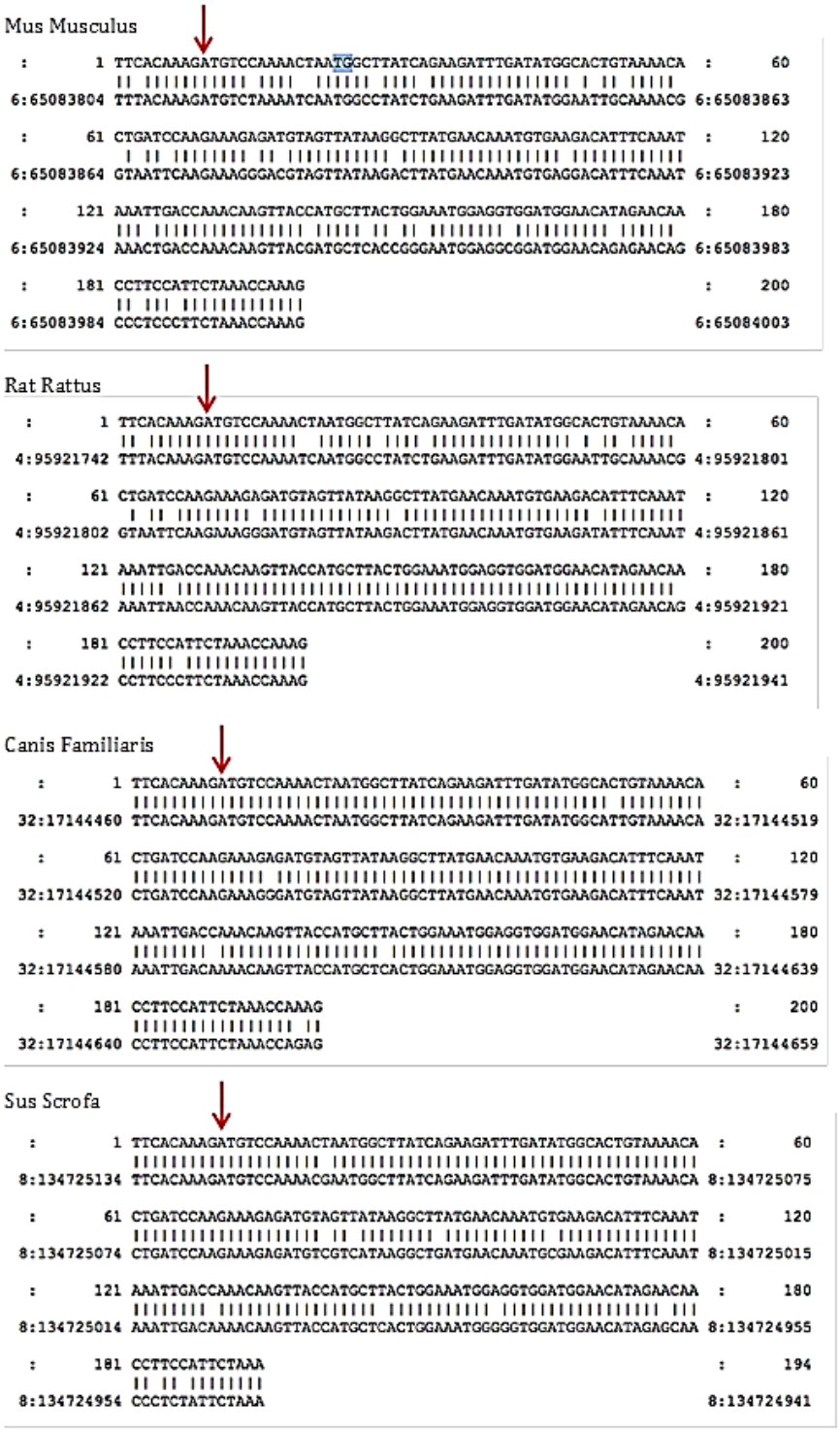

Figure 1.16. The alternative first exon of the shorter *SMARCAD1* isoform is conserved and in frame across mammalian species such as (top to bottom) mouse, rat, dog and pig. The red arrow indicates position of the ATG start codon, and each sequence is aligned against the short isoform first exon from human.

(Table Overleaf)

Table 3 (overleaf). Summary table of recent publications on mammalian SMARCAD1. Alongside the lead author and journal details, each publication is categorised by whether the focus of research was on the molecular, cell biological or biological impact of SMARCAD1 on the specific model organism used.

Publication overview		Experimental Impact.			
Authors	Outline	Model	Molecular	Cellular impact	Biological Impact
1: Xiao S et al.	Regulation of Naïve Pluripotency / histone modification.	Mouse	Histone citrullination	Pluripotency	Stem Cell Pluripotency
2: Taneja N et al.	Nucleosome Turnover and Epigenetic Inheritance during Replication.	Yeast	Nucleosome turnover	Cell division	Cell Division
3: Bantele SC et al.	DNA repair during replication	Human	N/A	N/A	DNA repair
4: Densham RM, Morris JR.	DNA repair pathways	Human	N/A	N/A	DNA repair
5: Densham RM et al.	DNA repair pathways	Human	N/A	N/A	DNA repair
6: Al Kubaisy E et al.	Cancer biology impact	Human	Comparative Gene Expression	N/A	Cancer biology
7: Tapak L et al.	Cancer biology impact / cancer metastasis	Human	N/A	N/A	Cancer biology
8: Li M et al.	Genome wide candidate identification / Basan Syndrome	Human	N/A	N/A	Basan Syndrome
9: Doiguchi M et al.	Histone modifications and transcription	Drosophila	Histone acetylation / gene expression	N/A	Gene regulation
10: Sittig LJ et al.	Identification of genes in mouse neurological responses.	Mouse	N/A	N/A	Neurological response
11: Bansal SK et al	Transcriptomic analysis of spermatozoa in infertility	Human	Expression	N/A	Spermatozoa
12: Tapak L et al.	Meta analysis of bladder cancer samples	Human	Expression	N/A	Bladder cancer
13: Nousbeck J et al.	Identification of mutations in fingerprint development disorders	Human	Expression	N/A	Fingerprint development
14: Marks KC et al.	Identification of mutations in Basane Syndrome	Human	Expression	N/A	Basan Syndrome
15: Costelloe T et al.	Molecular role of SMARCAD1 in DNA repair	Human and Yeast	DNA repair	N/A	DNA repair
16: O'Donnell PH et al.	Identification of sensitizers to capecitabine induced DNA damage	Human	DNA repair	N/A	DNA repair
17: Dereure O.	Role in fingerprint development.	Human	N/A	N/A	Fingerprint development
18: Mermoud JE et al.	Role in heterochromatin replication during cell division.	Human	Heterochromatin.	Cell division	Cell Division
19: Nousbeck J et al.	Identification of mutations in fingerprint development disorders	Human	Expression	N/A	Fingerprint development
20: Rowbotham SP et al.	Role in heterochromatin replication during cell division.	Human	Heterochromatin.	Cell division	Cell Division
21: Jasencakova Z, Groth A.	Role in heterochromatin replication during cell division.	Human	Heterochromatin.	Cell division	Cell Division
22: Hong F et al	Identifying genes influential in ESC differentiation.	Mouse	Expression	Pluripotency	Embryonic Stem Cells
23: Okazaki N et al.	Genomic localisation of SMARCAD1 to transcription start sites (TSS).	Human	Transcriptional start / expression	N/A	Transcriptomic
24: Cetin E et al.	Implication of genomic locus in head and neck cancers.	Human	N/A	N/A	Cancer biology
25: Lim DA et al.	Transcription and chromatin events in neurogenesis	Mouse	Transcriptomic	Pluripotency	Neurogenesis
26: Bluteau O et al.	Link of genomic region loss to hepatocellular carcinomas	Human	N/A	N/A	Cancer biology
27: Adra CN et al.	Genomic linkage of SMARCAD1 to chromosome instability and disease.	Human	N/A	N/A	Chromosome stability
28: Schoor M et al.	Impact of SMARCAD1 on murine development.	Mouse	N/A	N/A	Murine development.
29: Soininen R et al.	Comparison of murine SMARCAD1 with other species	Mouse/Drosophila	Transcriptional regulation	N/A	Gene regulation
30: Korn R, Schoor M, Neuhaus	SMARCAD1 expression detected in murine embryonic tissue.	Mouse	Expression	N/A	Murine development.

Table 3. Summary table of recent publications on mammalian SMARCAD1.

1.4 Genomic imprinting and the influence of imprinted genes on metabolism.

Genomic imprinting refers to the dosage control of a gene *via* epigenetic repression of one or other of the maternally or paternally inherited alleles. Imprinted genes have been shown to play a role in fetal development and neonatal survival, and influence feeding, metabolism, body temperature and maternal nurturing behaviour (Peters, 2014). Control is exerted by regulating the expression of genes which impact these factors and behaviours, sometimes during critical developmental windows. Furthermore, tissues and organs involved in metabolism are a primary location for imprinting mechanisms to exert this control (Figure 1.17).

1.4.1. Imprinted genes and metabolism.

A number of murine models of imprinting dysfunction have been created to understand the role that these genes play (Table 4). The impact of the loss of this dosage control can be severe (e.g. prenatal mortality), can be visible at birth (e.g. increased or decreased birth weight) and/or present throughout life (such as increased adiposity or dysregulation of blood glucose levels) (Peters, 2014). Interestingly, a number of these imprinted genes have overtly opposing functions. For instance, insulin-like growth factor 2 (*IGF2*) promotes embryonic growth, whereas the receptor IGF2R binds to IGF2 and facilitates clearance from the cell surface, preventing further IGF2-mediated signalling - thereby opposing IGF2 function (Gicquel et al., 2004). Other imprinted genes such as delta-like 1 homologue (*Dlk1*) and growth factor receptor-bound protein 10 (*Grb10*) also impart opposing functions. Loss of expression of *Dlk1* leads to low birth weight with adult-onset obesity in mice, whereas the loss of *Grb10* expression produces overweight pups which develop into lean adults (Haig, 2014).

Interestingly, many imprinted loci contain reciprocally regulated genes, i.e. some of the genes in the region are expressed only from the maternally-inherited allele, others only from the paternal allele. As an example, in the *Dlk1-Dio3* region of mouse chromosome 12, the genes *Dlk1*, Retrotransposon-like 1 (*Rtl1*) and Iodothyronine deiodinase 3 (*Dio3*) are all expressed from the maternal allele, whereas in the same region the genes Gene trap locus 2 (*Gtl2*) and miRNA containing gene (*Mirg*) are exclusively expressed from the paternal allele (Figure 1.18). Aberrant expression of *Dlk1* from the paternal allele or increased dosage of *Dlk1* leads to an increase in body mass and adiposity in mice,

although, conversely, decreased *Dlk1* expression is linked to dwarfism (Steshina et al., 2006; Teixeira da Rocha et al., 2009).

Gene and imprinted cluster	Expressed allele	Gene expression in mutant mice	Prenatal to weaning viability and birthweight	Suckling ability	Birth to weaning growth and metabolic phenotype	Adult feeding	Adult metabolic phenotypes
Rasgrf1 chromosome 9	Pat	Loss	• Viable to birth; weaning viability not recorded • Normal birth weight	NR	Growth retardation followed by catch-up growth	Unaffected	Leanness, increased lipid catabolism, glucose intolerance and hypoinsulinemia
Grb10 proximal chromosome 11	Mat	Loss	• Some perinatal lethality • Increased birth weight	NR	Larger at birth and weaning	Unaffected	Leanness, increased glucose tolerance and increased insulin sensitivity
	Mat	Increase	• Viable • Decreased birth weight	NR	Smaller at birth and weaning	NR	Small body size, insulin resistance and impaired glucose tolerance
Dlk1 chromosome 12	Pat	Loss	• Viable to birth with much perinatal lethality • Decreased birth weight	NR	Small at birth and weaning	NR	Obesity
	Pat	Increase	• Viable to birth with some neonatal lethality • Increased birth weight	Impaired	• Growth retardation followed by catch-up growth by adulthood • Euglycaemia	NR	Leanness, insulin resistance and impaired glucose tolerance
Dio3 chromosome 12	Pat	Loss	Some lethality around or before birth	NR	Growth retardation at weaning	NR	Leanness and glucose intolerance

Table 1.4. Models of imprinted gene dysregulation lead to developmental and/or metabolism-related phenotypes. Above is a subset of imprinted genes and the effect of gain or loss of expression on murine phenotype. For example, mice with over-expression of *Dlk1* exhibit increased birth weight with some neonatal lethality, post-natal growth retardation (with growth catch-up by adulthood), leanness and insulin resistance. Conversely, increased expression of *Grb10* leads to decreased birthweight, with no catch-up growth by adulthood (From Peters, 2014).

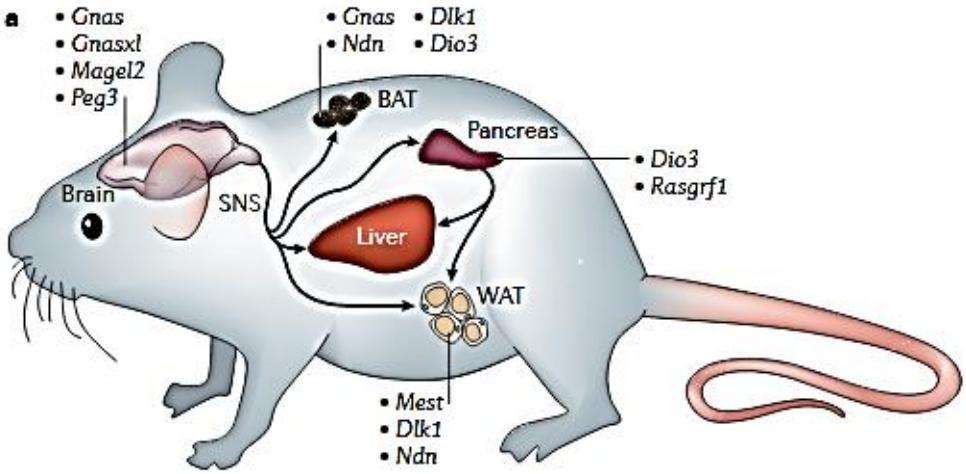

Figure 1.17. Imprinted genes impact mouse metabolism *via* expression in multiple metabolism-related organs. Effects include control of factors such as appetite in the brain, and regulation of blood glucose concentration. Dosage control may be evident during specific developmental windows, and hence identification of gene dysregulation in neonatal organs (e.g. WAT or liver) may identify the gene driving any subsequent phenotype (Kelsey, G, per comm.). From Peters, 2014.

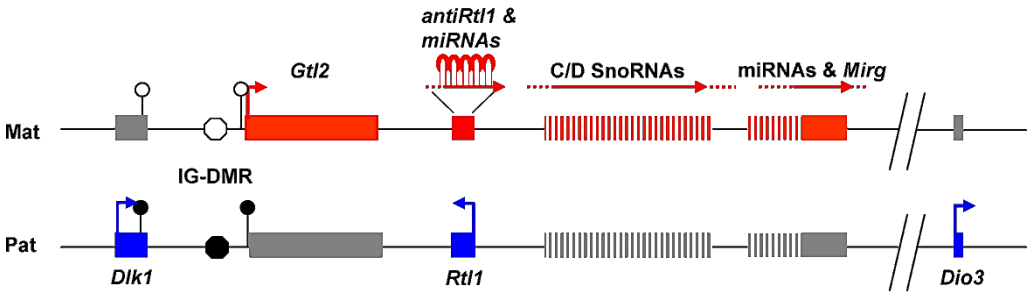

Figure 1.18 Imprinting in the *Dlk1-Dio3* region of mouse chromosome 12. Delta like homologue 1 (*Dlk1*) is expressed on the paternally-inherited allele (blue), alongside retrotransposon-like 1 (*Rtl1*) and deiodinase, iodothyronine, type iii (*Dio3*). Inappropriate expression of *Dlk1* has been shown to drive an increase in body mass and adiposity postnatally, with linked metabolic complications. By contrast, Gene Trap Locus 2 (*Gtl2*) is expressed from the maternally-inherited allele, and loss of the normal balance of *Dlk1/Gtl2* expression (and decreased *Dlk1* expression) is linked to dwarfism and partial neonatal lethality. From Edwards et al., 2008.

1.4.2. SWI/SNF chromatin remodellers and the KCNQ1 imprinted locus.

The chromatin remodelling factors SMARCAD1 and SMARCA5 have themselves been implicated in imprinted dosage control at the *KCNQ1ot1* imprinted gene locus. In this region, multiple genes are expressed from the maternally-inherited allele only (including *Ascl2, CD81, TSSC4* and *KCNQ1*), and expression of the anti-sense non-coding RNA transcript *KCNQ1ot1* from the paternal allele represses these genes (Figure 1.19). The knock-down of *Smarcad1* and *Smarca4* expression in embryo-derived stem cells led to increased expression of *Kcnq1* and *Cdkn1c*, but no difference in *Slc22a18*, indicating that the control of expression is not domain-wide. Furthermore, ablation of *Smarcad1* and *Smarca4* expression was linked to a decrease in *Kcnq1ot1* levels, suggesting that the effect is not mediated by KCNQ1ot1 but instead is a direct result of SMARCAD1 and SMARCA4 (Landschoot, 2014). Whether either of these remodellers impact other imprinted gene loci has yet to be explored.

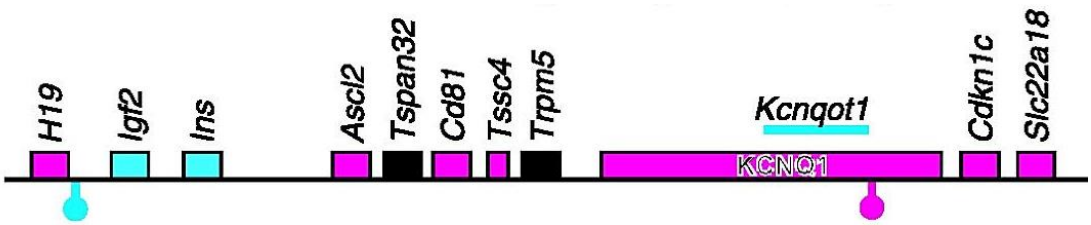

Figure 1.19. Mouse distal chromosome 7 contains the *Igf2* / *Kcnq1* imprinted region. Expression of the non-coding RNA *Kcnqot1* leads to repression of the *Ascl2*, *Cd81*, *Tssc4* and *Kcnq1* genes on the paternally-inherited allele. Repression of *Cdkn1c* and *Kcnq1* is facilitated by the chromatin remodellers SMARCAD1 and SMARCA5.

1.4.3. Chromatin remodelling controls *Dlk1* expression during adipogenesis.

Central to dosage control, chromatin binding factors direct the accessibility of imprinted genes. *Dlk1* – which is also known as pre-adipocyte factor 1 (*Pref-1*) - inhibits adipogenesis and is regulated by the histone binding protein Cooperator of PRMT5 (*Copr5*). In fact, COPR5 directs the binding of PRMT5 (Protein Arginine Methyltransferase 5) to chromatin and the subsequent methylation of histone H4 R3. The binding of PRMT5 to the *Dlk1* promoter reduces *Dlk1* expression, thereby aiding

adipogenesis. In *Copr5* knock-out mouse embryonic fibroblasts (MEFs) and white adipose tissue (WAT), expression of *Dlk1* was up-regulated, and indeed knockout mice showed reduced retroperitoneal white adipose tissue size by 8 – 16 weeks old (Paul, Sardet, & Fabbrizio, 2015). In parallel to this observation, the adipocyte lineage-controlling transcription factor, peroxisome proliferator-activated receptor γ2 (*PPARγ2*) requires the binding of PRMT5 to the *PPARγ2* promoter region, leading to formation of an accessible 3D-loop and binding of the ATPse dependent remodeller BRG1 (LeBlanc, Wu, Lamba, Sif, & Imbalzano, 2016).

1.5 Adipocyte lineage differentiation and chromatin.

1.5.1. Chromatin remodellers and adipocyte differentiation.

The pathways controlling adipogenic/osteogenic differentiation from bone marrow mesenchymal stem cell (MSC) precursors is known to be influenced by SWI/SNF chromatin remodelling complexes (Nguyen et al., 2015). Mesenchymal stem cells harbour the potential to differentiate into multiple different cell types, such as chondrocytes (which produce cartilage), osteocytes (bone cells), adipocytes (fat cells), myocytes (muscle), skin fibroblasts or astrocytes of the central nervous system (CNS) (Figure 1.20). Investigation of the SWI/SNF remodeller BRM revealed that *Brm* depletion favours differentiation toward the osteoblast lineage, as MSC populations depleted of *Brm* show an increase in the proportion of cells expressing the osteoblast markers Alkaline Phosphatase (*Alpl*) and Fibroblast Growth Factor Receptor type-2 (*Fgfr2*), with a marked reduction in the ability to differentiate down the adipocyte lineage following *in vitro* adipogenic stimulation (Figure 1.21). Furthermore, the increased commitment to the osteoblast lineage and impaired adipogenesis was recapitulated in primary mesenchymal stem cells isolated from *Brm-/-* mice and the mesenchymal stem cell line C3H10T1/2 (MSC), in addition to mouse embryonic fibroblasts (NIH-3T3, which harbour adipogenic potential) and the lineage committed 3T3-L1 preadipocyte and MC3T3-E1 osteoblast cell lines. Interestingly, closer examination of bone marrow from *Brm-/-* mice revealed a reduction in bone marrow adiposity and resistance to age-related osteoporosis. These results highlight the importance and potential of SWI/SNF remodelling complexes in differentiation and age-related pathologies (Nguyen et al., 2015).

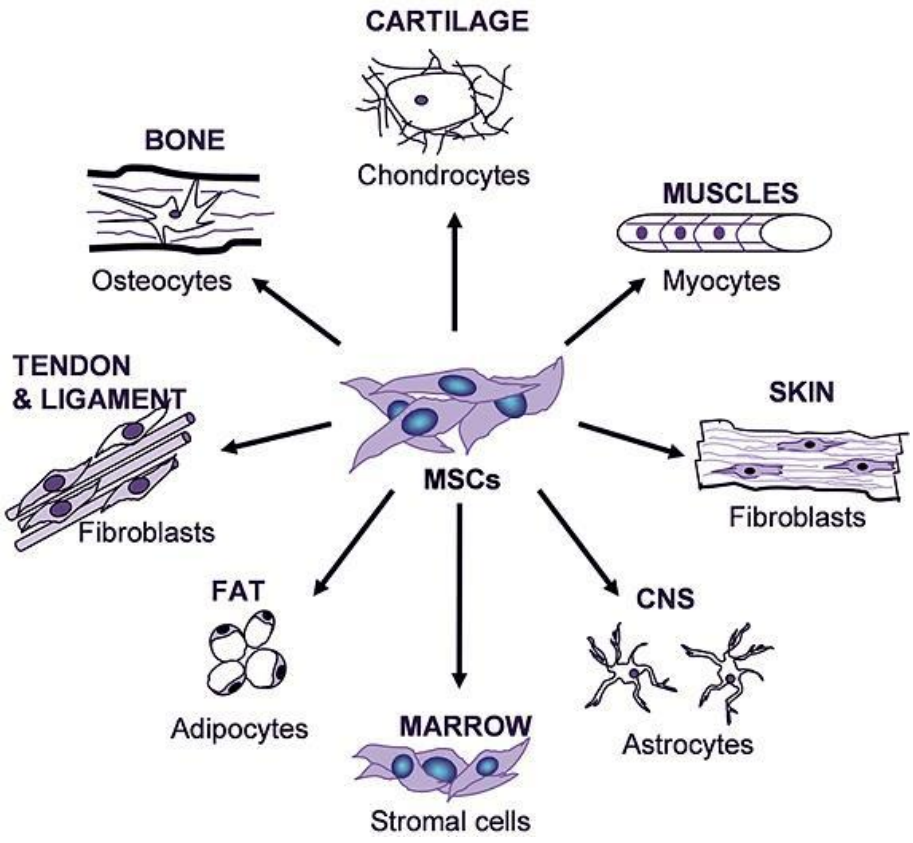

Figure 1.20. Mesenchymal stem cells (MSCs) can differentiate down different lineages, many of which are involved in structural and support roles within mammals. After isolation, MSCs can be differentiation *in vitro* depending on the experimental focus. For example, differentiation of MSCs with TGF-β produces chondrocytes, involved in production of cartilage. By contrast, differentiation of MSCs with BMP-2, ascorbic acid and dexamethasone in a suitable support matrix (e.g. alginate) produces osteocytes, the cellular constituent of bone. Of particular interest is the potential to differentiate MSCs with BMP-2, insulin, dexamethasone and IBMX, producing lipid-filled mature adipocytes. From Democratizing Cell Technologies (2014).

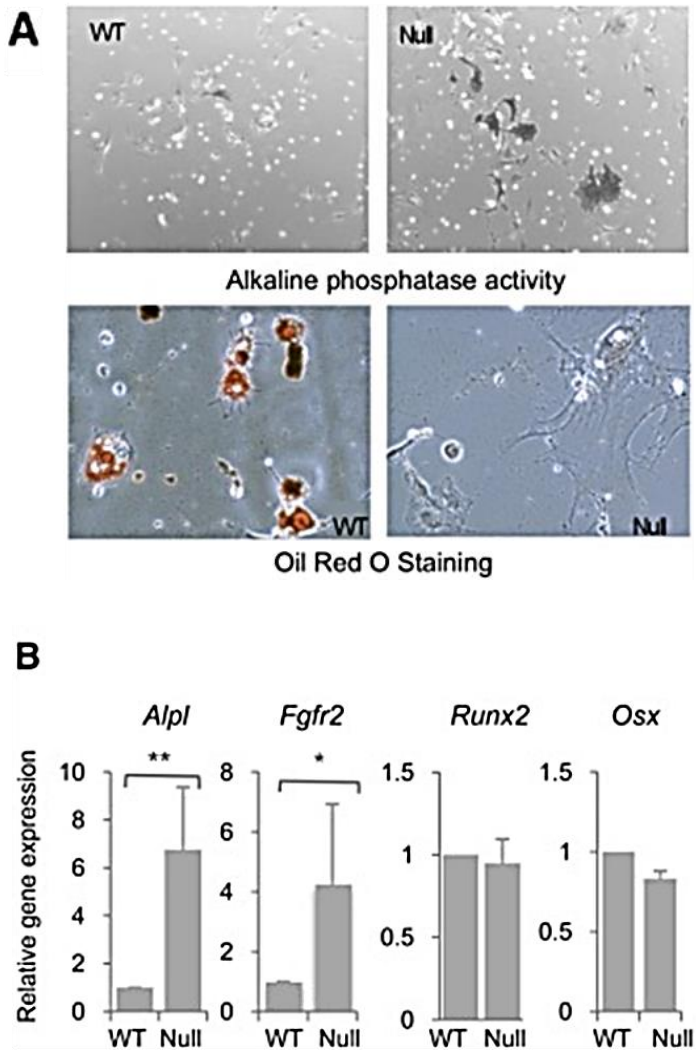

Figure 1.21. Mesenchymal stem cells depleted of the chromatin remodeller *Brm* (*Smarca2*) demonstrate (A) increased alkaline phosphatase and reduced (oil-red-O) lipid staining, alongside a (B) gain in osteoblastic lineage marker expression (Alkaline phosphatase and *Fgfr2*) as identified by qPCR. From Nguyen K.H et al (2015).

1.5.2. Major pathways involved in adipogenesis.

The molecular pathways which drive adipogenesis and adipose tissue expansion are well characterised. A number of key transcription factors – which are considered to be 'master-switches' in the cascade of signals that drive successful adipogenesis – have been studied over the previous decades, and serve as markers of adipogenic dysfunction. Of these, three particular 'master-switches,' *Ppar-γ* (Peroxisome proliferator-activated receptor-γ) *C/ebp-α* (CCAAT-enhancer-binding protein-α) and *Srebp1c* (sterol regulatory element-binding protein 1-c) are upregulated and begin the successful cascade of signals required for adipogenesis. Particular attention to these can reveal the mechanisms behind adipogenic dysfunction (Figure 1.22) (Siersbæk, Nielsen, & Mandrup, 2012).

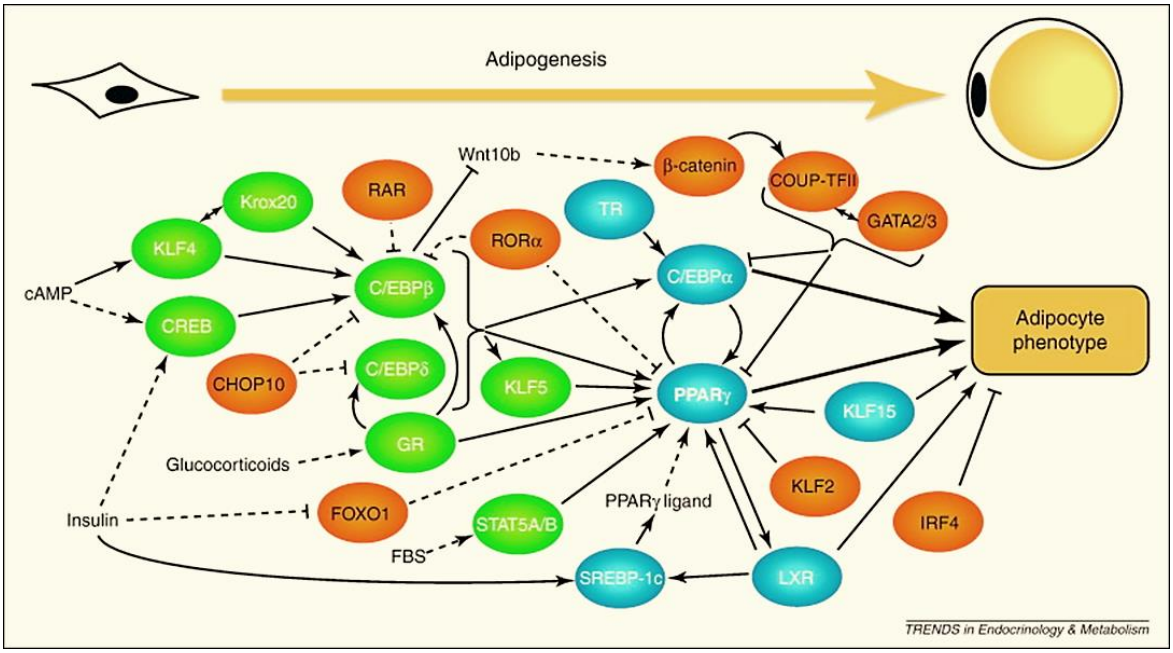

Figure 1.22. The major transcriptional networks controlling adipogenesis, with major nodes provided by C/EBPα, PPARγ and SREBP-1c. Aberrant levels of these transcription factors serve as markers for potential adipogenic dysfunction. From Siersbæk R et al 2012.

1.5.3. Approaches to the study of white-adipose tissue.

Two types of fat depot are found in mammals, subcutaneous WAT (e.g. inguinal WAT), and visceral fat (e.g. epididymal WAT) (Figure 1.23). Although both types were originally considered a simple metabolic energy store, more recent evidence now shows that visceral and subcutaneous WAT are distinct tissues which arise from different developmental origins, for instance subcutaneous WAT contains smaller multi-locular adipocytes and is thought to protect against metabolic dysfunction (Berry, Stenesen, Zeve, & Graff, 2013). Interestingly, while initial adipose tissue organogenesis does not require the presence of a stromal vascular niche (i.e. the surrounding network of mesenchymal stem cells, endothelial progenitor cells, and immune cells such as B- and T-cells and macrophages), development and expansion of adult adipose tissue is dependent on the presence of Sma+ve (Smooth Muscle Actin+) mural cells for maturation. It has to be remembered therefore that any differences found in adult murine adipocyte stem cell function may be influenced by the niche. Other factors present in white adipose tissue which are required for adipose tissue expansion and/or homeostasis include tissue resident macrophages. These are thought to play a role in both in the clearance of dead cells and in mechanisms driving adipose tissue modelling such as during nutrient excess or nutrient deficiency (Martinez-Santibañez & Nien-Kai Lumeng, 2014).

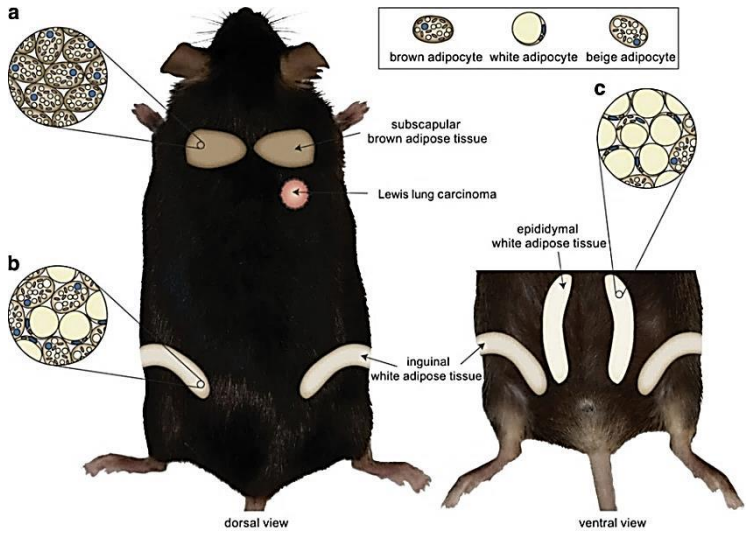

Figure 1.23. Location of brown adipose tissue, inguinal white adipose and epididymal white adipose tissue depots in mouse. Inguinal and epididymal WAT depots represent subcutaneous and visceral fat depots respectively. Image reproduced from:- http://www.nature.com/bonekeyreports/2015/150114/bonekey2014116/images/bonekey2014116-f1.jpg.

Other sources of material can be used for the study of adipogenesis: multiple non-WAT derived cell types are able to differentiate and undergo adipogenesis (Figure 1.24). Mouse embryonic stem cells can be differentiated under the influence of Retinoic Acid, Ascorbic Acid, insulin, and Rosiglitazone to become mature adipocytes, which more closely resemble isolated subcutaneous adipocytes than a number of established pre-adipocyte cell lines (e.g. 3T3-L1), based on gene expression profiles (Cuaranta-Monroy et al., 2014). Mouse embryonic fibroblasts (MEFs) can be prepared from disaggregated embryos at day E12 to E14 and subsequently differentiated into adipocytes (discussed later). These also harbour the potential for immortalization, providing a longer-lived substrate for studies of adipogenesis.

Brown adipocytes can also be driven by hormonal inducers down the white adipocyte lineage, as can extracts from adult tissues containing multipotent cells (such as bone marrow, skeletal muscle or adipose tissue) (Rosen & MacDougald, 2006). Interestingly, the immortalized mesenchymal stem cell line C3H10T1/2 was originally isolated from bone marrow (Reznikoff, Bertram, Brankow, & Heidelberger, 1973), and can be hormonally induced to become mature adipocytes. Together these give multiple potential substrates for the study of adipogenesis and mesenchymal stem cell differentiation (Figure 1.24).

1.5.4 Putative white adipocyte stem cells for studying adipogenesis.

The isolation of white adipocyte precursors (adipocyte stem cells) to allow the examination of the adipocyte-lineage differentiation in e.g. obesity has been the target of multiple studies. Conflicting reports exist as to the *bona fide* cell surface phenotype of adipocyte stem cells (Cawthorn, Scheller, & MacDougald, 2012). While the trial of published approaches would be beyond the scope of this thesis, the use of a proven method where mature adipocytes can be successfully differentiated was essential for *ex-vivo* investigation of murine SMARCAD1 in adipogenesis. The characterization of sorted cells by Church et al (2014) demonstrated the adipogenic potential of stromal vascular cells with the surface phenotype (CD45-CD31-) CD29+CD34+Sca1+, providing such a potential approach (Figure 1.25).

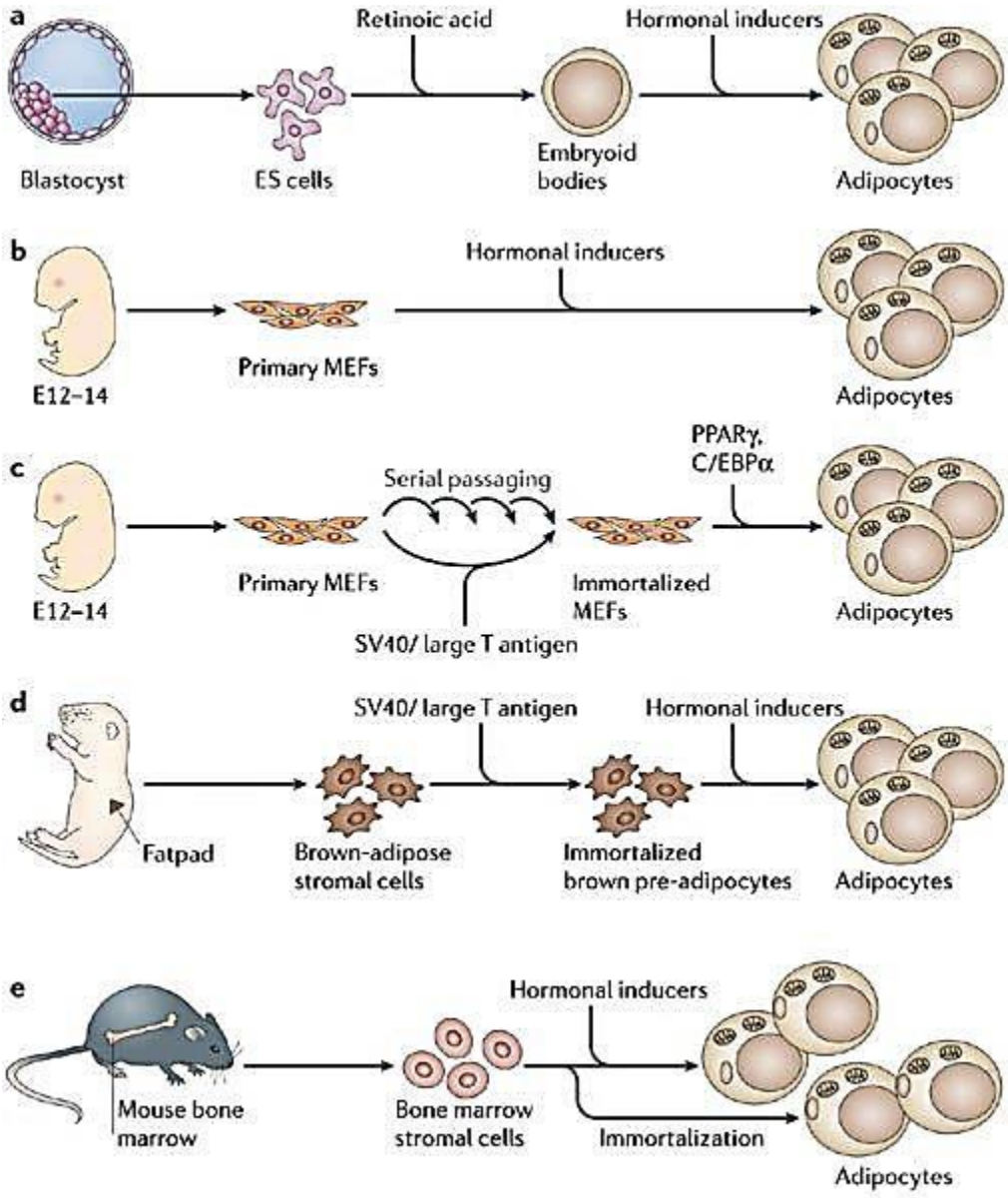

Figure 1.24. Anatomical and cellular sources for studying adipogenesis in mouse. Primary cells can be isolated from mouse embryos or blastocysts and stimulated to become mature adipocytes (panels a to c), and a stable substrate for the study adipogenesis can be generated from the serial passaging of mouse embryonic fibroblasts to generate an immortalized cell line (c). In a similar manner, extracted brown adipose stromal cells can be immortalized into brown pre-adipocytes, which are able to undergo adipogenesis into mature white adipocytes (d) and isolated bone marrow stromal cells (e) can also be immortalized to provide a substrate for studies of adipogenesis. From Rosen and. MacDougald (2006).

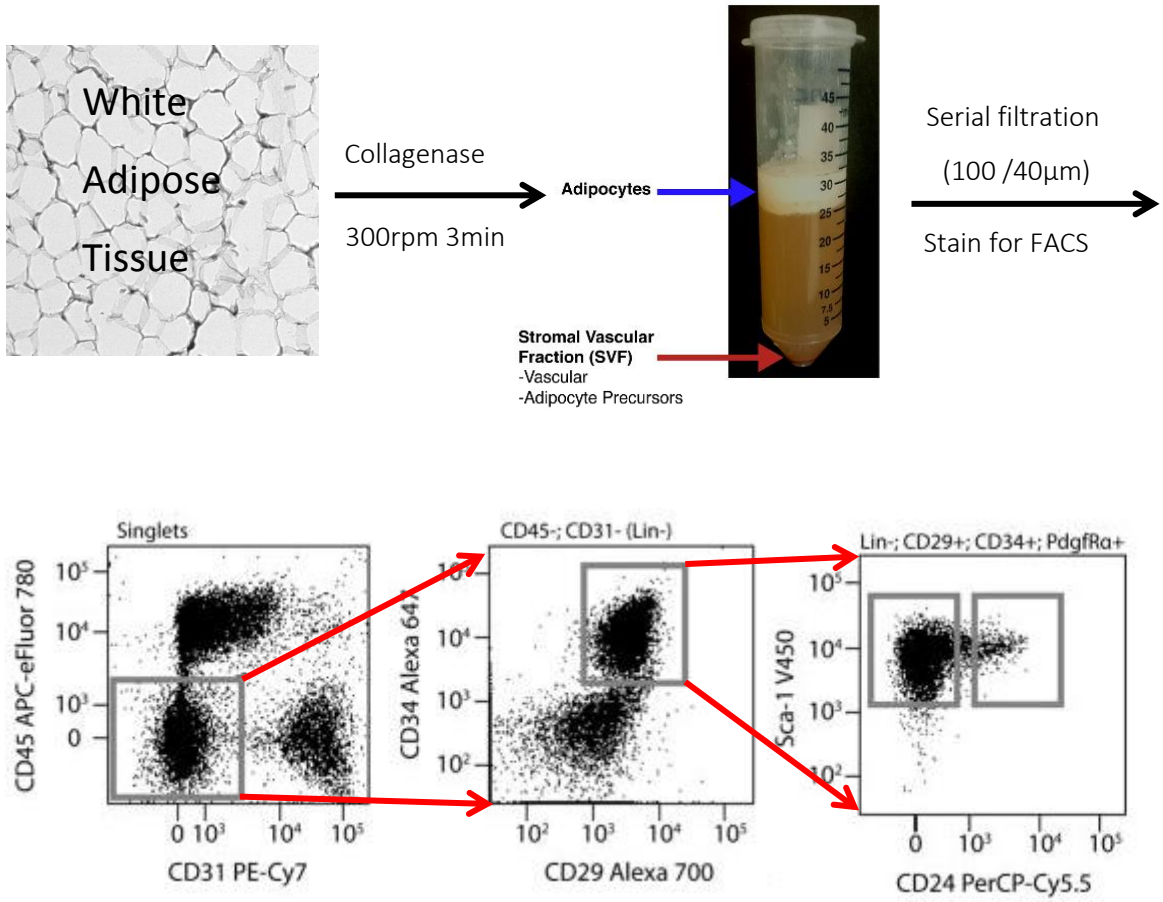

Figure 1.25. Strategy for isolation of adipocyte stem cells using collagenase digestion and flow cytometry. The stromal vascular fraction of white adipose tissue is first extracted by collagenase disaggregation and serial filtration, and the remaining cells are stained for flow cytometry using a panel of cell-surface markers specific for WAT-resident stem cells. From Church, Berry, & Rodeheffer, 2014.

1.5.5. Mouse Embryonic Fibroblasts (MEFs).

An alternative substrate for the study of murine adipogenesis is mouse embryonic fibroblasts (MEFs). These cells are obtained from the extraction of embryos from the uterus of expectant mothers, followed by mechanical disruption and trypsinisation of embryonic cells (Lei, 2013). Subsequent culture expands embryonic fibroblasts, which retain multipotency and are able to differentiate into multiple cell types, such as adipocytes, osteoblasts and chondrocytes (Dastagir et al., 2014). Further *in vitro* passaging immortalizes MEFs, although this also induces a loss in potency, reducing practical utility. One of the most widespread uses of MEFs is as a 'feeder' layer in the culture of Embryonic Stem Cells (ESCs), providing metabolites for stem cells without dividing themselves (Llames, García-Pérez, Meana, Larcher, & del Río, 2015). However, MEFs also provide a useful tool for other studies of differentiation given their ease of handling.

A number of studies highlight the utility of MEFs in non-mesoderm-type cell differentiation experiments e.g. for studies of innate immunity and responses to viral infection (do Valle et al., 2010, Balachandran, Thomas, & Barber, 2004) or studies of differentiation to lineages such as neurons or myocytes (Vierbuchen et al., 2010; Fong et al., 2012). The similarity between MEFs and bone marrow-derived stromal stem cells (BMSCs) has also been of specific interest, given that MEFs are often used as a surrogate for BMSCs during mesodermal differentiation experiments (Saeed, Taipaleenmäki, Aldahmash, Abdallah, & Kassem, 2012). Interestingly, MEFs exhibited higher telomerase activity and cell proliferation than BMSCs, while retaining the cell-surface phenotype characteristic of BMSCs (Sca-1+, CD73+, CD105+, CD29+, CD44+, CD106+, CD11b−, and CD45−). However, osteogenic differentiation of MEFs resulted in a less mature osteoblastic phenotype than BMSCs, even though the differentiation to adipocytes and chondrocytes appeared to be enhanced.

A more recent study investigated the scope of heterogeneity within MEFs (Singhal et al., 2016). Given the method of preparation (i.e. no isolation of specific cell types is involved), it is likely that MEFs constitute a mix of cell types – impacting any downstream application where a homogenous starting substrate has been perceived. Indeed, while this study highlighted that little morphological difference was visible among MEFs microscopically, the use of GFP expression driven from the vascular endothelial growth factor promoter (*Vegf*) revealed MEFs that were GFP-positive or MEFs that were GFP-negative. Interestingly, GFP-positive MEFs were shown to replicate

more quickly than GFP-negative cells, and became more prevalent in the population with serial passaging in culture. However, while GFP-negative cells were subsequently shown to subdivide into further distinct populations based on cell-surface markers, this (mixed) population retained the ability to differentiate into bone, muscle and fat lineages (Singhal et al., 2016).

Such studies reveal the potential of MEFs to differentiate into different cell types, reflecting lineage commitment. In contrast, the seminal work by Takahasi and Yamanaka, uncovered the potential of MEFs to dedifferentiate upon transfection with four key factors: OCT3/4, SOX-2, c-MYC, and KLF-4, (now known as the "Yamanaka factors"), becoming inducible pluripotent stem cells (iPCs) (Kazutoshi Takahashi & Yamanaka, 2006). Following on from this, more recent work also shown that MEFs demonstrate greater potency (i.e. broader differentiation potential) than mesenchymal stem cells (MSCs). One particular study showed that MEFs were able to generate tissue similar to ectodermal, mesodermal and endo-dermal lineages when injected into Balb/c mice, reflecting natural embryonic stem cell (ESC) type potential (Yusuf et al., 2013). Taken together, these studies demonstrate the utility of mouse embryonic fibroblasts for studies of adipocytic and chondrocytic differentiation in particular, while additionally showing the potential for use in other models of differentiation and areas such as innate immunity.

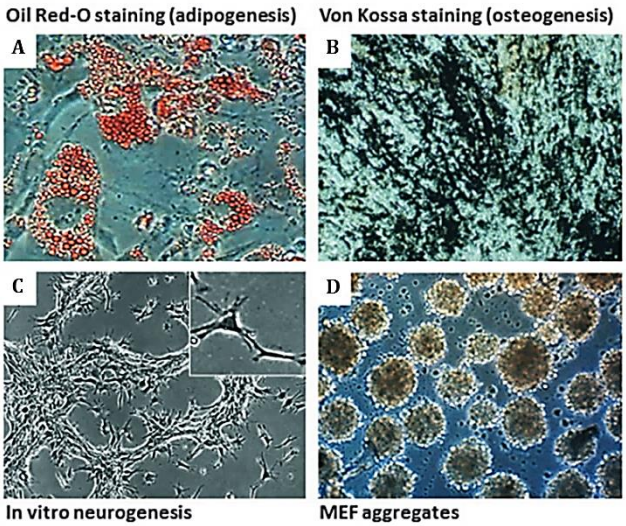

Figure 1.26. Mouse embryonic fibroblasts (MEFs) are able to differentiate down different lineages and become (a) adipocytes (b) osteoclasts (c) neurons (d) embryoid-body like aggregates. Such potency underlines the utility of MEFs as models for studies of differentiation. From Yusuf et al., 2013.

1.6 Intestinal microbiota and metabolism.

The mammalian intestine is host to a large number of microbes, and changes in the composition of intestinal microbiota have been the subject of many studies in the context of metabolic impact. Indeed, over 1000 different species of bacteria have so far been identified in the gastrointestinal tract of humans, including symbiotic commensal bacteria (which interact with and play a role in intestinal function), and species that contribute to pathology (Brown, DeCoffe, Molcan, & Gibson, 2012). Of the species present, four major phyla dominate: Actinobacteria, Bacteroidetes, Firmicutes and Proteobacteria. Firmicutes and Bacteroidetes make up the majority of species present in the mammalian colon, whereas Actinobacteria and Proteobacteria are found at much lower abundance. Furthermore, studies using an obese mouse model revealed an increase in the proportion of Firmicutes to Bacteroidetes of up to 50%. In line with this, germ free mice colonized with the intestinal microbiome derived from obese mice show increased weight gain compared to control mice fed the same diet, implicating microbial influence (Turnbaugh et al., 2006).

Exactly how the gut microbiota influences distal organs in mammals is yet to be completely understood. Links have been made between the microbiota and tissues/organs such as adipose tissue, lungs, pancreas and the brain (Schroeder & Bäckhed, 2016). A number of microbially-derived molecules are now known to interact with both the intestine and with distal organs. As an example, interactions between the microbiota and host intestinal immune system are modulated by the microbial catabolism of tryptophan into indole-3-aldehyde, which binds to the aryl hydrocarbon receptor (AHR) in host innate-lymphoid cells (ILCs) and intraepithelial lymphocytes (discussed later), driving the production of the cytokine interleukin-22 (Zelante et al., 2013). Dietary fibre can also be broken down by the microbiota into short-chain fatty acids (SCFAs) such as butyrate, propionate and acetate. These can themselves contribute to the daily energy requirement of humans, and in the case of calorie excess can be incorporated into white adipose tissue directly, thereby impacting adiposity (Bäckhed, Manchester, Semenkovich, & Gordon, 2007). However the same SCFAs provide signals to L-cells in the intestine, and bind to G-protein-coupled receptor (GPCR) GPR41, upregulating expression of glucagon-like peptide (GLP)-1. Secretion of GLP-1 increases insulin secretion from the pancreas and decreases appetite by delaying gastric emptying (Fava, 2014). A summary of associations between the microbiota, non-intestinal tissues/organs and pathology is shown in Table 5.

Organ	Process influences by gut microbiota	Disease associated with dysbiosis/microbial metabolites
Adipose tissue	Adipocyte volume Thermogenesis Browning Inflammation	Obesity/insulin resistance Insulin resistance
Liver	Bile acid metabolism Lipogenesis Energy expenditure	NAFLD/NASH
Pancreas	Insulin secretion	Type 2 diabetes
Whole body	Body growth	Undernourishment
Cardiovascular system		Stroke Atherosclerosis Thrombosis
Brain	Behavior Serotonin metabolism Intestinal gluconeogenesis Blood–brain barrier Appetite regulation	Autism spectrum disorder Stress response Metabolic disease
Lung	Gene expression	Allergic asthma

Table 1.5. The influence of intestinal microbiota on mammalian organs, and associated diseases. From Schroeder & Bäckhed, 2016.

Microbiota can also directly impact host chromatin. A number of microbially-derived products such as SCFS can provide substrates for epigenetic modification of the host genome (Table 6). Indeed, carbohydrate breakdown products produced by intestinal bacteria consist of >95% acetate, propionate or butyrate (den Besten et al., 2013), which in turn can be used by histone acetyltransferases (after oxidation in the case of propionate and butyrate) in the form of acetyl Co-A to covalently modify chromatin. In addition to this, butyrate has been shown to inhibit histone deacetylases (Davie, 2003) providing a two-pronged increase to acetylated histone levels.

An in-depth study of histone modifications (using mass spectrometry) in the context of different gut microbial populations built on these observations, and unveiled that these effects are not limited to the intestine. Comparison of histone modifications in conventionally raised (CONV-R) and germ-free mice (GF) revealed that acetylation of histone H4 at residues K5, K8, K12 and K16 was increased in both colon and white adipose tissue (WAT) of CONV-R mice, and that dual-acetylation of histone H3 at H3K9 and K14, or at H3K18 and K23, were increased in both the liver and colon of GF mice after colonization with microbiota from CONV-R mice (age-matched at 15 weeks old). The same mice showed an increase in the K27me/K36unmodified pairing on histone H3 in colon, liver and white adipose tissue in response to colonization, with additional increases in H3 K27me2 and H3 K27me3 in white adipose tissue (Krautkramer et al., 2016).

To further assess the impact of these chromatin changes, transcriptomic analysis of these tissues was performed (using RNA-seq) to identify gene expression changes associated with chromatin modifications in the liver of each of three mouse groups (CONV-R, GF mice, and GF mice that were subsequently colonized with microbiota from CONV-R mice). A total of 623 genes were differentially expressed between these three groups, and interestingly one set of genes identified between CONV-R and GF mice were involved in processes linked to insulin, PPAR and SREBP signaling (important factors in adipogenesis, discussed earlier). Indeed, 4% of the differentially expressed genes identified are known targets of PPAR and SREBP transcription factors in the liver, providing a transcriptional link between the microbiota and fat metabolism (Krautkramer et al., 2016).

To further investigate whether bacterially-derived SCFA were driving these changes, germ free mice were supplemented with dietary SCFAs (acetate, propionate and butyrate), and livers were again investigated for chromatin modification and transcriptional changes using mass spectrometry and RNA-seq as above. Comparison of histone modifications and differentially expressed genes between SCFA supplemented GF mice and the other three groups revealed that mice supplemented with SCFA closely resembled the GF mice supplemented with CONV-R microbiota in terms of gene expression and chromatin modifications. These data provide strong evidence that microbial populations in the intestine influence tissue and organs beyond the intestine at the chromatin and transcriptional level (Krautkramer et al., 2016).

Other studies have also investigated how the gut microbiota impact global chromatin structures in intestine-resident cell types directly. In one set of experiments, regions of open chromatin were identified from murine epithelial cells of the ileum and colon using DNAse-seq (i.e. sequencing DNAse-I digested DNA fragments, which exploits the affinity of DNAse-I for open chromatin (Song & Crawford, 2010). These reads were then compared from mice raised either conventionally or in germ-free conditions (i.e. with a normal microbiome or no microbiome); interestingly no significant differences were found in the genomic location of regions associated with open chromatin between the groups. However, differences in gene expression were found between normal and germ-free mice, suggesting that although the chromatin landscape may be pre-programmed in intestinal epithelial cells, the genes that are accessible can still be influenced by the microbiota (Figure 1.27) (Camp et al., 2014).

Metabolite Class	Members	Source	Direct Microbial metabolite:epigenetic effects = putative or demonstrated?	Model System	Effects
SCFAs	Lactate (C3)	Fermentation of microbial accessible carbohydrates	putative	*in-vitro*, mammalian cell culture	Weak HDAC inhibition (76)
	Acetate (C2)		putative	*in-vitro*, mammalian cell culture	Increases histone acetylation (17)
	Propionate (C3)		putative	*in-vitro*, mammalian cell culture; intestinal organoids	Weak-modest HDAC inhibition *in-vitro* (< butyrate) (77); Increase histone acetylation in HT-29 cells (78); modest increase in expression of *HDAC3* and *HDAC5* in gut organoids (79)
	Butyrate (C4)		demonstrated	*in-vitro*, mammalian cell culture, mouse, human	HDAC inhibition (8, 77), HAT activation, protection from colorectal cancer (61, 70); protection from high fat diet induced metabolic syndrome + associated with decreased HDAC activity (62); Increase histone acetylation in HT-29 cells (78); modest increase in expression of *HDAC3* and *HDAC5* in gut organoids (79)
	General (acetate, propionate, and butyrate)		demonstrated	mouse	Colonization affects host histone PTM states in multiple host tissues; SCFA supplementation of GF mice is sufficient to partially phenocopy histone methylation and acetylation patterns observed in colonized mice (71)
	Valerate (C5)		putative	Mammalian cell culture	Increase histone acetylation in HT-29 cells (78)
	Caproate (C6)		--	--	Does not induce histone H4 hyperacetylation in HT-29 cells (78)
Branched SCFAs (BCFAs)	Isobutyrate		putative	*in-vitro*, mammalian cell culture	Increase histone acetylation (78); Increase histone H3 acetylation in EBV-infected HH514-16 cells (80)
	Isovalerate		putative	mammalian cell culture	Increase histone H3 acetylation in EBV-infected HH514-16 cells (80)

Table 1.6. Microbial breakdown of carbohydrate generates short-chain fatty acids (SCFAs) which impact the host epigenome. SCFAs such as acetate, propionate and butyrate have been shown to increase histone acetylation, and supplementation of germ-free mice with these SCFAs partially replicate the histone acetylation and methylation patterns observed in colonized mice. From Krautkramer et al (2017).

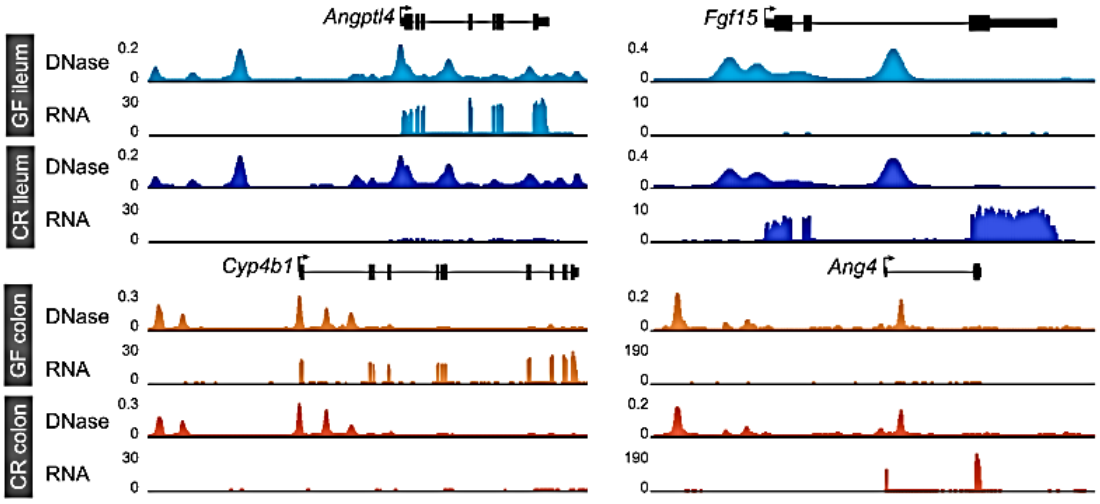

Figure 1.27. Microbiota do not influence the landscape of accessible chromatin in the murine small intestine (ileum) or large intestine (colon). The graphs show reads from open chromatin after DNAse-seq with peaks at areas of open chromatin, with corresponding expression RNA level traces below. Four genes are shown (Angptl4 and Fgf15 from the ileum, top, and Cyp4b1 and Ang4 from the colon, bottom) with open chromatin peaks plotted from conventionally raised vs germ free (no microbiota) mice. From Camp et al 2014.

Another study used a related technique (Assay for Transposase-Accessible Chromatin (ATAC)-seq) to examine intestine-related chromatin structure. Similar to DNAse-seq, ATAC-seq exploits the ability of the enzyme Tn5 Transpose to cut exposed DNA and ligate short external sequences (adaptors) onto the DNA fragment, thereby generating sequence-ready DNA templates from regions of open DNA (Buenrostro et al., 2015). By contrast, this study focussed on intestinal intraepithelial lymphocytes (IELs) rather than

intestinal epithelial cells (IECs); unlike IECs, IELs are not derived from the intestinal stem cell in crypt (discussed later) and can also be easily purified into homogenous cell types (e.g. γδ-T cells and αβ-T cells). Interestingly, the results from either γδ- or αβ-T cells revealed differing levels of open chromatin between conventionally raised or germ-free mice within enhancer sequences (Semenkovich et al., 2016), indicating that changes in chromatin landscape can be driven by the microbiota in some intestinal-resident cells.

The seemingly different conclusions from the two studies could be due to the input cell type, as IECs represent a heterogeneous population and thus some differences in open chromatin in one particular cell-type could be technically diluted beyond a detectable range by signals from multiple other cell types. Furthermore, the typical turnover for IECs in the mammalian intestine is 2-5 days (J.-H. Park et al., 2016), whereas IELs are resident for several weeks (Sheridan & Lefrançois, 2010), which thus presents a larger window for microbial influence.

Taken together, the experiments above - which examine mice raised under different conditions and with or without dietary challenge – reveal how changes in intestinal microbiota can influence the chromatin landscape and gene expression of the host organism, driving phenotypic differences. With this in mind, it is important to rule out (or rule in) any changes in the intestinal microbiome if model organisms present with an intestinal, hepatic or adipose tissue phenotype (which are potentially driven by the microbiota).

1.7 Intestinal anatomy and development.

Many insights into intestinal development and the importance of chromatin remodellers in intestinal function have been gained from studies in the Drosophila fruit fly. In the mammalian digestive tract, the intestine extends between the stomach and rectum, subdivided into the small intestinal duodenum, jejenum and ileum, the cecum marking the division between small/large intestines, and the ascending, descending and sigmoidal colon forming the large intestine prior to the rectum and anus marking the exit from the body. By contrast, the Drosophila intestine is divided into the foregut, midgut and hindgut representing an equivalent anatomical stretch. Furthermore, at the microscopic level the mammalian intestine is formed of anatomical villi and crypts along the length, presenting an increased surface area along the proximal-distal axis. The Drosophila intestine harbours a more simple tube-type anatomy, and with decreased diversity of cell types within the anatomical structure (Figure 1.28) (Apidianakis & Rahme, 2011).

The intestinal epithelia of higher organisms is one of the most rapidly renewing tissues, underpinned by high cell turnover (Vermeulen & Snippert, 2014). Within the mammalian intestine, stem cells reside at the base of the crypt and divide to produce the other cell types which project towards the lumen, forming the villi. By contrast, division of stem cells within the Drosophila intestine produce progeny which project along the anterior-posterior axis, extending the anatomical tube-like structure (Apidianakis & Rahme, 2011).

1.7.1. Chromatin remodellers and intestinal development.

The impact of chromatin remodellers and associated epigenetic factors in intestinal development/differentiation and function has been greatly informed by studies in Drosophila. In one study, the loss of function of the Osa-containing SWI/SNF chromatin remodelling complex altered the composition of cells in the Drosophila midgut, with increased numbers of intestinal stem cells present at the expense of enterendocrine cells and enterocytes (which normally differentiate from the iSCs) (Zeng, Lin, & Hou, 2013). This implies that specific chromatin remodelling is required for the production of appropriate cell populations from the intestinal stem cell.

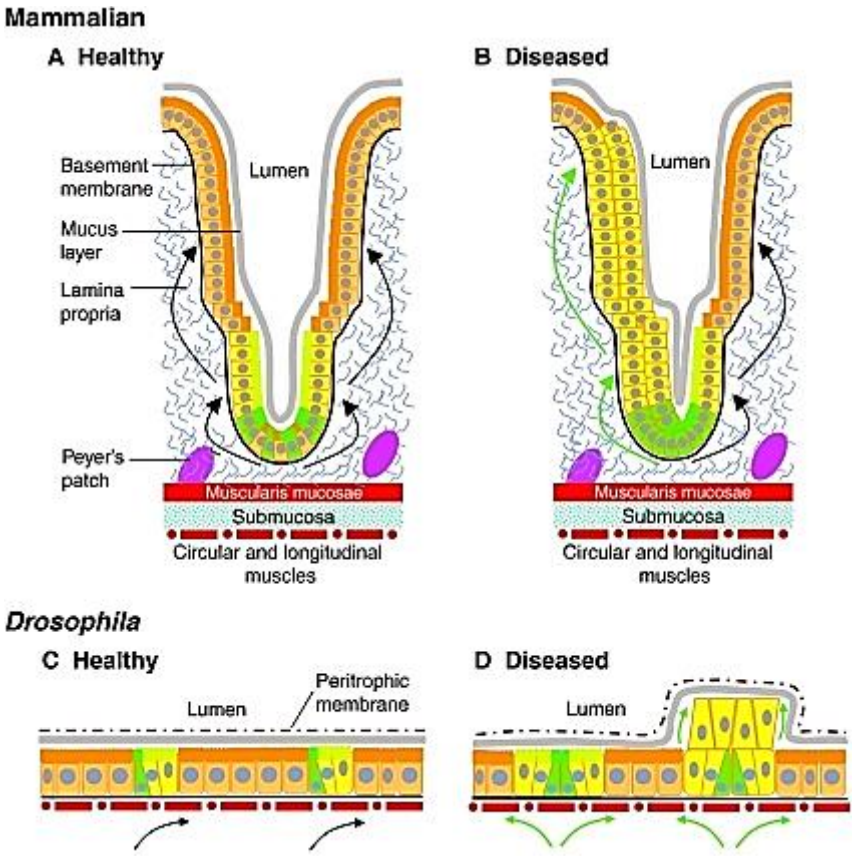

Figure 1.28. Comparison of microscopic anatomy of mammalian and Drosophila intestine. (A) In healthy mammals, intestinal stem cells divide and produce a single layer of cells (containing multiple cell types) from the base of the crypt to the top of the villus. (C) In contrast, intestinal stem cell division in Drosophila drives the production of a single layer of cells longitudinally along the intestine. In diseased states (B and D), the normal structure can becomes altered with the presence of multiple layers. From Apidianakis Y, Rahme LG (2011).

Another study looked at the impact of the chromatin remodeller *Chd1* on the Drosophila gut microbiota. Loss of *Chd1* was associated with a reduction in the diversity of bacterial species, with *Acetobacteraceae* becoming the dominant population in mutant intestines compared to wild-type flies. Furthermore, some bacterial species (such as *Lactobacillus* plantarum) could not be maintained in the midgut of *Chd1*-deficient over time. This study implicates chromatin remodellers in the establishment and maintenance of gut microbiota (Sebald et al., 2016). Furthermore, the link between chromatin remodelling and intestinal immunity was highlighted by a study using a genome-wide siRNA screen

for genes that increase susceptibility to lethal *Serratia marcescens* infection. This screen identified *CG5899* (the homologue of mammalian *SMARCAD1*) as a gene that confers susceptibility to lethal infection when ablated specifically in the intestine. Furthermore, many of the genes identified were involved in intestinal stem cell differentiation, and thereby regulation of the enterocyte compartment (Cronin et al., 2009). Taken together, these studies emphasize the importance of chromatin remodellers in intestinal biology, including intestinal immunity and microbial interaction on top of normal intestinal development or function.

1.7.2 Development of the vertebrate intestine.

Development of the gastro-intestinal (GI) tract follows morphological similarity in all vertebrate species studied (de Santa Barbara, van den Brink, & Roberts, 2003). At the end of gastrulation, two ventral invaginations at the anterior and posterior end of the embryo elongate in the endodermal layer and eventually fuse in the midline, producing a straight tube. Along the anterior-posterior axis, three distinct regions are then formed: the foregut (containing pharynx, oesophagus and stomach), the midgut (containing small intestines) and hindgut (containing the colon). Undifferentiated stratified cuboidal cells remain in place until midgestation when endodermal differentiation is driven by epithelial-mesenchymal interactions, and leads to mesodermal growth into the lumen and villi formation. Along the anterior-posterior axis differences appear between the villi in the small intestine (which are long and thin) and the colon (flatter and wider), and initially these villi are separated by intervillus epithelium. In the small intestine this intervillus epithelium is then reshaped downwards (i.e. in the opposite direction to the villi), producing crypts, while in the colon these crypts become tubular glands. By time of birth the villus-crypt anatomical unit is present in the small intestine, whereas the colonic villi reduce in length and disappear leaving just tubular glands (de Santa Barbara et al., 2003) (Figure 1.29).

The majority of cells within the mammalian intestinal crypt/villus unit are produced from the intestinal stem cell. (The intraepithelial T-lymphocytes of the adaptive immune system are an exception and are discussed later). Intestinal stem cells reside at the base of the crypt, and produce the rapidly dividing progenitor cells that form the transit-amplifying zone between the crypt and villus. Within the transit amplifying zone, the cell lineage decision is made, and cells differentiate into either secretory precursor (SP)

cells or absorptive precursor cells (AP). The SP cells differentiate further to become either goblet cells or enteroendocrine cells within the villus or Paneth cells which migrate back towards the base of the crypt, serving an immune-protective function for the intestinal stem cells. AP cells migrate further towards the lumen in human before differentiating into enterocytes within the terminal differentiation zone (TD) (Benoit et al., 2012). The number of cell divisions undergone at this stage underpins the anatomical composition of the crypt/villus, as SP cells go through two rounds of cell division yet AP cells go through four, and hence AP cell-derived cells such as enterocytes make up the majority of cells within the intestinal villus.

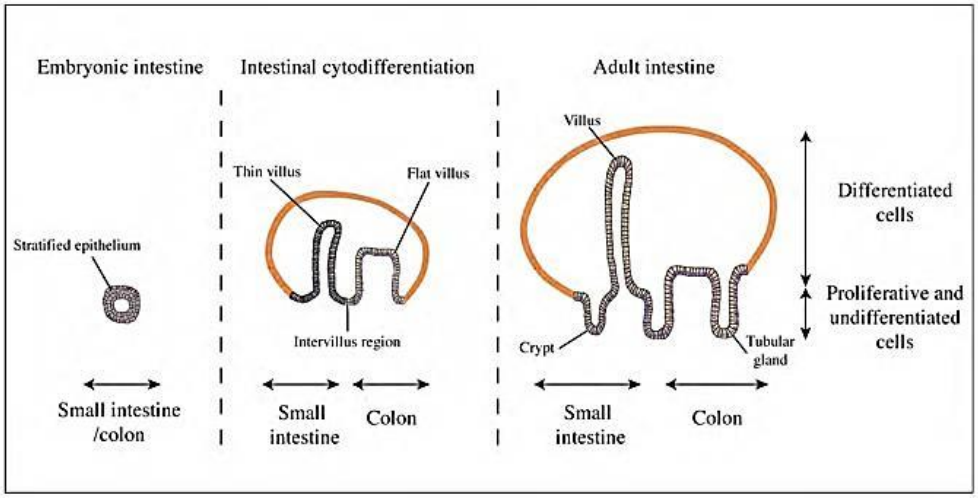

Figure 1.29. Development of mammalian small intestine and colon and formation of the crypt/villus unit. The embryonic intestine resembles a tube formed from stratified epithelium, from which villi and crypts are formed through postnatal differentiation. From de Santa Barbara et al., 2003.

The adult intestinal epithelium is thought to be the most rapidly self-renewing tissue in mammals. Epithelial cell turnover is driven by stem cells in the base of the crypt, and it has been estimated that around six cycling stem cells are present at the base of each crypt, which express the cell surface receptor LGR5 (Leucine Rich Repeat containing G protein receptor 5). Initial studies had identified LGR5 as a marker on colorectal cancer cells, and more recently in other cancers (Sato et al., 2009). However, during an investigation of (intestinal-expression-restricted) Wnt-signalling target genes (i.e. genes involved in body patterning, cell migration and proliferation processes during

embryonic development) LGR5 was identified as a marker for crypt-localisation (Barker et al., 2007). Subsequent lineage tracing (using an inducible Cre-knock in / LGR5 /Rosa26 reporter) demonstrated that *Lgr5+* cells at the crypt base were able to generate all epithelial lineages along the crypt-villus axis over a period of 60 days, confirming their role as intestinal stem cells (iSCs).

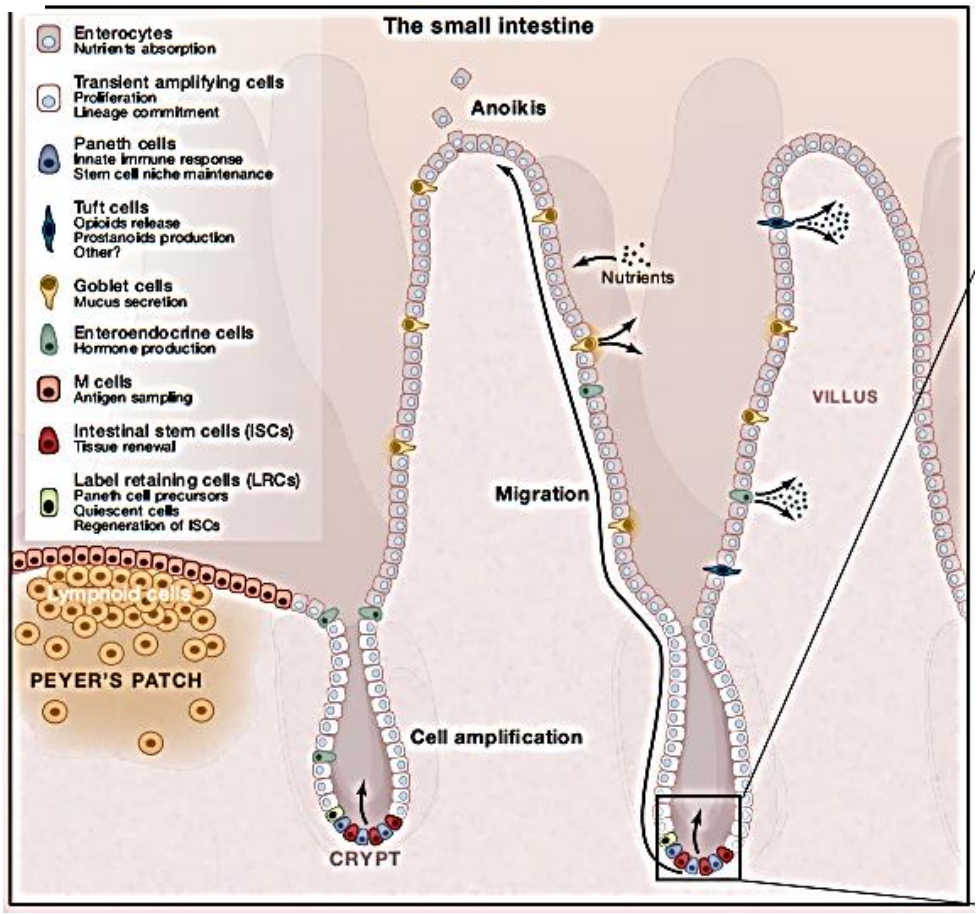

Figure 1.30. The crypt-villus unit in mammalian small intestine. The major cell types endogenous to the small intestine are derived from the intestinal stem cell (iSC) located at the base of the crypt (red). Adjacent to iSCs are Paneth cells which serve an immune-protective function to the iSCs. From the base of the crypt upwards, the transient amplifying cells region contains cells undergoing differentiation, from which the characteristic cell types migrate upwards to the top of the villus where they are finally shed in a process called anoikis. The small intestinal villi contain mostly enterocytes (involved in nutrient absorption) alongside mucous-secreting Goblet cells, hormone producing Enteroendocrine cells and opioid/prostanoid producing Tuft cells. From Clevers & Batlle, 2013.

In addition to the rapidly dividing LGR5+ iSCs in the intestinal crypt, the identification of quiescent, label-retaining cells (LRCs) has prompted a model whereby a number of slow-turning over cells are retained in the crypt which can serve as both the precursors of Paneth cells (which are also retained in the crypt) or differentiate into any of the other lineages present in the crypt/villus on response to damage (Figure 1.30). Paneth cells themselves function in an innate-immunity capacity - i.e. without adaptive or pathogen-specific immune responses, but secrete anti-microbial peptides in response to microbial challenge. As Paneth cells are located adjacent to LGR5+ iSCs in the crypt, these are thought to confer direct protection to the intestinal stem cell niche (Clevers & Batlle, 2013).

1.7.3. Chromatin remodellers in the mammalian intestine.

As with studies in Drosophila, work on the mammalian intestine has illustrated the importance of chromatin remodellers in intestinal function and homeostasis. Following on from the *Osa*-ablated fly model, murine overexpression of the high mobility group protein 1a (*Hmg1a*) in mouse drives the expansion of the intestinal stem cell and Paneth cell niche. HMG1a is associated with active transcription (Ozturk, Singh, Mehta, Braun, & Barreto, 2014), and these changes are associated with an increase in multiple signals within the Wnt-signalling family (Xian et al., 2017). Previous work using a knockout of *Smarca4* (the mammalian homologue of *Brg1*) also implicated this factor in the maintenance of intestinal stem cell turnover, and mice deficient in SMARCA4 showed a loss in villi segregation, while crypts lacking in SMARCA4 were gradually lost in these mice (Holik et al., 2013).

Of particular interest is the interaction between the intestinal microbiota and host cells, especially intestinal epithelial cells (IECs) which form the villus. One study compared the differences in gene expression and accessible chromatin between mice raised under normal conditions versus mice raised under germ-free conditions. Surprisingly, while there was a marked changed in gene expression between germ-free and control groups, this was not accompanied by equivalent changes in chromatin accessibility. This suggests that flexibility in gene expression in intestinal epithelial cells is not due to changes in chromatin structure, as these are set during the differentiation process from intestinal stem cells (Camp et al., 2014).

1.7.4. Deletion of a SMARCAD1-related factor leads to intestinal pathology.

Of the factors associated with SMARCAD1, deletion of murine histone deacetylase 2 (*Hdac2*) has also been shown to cause intestinal defects. *HDAC2 -/-* mice are around 25% smaller than littermates, with macroscopically smaller intestines (i.e. reduced thickness and length) and microscopic reductions in mucosal thickness in the small intestine and the colon (Figure 1.31). Furthermore, these mice showed a lower rate of tumour formation in the colon when crossed with APC^{min} (adenomatour polyposis coli) tumour-prone mice (Zimmermann et al., 2007). To what extent deletion of mammalian SMARCAD1 recapitulates this phenotype, and to what extent loss of SMARCAD1 directly impacts the normal function of HDAC2 is yet to be reported.

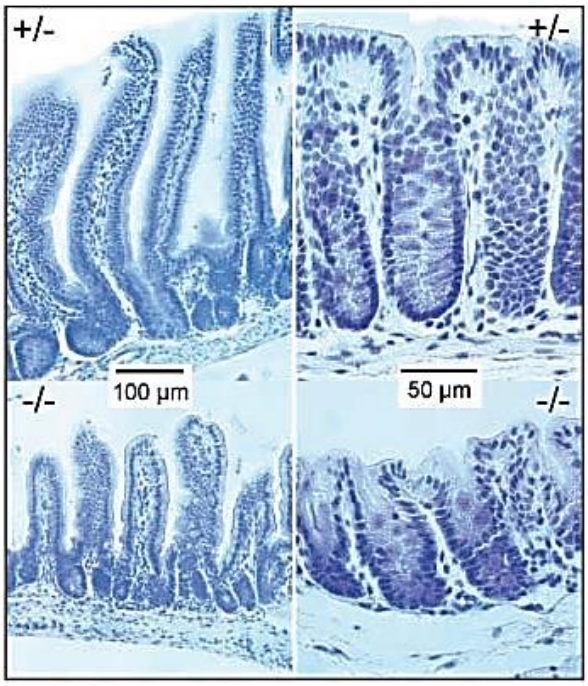

Figure 1.31. Intestinal pathology visible in *Hdac-/-* mice. Hematoxylin and Eosin stained small intestinal (left hand frames) and colonic (right hand frames) show visible differences in villi length and organization between *Hdac2* +/- (top) and *Hdac2*-/- (bottom) mice. From Zimmerman et al 2007.

1.7.5. Intestinal pathology is promoted by increased expression of an innate immune receptor Toll-Like Receptor 4 (TLR-4).

While the loss of expression of *Smarcad1* related factors drives intestinal pathology, the over-expression of innate immune receptor TLR-4 is linked to onset of Inflammatory Bowel Disease in humans (Dheer et al., 2016), and hence expression is tightly regulated in the mammalian small intestine. The conserved pattern recognition receptor TLR-4 binds to bacterially derived lipopolysaccharide (LPS) and initiates immune responses in the host. Expression is epigenetically down-regulated in the small intestine during normal intestinal homeostasis (Figure 1.32) (Kyoko Takahashi, Sugi, Hosono, & Kaminogawa, 2009), and in a recent study, targeted overexpression of *Tlr-4* in the small intestine of mice drove pathological changes and a change in the microbial composition, including impaired epithelial barrier function and exacerbated dextran-sodium sulfate induced colitis (Dheer et al., 2016). *Tlr-4* expression in mice lacking SMARCAD1 is therefore of major interest in the context of small intestinal immunity.

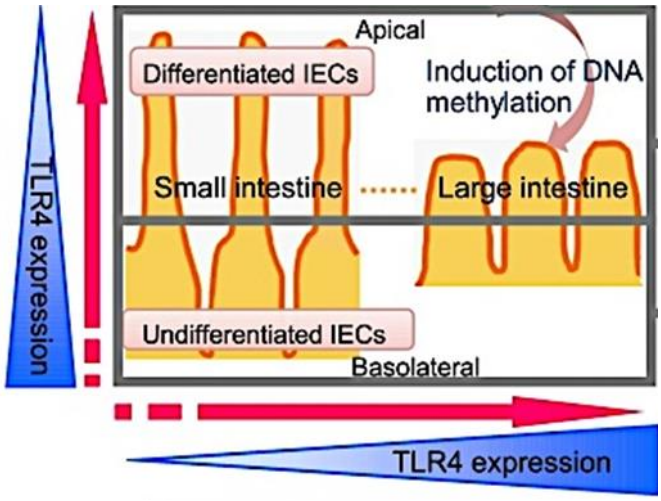

Figure 1.32. Schematic of the mammalian intestine and Toll-like receptor 4 expression. The innate immune receptor TLR-4 is epigenetically regulated in the small intestine, and expression is lowest in the villi of the duodenum where DNA methylation of the *Tlr-4* gene is highest. From Takahashi et al (2009).

1.7.6. SMARCAD1 intestinal expression is conserved and is required for intestinal immunity.

The pattern of SMARCAD1 tissue expression profiles is reported in numerous online protein-expression databases. Interestingly, specific SMARCAD1 expression in the intestine is evident in the human protein atlas (see http://www.proteinatlas.org/ENSG00000163104), where anti-SMARCAD1 staining is visible in the nucleus of intestinal glandular cells (Figure 1.33). Furthermore, a role for SMARCAD1 in intestinal immunity is suggested by studies in the fruit fly Drosophila, where intestine-specific knockdown of the SMARCAD1 homologue (CG5899) impaired the ability to fight a specific bacterial infection and led to premature death (Cronin et al., 2009). Exactly which cells in the intestine require SMARCAD1 expression, and how this influences intestinal immunity remained to be reported at this point.

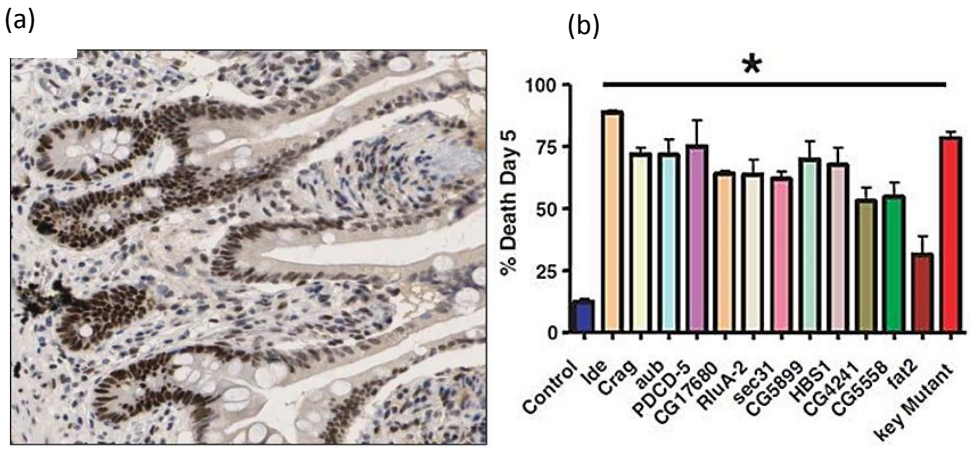

Figure 1.33. (a) Expression of SMARCAD1 in the nucleus of human small intestine glandular cells (taken from the human protein atlas, see link in Section 1.7.6) (b) Removal of *SMARCAD1* homologue (*CG5899*) using siRNA leads to decreased survival by day 5 in a drosophila model of intestinal immunity. From Cronin et al 2009.

1.8 Intestinal immunity and intraepithelial lymphocytes (IELs).

1.8.1. Immunobiology of intestinal intraepithelial lymphocytes (iIELs).

Cells of the adaptive immune system migrate into and are resident in the intestine. T-cells are found predominantly in two locations - in the epithelium (i.e. intraepithelial lymphocytes or iIELs) and in the lamina propria (the connective tissue beneath the epithelium, also known as LP T-cells) (Figure 1.34). In humans and mice, intraepithelial lymphocytes represent one of the largest populations of lymphocytes, and around 10-15% of the intestinal epithelium is thought to be made up of iIELs (Janeway, 2001). Furthermore, these T-cells differ from systemic T-lymphocytes (i.e. splenic/ circulatory or lymph node T-lymphocytes) in the composition of co-stimulatory receptors expressed. In systemic T-cells, either CD4 or the dimeric CD8αβ co-receptors are expressed, and co-stimulate T-cell receptor (TCR) binding to class II major histocompatibility (MHC) molecules (for CD4) or class I MHC (CD8 αβ) on infected host cells respectively. However, the majority of iIEL T-cells express a CD8αα homodimer co-receptor, which is thought to sterically interfere with co-stimulation and thereby confer a regulatory or tolerant phenotype (Cheroutre, Lambolez, & Mucida, 2011) (Figure 1.35). It is also estimated that up to 65% of CD8+ T-cells in the intestine express a γδ-T-cell receptor, which does not require antigenic peptide to be presented in host MHC molecules to initiate responses (Hayday, Theodoridis, Ramsburg, & Shires, 2001).

1.8.2. Function of iIELs.

While the function of these cells is the focus of much debate, iIELs are generally considered important for the conservation of epithelial integrity and prevention of microbial entry through the intestine. In addition to the expression of cytolytic factors (such as granzyme and perforin) and effector cytokines (such as interferon-γ (IFNγ), interleukin-2 (IL-2), interleukin-4 (IL-4) and interleukin-17 (IL-17)), these cells can also secrete keratinocyte growth factor (KGF), aiding the restoration of membrane integrity after physical or inflammatory damage (Boismenu & Havran, 1994). Indeed, mice lacking γδ-T-cells or deficient in KGF production demonstrate elevated intestinal tissue damage and are more susceptible to dextran sodium sulfate (DSS) induced colitis (Ferreira & Veldhoen, 2012).

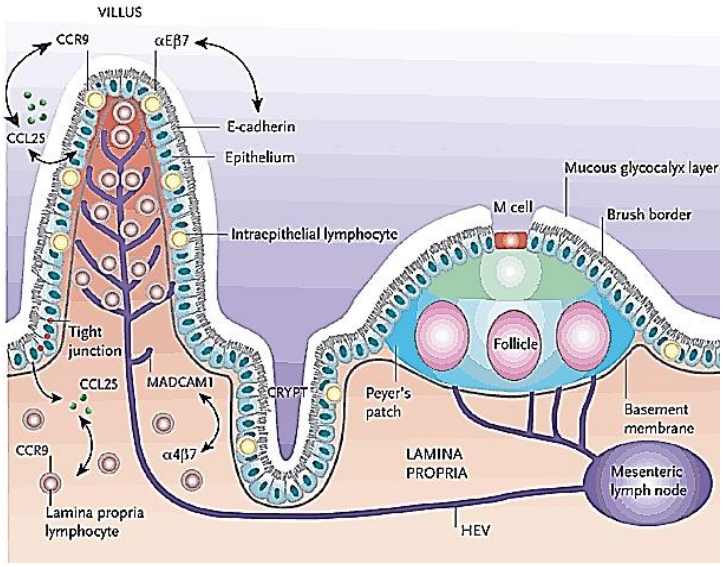

Figure 1.34. Location of intraepithelial lymphocytes in the murine small intestine (above) (yellow) which are typically γδ T-cells or CD8αα αβ T-cells which are essential for maintenance of gut homeostasis, and can be resolved by FACS. From http://www.prn.org/index.php/progression/article/hiv_1_gastrointestinal_galt_267

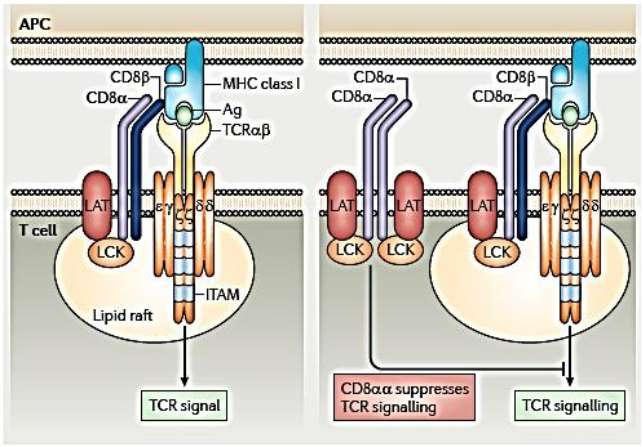

Figure 1.35. T-cell responses are normally mediated via antigenic peptide (Ag) presented in class I MHC molecules on infected cells (top) binding to the T-cell receptor, with co-stimulation from dimeric CD8αβ. Expression of the co-receptor CD8αα inhibits T-cell receptor/class I MHC binding and hence T-cell activation From Cheroutre et al., 2011.

While anti-bacterial responses of γδ IELs are initiated via signals from the epithelial cells (i.e. cell-extrinsic innate immune signals), the presence of γδ T-cells in undamaged intestinal tissue also suggests a homeostatic or regulatory role. Furthermore, the presence of species-specific microbiota in the gut has been shown as a requirement for the development and/or survival of intraepithelial lymphocytes, suggesting a symbiotic relationship between host immune cells and gut microbiota (H. Chung et al., 2012; Ferreira & Veldhoen, 2012). As the expression of the Aryl Hydrocarbon Receptor (AhR) – a cytosolic transcription factor activated by toxins (such as dioxins) and dietary breakdown products (such as 6-formylindolo[3,2-b]carbazole (FICZ) from cruciferous vegetables) - has also been shown as essential for maintenance of iIEL numbers in the gut (Y. Li et al., 2011), a more complex role beyond anti-microbial immunity for intestinal IELs clearly exists.

1.8.3. IELs in pathology.

Elevated numbers of iIELS are also associated with gut-related pathologies. In irritable bowel disease (IBD), the numbers of T-cells in the intestinal mucosa has been shown to directly correlate to the severity of the disease. Such findings are backed-up by mouse models in which T-cells have been shown to promote disease pathology in spontaneous colitis and other models of IBD (Hayday, A. Findly, R.C. Plehn-Dujowich, D. Viney, J.L. Owen, M.J. Roberts, 1994). The autoimmune disease Coeliac disease - in which aberrant responses to gluten-derived antigens (such as gliadin) lead to damage of the small intestine and reduced nutrient absorption – is characterized by elevated levels of γδT-cells alongside infiltration of CD8αβ-αβT-cells, leading to villus atrophy. In this context, it is not clear whether the elevated levels of γδT-cell IELs may be a response to suppress infiltration, as peak levels of these cells have been reported to inversely correlate with pathology (Hayday, A. Findly, R.C. Plehn-Dujowich, D. Viney, J.L. Owen, M.J. Roberts, 1994).

1.8.4. Enumeration of iIELs.

A number of studies enumerate intraepithelial lymphocytes in the small intestine of mice (Montufar-Solis & Klein, 2006). The ability of iIELs to degranulate quickly and without numerous co-stimuli also confers physical fragility, and so the careful manual handling required during extraction can confound accurate replication of cell counts. However, estimates as high as $2x10^7$ iIELs present in the small intestine of 6-8 week old female C57BL/6 mice have been made, although these counts were based on subjective

counting of leukocyte common antigen (CD45)+ cells during fluorescence and light microscopy (Montufar-Solis & Klein, 2006). Another study using multiple T-cell associated cell markers to facilitate cell counting by flow cytometry suggested that up to $1.1x10^7$ small intestinal IELs are present in female C57BL/6 mice from 3 months of age, with this number declining to $0.9x10^7$ at 12 months and $0.8x10^7$ by 24 months of age (Suzuki, 2012). However, this study did not discriminate based on intestinal specific markers such as the αE integrin CD103, hence the authenticity of these cells as iIELs is unclear.

One particular challenge in studies of iIELs is the degree of variability of iIEL numbers between mice. With the use of focused cell-surface markers, one study recently reported a numerical spread between $5x10^5$ and $4x10^6$ IELs per mouse (=mean of $2.25x10^6$ +/- 77%) (Figure 1.36) (X. Wang, Sumida, & Cyster, 2014). In this study, mice lacking the N-arachidonyl glycine receptor GPR18 showed a change in the proportion of CD8αα and CD8αβ iIELs present in the small intestine compared to *Gpr18+/-* mice, despite there being no significant difference in the overall number of iIELs.

1.8.5. Exogenous factors impact γδ T-cells numbers.

Other factors which impact on iIEL enumeration include the level of hygiene in animal facilities (e.g. germ-free mice show markedly reduced numbers of iIELs (H. Chung et al., 2012) which can lead to inter-facility variation in iIEL numbers (M Veldhoen, per comm.). The impact of diet must also be taken into account, as the importance of cruciform vegetables in mammalian intestinal immune development was recently reported (Y. Li et al., 2011). Furthermore, a number of studies suggest that mice fed with a high-fat diet show a drop in the number of iIELs with accompanying changes in intestinal anatomy (Soares, Beraldi, Ferreira, Bazotte, & Buttow, 2015). With the central role of iIELs in intestinal disease pathologies, understanding and controlling for such exogenous influences is of clear importance.

1.8.6. γδ T-cells are found in the spleen and altered ratios are linked to immune pathology.

While a large proportion of T-cells resident in the gut are γδ T-cells (~65%), the proportion of these cells in the circulation (or systemic immunity) is thought to be considerably lower - in the order of 5% of the total number of circulating T-cells

(Hayday et al., 2001). Investigation of γδ T-cell numbers in the spleen has been previously reported for indications of T-cell linked pathology. Following plasmodium infection, one study reported an increase up to four-fold in the proportion of splenic γδ T-cells over other splenocytes (van der Heyde, Batchelder, Sandor, & Weidanz, 2006). In addition, splenic T-cell proportions have also been used in the study of cellular responses to toxicological stimuli (Shieh, Varkey, Chen, Chang, & Huang, 2014) and changes in the splenic T-cell compartment have been reported after influenza infection (Hauge, Madhun, Cox, Brokstad, & Haaheim, 2007). These studies indicate that the proportion of specific T-cell populations within the spleen can provide a marker for immune-related pathology.

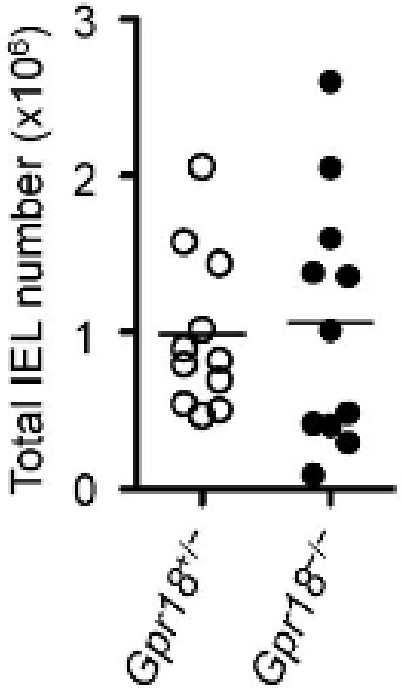

Figure 1.36. Natural variation in the number of iIEL T-cell numbers in the small intestine. In this study, there was no significant difference in the total number of iIELs between controls (heterozygous for the N-arachidonyl glycine receptor GPR18) and GPR18-/- mice. However, mouse-to-mouse variation in iIEL numbers is apparent (5x10^5 to 2x10^6 per mouse in the control Gpr18+/- mouse above), reflecting the need to use large numbers of mice to reach statistical significance in studies of iIELs. From X Wang et al., 2014.

1.9 Background to this project.

1.9.1. Construction of a ATPase (-) SMARCAD1 knockout mouse.

Identification of a short isoform of *Smarcad1* with an alternative transcriptional start site prompted the need for a new knockout model in which this isoform (which contains ATPase and helicase domains) was absent. For this reason a new murine knockout of *Smarcad1* was constructed using a Cre/lox recombination based approach (work done by J Ross Miller, Varga-Weisz group). In brief, a plasmid cassette containing DNA from the *Smarcad1* genomic region spanning exons 12 to 14 was created containing loxP sites flanking these exons, along with a selectable marker (Neomycin Resistance) (SEE Appendix 1 for schematic positioning of these features). This plasmid was then electroporated into murine embryonic stem cell (ES cell) lines, and incorporated into genomic DNA via homologous recombination. ES cell lines positive for a loxP-flanked ('floxed') *Smarcad1* (exons 12-14) after G418 (NeoR) selection were injected into mouse blastocysts. Floxed *SMARCAD1* mice were then mated with Cre recombinase+ mice to produce offspring containing *Smarcad1* deleted (exon 12-14 delete) alleles. Confirmation of the floxed/deleted alleles was performed by quantitative PCR (qPCR) of *Smarcad1* mRNA, and absence of full length SMARCAD1 peptide was confirmed by western blotting. The mating of floxed mice with mice expressing tissue-specific Cre-recombinase was also used to allow the selective deletion of SMARCAD1 either globally (using germline specific Zona-Pellucida-3 (ZP3)-Cre) or specifically in lymphocytes (using CD2-Cre).

1.9.2. Homozygous knockout of *Smarcad1* affects viability of offspring.

Initial genotyping of offspring from male and female mice heterozygous for *Smarcad1* revealed a bias against homozygous knockout mice in both sexes (Table 1). Furthermore, offspring from homozygous knockout female mice mated with heterozygous males revealed a reuction in the number of viable female offspring produced, with many *Smarcad1*-/- female mice dying perinatally. While a potential link to aberrant X-chromosome inactivation in these mice (i.e. due to a loss of SMARCAD1-driven heterochromatin formation) is possible, this is beyond the scope of this project (see General Discussion, section 6.1.1).

Offspring from Male heterozygous +/- and female heterozygous +/-						
Ratio	+/+	+/-	-/-	+/+	+/-	-/-
Expected %	25	50	25	25	50	25
Obtained %	35	58	7	35.5	50.8	8.5
Total	Male offspring n=59			Female offspring n=59		

Offspring from Male heterozygous +/- and female homozygous +/-						
Ratio	+/+	+/-	-/-	+/+	+/-	-/-
Expected %	0	50	50	0	50	50
Obtained %	5.4	58.9	35.7	7.3	80.9	4.8
Total	Male offspring n=73			Female offspring n=41		

Table 1.7. Initial analysis of offspring genotyped at 5 weeks old from *Smarcad1* +/- and -/- mice reveals a bias against homozygous -/- offspring in both sexes from +/- x +/- mice, and a bias against female offspring from male +/- x female -/-mice. Data courtesy of Dr Jacqueline Mermoud.

1.9.3. Homozygous *Smarcad1* -/- mice appear smaller than +/+ or +/- mice.

Homozygous knockout offspring were initially observed to be leaner and smaller than +/- or +/+ *Smarcad1* mice, and weights recorded (at time of sacrifice) from male mice confirm a difference between *Smarcad1*-/- and +/+ or +/- mice (Figure 1.37), and further study will confirm the extent and timing of this difference during postnatal growth.

Given the original observation that *Smarcad1* -/- mice weigh less than +/+ counterparts, it was important to determine the extent of this difference and at what stage of development these occur, e.g. are there differences in birth weight. Given the role of SMARCAD1 in the formation and maintenance of repressed chromatin, it seemed plausible that SMARCAD1 may impact the formation or maintenance of the repression of one allele as seen in imprinted genes, and furthermore given the metabolic impact of these genes, whether expression of these genes is affected in the absence of functional SMARCAD1. A closer examination of the metabolic physiology of SMARCAD1 mice, e.g. birth weights, onset of leanness or obesity, serum levels of key metabolic markers (such as insulin, glucose, free fatty acids) may implicate imprinted gene dysfunction during development.

The original *Smarcad1/Etl1* knockout mouse demonstrated low birth weight and growth retardation/leanness and neonatal mortality, which are phenotypic characteristics of the *Dlk1/Pref1* loss of imprinting (i.e. inappropriate increase in gene dosage) mouse model. The initial data from the new knockout of *Smarcad1* detailed in this thesis also revealed a reduction in body weight associated with smaller epididymal fat pads. As previous mouse models of *Dlk1/Pref1* overexpression in white adipose tissue have previously shown the requirement for *Dlk1* repression in adipogenesis (Lee et al., 2003), aberrant Dlk1 expression would be a candidate for these aspects of the *Smarcad1* knockout mouse phenotype.

1.9.4. Adaptive immunity in *Smarcad1* -/- and CD2-Cre $^{fl/fl}$ mice.

Previous work investigating systemic adaptive immunity in mice with globally deleted (*Smarcad1*-/-) or lymphocyte-specifically deleted (CD2-Cre$^{fl/fl}$) mice revealed no significant difference in either B- or T-cell arms (Figure 1.39) in spite of clear SMARCAD1 expression in both the thymus and spleen (Figure 1.38), suggesting there is no direct effect of SMARCAD1 loss on adaptive immune development (work done by Dr Louise Matheson). However, recent investigation of iIEL T-lymphocytes suggested these cells may be lost as a result of SMARCAD1 deletion (work done by the group of Dr Marc Veldhoen, Figure 1.40), and so this will be the subject of further investigation.

(a)

(b)

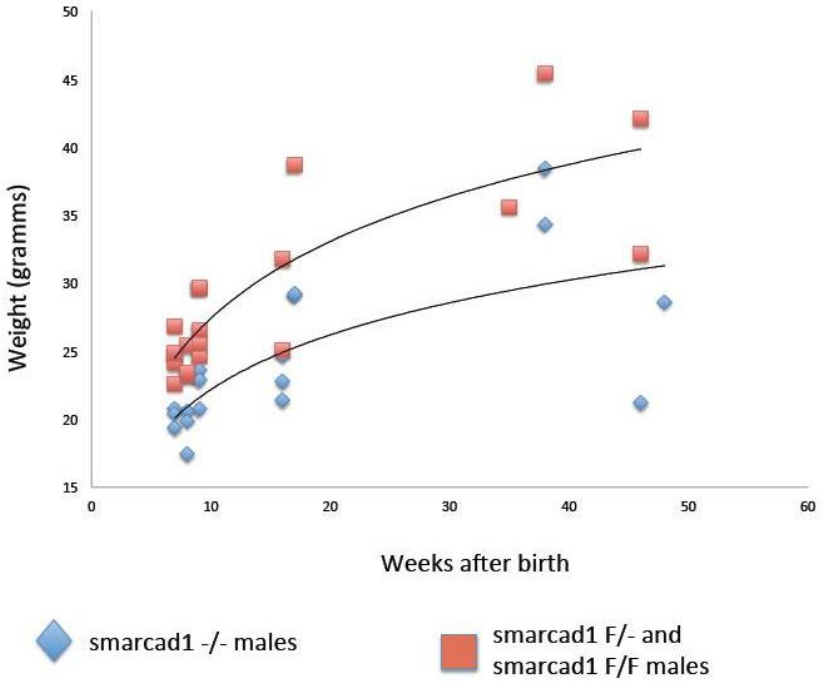

Figure 1.37. *Smarcad1*-/- mice weigh less than +/+ (fl/fl) and +/- (fl/-) mice at time of death. (a) Physical appearance of epididymal fat pads from *Smarcad1* +/+ and -/- mice. (b) Weights of male mice shown above were obtained at time of sacrifice, and trendlines indicate the difference between the two groups. Graph courtesy of Dr Patrick Varga-Weisz.

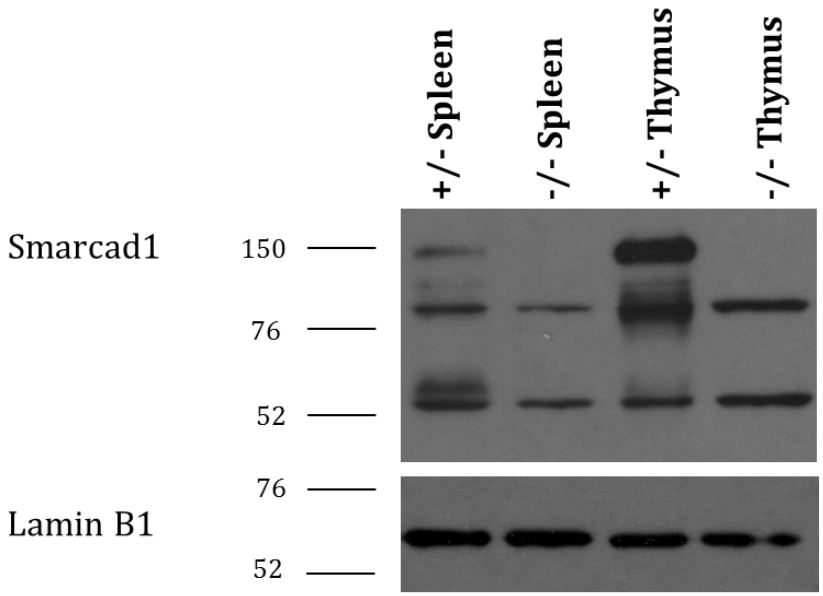

Figure 1.38. SMARCAD1 is expressed in major tissue and cells of the adaptive immune system, such as spleen and thymus. Western blotting of murine samples extracted from spleen and thymus reveal the expression of SMARCAD1 (band ~150kDa) in +/- animals and absence from -/- mice. Courtesy of Dr Louise Matheson.

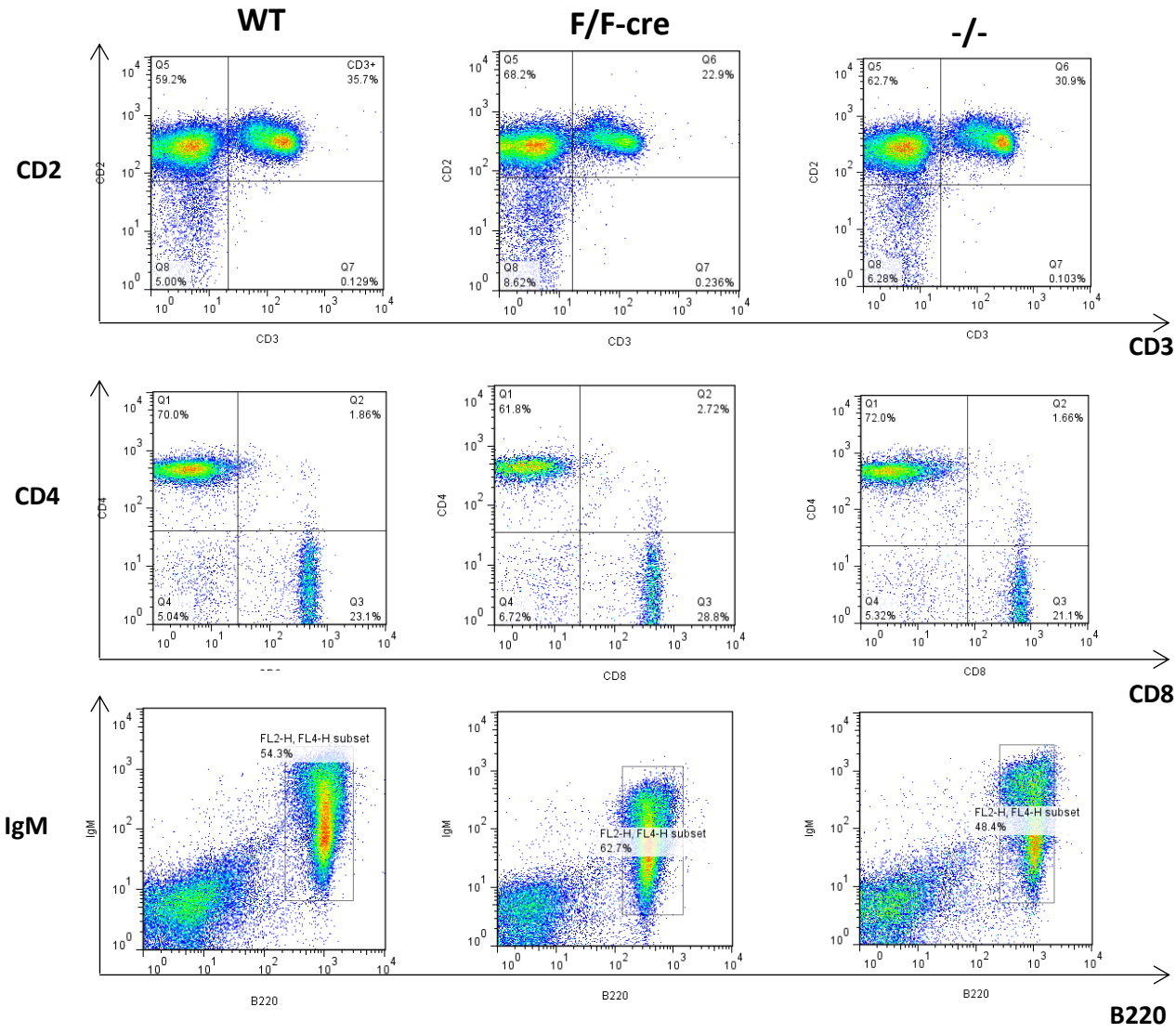

Figure 1.39. No major proportional loss (>20%) of systemic B-cells or T-cells is found in the spleen of *Smarcad1* knockout mice. Cells were stained with CD2 (all lymphocytes) and CD3 (T-cells only), CD4 (helper T-cells) and CD8 (cytotoxic T-cells), or IgM (B-cells) and B220 (common leukocyte antigen). Representative FACS plots illustrating the presence of CD2+/CD3+ T-lymphocytes (top), CD4+ or CD8+ T-lymphocytes (middle) and IgM+B220+ B-lymphocytes from WT, CD2-Cre Fl/Fl conditional knockout and ZP3-germline knockout mice. Courtesy of Dr Louise Matheson.

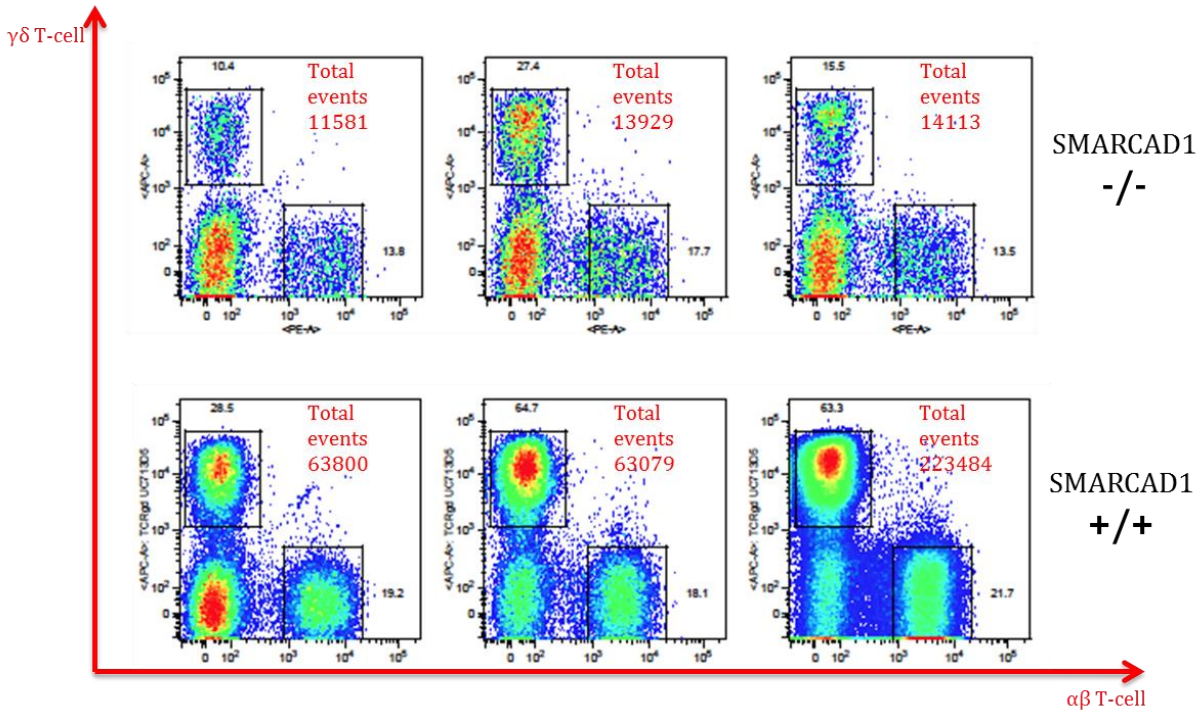

Figure 1.40. Loss of T-cells (both αβ and γδ T-cells) is visible in the small intestine of *Smarcad1*-/- mice (top row) compared to the small intestine of *Smarcad1*+/+ mice (bottom row). Loss is clear both in terms of % of T-cells in each plot and the total number events enumerated from equal intestinal starting material. Data courtesy of Marc Veldhoen.

1.10 Aims and objectives of this thesis:

This thesis aims to :-

- Describe the basic physical characteristics of mice lacking *Smarcad1*, including parameters such as mass and weight. The major tissues in which SMARCAD1 is expressed should also be elucidated and particular cells or tissues of interest identified to guide further studies.

- Confirm the loss of intestinal Intraepithelial lymphocytes previously observed, and give insight as to what difference in the murine intestine exist which underpin this loss.

- Detail the extent of the impact of SMARCAD1 loss on white adipose tissue.

Chapter 2 –
Materials and Methods

2.1 Experimental Animals.

All experiments were carried out in accordance with UK Home Office regulations. Animal breeding and husbandry was carried out by the Babraham Services Unit (BSU). Physical measurements (i.e. weekly weight measurements), extraction of blood and ear punches for genotyping were also performed by the BSU. Genotyping PCR, extraction of serum, additional weight (time of death) and length measurements, dissection of all tissue and organs and subsequent laboratory procedures were performed by Keith Porter. Selection of suitable animals for breeding was undertaken by Keith Porter and Patrick Varga-Weisz. All relevant procedures were covered under procedure project licence PPL 80/2488.

2.2 Genotyping of *Smarcad1*$^{+/+\ +/-\ -/-}$ and wild-type (WT) mice.

DNA was extracted from murine ear punches by boiling in 50mM NaOH (95°C) for 90 minutes, vortexing on full speed for 15seconds and quenching in 25µl Tris (pH7,4) before centrifugation at 12000g for 15 minutes at 4°C. 2µl of supernatant was subsequently used as template in genotyping PCR reactions.

Identification of *Smarcad1* wild-type/floxed or deleted alleles was performed by PCR using primer pairs diagnostic for each allele (see Table 2.1) For Neo-cassette containing (i.e. floxed) or deleted alleles, primer pairs NeoF/NeoR (Floxed) and Del-for/Del-rev (del) were used in a single PCR-reaction to amplify genomic DNA yielding 288bp or 623bp products respectively. To identify thepresence of the wild-type allele of *Smarcad1*, primers WT/Flox-for and WT/Flox-rev were used to amplify a product of 308bp, and combined in a single reaction with primers to identify Cre-recombinase alleles using primers Cre-For and Cre-Rev (CD2-Cre) to produce a 522bp product, or ZP3-for and ZP3-rev to produce a 656bp product.

For each PCR reaction, 1x KOD Reaction Buffer and 1U of KOD Polymerase (Merck 71086), was mixed with 3xSucrose/Cresol Red Loading Buffer (28% w/v Sucrose, 0.008% Cresol Red in sterile water) and 0.3M Betaine was mixed in a final volume of 20µl with primer concentrations as stated (see Table 2.1). Reactions were then thermal cycled as follows 95°C for 2min then 36 cycles of 95°C for 15s, 58°C for 30s, 72°C for 2min, and a final extension of 72°C 2min. 10µl of each product was resolved on 2%

agarose/EtBr gel 120V 60min alongside 5µl MassRuler marker (ThermoFisherScientific SM0403).

Discrimination	Target	Primer	Concentraton	Sequence	Product Size
Floxed/Deleted alleles	Deleted allele	Del-For	20µM	TGTGATGCCATTTTTGTTATTTG	623bp
		Del-Rev	20µM	TTCCAAAATAGACCCTGACAGAA	
	Floxed Allele	Neo-For	10µM	GGCTATTCGGCTATGACTGG	288bp
		Neo-Rev	10µM	ATACTTTCTCGGCAGGAGCA	
WT allele and Cre Presence	WT allele	WT For	30µM	CTCTTCCCCCTGAATCCTTC	308bp
		WT Rev	30µM	TGTGATGCCATTTTTGTTATTTG	
	CD2-Cre	Cre-For	10µM	GACAGGCAGGCCTTCTCTGAA	522bp
		Cre-Rev	10µM	CTTCTCCACACCAGCTGTGGA	
	ZP3-Cre	ZP3-For	10µM	GGTGTCATGGTAGGTATGGGT	656bp
		ZP3-Rev	10µM	CGCACAATCTCACGTTCAG	

Table 2.1. Primer sequences, discrimination and concentrations required for genotyping of *Smarcad1*+/+, +/- and -/- mice with or without CD2- or ZP3-Cre.

2.3 Physical dimensions and serum measurements of *Smarcad1* +/+ and -/- mice.

2.3.1. Physical measurements of *Smarcad1+/+ and -/-* mice.

For construction of growth curves, mice were weighed every 7 days from 14 days post-partum up until day 102. Neonatal weights and lengths were recorded within 24 hours of birth. All length measurements were made by straightening freshly euthanized mice and the anal-nasal (A-N) length recorded.

2.3.2. Serum analyses.

Serum used for biochemical analysis was extracted from the tail immediately after sacrifice, dispensed immediately into anti-coagulant (EDTA) collection tubes and centrifuged at 1000g for 20 minutes at 4°C. The top clear layer was then aliquoted to a fresh tube and snap frozen. All serum analysis was performed by the Core Biochemistry Assay Laboratory at Addenbrookes Hospital, Cambridge.

2.3.3. Measurement of fat pad mass.

Subcutaneous inguinal and visceral epididymal fat pads were excised from surrounding tissue by examination of tissue colour contrast to mark fat-pad anatomical boundaries. Symmetry of pads from the left and right depots was visually checked at time of weighing to confirm accurate dissection.

2.3.4. Tissue Panel western blotting for SMARCAD1.

Western blotting of adult murine tissues for SMARCAD1 expression was performed on tissue snap-frozen in liquid nitrogen at time of sacrifice. Organs were dissected and snap-frozen in a time-critical order as follows: Brain, Small Intestine, Caecum, Large Intestine, Pancreas, Liver, Kidney, Stomach, Thymus Heart, Lungs, White adipose tissue, Testes, Brown adipose tissue, Muscle, Skin, and Bone. Organs were mechanically dissociated with a mortar and pestle on dry ice before transfer to RIPA lysis buffer (150 mM sodium chloride, 1.0% Triton X-100, 0.5% sodium deoxycholate, 0.1% SDS , 50 mM Tris, pH 8.0) and immediate addition of an equal volume of 2x Laemmli Buffer/5% βME, with repeated aspiration before boiling for 10 minutes at 95°C prior to loading.

Samples were resolved on a 16% polyacrylamide gel for 20 minutes at 70V then 60 minutes at 130V. Transfer of samples to nitrocellulose membranes (Hybond-ECL, Amersham) was performed in Tris/Glycine/Methanol Buffer (150mM Tris, 770mM Glycine, 20% Methanol) at 15V for 50 minutes. Membranes were briefly washed in milliQ water before blocking in PBS/0.1% Tween20/5% milk for 1 hour at room temperature, and then incubating with primary antibody for 1 hour at room temperature (see Table 2.2). Membranes were then washed as follows: 3 washes for 1 minute each in PBS/0.1% Tween20, then 2x 15 minute washes in PBS/0.1% Tween, before incubation with secondary antibody for 1 hour at room temperature. Wash steps were then repeated before detection using enhanced luminescent detection (ECL) (Amersham RPN2106/2109) of horse-radish peroxidase-linked secondary antibody and blue light radiography sensitive film (Amersham RPN2134).

Equal loading of samples was determined empirically by iterative PAGE/western blot. Comparative analysis of peptide expression levels was performed using GelQuantNet densitometry software (see Appendix 1). In brief, band signals were obtained from scanned radiograph film images and quantified based on size/area and colour intensity, before local background signal subtraction. Each band of interest was then expressed as fold expression over the loading control (Lamin B1) for respective samples.

Antibody	Company	Dilution	Secondary antibody	Dilution
SMARCAD1	Sigma HPA016737	1:5000	anti-Rabbit-HRP	1:5000
Lamin B1	AbCam ab16048	1:5000	anti-Rabbit-HRP	1:5000

Table 2.2. Antibodies used for tissue panel screening of SMARCAD1 expression.

2.4 Intestinal lymphocyte extraction and analysis by flow cytometry.

2.4.1. Intestinal extraction and purification of intraepithelial lymphocytes.

Intestines were dissected between stomach and cecum, flushed once with 20ml of cold PBS, cut longitudinally into 10mm fragments, then incubated in 20ml IEL buffer (Mg+ free PBS/5%FCS/10mM HEPES/PolymixinB) in 50ml tubes place horizontally in a Infors HT Multitron Standard Shaker for 30 minutes at 37°C, 100rpm. Supernatant was passed through a 100μm cell strainer and centrifuged at 500g for 8 minutes at 4°C. Pellets were re-suspended in 9ml 37.5% isotonic Percoll/5% FCS and centrifuged at 700g for 10 minutes at room temperature, before washing in 5ml cold PBS/5% FCS and further centrifugation at 700g for 10 minutes at 4°C. Cells were then re-suspended in 1ml PBS/5% FCS, and 10% of the volume (100μl) removed and stained for FACS.

Spleens harvested from mice were mechanically disrupted and passed through a 40μm cell strainer into a 50 ml tube containing 3ml cold PBS, with 2x 1ml cold PBS washes of the cell strainer to remove residual tissue (into a final volume of 5ml cold PBS). Cells were pelleted at 500g for 5 minutes at 4°C, the supernatant removed, and re-suspended in 1ml cold PBS. 5% of the cell suspension was removed (50μl) and stained for flow cytometry.

2.4.2. Cell Staining for flow cytometry.

Cells collected as described were pelleted and incubated for 1 hour on ice (in the dark) in a total volume of 100μl PBS containing the following (final) concentrations of directly-conjugated antibodies: 2.5ng/μl anti-CD3-FITC (Biolegend 100204), 0.33ng/μl anti-CD8β-PerCP-Cy5.5 (Biolegend 126610), 0.5 ng/μl anti-CD103-AF647 (Biolegend 121410), 2.5ng/μl anti-CD4-AF700 (Biolegend 100430), 2.5ng/μl anti-TCRβ-Pacific Blue (Biolegend 109226), 2.5ng/μl anti-CD8α -V500 (Biolegend 560776), 0.25ng/μl anti-TCRγδ-PE (Biolegend 118108), and a live/dead amine-reactive cell viability dye was added to a final dilution of 1:10000 (Live/Dead near-IR fixable stain mix, Life Technologies L10119).

Cells were then washed twice by centrifugation 500g 5 min 4°C, tipping off supernatant and re-suspending in 200µl PBS/0.5% FCS. After the second centrifugation, cells were re-suspended in 240µl PBS/0.5%FCS (IEL prep) or 400µl PBS/0.5%FCS (spleen) and passed through a 40µm cell strainer prior to flow cytometric analysis using a Becton Dickinson LSR-Fortessa flow cytometer.

2.5 Extraction of RNA from murine small intestine and qPCR.

2.5.1. Dissection and preparation of murine duodenum.

The first 4cm of small intestine adjacent to the stomach was removed from each mouse to provide duodenal samples. Each duodenum was flushed with ice cold PBS/5% FCS and snap-frozen in liquid nitrogen. Prior to RNA extraction and purification, each sample was weighed and 100mg of tissue was mechanically dissociated in 1ml Tri-reagent (Sigma) using a mortar and pestle on dry-ice.

2.5.2. RNA Extraction.

Total cellular RNA was extracted using Tri-reagent (Sigma) following the manufacturer's instructions. In brief, homogenized material was centrifuged (12000g, 10 minutes, 4°C) and the top layer containing residual fat removed. Chloroform was then added (0.2ml per ml starting volume) and after vigorous mixing and standing at room temperature, phases were separated after centrifugation (12000g 15 minutes, 4°C). The colourless upper phase containing RNA was then removed into a fresh tube, and nucleic acid precipitated with 0.5ml isopropanol, then washed with 1ml 75% ethanol. RNA was pelleted at 7500g 5 minutes 4°C and resuspended in 100µl nuclease free H_2O. RNA purity and concentration was determined using a NanoDrop 1000 Spectrophotometer (Thermo Scientific).

2.5.3. Generation of cDNA using Reverse Transcriptase.

Extracted RNA was then used to generate cDNA using the RevertAid Kit (ThermoFisherScientific EP0441) following the manufacturer's instructions. In brief, 500ng of total RNA was mixed with Oligo (dT) (100pmol) in a final volume of 12.5µl and

incubated at 65°C for 5 minutes before cooling on ice. This was then mixed with 20 units of Thermo Scientific™RiboLock RNase Inhibitor, 1mM dNTP mix, 200units of reverse transcriptase and 1x (final) reaction buffer in a final volume of 20µl, and incubated for 60 minutes at 42°C before reaction termination at 70°C for 10 minutes.

2.5.4. Quantitative PCR (qPCR) of transcript levels.

Template cDNA samples prepared as above were diluted 1 in 2, then run in triplicate on an BioRad CFX96 qPCR station, in a total reaction volume of 25µl containing 1x SyBr Green mastermix (Applied Biosystems 4309155), 5µM of each primer and 5.5µl of each diluted template cDNA. Samples were cycled under the following conditions: 95°C for 15 seconds, 60°C for 30 seconds for 45 cycles, then melt curve analysis performed by incremental temperature increases (ΔT) at +1°C/s from 55°C to 95°C. Threshold fluorescence was detected using default settings. Primers used for qPCR analysis can been found in Table 2.3

Gene	Forward Primer 5' - 3'	Reverse Primer 5' - 3'
Smarcad1	TCAGACATTGAAGGAACTGTTTC	CATCAGCAAGGCAGCAG
HPGDS	CACGCTGGATGACTTCATGT	AATTCATTGAACATCCGCTCTT
TLR4	AAGCCGAAAGGTGATTGTTG	CTGAGCAGGGTCTTCTCCAC
TNFα	ACAGAAAGCATGATCGGCG	GCCCCCCATCTTTTGGG
IFNγ	AGCTCTTCCTCATGGCTGTT	TTTGCCAGTTCCTCCAGATA
Myc	GCTCGCCCAAATCCTGTACCT	TCTCCACAGACACCACATCAATTTC
Notch1	GATGGCCTCAATGGGTACAAG	TCGTTGTTGTTGATGTCACAGT
Notch2	ATGTGGACGAGTGTCTGTTGC	GGAAGCATAGGCACAGTCATC
Lgr5	TGCCCCGTGGCTTTCTTATC	TTTCCCAGGCTGCCCATATC
Dlk1	CCCAGGTGAGCTTCGAGTG	GGAGAGGGGTACTCTTGTTGAG
Gtl2	TTGCACATTTCCTGTGGGAC	AAGCACCATGAGCCACTAGG
Actin	GCCCTGAGGCTCTTTTCCAG	TGCCACAGGATTCCATACCC
TBP	AAGGGAGAATCATGGACCAG	CCGTAAGGCATCATTGGACT

Table 2.3. Primers used for qPCR analysis

2.6 Analysis of cell proliferation in the murine intestine by EdU incorporation.

2.6.1. Administration of EdU and processing of murine intestine for cryo-sectioning.

Mice were administered 200µl of 0.75mg/ml EdU (in DPBS) *via* intra-peritoneal injection 18 hours prior to sacrifice following regulated procedures. After euthanizing, small and large intestines were dissected, flushed in ice cold PBS/5%FCS, and fixed for 24 hours in 4% formaldehyde at 4°C. Intestinal samples were then incubated in 30% w/v sucrose for 24 hours at 4°C and snap frozen in Shandon embedding matrix (Thermo Scientific) on dry ice. Individual 8µm sections were cut using a Leica CM1950 cryostat at -18C° then adhered to frosted microscope slides on dry ice before storing at –80°C.

2.6.2. Click-iT EdU fluorescence detection.

Immunofluorescence detection of incorporated EdU was performed using the Click-iT® EdU Alexa Fluor® 594 Imaging Kit (Thermo Scientific) as per manufacturer's instructions. Slide-mounted intestinal sections (described above) were heated at 65°C for 5 minutes, washed twice in PBS/3% BSA and permeabilised in 0.5% Tween20/PBS at room temperature for 20 minutes. After two further washes in PBS/3% BSA, slides were air dried and a hydrophobic barrier applied around the area of interest using an ImmEdge™ hydrophobic barrier pen (Vector Labs H-4000). Covalent binding of fluorescent dye (Alexa-594) to EdU was then performed using 50µl Click-iT® reaction cocktail (1xTBS buffer, 20mM CuSO4, 1:100 Alexa-594 dye and 1x proprietary EdU buffer additive) for 30 minutes in the dark at room temperature. Slides were washed twice in PBS/3% BSA and stained with 5µg/ml Hoechst solution for 30 mins at room temperature in the dark, before two final washes in PBS and then mounting each slide with Vectashield (Vector Labs H-1000) under a varnish-sealed coverslip. Stained and mounted slides were stored at 4°C in the dark prior to analysis.

2.6.3. Enumeration of EdU+ve cells.

Images of in-plane intestinal crypt/villus units were captured on an Olympus BX61 microscope on a 20x objective, and fields where clear EdU/Alexa594 signal and nuclear Hoeschst staining could be unambiguously identified were used to score the number of EdU positive cells from the base of the crypt along the corresponding villus.

2.7 Immunofluorescent detection of goblet and paneth cells in the murine small intestine.

2.7.1. Slide preparation.

Murine small intestine was dissected, fixed and cut to 8µm cryosections as detailed in section 2.6.1. Slides were initially dried at room temperature for 15 minutes before fixing in 4% formaldehyde at room temperature for 15 minutes, washing twice in PBS/3%BSA (5 minutes each) and air drying. A hydrophobic border was applied to each area of interest on individual slides using an ImmEdge pen, and each section was permeabilised with 0.5% Triton/PBS for 20 minutes at room temperature.

2.7.2. Antibody/fluorophore binding, stringency washes and slide mounting.

Slides were washed twice in PBS, then blocked for one hour with blocking buffer (1% Triton X-100, 2% BSA, 5% FBS in PBS). Slides were then probed overnight at 4°C using either 12µg/ml anti-Lysozyme rabbit-pAb (AbCam ab2408) in blocking buffer, or 0.8µg/ml anti-Mucin rabbit-pAb (Santa Cruz Biotechnology H-300) in blocking buffer. The following day slides were washed 3 times in PBS (5 minutes each) then probed with anti-rabbit-Alex-488 secondary antibody for 1 hour at room temperature in the dark. Slides were then washed 3 times in PBS (5 minutes each) before mounting with 30µl Vectashield (with DAPI) under varnish-sealed 22 x 40mm coverslips.

2.7.3. Intestinal Immunofluorescence Analysis.

Small intestinal sections were visualised using an Olympus BX61 microscope and a 20x objective. For each section the presence/absence and crypt/villus location of anti-Lysozyme signal was recorded for the correct presence/location of Paneth Cells, and anti-Mucin for correct presence/location of Goblet Cells.

2.8 Analysis of intestinal microbiota.

2.8.1. Extraction of microbial DNA.

DNA from homogenized tissues was extracted using QIAmp DNA Stool Kit (Qiagen 51504) according to the manufacturer's instructions. In brief, a maximum of 220mg of fresh stool sample was removed from the small intestine or colon and lysed at 95°C for 5 minutes in 2ml Buffer ASL. After vortexing for 15 seconds, samples were then centrifuged at full speed for 1 minute. Supernatant was transferred to a fresh tube and one INhibitEx® tablet added per tube and vortexed immediately for 1 minute to dissolve. Samples were then centrifuged for 3 minutes at full speed and supernatant transferred to a fresh tube containing Proteinase K, before addition of 200µl of Buffer AL, vortexing for 15 seconds and incubation at 70°C for 10 minutes. After incubation, 200 µl of 96-100% ethanol was added to each sample and samples then applied to QIAmp spin columns. After centrifugation at full speed for 1 minute, DNA bound to columns was then washed once in 500µl Buffer AW1 then once in Buffer AW2 and centrifuged again to dry the column. Samples were then eluted into fresh collection tubes from QIAmp columns by addition of 50µl AE Elution Buffer, incubation at room temperature for 1 minute and centrifugation at full speed for one minute. Concentration of extracted stool DNA was confirmed using a Nanodrop 1000 Spectrophotometer (Thermo Scientific).

2.8.2. Thermal cycling and selective amplification of microbial DNA by PCR.

Extracted stool DNA was then analysed by qPCR using a CFX96 Real-Time system (BioRad). Reactions were prepared in a final volume of 20µl containing 2µl DNA, 10µl SyBr Green Mastermix (Applied Biosystems), 10mg/ml BSA and 10µM of each Primer (see Table 2.4 for primer pairs and target species). Each reaction was set up in triplicate and cycled under the following PCR conditions: 20 seconds at 95°C, then 40 cycles of 30 seconds at 95°C and 30 seconds at the appropriate annealing temperature (see Table 2.5):-

Target group	Primer sequence (5'- 3')	Primer name
All groups	ACT CCT ACG GGA GGC AGC AG	Eub338
All groups	ATT ACC GCG GCT GCT GG	Eub518
αProteobacteria	TCT ACG RAT TTC ACC YCT AC	Alf685
βProteobacteria	TCA CTG CTA CAC GYG	Bet680
Actinobacteria	CGC GGC CTA TCA GCT TGT TG	Actino235
Firmicutes	GCA GTA GGG AAT CTT CCG	Lgc353
Bacteroidetes	GTA CTG AGA CAC GGA CCA	Cfb319

Table 2.4 – Primer sequences for intestinal microbiota analysis

Target group	Forward primer	Reverse primer	Annealing temp.
All *Bacteria*	Eub338	Eub518	53
αProteobacteria	Eub338	Alf685	60
βProteobacteria	Eub338	Bet680	60
Actinobacteria	Actino235	Eub518	60
Firmicutes	Lgc353	Eub518	60
Bacteroidetes	Cfb319	Eub518	65

Table 2.5 – Annealing temperatures for intestinal microbiota PCR

2.9 Library construction and RNA seq of murine white adipose tissue.

2.9.1. DNAse and Ribolock treatment of RNA.

A total of 100µg RNA (extracted as in step 2.5.2) was treated with 10 Units DNAseI (Fermentas EN0521), 400 Units of Ribolock RNAse inhibitor (Fermentas EO0381) and 2mM DTT for 1 hour at 37°C. These were then applied to poly(dA) magnetic beads for mRNA purification (see below).

2.9.2. Purification of polyA+ mRNA.

Isolation of mRNA was then performed on DNAse/Ribolock treated total RNA using Oligo-dT magnetic beads (Dynabeads mRNA purification Kit, Ambion 61006) as per the manufacturer's instructions. In brief, 100µg total RNA was diluted into 150µl nuclease-free water and heat-denatured at 65°C for 2 minutes before placing immediately on ice. A total of 300µl Dynabeads was pre-washed with Ambion Binding Buffer, and resuspended in a total volume of 150µl Binding Buffer, prior to mixing in a 1:1 ratio with denatured total RNA for 5 minutes at room temperature. Bead-bound polyA+ mRNA was separated from supernatant on a magnetic stand, washed twice with Ambion Wash Buffer B, before elution in 30µl 10mM Tris HCl pH 7.5 for 6 minutes at 65°C.

2.9.3. Fragmentation of mRNA.

Purified mRNA was fragmented to yield single stranded RNA with a size range from 100-300 bases as per manufacturer's instructions. 250ng of purified mRNA was mixed with 2µl (10x) fragmentation buffer in a sterile PCR tube and made up to 20µl with sterile nuclease-free water, then incubated on a pre-heated thermal cycler at 94°C for 5 minutes before placing immediately on ice and addition of 2µl (10x) RNA fragmentation stop buffer. Fragmented mRNA was then precipitated using 2µl (0.1x vols) 3M sodium acetate pH 5.5, 1.2µl (10mg/ml) linear acrylamide and 60µl (3x vols) 100% ethanol at -80°C for 1 hour, pelleted by centrifugation at 14000rpm for 25 minutes at 4°C, washed with 300µl 70% ethanol and air dried for 10 minutes at room temperature, before re-suspension in 14.5µl nuclease free water. 1µl was then removed for quantitation on the Nanodrop ND-1000 spectrophotometer.

2.9.4. First and Second Strand Synthesis.

For first strand cDNA synthesis, 13.5µl of fragmented mRNA from above was mixed with 1.0µl random primer mix and denatured at 65°C for 5 minutes before placing immediately on ice. To these tubes were added 4µl (5x) first strand synthesis reaction buffer and 0.5µl Murine RNAse Inhibitor before incubation at 25°C for 2 minutes, then addition of 1.0µl M-MuLV Reverse Transcriptase and incubation at 25°C for 10 minutes, 42°C for 50 minutes and inactivation at 70°C for 15 minutes before returning to ice. For second strand cDNA synthesis, 8µl (10x) second strand synthesis buffer and 4µl second strand synthesis enzyme mix were added to the first strand synthesis reaction and made up to 80µl with nuclease free water, before incubation at 16°C for 150 minutes then holding at 4°C before proceeding with magnetic bead purification (see below).

2.9.5. Purification of double-stranded cDNA using Sera Mag beads .

Double stranded cDNA synthesized above were then purified using Sera Mag beads (Fisher Scientific). Beads were prepared from concentrate (50x) using two washes in 1ml TE buffer/20µl concentrate (using magnetic stand to separate beads from TE) prior to resuspension in 1ml binding buffer (1.8% PEG8000, 2.5M NaCl, 10mM Tris HCl pH 8.0, 1mM EDTA, 0.05% Tween 20).

1.8x volumes of SeraMag beads (144µl) were then added to d/s cDNA, mixed by vortexing and incubating at room temperature for 5 minutes before placing on a magnetic stand to allow bead separation. Bound cDNA was then twice washed with fresh 80% ethanol before air drying (in magnetic stand) for 10 minutes at room temperature, elution with 52µl sterile water and transfer to DNA Lo-Bind tubes (Sigma Z666548).

2.9.6. End Repair of cDNA library.

Purified d/s cDNA (50µl from above) was then end repaired in a reaction mix using 10µl (10x) phosphorylation reaction buffer, 4µl dNTP mix, 5µl T4 DNA polymerase, 1µl E.Coli Large Klenow fragment, 5µl T4 Polynucleotide Kinase and 25µl nuclease free water (to a final volume of 100µl) before incubating at 20°C for 30 minutes. End repaired cDNA was then purified using 1.8x Sera Mag beads as detailed above, and eluted in 34µl nuclease free water before transferring 32µl to a fresh DNA Lo-Bind tube.

2.9.7. dA tailing of cDNA library.

Purified end-repaired cDNA (32µl from above) was then dA-tailed in a reaction mix using 5µl NEBuffer 2, 10µl deoxyadenosine 5' triphoshphate (1mM) and 3µl Klenow fragment (3' – 5' exo-) at 37°C for 30 minutes. dA tailed cDNA was then purified using 1.8x Sera Mag beads as detailed above, and eluted in 25µl nuclease free water before transferring 23µl to a fresh DNA Lo-Bind tube.

2.9.8. Adaptor and index primer ligation.

To allow sequencing using Illumina platforms, and subsequent identification of respective cDNA libraries, the dA tailed cDNA libraries were ligated with TruSeq universal adaptors (for Illumina sequencing) and single-ended barcoded adaptors (index primers for library ID). Adapters and Index Primers were diluted to 30µM each, then diluted 1:10 into a single mix containing 3µM adapter and 3µM index primer in sterile water. These were pre-annealed at room temperature for 30 minutes before addition to ligation reaction. The 23µl of A-tailed cDNA was then mixed with 1µl pre-annealed primers, 25µl (2x) Quick Ligation Reaction buffer, 1µl T4 DNA ligase, and incubated at room temperature for 15 minutes. Adaptor and index primer ligated products were then purified using 1.8X Sera Mag beads as previously described, and eluted with 150µl nuclease free water.

2.9.9. Size selection of adapter/index primer ligated cDNA libraries.

The cDNA products with ligated adapter and index primers were then size selected using different relative volumes of Sera Mag beads to product. Larger molecular weight products were first removed by incubation and magnetic selection with 0.9x volumes of Sera Mag beads, after which the beads were discarded and the supernatant transferred to a fresh low bind tube. Next, smaller molecular weight cDNA was removed using 0.2x volumes of Sera Mag beads (with incubation and magnetic selection) after which supernatant was discarded, and bead-bound cDNA washed with fresh 80% ethanol then eluted with 35µl nuclease free water. 33µl was transferred to a fresh DNA lo-bind microfuge tube.

Amplified libraries were then purified using 1.8x Sera Mag beads as previously described, and eluted into 40µl nuclease free water.

Quality control of the amplified adapter/index primer ligated cDNA libraries was performed by electropherogram using a BioAnalyzer (Agilent), providing size distribution and concentration (see Appendix). Concentrations were confirmed using qPCR against standards of known concentration.

Libraries were sequenced using pair-end reads on an Illumina platform and aligned to mouse genome and analysed as described in the Results section of this thesis.

Oligonucleotide sequences for TruSeq™ RNA and DNA Sample Prep Kits	
TruSeq Universal Adapter	AATGATACGGCGACCACCGAGATCTACACTCTTTCCCTACACGACGCTCTTCCGATCT
TruSeq Adapter, Index 1	GATCGGAAGAGCACACGTCTGAACTCCAGTCACATCACGATCTCGTATGCCGTCTTCTGCTTG
TruSeq Adapter, Index 2	GATCGGAAGAGCACACGTCTGAACTCCAGTCACCGATGTATCTCGTATGCCGTCTTCTGCTTG
TruSeq Adapter, Index 3	GATCGGAAGAGCACACGTCTGAACTCCAGTCACTTAGGCATCTCGTATGCCGTCTTCTGCTTG
TruSeq Adapter, Index 4	GATCGGAAGAGCACACGTCTGAACTCCAGTCACTGACCAATCTCGTATGCCGTCTTCTGCTTG
TruSeq Adapter, Index 5	GATCGGAAGAGCACACGTCTGAACTCCAGTCACACAGTGATCTCGTATGCCGTCTTCTGCTTG
TruSeq Adapter, Index 6	GATCGGAAGAGCACACGTCTGAACTCCAGTCACGCCAATATCTCGTATGCCGTCTTCTGCTTG
TruSeq Adapter, Index 7	GATCGGAAGAGCACACGTCTGAACTCCAGTCACCAGATCATCTCGTATGCCGTCTTCTGCTTG
TruSeq Adapter, Index 8	GATCGGAAGAGCACACGTCTGAACTCCAGTCACACTTGAATCTCGTATGCCGTCTTCTGCTTG
TruSeq Adapter, Index 9	GATCGGAAGAGCACACGTCTGAACTCCAGTCACGATCAGATCTCGTATGCCGTCTTCTGCTTG
TruSeq Adapter, Index 10	GATCGGAAGAGCACACGTCTGAACTCCAGTCACTAGCTTATCTCGTATGCCGTCTTCTGCTTG
TruSeq Adapter, Index 11	GATCGGAAGAGCACACGTCTGAACTCCAGTCACGGCTACATCTCGTATGCCGTCTTCTGCTTG
TruSeq Adapter, Index 12	GATCGGAAGAGCACACGTCTGAACTCCAGTCACCTTGTAATCTCGTATGCCGTCTTCTGCTTG

Table 2.6. Oligonucleotide adaptor bar codes used for read/sample identification in RNA-seq analysis of whole WAT extracts.

2.10. Measurement of adipocyte sizes.

2.10.1. Fixing and sectioning of white adipose tissue (WAT).

White adipose tissue from epididymal or subcutaneous fat depots were dissected and fat-pad pairs were visually inspected for symmetry (to check accurate dissection) before fixation in 4% formaldehyde overnight at 4°C. The following day sections were washed at room temperature for one hour each in 30%, 50%, 70% and 100% ethanol sequentially. After a further wash in 100% ethanol, sections were incubated twice in Xylene for 1 hour each (all at room temperature). Sections were then left overnight in the final Xylene wash at 4°C. The following day sections were incubated in Xylene at 60°C for 30 minutes, then an equal volume of paraffin wax was added and samples were incubated again at 60°C for 30 minutes. The total volume of liquid was then removed and replaced with fresh paraffin wax, before incubation at 60°C for 1 hour. Samples were then embedded in a sectioning chamber and left overnight at room temperature.

Samples were removed from the embedding chamber and maintained at 4°C, prior to sectioning to 10μm. Each individual section was immediately placed in a water bath at 44°C and adhered directed to a Poly-L-Lysine coated microscope slide. Slides were dried overnight before further staining.

2.10.2. Hematoxylin and Eosin staining.

Slides containing WAT sections were incubated at 65°C for 20 minutes to melt the paraffin, then incubated with first Xylene for 10 minutes then 100% ethanol for 5 minutes and air dried. Slides were then stained with Haematoxylin for 10 minutes at room temperature and rinsed in water for 5 minutes, then stained in eosin (0.5% in 95% ethanol) by transfer of slides through 8 sequential jars each containing eosin stain solution. Slides were then rinsed in water and dehydrated in a series of 50%, 70%, 95% and 100% ethanol jars before briefly incubated in xylene prior to mounting with cytoseal (VWR 48212-154).

2.10.3. Imaging and measurement (ImageJ/Watershed).

Images of adipocyte sections were captured on an Olympus BX61 microscope using a 10x objective, and images were processed using ImageJ software and the Watershed algorithm (see http://dev.mri.cnrs.fr/projects/imagej-macros/wiki/Adipocytes_Tool) was utilised to calculate the sizes of each adipocyte clearly distinguishable in each

captured field (see Appendix 3). In brief, cell boundaries were identified by the software and estimates of cell length and width used to calculate the size of a best-fit ellipse. The area of each ellipse was then used as an estimate of individual adipocyte size.

2.11 Isolation and enumeration of adipocyte stem cells and tissue-resident macrophages by flow cytometry.

2.11.1. Isolation of stromal-vascular fraction of white adipose tissue (WAT).

White adipocyte isolation and flow cytometry was based on the original procedure detailed by Church et al (2008). First, white adipose tissue was dissected from mice as described in section 2.10.1. Each pad pair was immediately placed in PBS/5% FBS on ice before cutting to 5-10mm pieces, then incubating in Collagenase buffer (10mg/ml Collagenase (Sigma) containing 3% bovine serum albumin (BSA), 1.23mM calcium chloride, 1.03mM magnesium chloride and 0.83mM zinc chloride for 60 minutes at 37°C, followed by vigorous shaking by hand for 15 seconds, then a further incubation at 37°C for 15 minutes. Dissociated tissue was then centrifuged at 300g for 3 minutes, and the supernatant (containing a top layer of fat) removed. The remaining stromal-vascular fraction was washed in 5ml cold PBS/3% BSA and filtered through a 40µm cell strainer, washed again in 5ml cold PBS/3% BSA then pelleted again ahead of immediate re-suspension in antibody staining mix for flow cytometry (below). For enumeration of adipocyte-stem cells, 10% of the total volume of isolated stromal-vascular fraction was pelleted and then stained for cytometry.

2.11.2. Staining of WAT stroma-vascular fraction for flow cytometry.

For enumeration of adipocyte-stem cells, 10% of the total volume of isolated stromal-vascular fraction was pelleted and then stained for cytometry in 100µl of antibody-stain mix, for cell sorting 95% of the fraction was stained in 950µl stain mix; the samples were incubated for 1 hour on ice with the following antibody mix: 2µg/ml anti-CD24-e450 (eBioscience 48-0242-80), 0.5µg/ml anti-CD29-PE-Cy7 (Biolegend 102221), 0.167µg/ml anti-CD31 (eBioscience 46-0311-80), 1µg/ml anti-CD34-PE (Biolegend 119307), 0.1µg/ml anti-CD45-AF488 (Biolegend 103121), 0.2µg/ml anti-Sca-1-APC (Biolegend 108111), Live/Dead fixable near IR viability stain (Life Sciences L10119) 1:10000 dilution. After staining cells were washed twice in 1ml PBS/3%BSA (centrifuged at 300g

5 minutes, supernatant removed, pellet re-suspended in1ml PBS/3% BSA) then re-suspended in 300µl PBS/1% BSA (enumeration) or 3ml PBS/1% BSA (sorting). For enumeration samples were then analysed on a Becton Dickinson LSRFortessa flow cytometer, for cell purification samples were run on a BD Influx cell sorter and collected in 3% BSA/PBS pre-coated FACS tubes containing DMEM/10% FCS/1x Pen/Strep.

2.11.3. Culture of FACS-sorted putative adipocyte stem cells (ASCs).

Cells purified by FACS in step 2.11.2 were pelleted by centrifugation (1200rpm, 5 minutes, 4°C) and re-suspended in 1ml fresh media (DMEM/10% FCS/1xAnti-Anti). Three different fractions were sorted (Lin+ve [CD31/CD45+ve). "Lin-ve"(CD31-CD45-CD29-CD34-) and "Sca1+ve" (CD31-CD45-CD29+CD34+Sca1+)) and each was seeded into 24 well plates (carboxyl coated) at a density of 5000 cells/well. Plates were incubated for 48 hours before media was changed to DMEM/10% FCS/1xPen/Strep, then changed every subsequent 72 hours. Cells of the Sca1+ original lineage were expanded after morphological change to fibroblastic appearance prior to further experiments.

2.11.4. Differentiation of ASCs into lipid-storing adipocytes.

Cells expanded from the Sca1+ lineage were seeded into 12 well plates at a density of 20,000 cells per well and allowed to grow to confluence (~72 hours). 2 days post-confluence the media was changed to an adipocyte-differentiation cocktail (DMEM/10% FCS/Pen/Strep containing 30µg/ml IBMX, 1µg/ml Insulin, 0.25µg/ml Dexamethasone) for 72 hours, then media was again changed to maintenance media (DMEM/ 10% FCS/Pen/Strep) every 48 hours for 20 days.

2.11.5. Oil-Red O staining and quantitation of differentiated adipocytes.

After differentiation and maintenance culture, putative adipocytes were fixed in 1ml 2% formaldehyde at room temperature for 15 minutes, rinsed in 1ml PBS then 1ml water and 1ml 60% ethanol, before staining in Oil-Red-O solution (0.7%w/v Oil Red O (Sigma) in 60% isopropanol).

2.11.6. RNA isolation and qPCR.

Cells differentiated as in step 2.11.4 were carefully washed in PBS before scraping in 200µl/well Tri Reagent (Sigma), transfer to a 2.0ml microfuge tube and snap freezing on

dry ice before storing at -70C prior to RNA extraction. RNA extraction was performed as detailed in step 2.4.2.

2.11.7. Western Blotting of sorted fractions (Lin+, Lin-, Sca1+).

Cells isolated by FACS as in step 2.11.2 were pelleted and re-suspended in RIPA protein-lysis buffer then mixed in an equal volume of 2xLaemmli Buffer/5% βME Supernatants were boiled for 10 minutes at 95°C prior to resolving by PAGE and western blotting as previously described in section 2.3.4.

2.11.8. Enumeration of WAT-resident macrophages by flow cytometry.

The stromal-vascular fraction of dissected white adipose tissue epididymal and subcutaneous fat pads was isolated as previously detailed in section 2.11.1. For enumeration of WAT-resident macrophages, 10% of the re-suspended fraction was pelleted and incubated for 1 hour on ice in 100µl of the following antibody stain mix: 2µg/ml anti-CD45-AF488 (Biolegend 304019), 0.625µg/ml F4/80-AF647 (Biolegend123121), Live/Dead near IR cell viability stain (Life Sciences L101l9) diluted 1 in 10000. After washing, cells were washed twice in 1ml PBS/3% BSA (centrifuged at 300g 5 minutes, supernatant removed, pellet re-suspended in 1ml PBS/3% BSA) then re-suspended in 200µl PBS/1% BSA and analysed on a Becton Dickinson LSRFortessa flow cytometer.

2.12 High fat diet (HFD) mice.

Mice for high fat challenge were singly caged and allowed to feed modified 60% fat chow *ad libitum*. Each mouse was weighed at exactly 7 day intervals and the increase in weight plotted for each mouse/week. After six weeks of HFD, mice were euthanised and serum extracted for triglyceride and free fatty acid content (extraction as in section 2.2.2). Subcutaneous inguinal and visceral epididymal WAT were then dissected and tissue-resident macrophages and putative adipocyte stem cells enumerated as described using 50% of each tissue. The other 50% of WAT tissue from each depot was fixed and analysed for adipocyte area (as described in section 2.10).

In addition to metabolic experiments, intestinal sections were dissected and analysed for microbial content as described in section 2.8.

2.13 Differentiation of Mouse-Embryonic Fibroblasts to lipid-storing adipocytes

Mouse embryonic fibroblasts were generated as described and stored in liquid nitrogen. Cells were resuscitated in DMEM/F12 media containing 10% FCS and 1x penicillin/1x streptomycin using standard methods, and seeded into T25 flasks overnight. After one media change the next day, cells were split into T75 flasks 72 hours after thaw and maintained at >50% confluence for a maximum of 10 passages. Aliquots were taken and seeded at 10,000 cells per well in a 12 well plate for subsequent counting and cell differentiation experiments.

For differentiation experiments, cells seeded into a 12 well plate were maintained until 2 days post confluence, then media was changed to the differentiation mix as described in section 2.11.4. After 72 hours media was changed back to maintenance media, and from then changed every 2 days for a further 10 days. Cells were then fixed and stained for Oil Red O as described in section 2.11.5. Three wells from three MEF lines of each genotype were differentiated, in parallel to three wells each of undifferentiated cells as a control.

For cell proliferation studies, 10,000 cells per well were seeded into 12 wells of a 12 well plate from each of 8 MEF lines (4 experimental and 4 control). After 24 hours, four wells were trypsinized, washed in PBS and counted from each plate (phase-bright cells were counted), then after 48 and 72 hours this process was repeated.

2.14 Cell Cycle analysis of *Smarcad1*+ve and –ve MEFs by flow cytometry.

For cell cycle analysis, MEF cell lines were split and seeded at a density of 25000 cells/well in a 12 well plate in DMEM/F12 media containing 10% FCS 100U Pen/Strep. After 24 hours cells were detached by trypsinisation, transferred to a 50ml tube and centrifuged at 1200rpm for 5 minutes. Supernatant was decanted and cells were washed in 10ml PBS and centrifuged again at 1200rpm for 5 minutes. After decanting of supernatant, cells were vortexed briefly in residual supernatant and resuspended by dropwise addition of 10ml ice-cold 70% ethanol while vortexing. Samples were

incubated for a minimum of 1 hour at 4°C before pelleting and two further washes in PBS (as performed above). After the second of these centrifugation steps, the supernatant was removed and cells were stained in 500µl of PI solution (0.1% TritonX-100, 50µg/ml RNAseA (SigmaR6513), 25µg/ml propidium iodide) for 1 hour at room temperature prior to analysis by flow cytometry.

2.15 Western blotting of MEFs for epigenetic marks.

To assess whether the absence of SMARCAD1 impacted markers of repressive chromatin (previously linked to SMARCAD1 function), MEFs maintained in culture and split every 2 days were harvested and lysed in RIPA buffer for 30 minutes at 4°C then boiled for 10 minutes in an equal volume of 2xLaemmli buffer/5% β-ME and loaded onto a 16% polyacrylamide gel. The equivalent of 100,000 cells per lane was loaded and resolved for 20 minutes at 70V then 1 hour at 130V before transfer as previously described. Membranes were probed with the antibodies as described in Table 2.7.

Antibody	Company	Dilution	Secondary antibody	Dilution
HP1α	Cell Signalling Techology #2616	1:5000	anti-mouse HRP	1:5000
H3K9me3	AbCam ab8898	1:5000	anti-Rabbit-HRP	1:5000
SMARCAD1	Sigma HPA016737	1:5000	anti-Rabbit-HRP	1:5000
Lamin B1	AbCam ab16048	1:5000	anti-Rabbit-HRP	1:5000

Table 2.7 – Antibodies used for western blot analysis of Smarcad1+ve/-ve MEFs.

Chapter 3 -
Phenotypic overview of *Smarcad1*-/- mice.

3.1 Introduction

This chapter details the basic physical, genetic and metabolic characteristics of the *Smarcad1*-/- mice, and point towards key tissues where further investigation would give deeper insight into the impact of SMARCAD1 loss.

3.2 Physical, genetic and metabolic overview of *Smarcad1*-/- mice.

3.2.1 Fewer than expected *Smarcad1*-/- offspring are produced from +/- x +/- matings, as revealed by a novel genotyping strategy.

To assess the impact of SMARCAD1 loss on neonatal/perinatal viability, offspring from *Smarcad1* heterozygous inter-crosses (+/- x +/-) were genotyped at 10 days post-partum. A novel genotyping PCR strategy was designed to facilitate multiplexing (i.e. primers with common annealing conditions, readily distinguishable PCR product sizes (Figure 3.1), see materials and methods section 2.1), facilitating large scale screens (e.g. >100 samples), thereby increasing sample size for analysis. Comparison of offspring genotypes with the expected genotypes from Mendelian inheritance revealed that fewer than expected -/- pups were present at day 10, with the number of female -/- pups more greatly reduced than male -/- mice (3.49% female and 6.25% male offspring respectively, cf. expected 25%) (Figure 3.2). Conversely, a relative increase in the expected number of +/+ offspring was seen in both female and male pups, with 37.2% and 40.0% respectively. These data confirm that offspring lacking SMARCAD1 are more susceptible to pre/perinatal mortality, as was also observed in a previous knockout model of SMARCAD1 (Schoor et al., 1999).

(a)

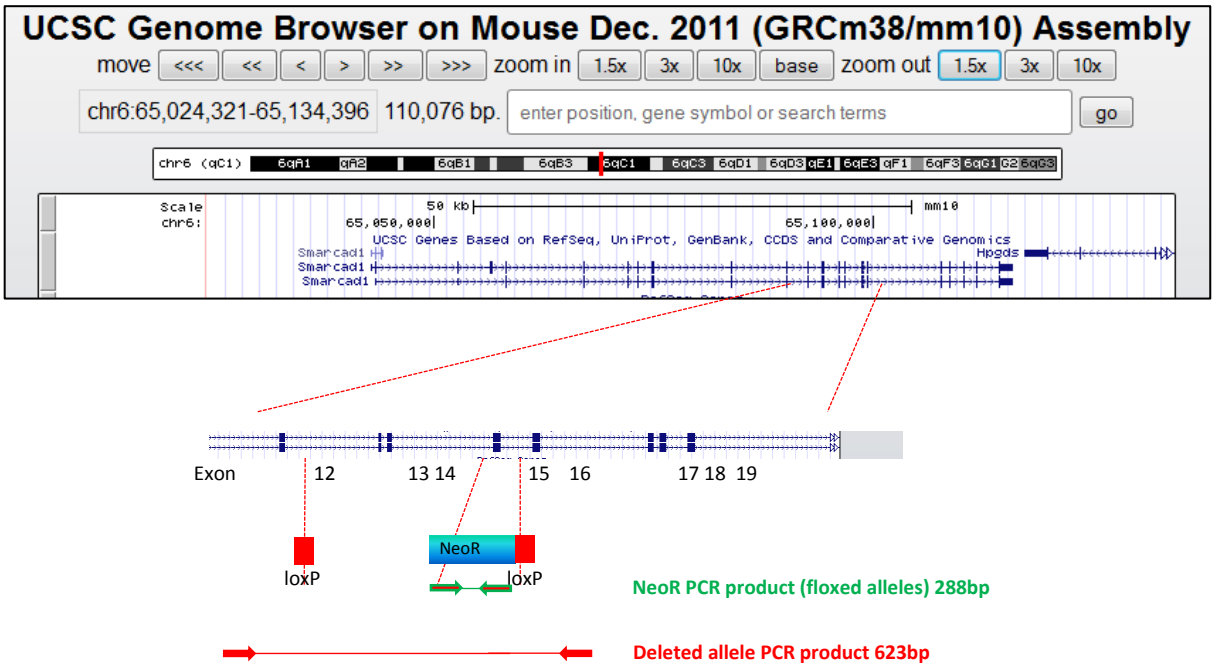

(b)

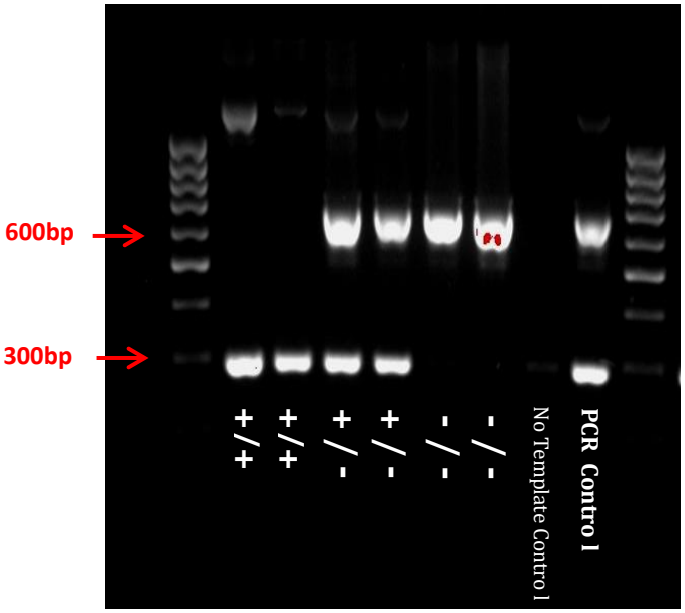

Figure 3.1: Novel genotyping PCR design allows multiplexed and rapid resolution of offspring genotypes. (a) Primers designed to the floxed allele produce a band at 288bp, whereas primers targeted to the deleted (ATPase -ve) allele produce a band at 623bp. Heterozygous offspring produce both bands from the same reaction. (b) Two mice of each genotype were screened to QC the reaction, alongside a no DNA template control, and a control sample containing both deleted and floxed alleles.

As the observed genotypes were determined from samples obtained at day 10 post-partum, the specific time of death is unknown for any pups that had deceased by the time of sample (i.e. ear punch) collection. However, clues as to a cause of death are available from the known impact of SMARCAD1 and other mouse models (Turgeon & Meloche, 2009). Respiratory failure can be an early driver of mortality in the hours immediately after birth, and is linked to factors such as lung function and rib cage development (Ivkovic et al., 2003). As *Smarcad1/Etl1* knockout mice were previously reported with a reduced rib-cage size (and skeletal dysplasia), it is possible that this may underlie postnatal respiratory failure and mortality (Schoor et al., 1999). Alternatively, the expression of a short isoform of *SMARCAD1* in human skin suggests that a similar skin-specific isoform of *Smarcad1* may exist, and harbour an important function in murine skin. Failure of skin barrier-function in early-postnatal mice can lead to trans-epidermal water loss and mortality (Furuse et al., 2002). However, this particular defect is also associated with a loss of pup mass during the hours immediately after birth, and *Smarcad1*-/- neonates showed no significant difference in mass when weighed postnatally (alongside +/- littermates). Any defect in skin barrier function in *Smarcad1*-/- mice is unlikely to be as severe as those previously reported, which themselves lead to postnatal mortality (Turgeon & Meloche, 2009).

ALL OFFSPRING			
SMARCAD1+/+	SMARCAD1+/-	SMARCAD1-/-	TOTAL MICE
58	86	7	151
38.41%	56.95%	4.64%	100%

MALE			
SMARCAD1+/+	SMARCAD1+/-	SMARCAD1-/-	TOTAL MICE
26	35	4	65
40.00%	53.85%	6.15%	100%

FEMALE			
SMARCAD1+/+	SMARCAD1+/-	SMARCAD1-/-	TOTAL MICE
32	51	3	86
37.21%	59.30%	3.49%	100%

Figure 3.2. Offspring ratios of mice from *Smarcad1* heterozygous inter-crosses (+/- x +/-) confirm that fewer than expected *Smarcad1*-/- mice survive pre- or perinatally by day 10 post-partum. The cause of peri-natal mortality of Smarcad1-/- mice was not investigated in this study.

3.2.2 Growth and development of *Smarcad1+/+ vs -/-* mice.

Although preliminary data suggested that mice lacking SMARCAD1 weighed less than SMARCAD1 expressing counterparts (with smaller white-adipose tissue fat pads) (see Section 1.9.3), further experiments to clarify the magnitude of this difference revealed a more complicated picture. Firstly, a compilation of weights obtained at time of death during this study were used to project growth curves for *Smarcad1*+/+ vs -/- mice (Figure 3.3a). Trend curves extrapolated from these data suggest that *Smarcad1*-/- mice initially weigh less than +/+ mice, but show subsequent catch-up growth. Next, to provide a more detailed picture, five mice from each genotype were weighed on a weekly basis from two weeks post-partum until the age of 16 weeks. Weights were combined by genotype, and mean weights plotted for each week (Figure 3.3b). Although growth curves constructed from these weekly time points mirrored the trend of curves extrapolated time-of-death, no significant difference in weight was seen over the 16 weeks between the two genotypes. Interestingly, the magnitude of the difference in weight at 5 weeks of age was ostensibly smaller than the difference seen in a previous study of *Smarcad1/Elt1* knockout mice (Schoor et al 1999, see Section 1.3.6). While further study with larger sample numbers and an increased number of time points may reveal statistical significance, this was beyond the logistical constraints of this project.

3.2.3 *Smarcad1*-/- mice show weight-specific differences to *Smarcad1*+/+ mice, rather than generic development retardation from 4 months of age.

Differences in weight empirically recorded in mice >4 months old were further examined to confirm whether any generic developmental retardation was present in *Smarcad1*-/- mice. As other physical or dimensional reasons may underpin a difference in mouse body mass (e.g. a general defect or delay in development), and as such plots of A-N length (anal-nasal length) vs weight were constructed for *Smarcad1*+/+ and -/- mice. Generalised development delay would follow the same combined linear increase in both weight and length at the same time, i.e. growth retarded mice would retain the same length/weight proportions as normal mice. However, if differences in weight are driven by different sizes of discrete organs within the body (e.g. adipose tissue), then mice of the same length would harbour differences in mass. Comparison of length vs weight of *Smarcad1*-/- v +/+ mice revealed precisely this (Figure 3.4).

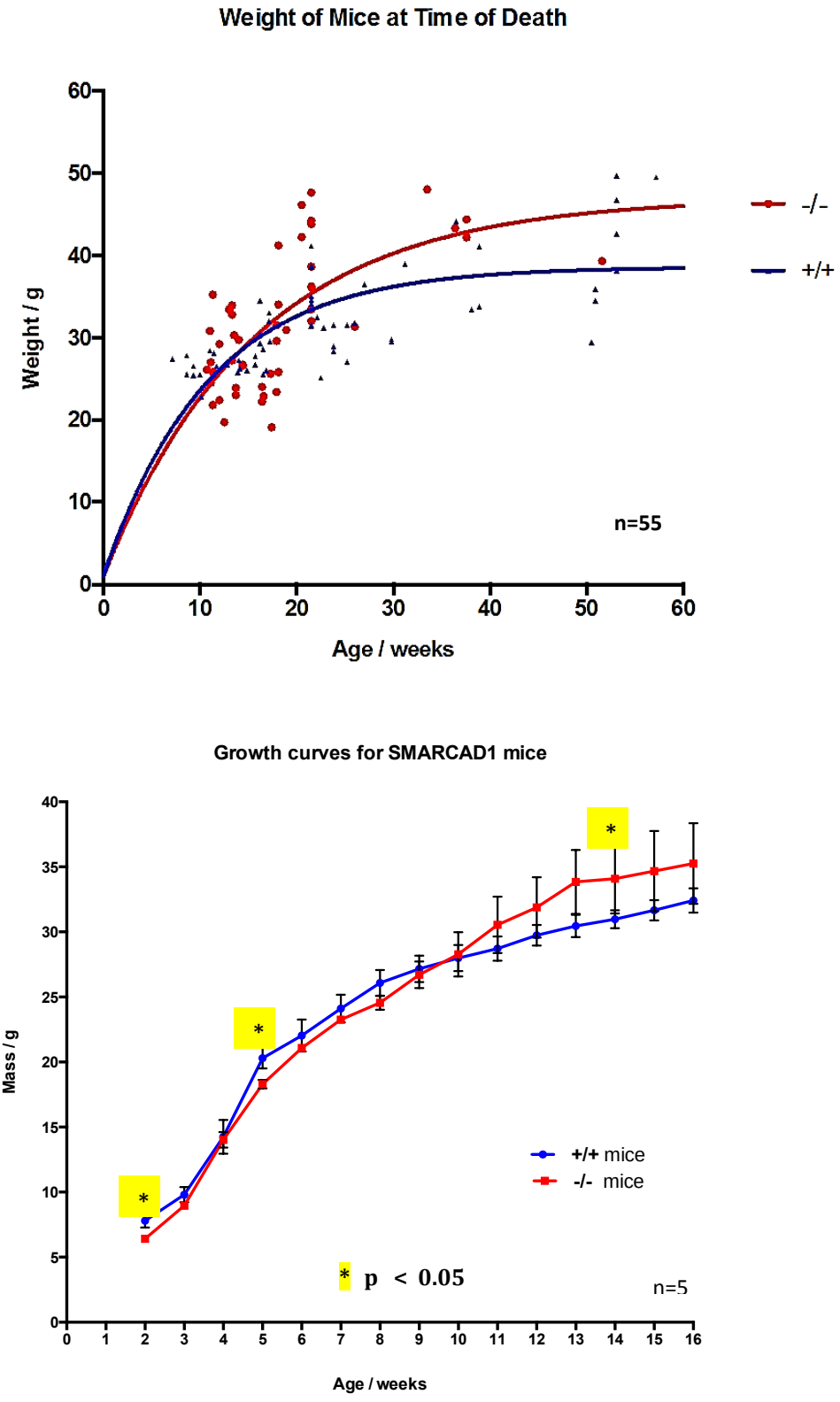

Figure 3.3. *Smarcad1*-/- male mice show a difference in body mass compared to +/+ controls. (a) Mice measured at time of death indicate lower post-natal weight with catch up growth (b) More detailed growth curves of male mice over the first 16 weeks post-partum support an initial lean phenotype for *Smarcad1*-/- mice.

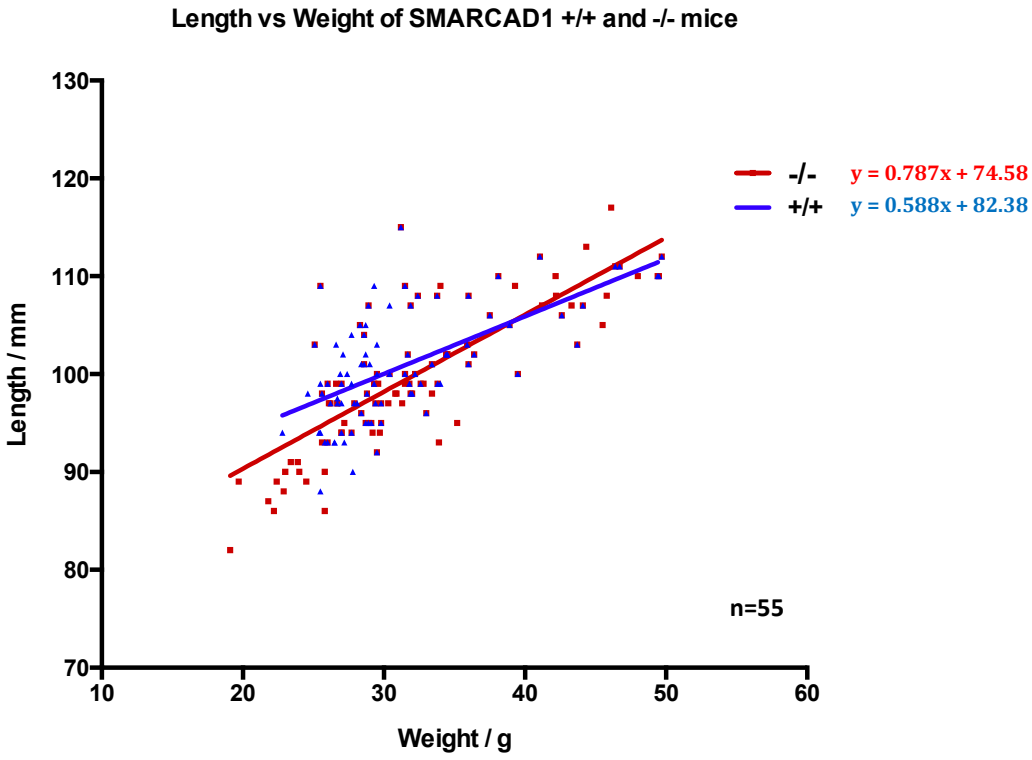

Figure 3.4. Changes in the mass v length proportions of *Smarcad1*-/- mice do not follow the same changes seen with natural (age-related) growth increase in *Smarcad1*+/+ mice. Trend lines plotted for weight versus A-N length for both groups, using mice 4 to 12 months of age.

3.2.4 Neonatal male *Smarcad1*-/- mice show no significant difference in birth weight compared to +/- litter-mates.

To gain further insight into whether any physical defects in adult *Smarcad1*-/- mice were influenced by gestational development, littermates were weighed at birth to check for any gross differences in mass. Given the logistical challenges in producing +/+ and -/- littermates, *Smarcad1*+/- and -/- littermates were bred and compared (Figure 3.5). While a number of developmental defects present with differences in birth weight, no statistical difference was observed between +/- and -/- groups. Furthermore, of the known developmentally-influential genes which impact birthweight (with potential post-natal metabolic impact), the genes Delta-Like 1 homologue (*Dlk1*) and Gene Trap Locus 2 (*Gtl2*) were analysed by qPCR in the liver of these neonates. No significant difference was found in *Dlk1* or *Gtl2* expression at time of birth (Figure 3.6). Taken

together, these data suggest that there are no significant differences during gestation which impact postnatal metabolism in (surviving) *Smarcad1*-/- male mice.

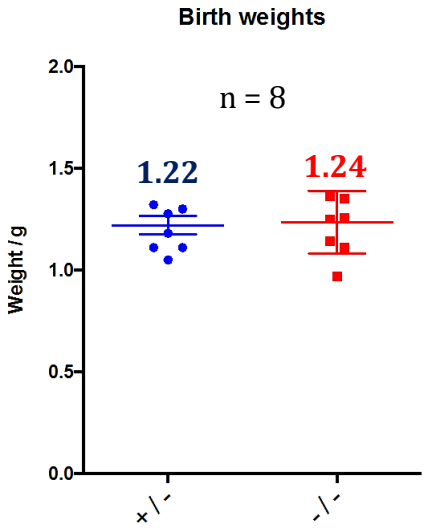

Figure 3.5. No difference is seen in birth weights between *Smarcad1*+/- and -/- littermates. As very few +/+ and -/- littermates are successfully produced this study required the comparison of heterozygous *Smarcad1*+/- and *Smarcad1*-/- mice.

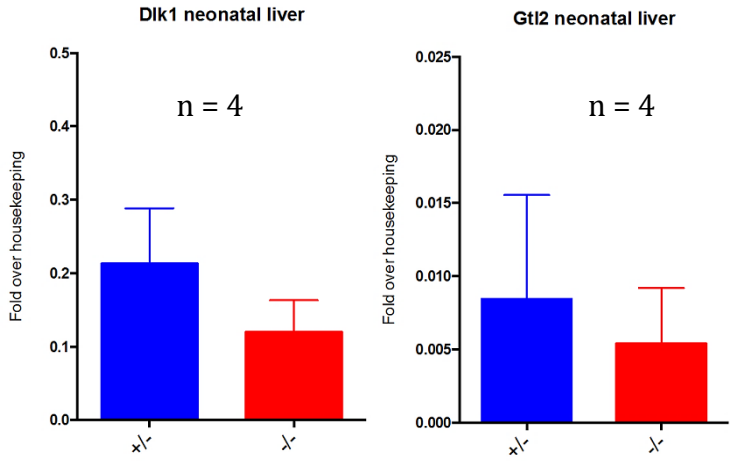

Figure 3.6. Analysis by qPCR of the developmentally influential genes Dlk1 and Gtl2 in the liver of neonates shows that no significant difference in expression was observed for either gene. Four livers from each genotype were analysed, using the ddCT analysis and two housekeeping genes (Actin and TBP) as a basis for normalisaton.

3.2.5 Food intake is not affected by loss of SMARCAD1.

To address whether any differences in food intake exist between *Smarcad1*+/+ and -/- mice (that may underpin difference in mass), four singly-housed *Smarcad1*+/+ and four singly-housed *Smarcad1*-/- age-matched mice was recorded over a period of four weeks, (via change in food-hopper weight). Comparison of the 16 food intake values per genotype revealed no significant difference in food intake between the two groups (Figure 3.7).

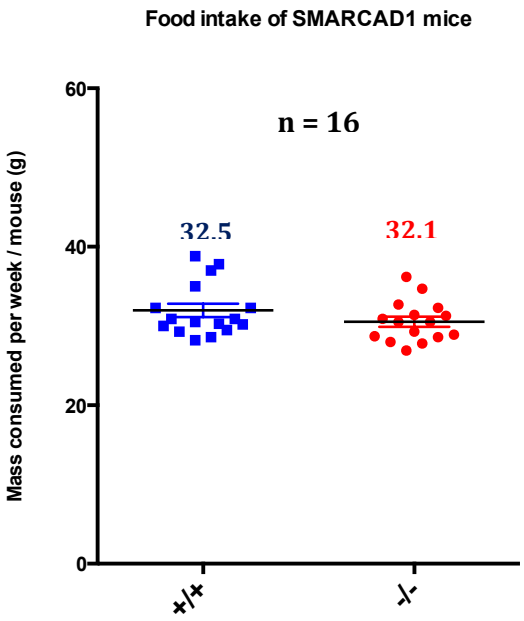

Figure 3.7. No significant difference in food intake was observed between four +/+ and four -/- mice over a period of four weeks (giving n=16 for each group). These data suggest that any change in the mass of *Smarcad1*-/- mice are not due to differences in appetite.

3.2.6 Serum free-fatty acid and triglyceride concentrations are elevated in mice lacking SMARCAD1 but not serum Insulin or Glucose concentrations.

The concentrations of serum peptides and metabolites from six *Smarcad1*+/+ and six *Smarcad1*-/- mice before and after a 16 hour (overnight) fast was assayed to give insight into any basal metabolic differences in mice lacking SMARCAD1. No significant difference was found in serum glucose or serum insulin concentrations between +/+ and -/- groups before or after fasting. However, serum triglyceride levels were significantly higher in *Smarcad1*-/- mice prior to fasting, and a trend was observed for elevated serum concentrations of Free Fatty Acids before and after fasting in the *Smarcad1*-/- animals (Figure 3.8).

While the increase in serum triglycerides found in *Smarcad1*-/- was statistically significant, the proportional increase over +/+ mice (~30% increase in serum [TG]) was not at a level comparable to other mouse models of metabolic dysfunction, such as the obese (*ob/ob*) mice (~50% increase in serum [TG] over WT mice, with blood concentration of 1.31mmol/L cf. 0.83 for *Smarcad1*-/- mice) (Ku et al., 2016), or the growth-retarded and obese *Dlk1*-/- mice (34% and 76% increase in serum [FFA] and [TG] over WT respectively, cf. 20% increase [FFA] and 30% [TG] for *Smarcad1*-/- mice over +/+ mice respectively) (Moon et al., 2002). These results suggest that any metabolic phenotype observed in *Smarcad1*-/- mice is not as severe as m other mouse models of metabolic pathology.

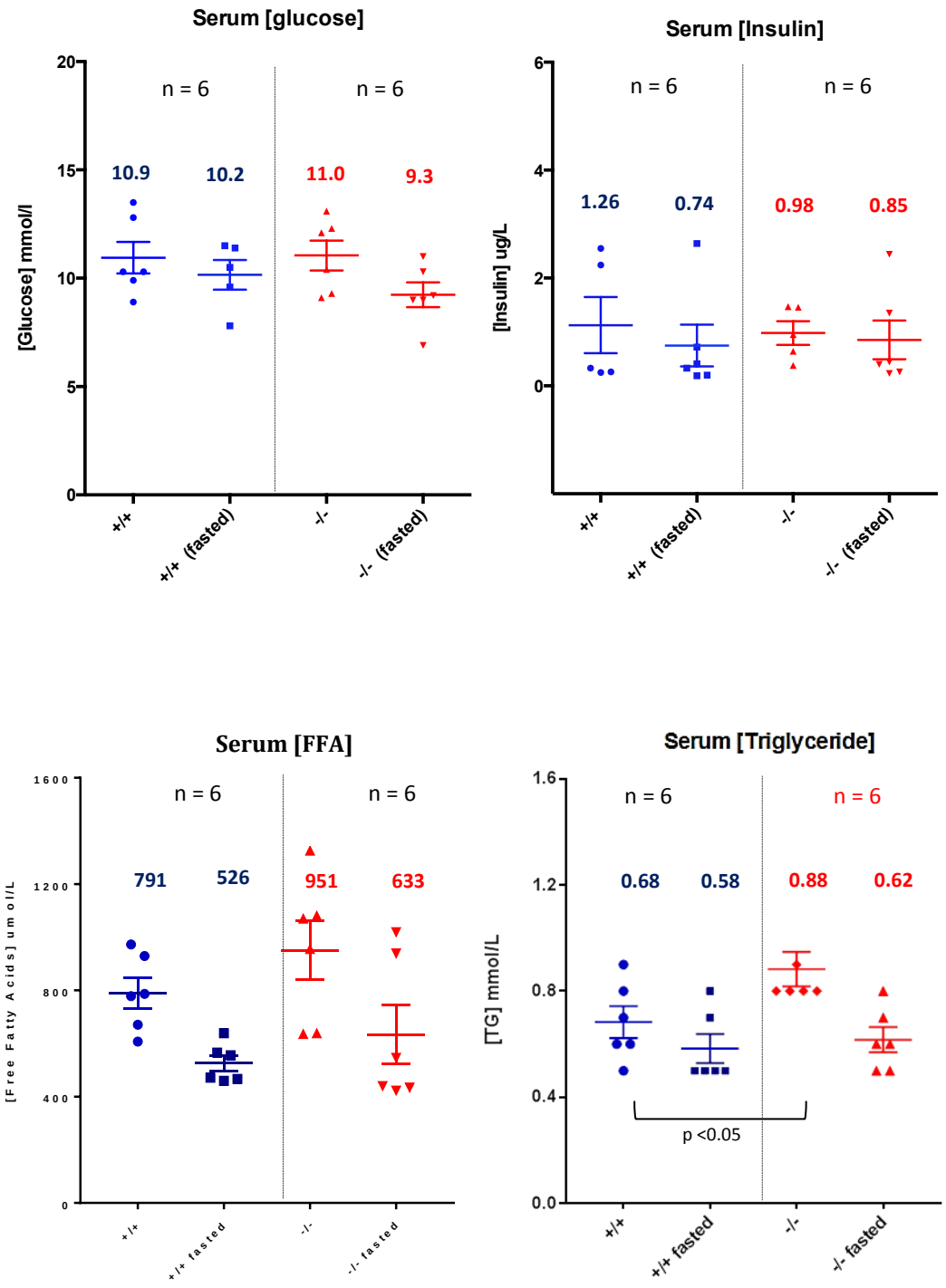

Figure 3.8. Serum analysis of six *Smarcad1*+/+ and six -/- mice, before and after a 16 hour fast. Prior to fasting, a significant difference was seen in serum triglyceride levels between the +/+ and -/- groups (student t-test), but not between serum glucose or insulin levels. Power calculation indicated that an increased sample number (to n=9) would prove significant for serum free fatty acid concentrations between fasted +/+ and -/- groups.

3.2.7 The liver of *Smarcad1* -/- mice shows a greater increase in size with ageing compared to *Smarcad1*+/+ mice.

In parallel to the examination of fat-related metabolites in serum, livers from *Smarcad1*+/+ and -/- mice were weighed to determine if any gross anatomical differences were present. Firstly, trend lines were constructed to provide an overview of increasing size in the context of age (Figure 3.9). As the trend lines were divergent and suggested that the increase in liver size was greater in *Smarcad1*-/- mice, two specific age groups were selected to assess potentially significant size differences.

As suggested by the trend lines, mice aged 4-5 months old did not show any significant difference in liver mass (n=12), however by 10-12 months of age the livers from *Smarcad1*-/- mice were significantly larger than +/+ counterparts (n=4). This may reflect an increase in hepatic metabolic challenge over time in the *Smarcad1*-/- mice (Figure 3.10), although interestingly no visible liver tumours were observed in these mice.

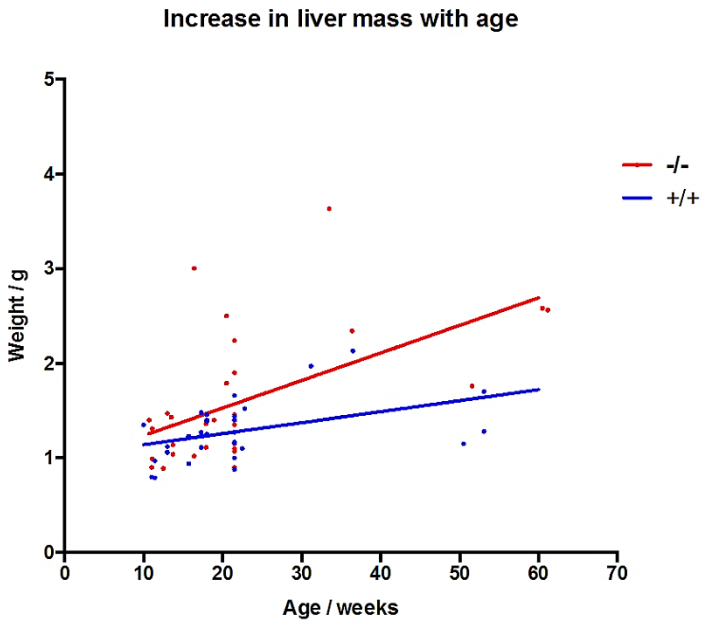

Figure 3.9. The age-related increase in liver size in *Smarcad1*-/- mice is greater than in +/+ mice. A total of 28 murine livers were weighed for each genotype, from mice of ages between 10 weeks to 60 weeks old, and trend lines plotted for each genotype.

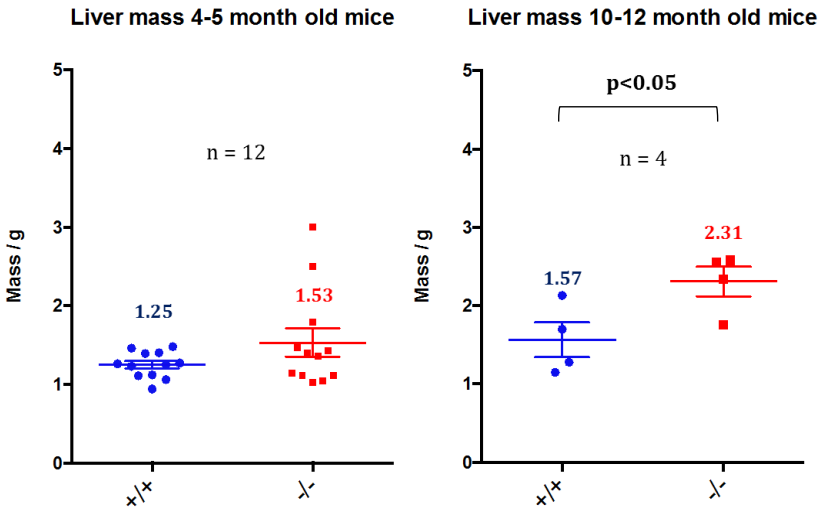

Figure 3.10. Liver masses of *Smarcad1*-/- and +/+ mice are not significantly different at 4-5 months of age, but become significantly different as the mice age to 10-12 months of age (student t-test).

3.2.8 The canonical SMARCAD1 peptide is expressed in the majority of murine tissues including lymphoid organs, the intestine and adipose tissue.

To identify suitable tissues for further investigation of the impact and function of SMARCAD1, a panel of mouse tissue and organs was probed by western blot to identify where SMARCAD1 is expressed, and which tissues contain the highest levels of expression. Samples prepared as described in section 2.2.4 were resolved by polyacrylamide gel electrophoresis (PAGE) and probed initially for presence of SMARCAD1 before equal loading was confirmed using a probe directed against the nuclear protein LaminB1.

As expected, SMARCAD1 was widely expressed across the majority of murine tissues with notably strong staining in testes, spleen and thymus as had been previously observed (L. Matheson, per comm.). Of particular interest was the expression of *SMARCAD1* in the small and large intestine, and organs with metabolic function (white adipose tissue and pancreas). Of major interest was the visible increase in SMARCAD1 expression in WAT versus Liver and brown adipose tissue, which would suggest that any

WAT-related phenotype is mostly due to a tissue-intrinsic loss of SMARCAD1 in WAT (Figure 3.11).

To confirm the successful knockout of SMARCAD1 peptide in -/- adult tissue, and investigate the relative levels of peptide in +/+ vs +/- metabolism-related organs, protein extracts from WAT, BAT, Muscle and Pancreas were probed from -/-, +/- and +/+ mice (Figure 3.12). The successful removal of full length SMARCAD1 peptide was confirmed in all -/- tissues, and of the level of peptide detected in +/- and +/+ extracts mirrored the level of RNA seen in duodenal extracts (Section 4.2.3) in WAT, BAT and pancreas. However, protein extracts from muscle suggested that the level of peptide present in both +/+ and +/- were similar, and hence further experimentation is needed to clarify the relationship between gene copy number and peptide expression level in *Smarcad1*+/+ and +/- mice (see Section 6.1.3).

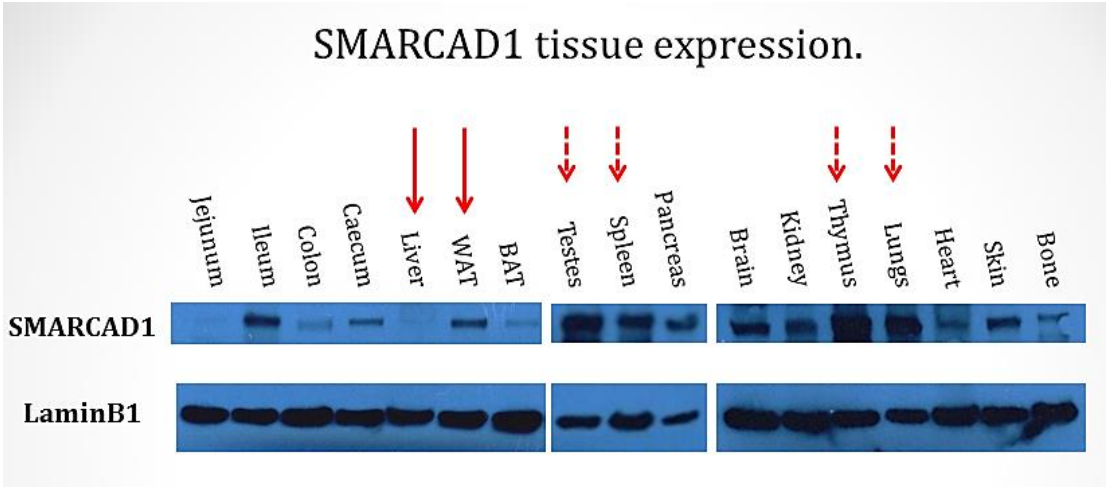

Figure 3.11. SMARCAD1 is widely expressed in mouse tissues, and elevated in white adipose tissue over liver (see arrows) while also highly expressed in testes, spleen, thymus and lungs in particular. These tissues therefore make appropriate substrates for the investigation of SMARCAD1 function.

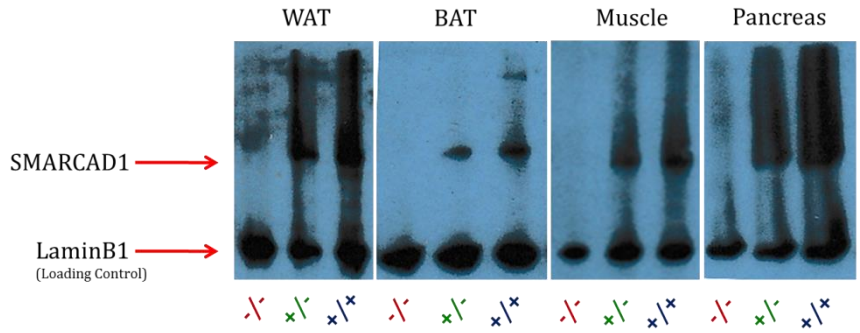

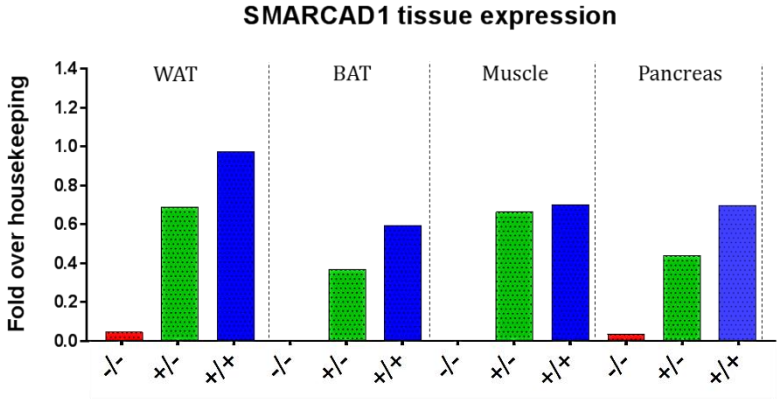

Figure 3.12. Full-length SMARCAD1 peptide is not found in tissue from adult -/- mice, and levels of peptide in +/+ and heterozygous +/- mice reflect the gene copy number in WAT, BAT and Pancreas. (a) Western blot of WAT, BAT, Muscle and Pancreas tissue, from -/-, +/- and +/+ mice respectively. (b) Densitometry of each SMARCAD1 band expressed as fold over each Lamin B1 loading control band. Heterozygous *Smarcad1*+/- mice express SMARCAD1 peptide at lower levels to +/+ mice as expected in WAT, BAT and Pancreas.

3.3 Perspectives.

Physical measurements of *Smarcad1*-/- mice from birth show that phenotypic differences are not immediately apparent in surviving knockout mice. Furthermore, the emergent phenotype with age does not accurately mirror those of known disorders of genomic imprinting. While a physical and metabolic phenotype does emerge after several months (e.g. elevated serum markers, increased liver mass) this would appear not to be linked to gestational development or dysregulation of the imprinting-associated genes *Dlk1* and *Gtl2*, and hence is more likely driven by cell or organ endogenous defects later on in life.

Examination of adult mouse tissue for the presence of SMARCAD1 by western blot confirms wide expression of SMARCAD1, and candidate tissues such as white adipose tissue, the small intestine, lungs, and organs of the immune system (e.g. spleen and thymus) are suitable targets for further investigation of the impact of SMARCAD1 on murine biology. In addition, blots using specific tissues from *Smarcad1*-/- , +/- and +/+ mice confirm the absence of SMARCAD1 peptide expression in metabolism-related tissues of *Smarcad1*-/- mice (and also the ablation of SMARCAD1 peptide expression in adult tissue), while also agreeing with transcriptional data from the duodenum - whereby *Smarcad1* +/- mice produce SMARCAD1 peptide (and RNA) at reduced levels in +/- mice compared to +/+ mice.

Taken together these data suggest that adult tissues such as white adipose tissue, small intestine, lung and cells of adaptive immunity – would be suitable for the investigation of SMARCAD1 function and impact.

Chapter 4 – Intestinal intraepithelial lymphocytes (iIELs) are reduced in number in *Smarcad1*-/- mice by 12 months of age.

4.1 Introduction

This chapter follows up previous work which had investigated the impact of SMARCAD1 on B- and T-cells in adaptive immunity, alongside previous observations of the impact of chromatin remodellers on the mammalian adaptive immune system. Of the cellular subsets investigated, T-cells resident in the small intestine epithelium (intestinal intra-epithelial lymphocytes or iIELs) appeared to be depleted in *Smarcad1*-/- mice. Mice harbouring a global loss of SMARCAD1 (using ZP3-Cre) in addition to lymphocyte-specific deletion of SMARCAD1 (CD2-Cre) were used to address this question. In addition, the impact of SMARCAD1 loss on related factors within the small intestine (e.g. transcriptional impact, cell proliferation within the crypt/villus, anatomical loss of secretory cells and changes in microbiota) were also addressed. Finally, the loss of iIELs was examined in the context of age.

4.2 Results

4.2.1 *Smarcad1* full-length transcript expression is deleted in iIELs by CD2-Cre.

While CD2-Cre is known to be expressed early in lymphocyte development, it is not clear whether intestinal IELs follow the same developmental route as other lymphocytes or indeed whether CD2 is expressed in iIELs. As such, the success of Cre-recombinase expressed from a CD2 promoter (CD2-Cre) in deleting floxed *Smarcad1* alleles (and hence ablating expression of the canonical transcript) was confirmed by qPCR analysis of iIELs isolated by flow cytometry (Figure 4.1a).

Cells extracted from the murine small intestine as described were stained for the T-cell co-receptor CD3, the T-cell receptor γδ and the integrin molecule CD103 to allow flow sorting of a defined intra-epithelial lymphocyte population (Figure 4.1a). Sorted cells were analysed by qPCR to confirm the presence of the floxed *Smarcad1* allele, in addition to the deleted allele (Figure 4.1b).

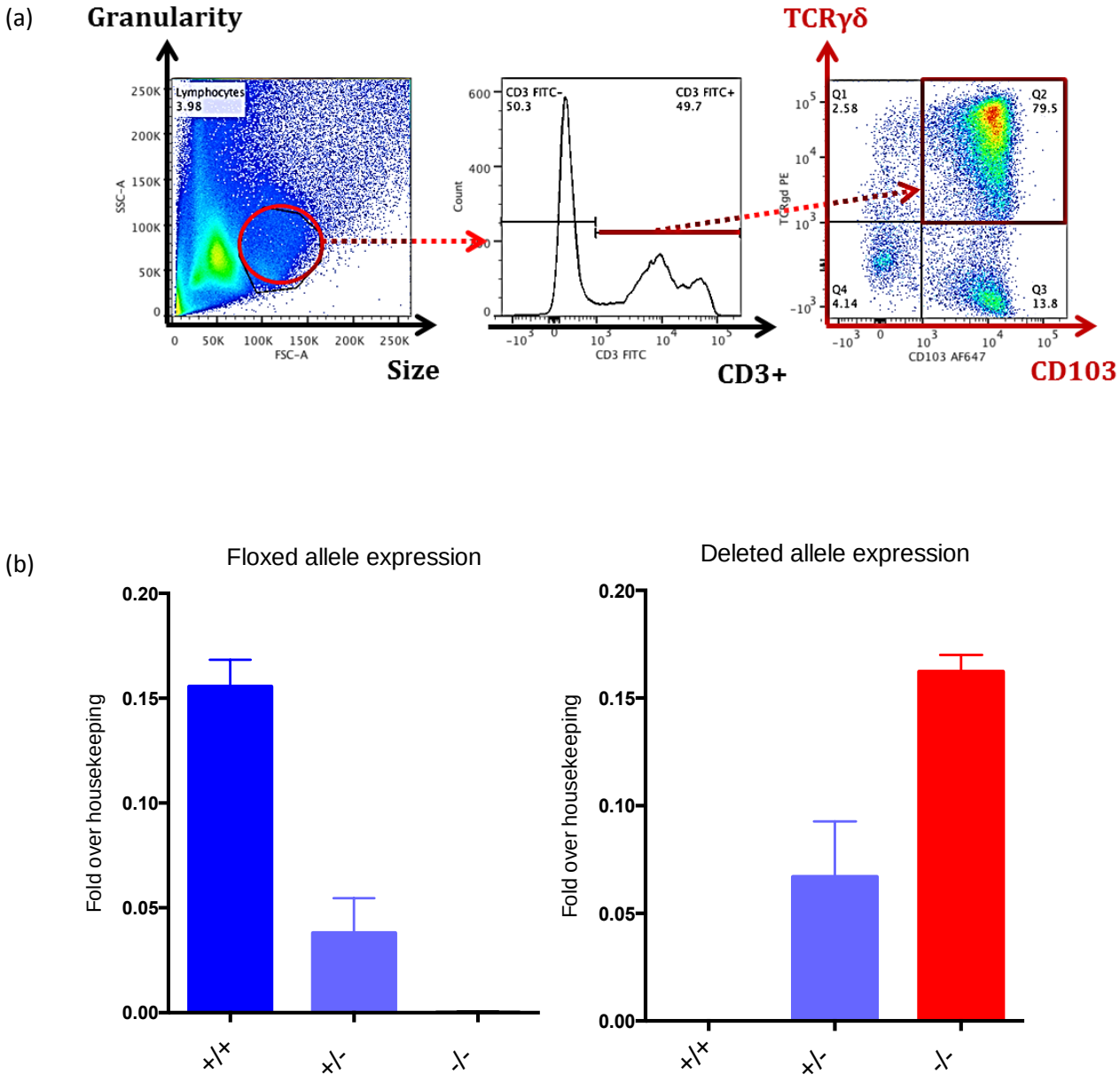

Figure 4.1. (a) Gating strategy for isolation of CD3⁺γδTCR⁺CD103⁺ iIELs by flow sorting. A more detailed description is available in Appendix 3. (b) qPCR of sorted iIELs confirms the expression of the *Smarcad1*^{fl} allele from *Smarcad1*+/+ and CD2-Cre $^{fl/wt}$ (+/-) mice but not CD2-Cre$^{fl/fl}$ (-/-) mice, whereas the deleted allele is detected in CD2-Cre $^{fl/wt}$ mice and CD2-Cre$^{fl/fl}$ mice but not *Smarcad11*+/+ mice. Expression of *Smarcad1* is shown as the mean fold over the housekeeping gene TATA-binding protein (TBP).

4.2.2 Enumeration of iIELs by flow cytometry

To build on initial the observations that *Smarcad1*-/- mice lose iIELs, the gating strategy described in section 4.2.1 was used to enumerate iIELs from mice with *Smarcad1* (+/+), without (-/-), and with the conditional lymphocyte-specific knockout of *Smarcad1* (CD2-Cre). For each group, splenic T-cells were also examined for the ratio of γδ to αβ T-cells as a control for systemic T-cell proportional aberrations (Figure 4.2).

No significant difference was found in iIEL number between groups either at 2-4 months of age or 4-6 months of age (Figure 4.3). Inspection of splenic ratios also revealed that no significant differences were seen in the proportions of circulating T-cells, which confirms the previously observed parity between *Smarcad1*+/+, -/- and CD2-Cre$^{f/f}$ groups in this age range.

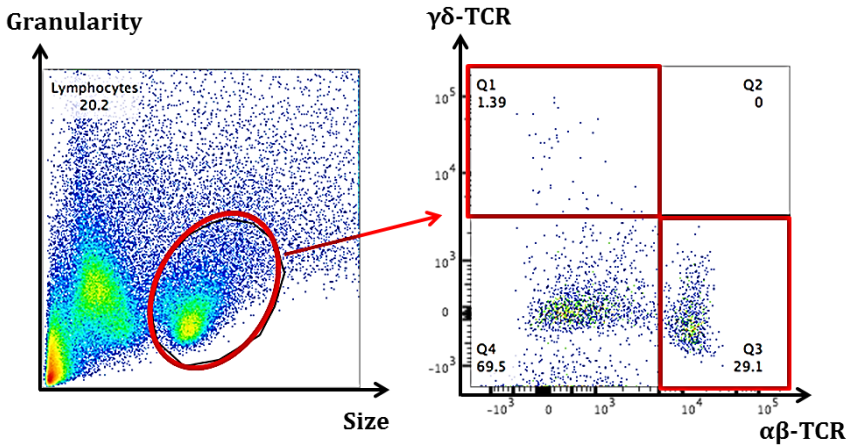

Figure 4.2. Gating strategy for the enumeration of splenic γδ and αβ T-cells ratios. Cells are first identified based on Size (FSC setting) and Granularity (SSC) (above left) and subsequently appropriate anti-γδ or αβ T-cell receptor fluorescence recorded.

(a) Counts of CD103+γδ T-cells from 2-4 and 4-6 month old mice.

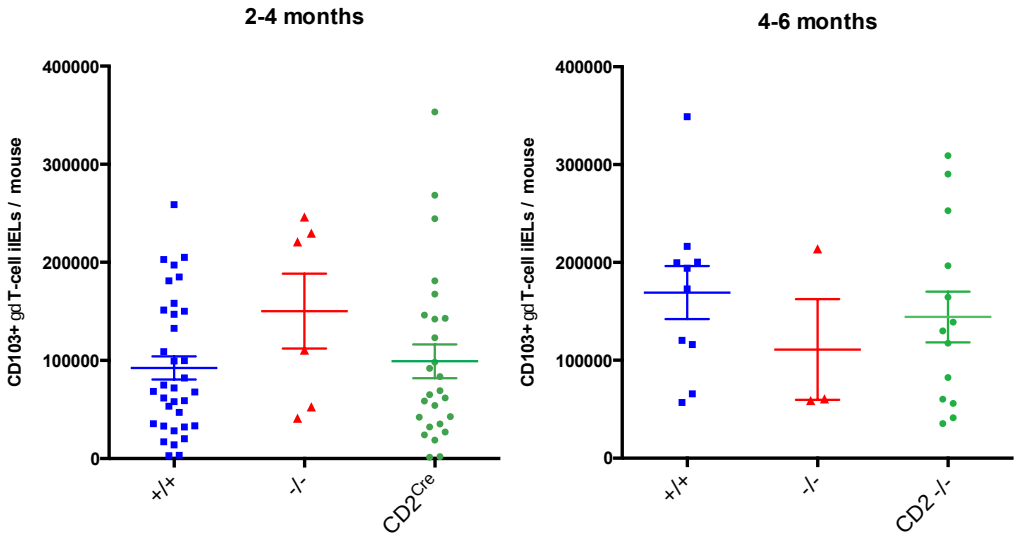

(b) Ratios of αβ /γδ T-cells from the spleens of 2-4 and 4-6 month old mice.

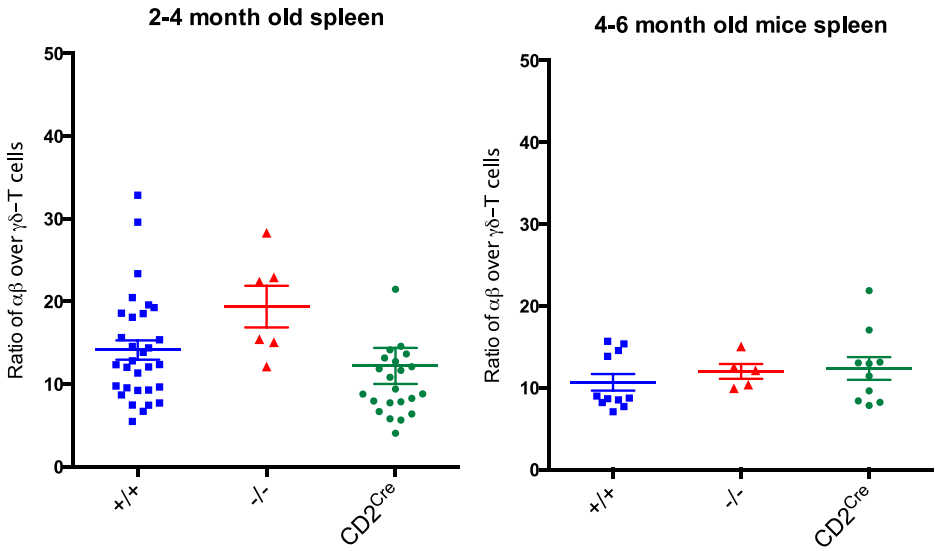

Figure 4.3. (a) Total iIEL numbers are not significantly different between control mice (+/+), mice globally lacking *Smarcad1* (-/-) and mice with lymphocyte-specific deletion of *Smarcad1* (CD2-Cre) (Mann-Whitney test). (b) Analysis of splenic T-cell ratios confirms that there is no significant difference in circulating γδ v αβ T-cells between (+/+), (-/-) and CD2-Cre mice.

4.2.3 Expression analysis of whole-duodenum RNA by qPCR.

To investigate the impact of SMARCAD1 loss on the small intestine, duodenal RNA was analysed by qPCR for the expression of immune-related, intestinal development-related and intestinal stem cell markers (Figure 4.4). Each of these factors could impact the numbers and presence/absence of iIELs. Three *Smarcad1*+/+ and three *Smarcad1*-/- mice (aged 4 months) were screened using two housekeeping genes (TBP and β_2M), and the mean fold over housekeeping for each sample was normalised to that of *Smarcad1*+/+ mice. Two control genes were also screened, *Smarcad1* itself and the genomically adjacent gene, *Hpgds* (hematopoietic prostaglandin D synthase).

As expected, the expression level for *Smarcad1* reflected the genotype of the subject mice (i.e. *Smarcad1*+/- mice showed reduced *Smarcad1* RNA levels to +/+ mice, and *Smarcad1*-/- mice do not produce any detectable levels of transcript). Importantly, no significant difference in the level of *Hpgds* was seen in either +/- or -/- mice, as this gene has potent immunomodulatory effects, and hence the removal of exons 12 to 14 of Smarcad1 in the mouse genome does not ostensibly impact expression of this genomically adjacent gene (Figure 4.4).

To address whether any immune-phenotype (e.g. inflammation) was present in the small intestine of *Smarcad1-/-* mice, three genes involved in inflammatory responses were screened by qPCR. Of these, *Tlr-4* (which binds to bacterial-derived LPS) expression was elevated in *Smarcad1*-/- mice, although by contrast the pro-inflammatory cytokines *Tnfα* and *Ifn-γ* showed little change and a decrease in expression respectively. Together these suggest that inflammation is not increased in the small intestine of *Smarcad1*-/- mice (Figure 4.4).

Differences in genes linked to intestinal development and the cellular make-up of the small intestinal crypt/villus was also assayed. No significant difference was seen in the intestinal stem cell marker *Lgr-5*, suggesting that there is no difference in the number of stem cells present in this niche. However, the developmental markers *c-Myc* (which antagonises Paneth Cell development), and *Notch-1* and 2 (that promote stem cell maintenance and antagonise the formation of Goblet secretory cells) all reflected an increase in expression in the murine duodenum (Figure 4.4).

Taken together, these results suggested that development of the small intestinal crypt/villus may be altered in *Smarcad1*-/- mice, but not due to differences in the intestinal stem cells.

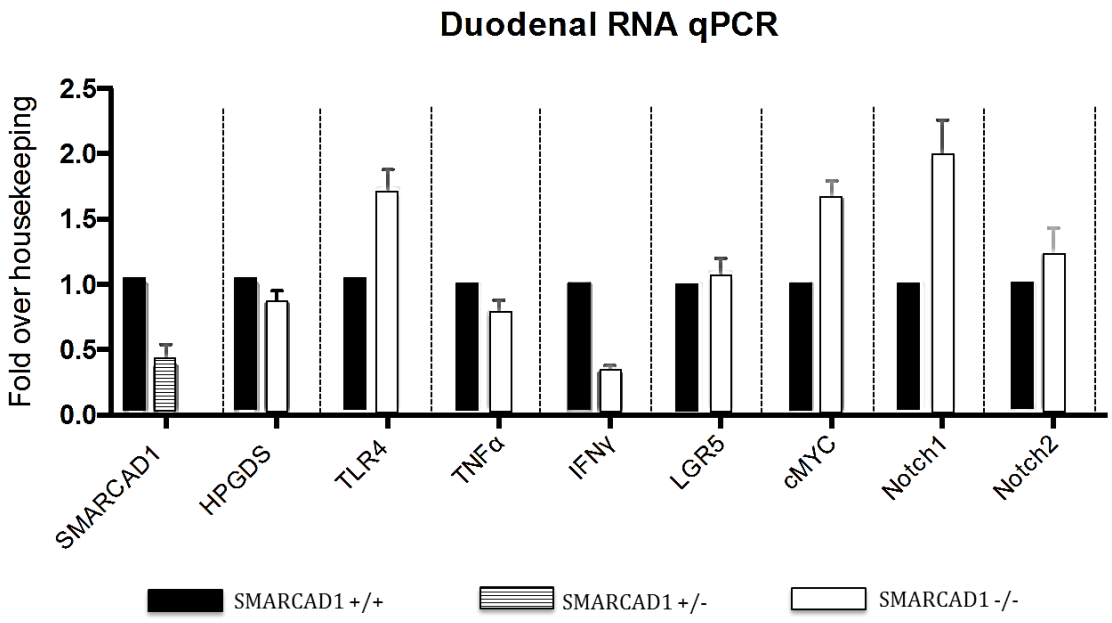

Figure 4.4. Analysis of key markers of inflammation and intestinal development by qPCR. Each bar represents the three dCt values obtained from three mice, using the mean of two housekeeping genes (*Tbp* and $\beta_2 M$) with standard error mean plotted. These data suggest that developmental differences – rather than intestinal inflammation – may underpin any intestinal phenotype in *Smarcad1*-/- mice linked to iIEL biology.

4.2.4 Immunofluorescence staining of the small intestine confirms the presence of Paneth cells and Goblet cells in *SMARCAD1*-/- mice.

To investigate whether the presence of secretory cells (Goblet cells and Paneth cells) was affected in the small intestine of *Smarcad1*-/- mice, duodenal sections from three +/+ and three -/- mice (aged 4 months) were examined by immunofluorescence microscopy. In both experimental and control mice the presence of Goblet Cells (α-Mucin antibody) was readily seen along small intestinal villi (Figure 4.5a), and clear Paneth Cell staining (α-Lysozyme antibody) was apparent within small intestinal crypts (Figure 4.5b). While more subtle changes in population number or proportion could not be ruled out, the parity of iIEL number found in the intestine of age-matched mice suggested that such subtle changes would not impact the original question of iIEL loss.

4.2.5 EdU incorporation assay to assess cell proliferation in the small intestine.

Elevated expression of cMYC in the murine small intestine has previously been associated with both a vastly reduced number of Paneth Cells and intestinal tumorigenesis. To assay whether cell proliferation was indeed affected by the lack of SMARCAD1 in the murine small intestine, mice were fed *ad libitum* with EdU-containing drinking water for 18 hours and duodenal cryosections screened for EdU incorporation (Figure 4.6a).

Cells which stained positive for EdU were enumerated from the base of the crypt to the top of each adjacent villi. Fifty crypt/villi units were scored from each of three *Smarcad1*+/+ and three -/- mice, and results collated for both genotypes. No significant difference was found in cell proliferation in the small intestine of *Smarcad1*+/+ and -/- mice (Figure 4.6b).

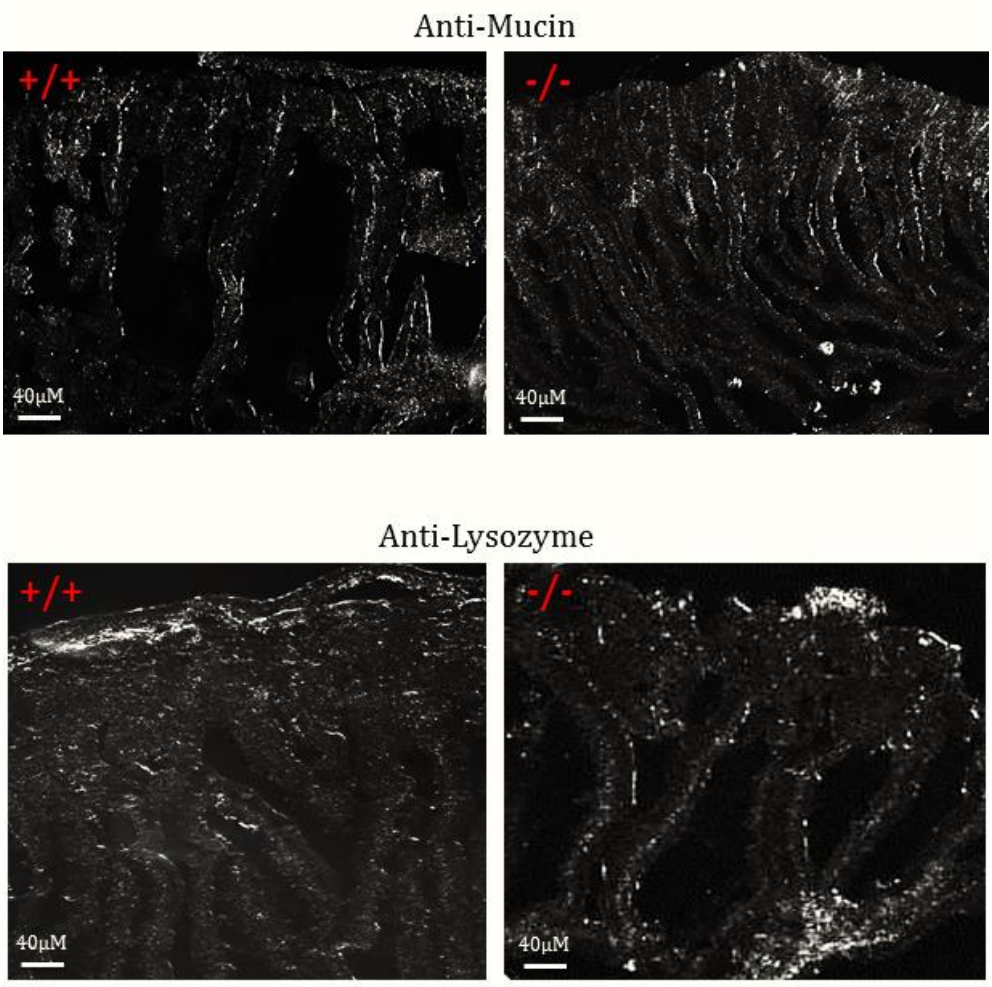

Figure 4.5. Immunofluorescent staining of duodenal sections from 4 month old *Smarcad1*+/+ and -/- mice. (a) Signal from anti-Mucin antibody indicates the clear presence of Goblet cells along the intestinal villi in both *Smarcad1*+/+ and -/- mice. (b) Paneth cells are visible in the crypt of both *Smarcad1*+/+ and -/- mice after anti-Lysozyme fluorescence staining.

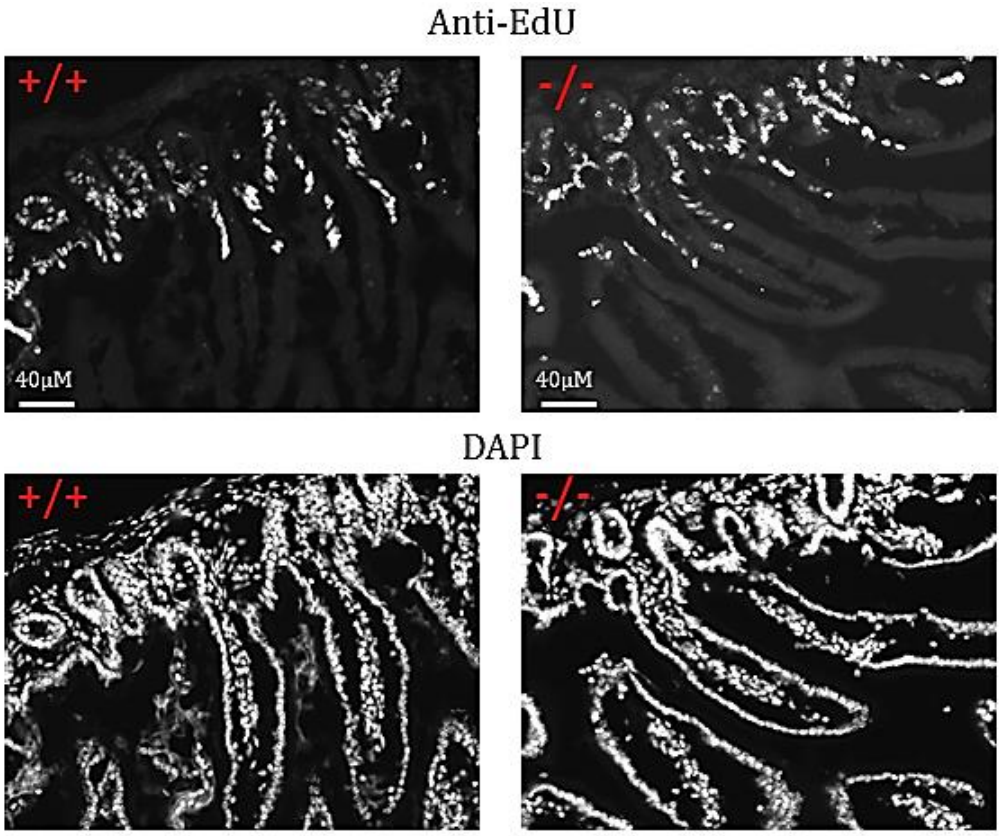

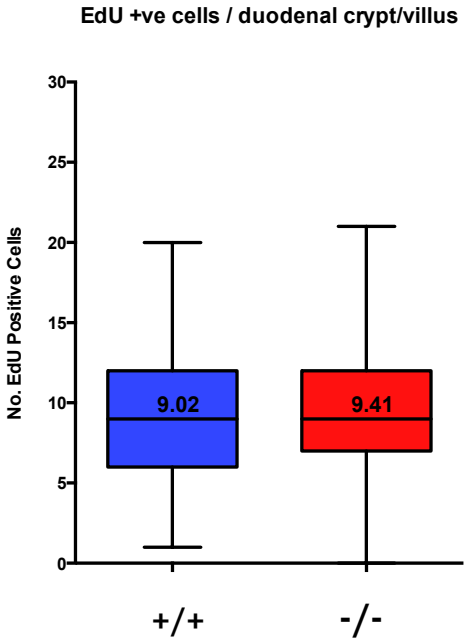

Figure 4.6 (a) Immunofluorescence detection of EdU incorporated into the small intestine of *Smarcad1*+/+ and -/- mice. (b) No significant difference was found in the number of EdU+ve cells present in the duodenal crypts/villi of three *Smarcad1*+/+ versus three -/- mice, indicating no difference in cell proliferation between these mice (n=150 crypt/villi units counted for each genotype)

4.2.6 SMARCAD1 does not significantly impact the murine intestinal microbiome.

To further understand the impact of the loss of SMARCAD1 on murine intestinal biology, the small and large intestines of 6 month old *Smarcad1*+/+ and -/- mice were analysed for microbial content. Intestinal microbiota are known to influence the presence of iIELs within the intestine, along with factors outside the intestine (such as white adipose tissue/metabolism) and host chromatin (see Section 1.6). Excluding changes in the microbiota (such as changes in the proportions of the major species present) as a cause of any iIEL/intestinal (or metabolic) phenotype observed in *Smarcad1*-/- mice was required to allow the focus to remain on host cell-intrinsic mechanisms. Hence, the four known dominant phyla present within the mammalian gut (Actinobacteria, Bacteroidetes, Firmicutes and Proteobacteria) were assayed for proportional content by qPCR. Microbial subpopulations were quantified against total microbial DNA using qPCR and primers targeting the 16S rRNA of individual populations normalised against primers targeted to a common microbial rRNA sequence.

As expected, levels of Firmicutes and Bacteroidetes were elevated in the colon over the small intestine, however no significant difference was seen between *Smarcad1*+/+ and -/- groups for any of the bacterial phyla examined. Furthermore, no Proteobacteria were detected in the small intestine of mice using this approach (Figure 4.7). These results suggest that any changes in intestinal expression brought about by the lack of SMARCAD1 do not impact the microbial content in the murine gut, although more detailed approaches more give deeper insight.

4.2.7 Intestinal IEL numbers are significantly reduced in *SMARCAD1*-/- mice by 11-12 months of age.

To examine further the age-related changes in *Smarcad1*-/- mice, intestinal IELs were enumerated from normal (+/+), global knockout (-/-) and conditional knockout (CD2-Cre) mice alongside splenic controls (Figure 4.8). While no significant difference was seen between *Smarcad1*+/+ mice and the lymphocyte specific CD2-Cre knockout, mice with a global knockout of *Smarcad1* (-/-) showed a significant loss in intestinal IELs. Furthermore, examination of the splenic ratios of αβ versus γδ T-cells revealed a significant increase in this ratio, concordant with the intestinal loss of γδ T-cells.

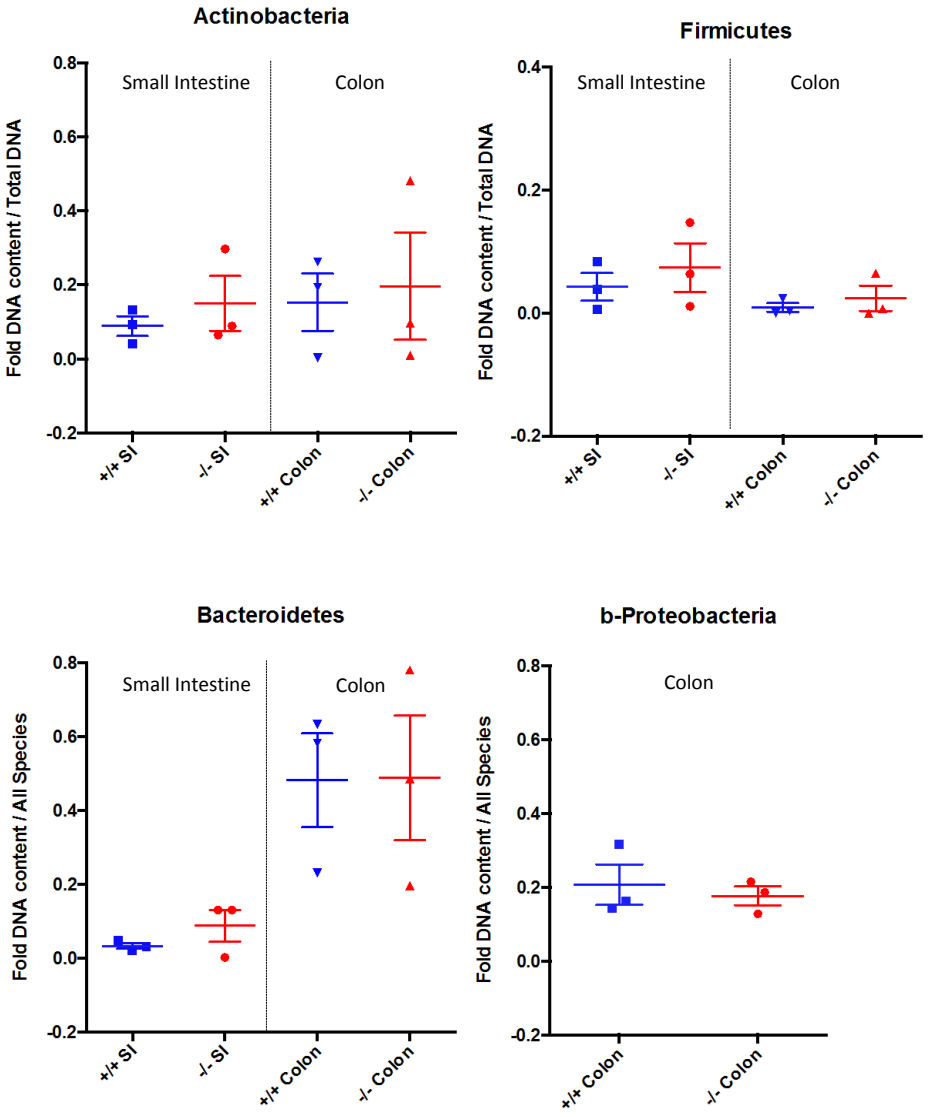

Figure 4.7. No significant changes in the major intestinal bacterial phyla are seen in *Smarcad1*-/- mice compared to +/+ mice (n=3). Expected elevations in the proportion of Firmicutes and Bacteroidetes were found in colon versus small intestine, and no Proteobacteria were detected in murine small intestine using this approach. Intestines from three *Smarcad1*+/+ and three -/- mice were examined each case.

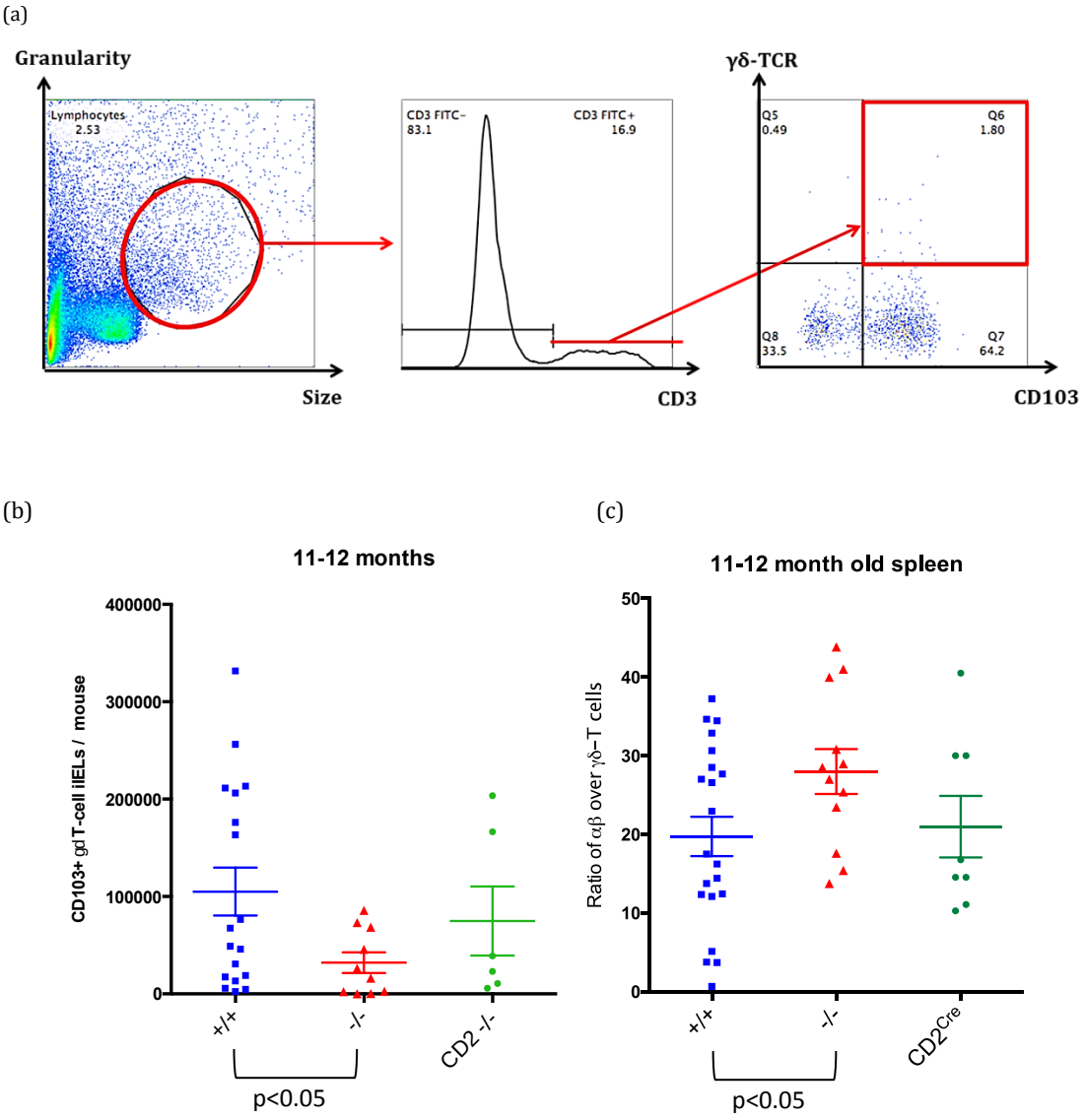

Figure 4.8. By 11-12 months *Smarcad1* -/- mice significantly lose iIELs compared to +/+ mice (Mann-Whitney statistical test). (a) Flow cytometric plots for 12 month old *Smarcad1* -/- mice demonstrate a loss of CD103+ iIELs. (b) and (c) Changes in iIEL number and splenic ratio of αβ to γδ T-cells by 11-12 months of age indicated a decrease in the systemic γδ T-cell population with respect to systemic αβ T-cells in plot (c).

4.3 Perspectives.

This chapter confirms that *Smarcad1*-/- mice present a significantly reduced number of intestinal intraepithelial lymphocytes by 11-12 months of age. This loss is not due to cell-intrinsic loss of SMARCAD1, as lymphocyte-specific CD2-Cre SMARCAD1 deleted mice do not reproduce this loss. However, changes in the ratio of T-cell subsets within the spleen (i.e. fewer γδ T-cells with respect to αβ-T cells) suggest that γδ T-cell numbers are affected both inside and outside the intestine, hence the loss of γδ T-cell iIELs may not be due to intestine-intrinsic causes.

Closer examination of the murine intestine suggests that in the absence of SMARCAD1, changes in the expression of developmentally-influential genes (such as *Notch-1*, *Notch-2* and *cMyc*) exist alongside a reduction in the expression of inflammation-related genes (e.g. *TNFα* and *IFNγ*). Further investigation of cell proliferation and the presence/absence of key secretory cells revealed no significant difference in the intestinal anatomy or intestinal cell turnover within *Smarcad1*-/- mice. While deeper insight into differences in intestinal function and phenotype may be revealed with alternative experimental approaches (such as next-generation sequencing of microbial populations, use of intestinal specific (villin-Cre) SMARCAD1 knockout mice) the parity in iIEL number in mice aged 2-6 months suggests that this would shed no further light on the original investigation of iIEL loss in age-matched mice.

The challenge of breeding adequate numbers of of *Smarcad1*-/- males for iIEL-based experimentation - in addition to the financial and time cost of housing mice until one year of age – made further investigation of the loss of iIELs logistically prohibitive within this project. A parallel phenotype that was apparent in younger mice was therefore pursued in spite of the clearly fascinating observation of iIEL loss with age.

Chapter 5 - Differences in white-adipose tissue are found in mice lacking SMARCAD1, but are not linked to adipogenesis.

5.1 Introduction.

This chapter presents the differences found in white adipose tissue and related factors (e.g. macrophages and intestinal microbiota) between *Smarcad1*-/- and +/+ mice. A number of previous reports had linked chromatin remodellers to white adipose tissue development (see Section 1.5.1), and while differences in weight had been reported between *Smarcad1*+/+ and -/- mice (Schoor et al., 1999), this previous study did not specifically investigate whether these differences (in body mass) were influenced by differences in adiposity. The initial observation that epididymal fat pads are reduced in size (in the *Smarcad1*-/- mice described in this thesis) was investigated in greater detail, and understanding of WAT-related factors (adipose depot size, macrophage infiltration, related microbiota and expression of adipogenesis-related factors) is described under both normal conditions and after high-fat-diet challenge. Particular focus was given to putative adipocyte stem cells (ASCs) isolated from control and experimental mice as previously described. In parallel, mouse embryonic fibroblasts (which can also undergo adipogenic differentiation) were also used to confirm *in-vivo* and *ex-vivo* observations.

5.2 Biology of white-adipose tissue in *Smarcad1*-/- and +/+ mice.

5.2.1 Subcutaneous and epididymal white adipose tissue fat depot sizes do not significantly differ between *Smarcad1*-/- and +/+ mice.

To investigate further whether significant differences are found in the sizes of white adipose fat depots, the mass of subcutaneous and epididymal fat pads was compared between experimental and control mice aged 4-5 months old (Figure 5.1). While an initial observation had suggested a potential difference in fat pad size, no significant difference was seen in either fat depot with an increased sample size. It seems likely that initial observations had been skewed by out-lying data points as seen within the larger sampling size, and would be expected should one of the two initial mice observed be an alpha animal within the litter (hence would take a more dominant position with respect to food intake).

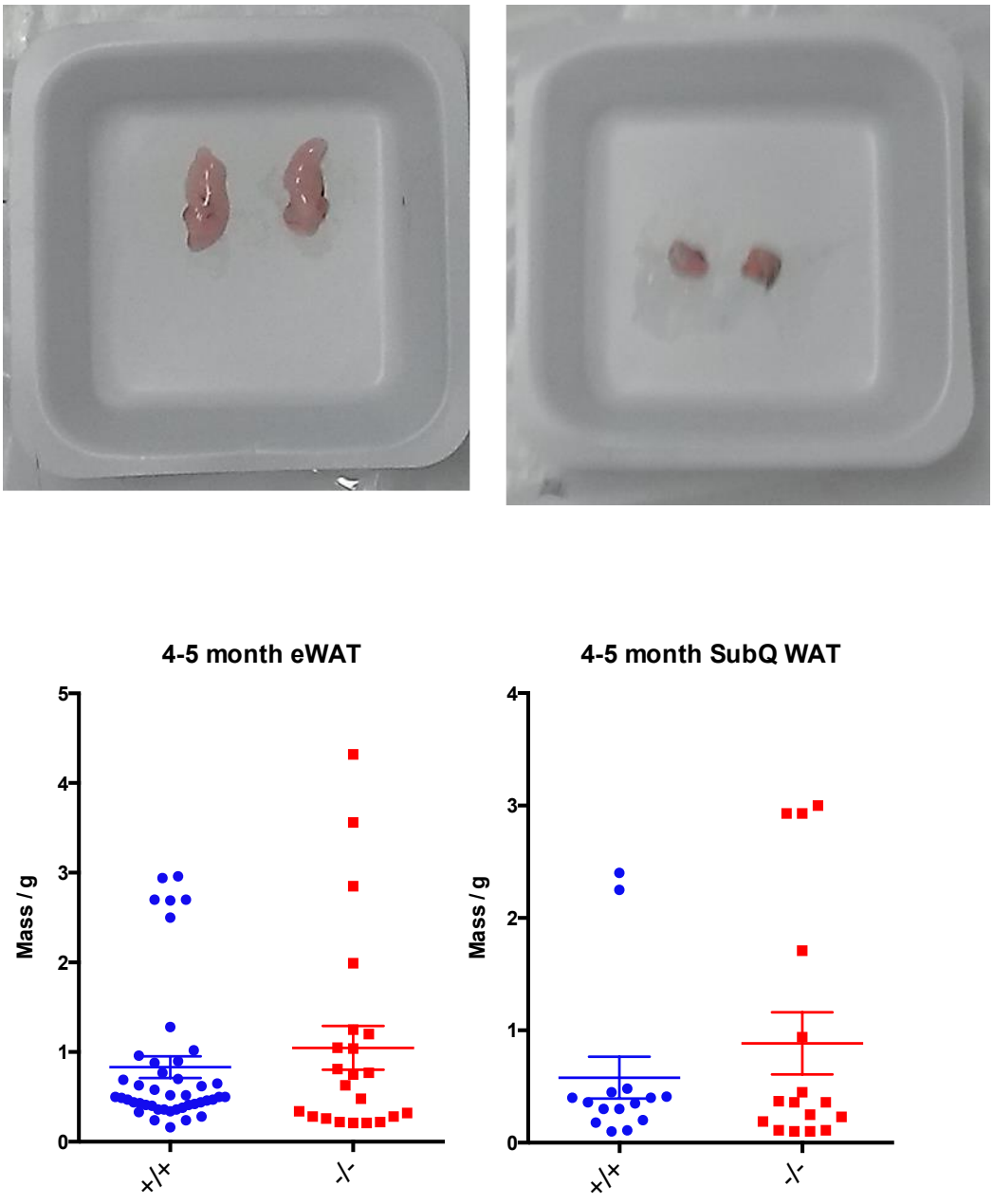

Figure 5.1 Epididymal (left) and subcutaneous (right) fat pads were visually checked for symmetry prior to weighing, as a measure of accurate dissection. No significant difference was found between epididymal or subcutaneous fat pad sizes from *Smarcad1*+/+ (blue) or *Smarcad1*-/-(red) mice.

5.2.2 SMARCAD1 does not impact the size of white adipocytes.

Although there was no significant difference in the size of WAT-depot fat pads examined from experimental or control mice, it was still unclear as to why the serum levels of triglyceride and free-fatty acids differed between +/+ and -/- groups, and what impact this may have on adipocyte biology. To assess whether adipocyte size was affected, fat pad sections from three +/+ and three -/- mice were stained with hematoxylin and eosin (to mark cell boundaries) and images captured to determine adipocyte cell size distribution. Multiple sections for each fat-pad were analysed in ImageJ using the Watershed algorithm (as described), then adipocyte sizes were combined from three mice of each genotype. Ranked adipocyte sizes for each genotype were then used to construct a cumulative frequency curve, and curves compared from both genotypes (see Figure 5.2). For both genotypes, 95% of white adipocytes had an area of 2300μm^2, and both curves demonstrated a near-transposable pattern of distribution, indicating that no significant difference in adipocyte size is seen in the absence of SMARCAD1, also inferring that no major difference in adipogenesis is also present.

These results revealed no clear difference in the size of white adipocytes between control and experimental mice, indicating that any difference in fat pad size observed was due to an increased number of adipocytes present (cell hyperplasia) rather than an increase in adipocyte size (cell hypertrophy).

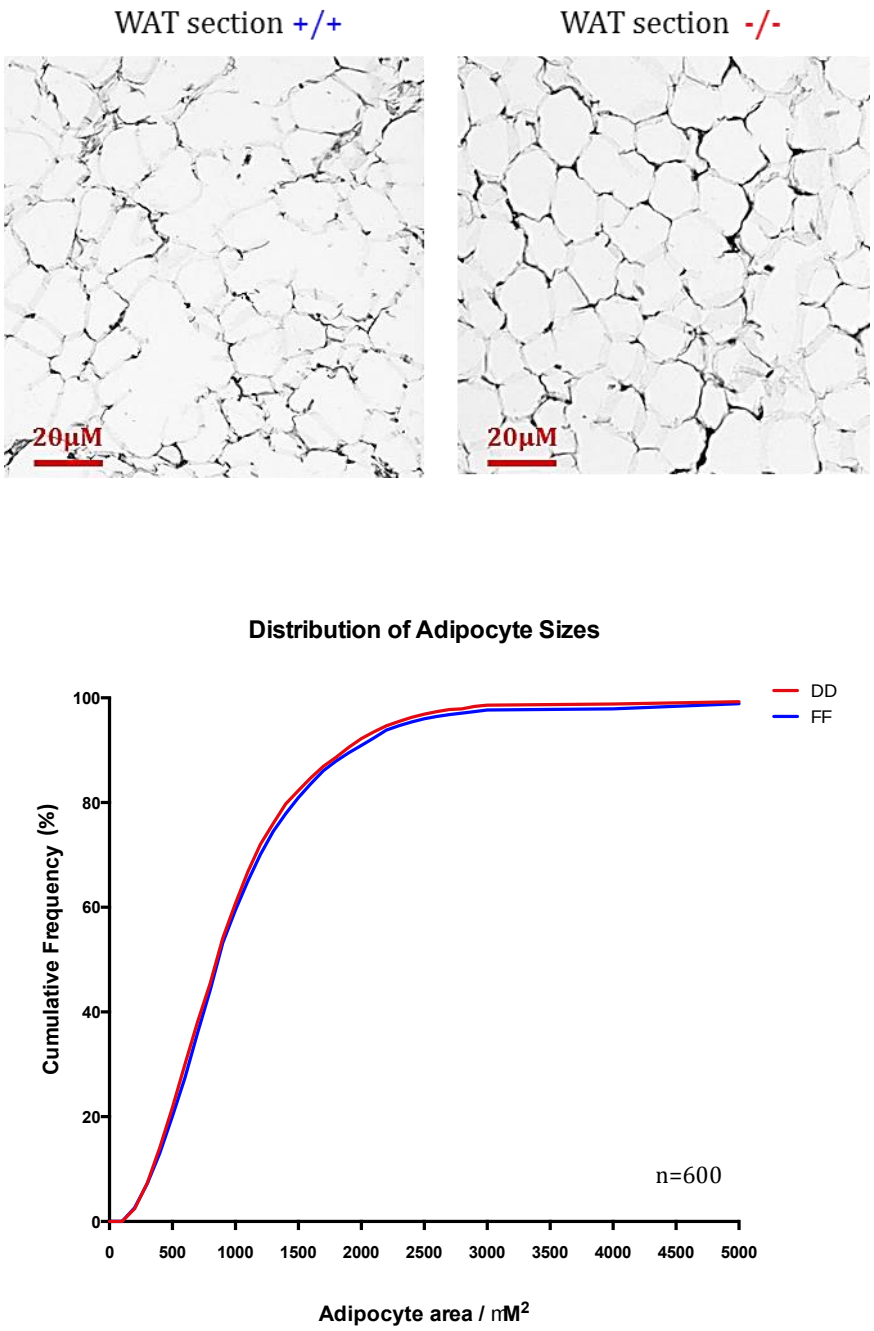

Figure 5.2. No difference is seen in adipocyte size between *Smarcad1*+/+ and -/- mice. Formalin fixed WAT sections were stained with hematoxylin and eosin (top) and captured images analysed using the Watershed algorithm appended to ImageJ software. Images capture using 10x magnification, scale bars represent 20µm. A cumulative distribution of adipocyte sizes was plotted, which reveals almost identical adipocyte size distributions within +/+ and -/- tissue.

5.2.3 Transcriptomic analysis of whole WAT by RNA-seq.

To investigate further the impact of SMARCAD1 on white adipose tissue biology, transcriptomic analysis was performed to identify changes in gene expression between experimental and control groups. Four mice approximately 6-months old were analysed (2x *Smarcad1*+/+, 2x *Smarcad1*-/-), using RNA extracted from whole epididymal white adipose tissue, from which mRNA was isolated using poly-dT magnetic beads (see Materials and Methods or full details). Library content size and concentration (checked by Bioanalzyer) is shown in Appendix 4, and paired-end reads (aligned to the mouse GRCM38/mm10) visualised in SeqMonk. Relative transcriptomic profiles were compared to confirm the clustering of same-genotype murine transcriptomes (shown as cluster tree, Figure 5.3) and probe-intensity cumulative plots were normalised to allow subsequent differential transcription analysis.

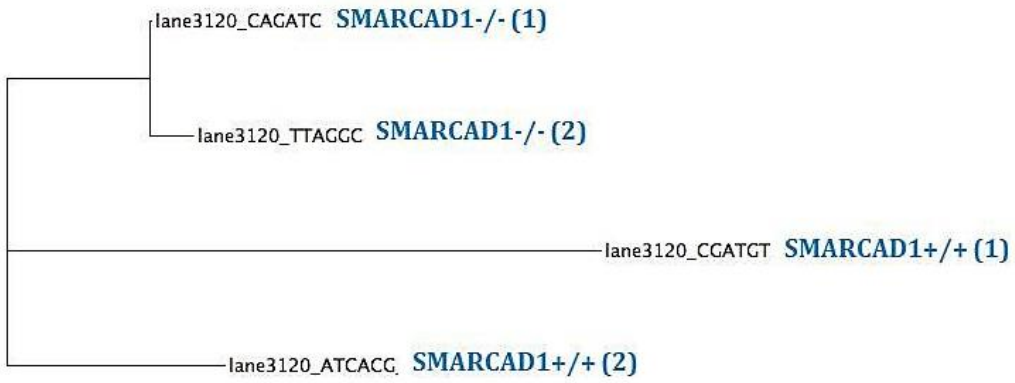

Figure 5.3. Transcriptomic reads are most similar from mice of the same genotype. Comparison of RNA-seq read intensity distributions confirms the clustering of *Smarcad1*-/- whole-WAT transcriptomes as expected.

Identification of differential gene expression was performed using the DeSeq algorithm (see https://www.bioconductor.org/packages/devel/bioc/vignettes/DESeq2/inst/doc/DESeq2.pdf) and results were visualised using SeqMonk software (http://www.bioinformatics.bbsrc.ac.uk/projects/seqmonk/). A list of differentially expressed genes was then examined by literature searching on PubMed to identify candidate genes linked to known aspects of the mouse phenotype.

From the differential expression analysis, two genes of interest were identified due to the known expression by macrophages. As macrophage infiltration into white adipose tissue is a known marker for WAT-related pathology (Surmi & Hasty, 2008) (as necrotic adipocytes are phagocytosed by macrophages), these findings were investigated further to confirm the putative increase in macrophage levels in the white adipose tissue of *Smarcad1*-/- mice (see section 5.2.3) .

In agreement with the result of adipocyte size measurement (section 5.1.1), transcriptomic analysis revealed no difference in the major adipogenesis-related factors between *Smarcad1*-/- and +/+ mice. The major factors upregulated during adipogenesis are well characterised, and serve as markers for potential adipogenic dysfunction. However, none of the following demonstrated significant differential expression: PPARγ (Peroxisome proliferator-activated receptor γ – a nuclear receptor critical for adipogenesis and maintenance of the differentiated state); C/EBPβ and C/EBPδ (CCAAT/enhancer-binding proteins which induce the expression of PPARγ); SREBP1 (Sterol regulatory element-binding protein-1, which is involved in cholesterol homeostasis and is upregulated during adipogenesis); ZFP423 (a zinc finger transcription factor enriched in preadipocytes which also induces PPARγ expression) and KLF2 (Kruppel life factor has been reported to inhibit PPARγ expression).

To examine whether groups of genes from common functional pathways were affected (thereby implicating the pathway) Gene Ontology analysis was also performed using the list of genes identified prior to intensity filtering. As such genes may not on their own report a significant change in expression between experimental and control groups, the weighting of significance based on linked function provides an alternative analysis to identify potentially important transcriptomic effects. Analysis of differentially expressed genes in this way revealed that the major biological processes impacted by the loss of SMARCAD1 were linked to metabolism (Figure 5.5A). Furthermore, a second analysis of

intensity filtered (differentially expressed) genes suggested that the cellular pathways most affected were the 'Inflammation mediated by chemokine and cytokine signalling' and 'Integrin signalling pathways' (Figure 5.5B). As integrin signalling pathways are important in macrophage-driven WAT inflammation (Zheng et al., 2015), these likely reflect stages of the same inflammatory process in the white adipose tissue of *Smarcad1* -/- mice.

While the genes identified provide insight into a WAT-related phenotype in *Smarcad1*-/- mice, it should be noted that a subset of differentially expressed genes identified in this screen (see section 5.2.4), are implicated in testis/ spermatozoa biology (e.g. the following genes: sperm mitochondria-associated cystein-rich protein (smcp), outer dense fiber of sperm tails 1 (odf1), spermatogenic leucine zipper 1 (spz1), Germ cell specific gene 2 (gsg2), histone H1-like protein in spermatids 1 (hils1), Poly (a) polymerase beta (testis specific) (papolβ)). The identification of these implies that RNA originating from the testis (or testis-related material) was present in this screen, and hence the original dissection contained non-WAT material in addition to the epididymal fat pad. Any future experiments would benefit from more accurate dissection and/or isolation of white adipose tissue from a different fat depot (e.g. subcutaneous WAT).

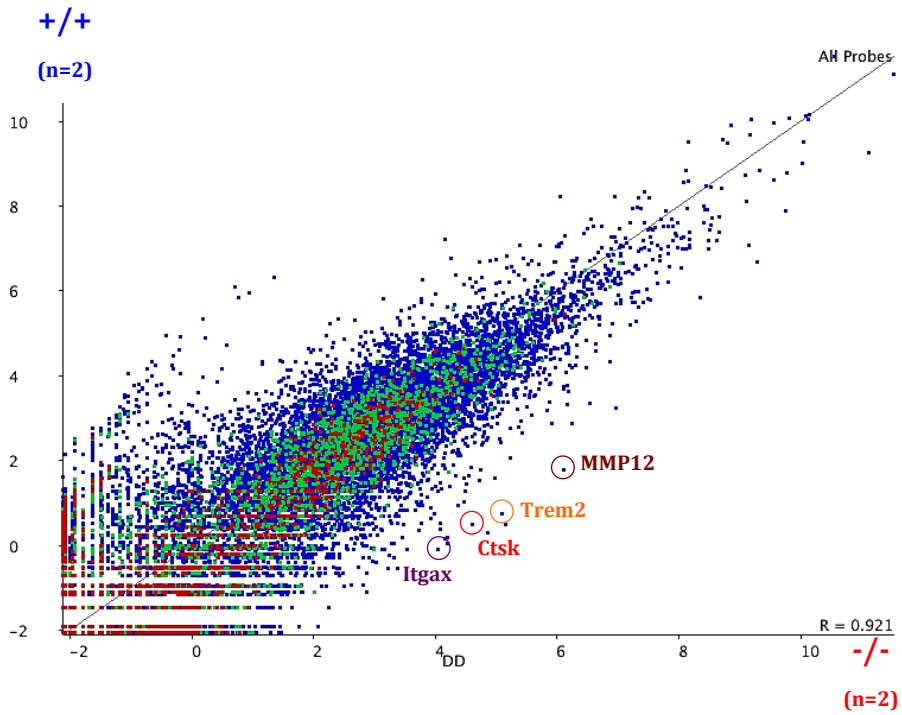

Figure 5.4. Scatter plot comparison of transcriptomic reads from two *Smarcad1*+/+ mice versus two *Smarcad1*-/- mice. Genes which show differential expression diverge from the central cluster and appear as outliers. A number of genes associated with macrophage function are elevated in *Smarcad1*-/- mice over +/+ mice. Absent from the differentially expressed genes are genes known to have a major influence during adipogenesis, suggesting this process is not grossly affected in the absence of SMARCAD1.

Fold	Feature	ID	Description
9.199899	Tnp2	ENSMUSG00000043050	transition protein 2 [Source:MGI Symbol;Acc:MGI:98785]
9.040754	Prm1	ENSMUSG00000022501	protamine 1 [Source:MGI Symbol;Acc:MGI:97765]
8.96953	Tnp1	ENSMUSG00000026182	transition protein 1 [Source:MGI Symbol;Acc:MGI:98784]
8.88594	Prm2	ENSMUSG00000038015	protamine 2 [Source:MGI Symbol;Acc:MGI:97766]
8.713503	Fhl4	ENSMUSG00000050035	four and a half LIM domains 4 [Source:MGI Symbol;Acc:MGI:1338765]
8.543867	Akap12	ENSMUSG00000038587	A kinase (PRKA) anchor protein (gravin) 12 [Source:MGI Symbol;Acc:MGI:1932576]
7.897457	Akap4	ENSMUSG00000050089	A kinase (PRKA) anchor protein 4 [Source:MGI Symbol;Acc:MGI:102794]
7.795123	Dbil5	ENSMUSG00000038057	diazepam binding inhibitor-like 5 [Source:MGI Symbol;Acc:MGI:108039]
7.657875	Smcp	ENSMUSG00000074435	sperm mitochondria-associated cysteine-rich protein [Source:MGI Symbol;Acc:MGI:96945]
7.5197725	Pgk2	ENSMUSG00000031233	phosphoglycerate kinase 2 [Source:MGI Symbol;Acc:MGI:97563]
7.4771447	Ybx2	ENSMUSG00000018554	Y box protein 2 [Source:MGI Symbol;Acc:MGI:1096372]
7.3203406	Atp8b3	ENSMUSG00000003341	ATPase, class I, type 8B, member 3 [Source:MGI Symbol;Acc:MGI:1914581]
7.2822294	Odf1	ENSMUSG00000061923	outer dense fiber of sperm tails 1 [Source:MGI Symbol;Acc:MGI:97424]
7.226114	Oaz3	ENSMUSG00000028141	ornithine decarboxylase antizyme 3 [Source:MGI Symbol;Acc:MGI:1858170]
7.155739	Spz1	ENSMUSG00000046957	spermatogenic leucine zipper 1 [Source:MGI Symbol;Acc:MGI:1930801]
7.137503	Crisp2	ENSMUSG00000023930	cysteine-rich secretory protein 2 [Source:MGI Symbol;Acc:MGI:98815]
7.0009	4933411K16Rik	ENSMUSG00000090369	RIKEN cDNA 4933411K16 gene [Source:MGI Symbol;Acc:MGI:1914015]
6.9516263	Hmgb4	ENSMUSG00000048686	high-mobility group box 4 [Source:MGI Symbol;Acc:MGI:1916567]
6.81175	4930571K23Rik	ENSMUSG00000090457	RIKEN cDNA 4930571K23 gene [Source:MGI Symbol;Acc:MGI:1923111]
6.81175	Gsg2	ENSMUSG00000050107	germ cell-specific gene 2 [Source:MGI Symbol;Acc:MGI:1194498]
6.81175	Hils1	ENSMUSG00000038994	histone H1-like protein in spermatids 1 [Source:MGI Symbol;Acc:MGI:2136691]
6.7371926	Tcp11	ENSMUSG00000062859	t-complex protein 11 [Source:MGI Symbol;Acc:MGI:98544]
6.658594	Papolb	ENSMUSG00000074817	poly (A) polymerase beta (testis specific) [Source:MGI Symbol;Acc:MGI:1932115]
6.4456058	1700003F12Rik	ENSMUSG00000038523	RIKEN cDNA 1700003F12 gene [Source:MGI Symbol;Acc:MGI:1922730]
5.922679	Lrrc8b	ENSMUSG00000070639	leucine rich repeat containing 8 family, member B [Source:MGI Symbol;Acc:MGI:2141353]
1.7899683	Gpnmb	ENSMUSG00000029816	glycoprotein (transmembrane) nmb [Source:MGI Symbol;Acc:MGI:1934765]
1.7899683	Lgals3	ENSMUSG00000050335	lectin, galactose binding, soluble 3 [Source:MGI Symbol;Acc:MGI:96778]
-0.06991831	Itgb2	ENSMUSG00000000290	integrin beta 2 [Source:MGI Symbol;Acc:MGI:96611]
-0.16991831	Mmp12	ENSMUSG00000049723	matrix metallopeptidase 12 [Source:MGI Symbol;Acc:MGI:97005]
-0.3320362	Ctsk	ENSMUSG00000028111	cathepsin K [Source:MGI Symbol;Acc:MGI:107823]
-0.945378	Clec12a	ENSMUSG00000053063	C-type lectin domain family 12, member a [Source:MGI Symbol;Acc:MGI:3040968]
-0.945378	Trem2	ENSMUSG00000023992	triggering receptor expressed on myeloid cells 2 [Source:MGI Symbol;Acc:MGI:1913150]
-1.8741144	Itgax	ENSMUSG00000030789	integrin alpha X [Source:MGI Symbol;Acc:MGI:96609]
-1.8741144	Ubd	ENSMUSG00000035186	ubiquitin D [Source:MGI Symbol;Acc:MGI:1344410]
-1.8741144	Emr1	ENSMUSG00000004730	EGF-like module containing, mucin-like, hormone receptor-like sequence 1
-2.1304328	Tph2	ENSMUSG00000006764	tryptophan hydroxylase 2 [Source:MGI Symbol;Acc:MGI:2651811]

Table 5.1. List of genes identified as differentially expressed between *Smarcad1*+/+ and *Smarcad1*-/- mice. Genes in blue background = elevated in +/+, red = elevated in -/- mice. Literature searching using the gene name in addition to the terms "adipogenesis" or "adipocyte" highlights a subset previously identified as influential in white-adipose tissue biology. The fold value indicates the level of expression difference between control and experimental groups.

(A)

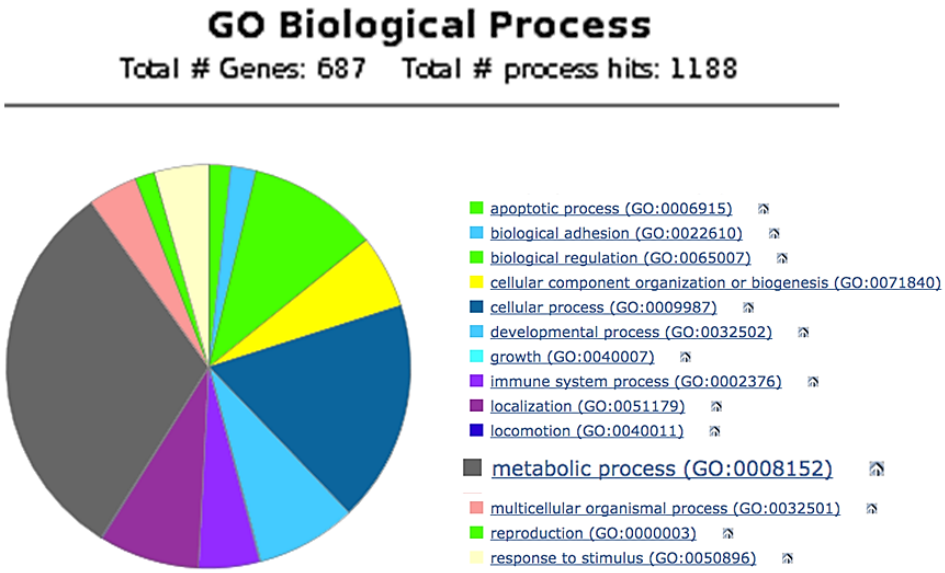

(B)

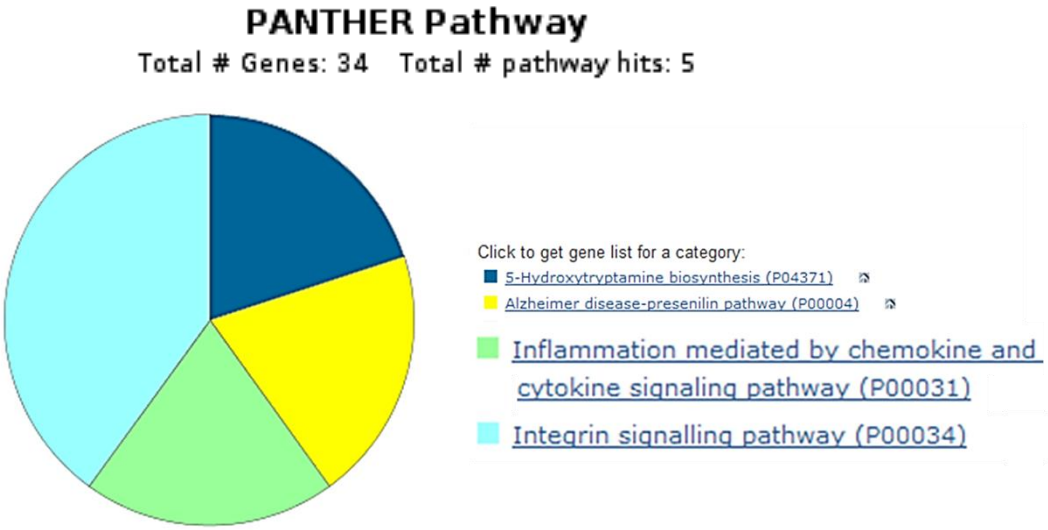

Figure 5.5. (A) Gene Ontology analysis of (non-intensity filtered) differentially expressed genes from *Smarcad1*+/+ vs -/- whole-WAT RNA-seq experiments. As expected, the category "Metabolic Processes" is the largest Biological Process group identified as different between +/+ and -/- mice indicating that further investigation of WAT-tissue is warranted. (B) Identification of common pathways within the GO search engine revealed the defined "Inflammation…and cytokine signalling pathway" and "Integrin signalling pathway" were different between *Smarcad1*+/+ and -/- mice, both of which are connected to macrophage-driven mechanisms of inflammation. Analysis was performed using the online analysis tool at http://pantherdb.org/geneListAnalysis.do using default settings.

5.2.4 Genes elevated in *Smarcad1*-/- mice over+/+ mice.

Literature searching of genes differentially expressed produced four candidates with potential impact on white adipose tissue. In each case the genes are linked to the presence of macrophages within adipose tissue, which are known to increase in number as adipose tissue expands and contribute to inflammation during adipose tissue pathology.

MMP12 (Matrix Metalloproteinase 12) is an elastinolytic protease highly expressed by macrophages, which is highly expressed in tissue resident macrophages. Recent studies suggest that MMP12+ve adipose tissue macrophages help protect against obesity, while also promoting insulin resistance (M. Park et al., 2015). Ctsk (Cathepsin K) is a cysteine-protease also expressed by macrophages, and degrades type I collagen during adipocyte differentiation. It has been shown to be over-expressed in the white adipose tissue of obese mice (Yang et al., 2008), and promotes dyslipidaemia during high-fat diet challenge (Funicello et al., 2007). Trem2 (Triggering receptor expressed on myeloid cells 2) is expressed on inflammatory macrophages and promotes macrophage survival, and is also implicated in adipogenesis and diet induced obesity (M. Park et al., 2015). Itgax (Integrin alpha X, also known as CD11c) is highly expressed on inflammatory macrophages, and this subset of macrophages have been shown to increase in number in the white adipose tissue of diet-induced obese mice (Lumeng, Bodzin, & Saltiel, 2007).

Taken together, the elevated expression of these genes in the white adipose tissue of *Smarcad1*-/- mice suggests an increased presence and/or function of macrophages in the absence of SMARCAD1. These findings were therefore followed up by flow cytometry to confirm the increase in macrophage numbers in these mice.

5.2.5 Flow cytometric analysis confirms an increase in white-adipose-tissue resident macrophage numbers in *Smarcad1*-/- mice.

The elevated expression of the macrophage markers in whole-adipose tissue RNA-seq suggested an increase in infiltration of macrophages into the white-adipose tissue of *Smarcad1*-/- mice. To confirm this, multicolour flow cytometry was performed to enumerate macrophages from the epididymal and subcutaneous WAT depots of *Smarcad1*-/- and +/+ mice. Stromal-vascular fractions of white adipose tissue were

stained with a cell-viability marker and for the common lymphocyte marker CD45 in addition to the macrophage-specific marker F4/80 (Figure 5.6). Live cells positive for CD45 and F4/80 were counted as tissue-resident macrophages.

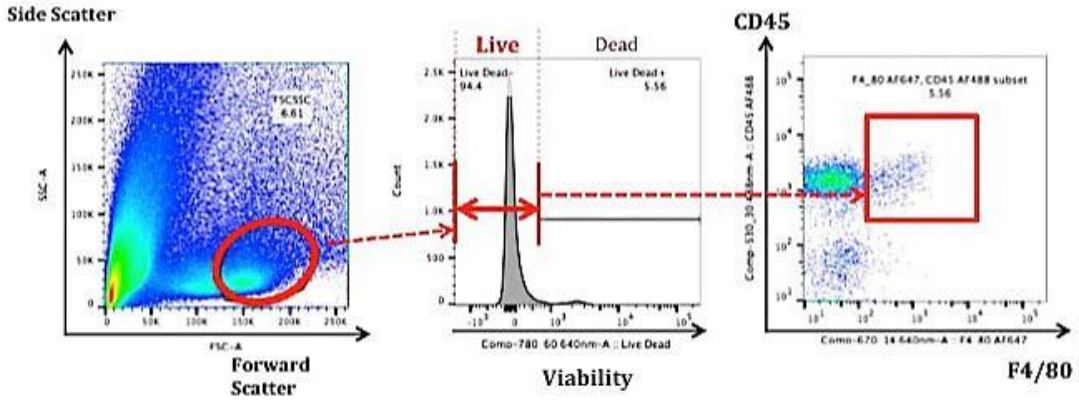

Figure 5.6. Flow cytometric gating scheme to enumerate tissue-resident macrophages in the white adipose tissue of *Smarcad1*+/+ and -/- mice. Cells with the phenotype Live/Dead-ve CD45+ve F4/80+ve were counted as macrophage positive.

Analysis of white adipose tissue from 4-6 month old mice revealed that macrophage numbers are significantly increased in the epididymal fat of *Smarcad1*-/- mice (mean nos. 3983 and 1815 respectively) (Figure 5.7) and although a similar trend appears with subcutaneous macrophage numbers (mean nos. 621 and 232 respectively) a power calculation based on these data indicates that an increase in sample size up to n=9 for both experimental and control groups would also result in statistical significance.

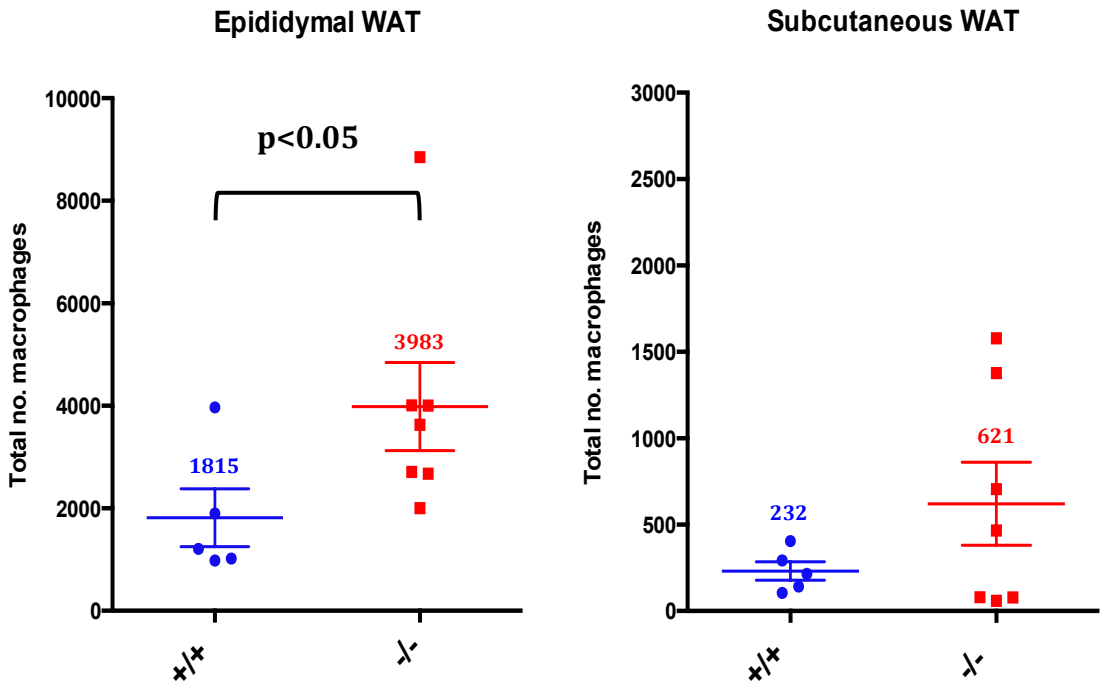

Figure 5.7. Flow cytometric analysis of Macrophages resident in the stromal-vascular section of white adipose tissue. The mean number for each genotype is shown above the error bars. Macrophage numbers are significantly increased in epididymal WAT of *Smarcad1*-/- mice (p<0.05, students t-test), whereas the same trend is seen in subcutaneous WAT - which would reach significance with an increase in sample number (up to n=9).

5.3 Flow cytometric analysis of putative adipocyte-stem cells from *Smarcad1* +/+ mice.

Putative stem cells resident in white adipose tissue have been described which retain multipotency and are able to differentiate into mature adipocytes (see references 39 and 42). Of the putative stem cell phenotypes published, common cell surface markers used to isolate ASCs from the stromal vascular fraction of adipose tissue include CD45 and CD31 (to negatively select cells already lineage-committed), the cell-adhesion molecules CD24, CD29 and CD34, and stem-cell antigen-1 (Sca-1). While some debate may remain as to the authenticity of CD24 as an adipocyte stem cell marker these markers were used to create a cell staining panel for flow cytometric analysis of ASC numbers and allow flow sorting of this cell population (Figure 5.8). Sorted Lin-(CD31-CD45-) CD29+CD34+Sca-1+ cells were then cultured *in vitro* to confirm adipogenic potential *via* differentiation with known activators of adipogenesis (Insulin, IBMX and dexamethosone). After differentiation, cells from *Smarcad1*+/+ and -/- mice were stained for lipid content using Oil Red O and adipogenesis compared between control and experimental groups.

5.3.1 No difference in numbers of putative ASCs are seen in *SMARCAD1*-/- mice.

Mice aged 4-5 months were analysed for the number of putative ASCs present in both epididymal and subcutaneous white adipose fat depots. No significant difference was found between experimental and control groups with either depot (Figure 5.9). However, a significant difference in ASC numbers was observed in the epididymal WAT of older (11-12 month old) mice, with fewer ASCs observed in *Smarcad1*-/- mice (Figure 5.10).

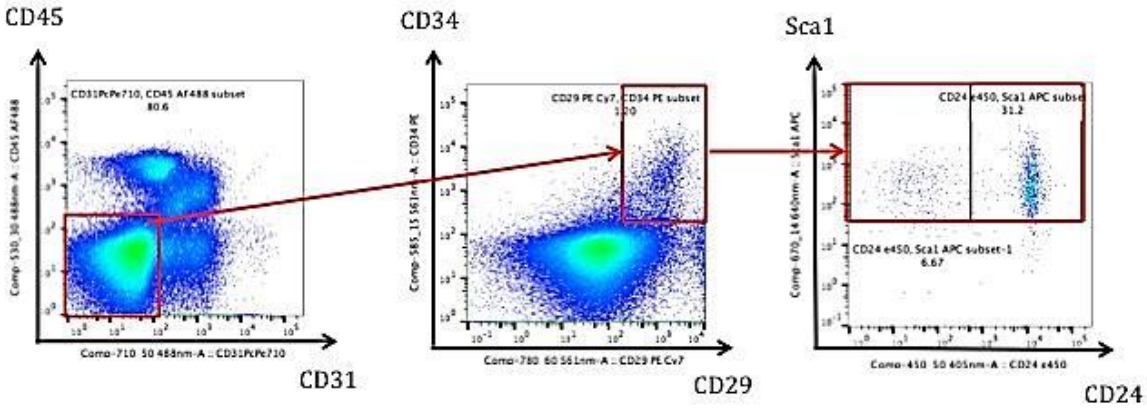

Figure 5.8. Flow cytometric gating strategy for the analysis of Lin$^-$(CD45-CD34-) CD29+CD34+Sca1+ adipocyte stem cells. While debate remains as to the authenticity of CD24 as a *bona-fide* adipocyte stem cell marker, both CD24+ and CD24- cells were pooled and sorted/used in subsequent studies together.

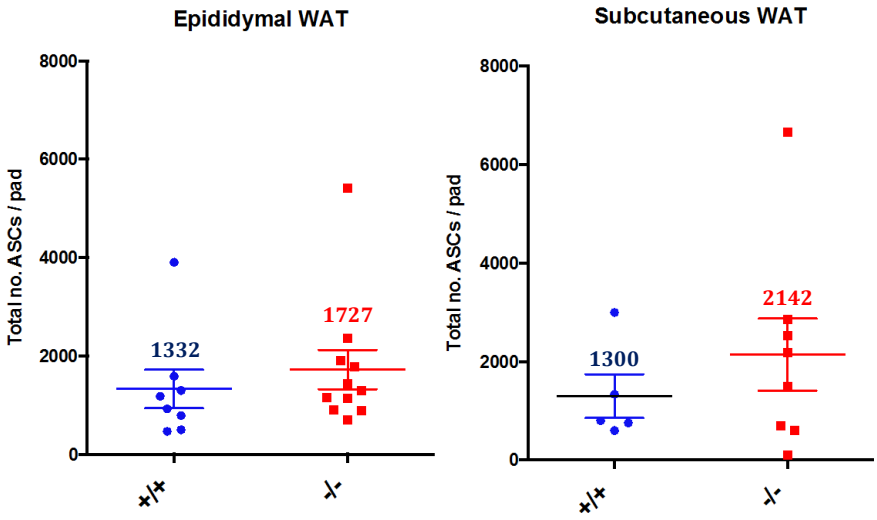

Figure 5.9. No significant difference was observed in the number of (putative) adipocyte stem cells between 4-5 month old *Smarcad1*+/+ and -/- mice, in either epididymal or subcutaneous WAT depots.

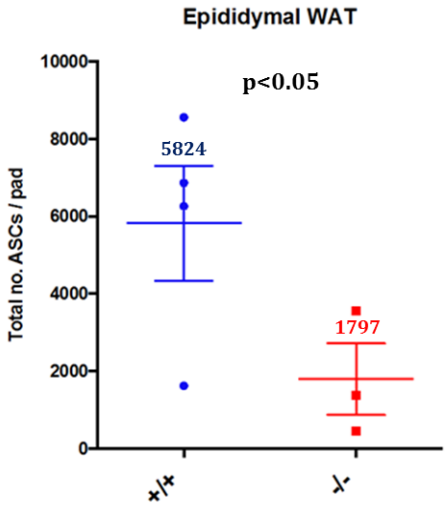

Figure 5.10. A significant decrease was observed in the number ASCs in the epididymal WAT depot of 11-12 month old *Smarcad1* -/- mice (n=4) (p<0.05, students t-test).

5.3.2 SMARCAD1 is expressed in putative adipocyte-stem cells and lineage-positive cells within the stromal-vascular fraction of white adipose tissue.

To confirm whether the cells described in section 5.3.1 were *bona fide* adipocyte precursors and expressed SMARCAD1, flow sorted cell fractions were analysed by western blot for the presence of SMARCAD1, then cultured/differentiated *in-vitro* to assess adipogenic potential. Results of the three different sort fractions (Lin+ve, Lin-ve, Sca+ve, see Figure 5.7) blotted and probed for SMARCAD1 are shown in Figure 5.11 (below). Highest expression of SMARCAD1 was seen in the Lineage positive population (as expected) and expression was also seen in the Sca1+ve fraction (Figure 5.11), confirming the expression of SMARCAD1 in putative adipocyte stem cells.

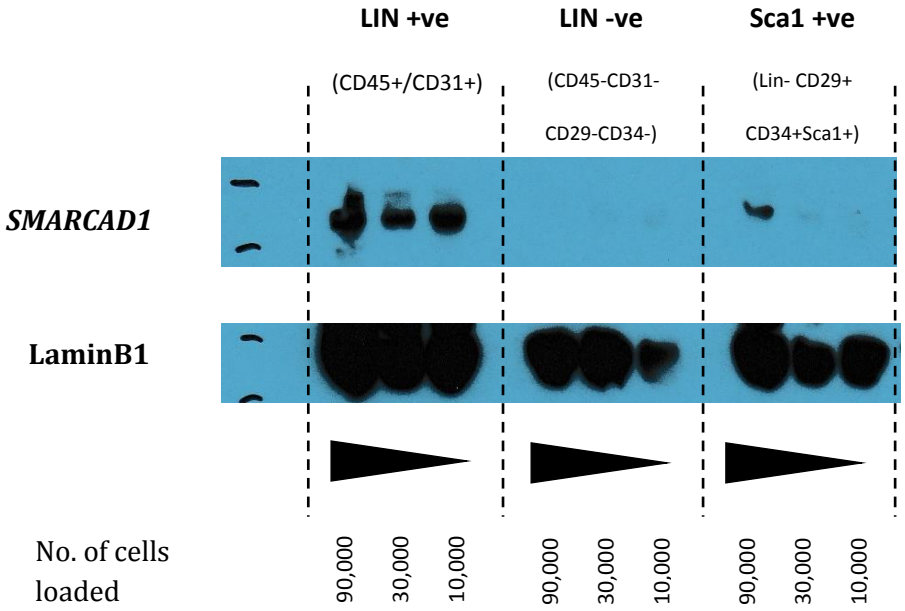

Figure 5.11. SMARCAD1 is expressed in the Lineage positive (CD31/CD45+ve) fraction from murine white adipose tissue, in addition to the Sca1+ve (Lin-ve, CD29+CD34+) putative adipocyte stem cell fraction.

5.3.3 Ex-vivo culture and differentiation of flow-sorted adipocyte stem cells confirms that adipogenesis is not impaired in the absence of SMARCAD1.

Cells sorted using the gating strategy outlined in Figure 5.8 were cultured and differentiated *in vitro* to confirm adipogenic potential. After the first 5 days in culture morphological changes could be seen, as cells increased in size took on a fibroblast-like appearance. Confluency was reached after a further 5 days, and subsequent application of the differentiation cocktail led to the appearance of lipid droplets after a further week (Figure 5.12), indicating that successful adipogenesis was underway. Cells were fixed and stained with Oil Red O to confirm lipid content after a total of 21 days in culture.

While this confirmed that cells of the Lin-ve, CD29+ve CD34+ve Sca1+ve phenotype are authentic adipocyte precursors, subsequent measurement of Oil Red O content indicated that there was no significant difference in adipogenesis between ASCs isolated from *Smarcad1*+/+ and -/- mice (Figure 5.13). Together with the equal size of adipocytes seen during histological of WAT tissue, these data suggest that any difference in fat pad size observed between *Smarcad1*+/+ and -/- mice is not driven directly by adipogenesis-related mechanisms.

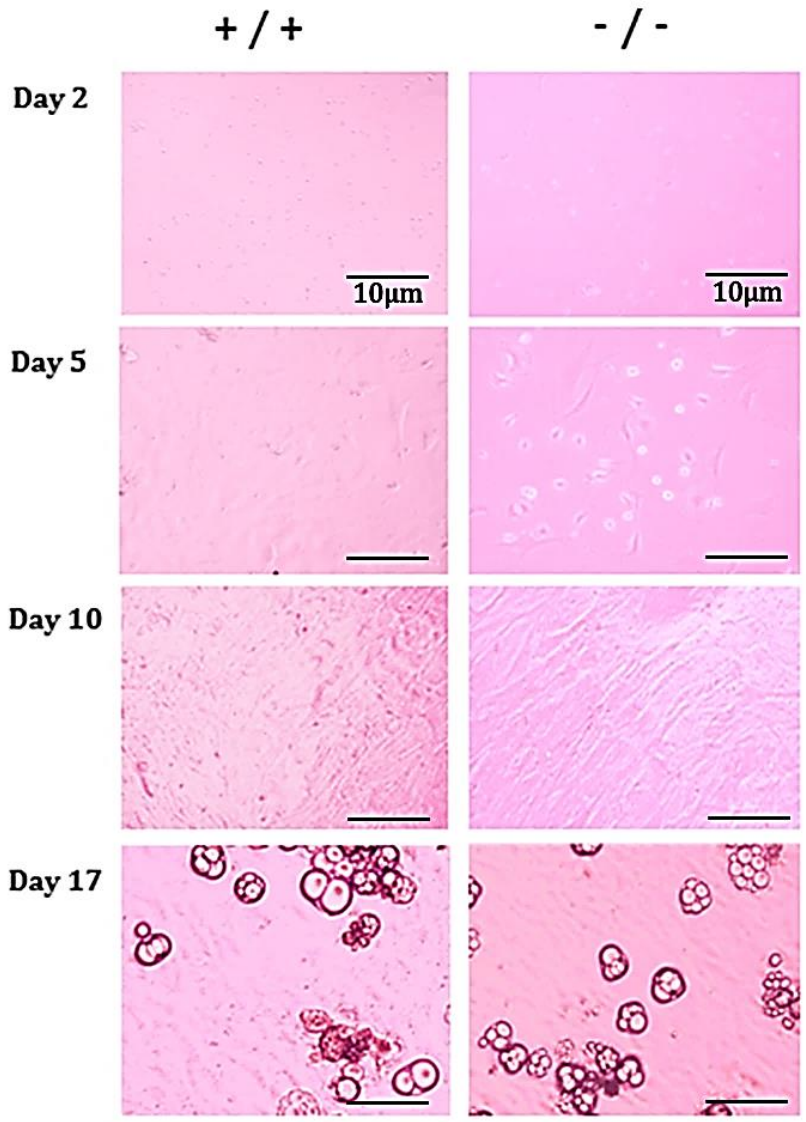

Figure 5.12. Morphological changes seen in flow-sorted adipocyte stem cells (ASCs) during culture and adipogenic differentiation. After 5 days post-sort cells start to assume a fibroblast-type morphology, which becomes the majority cell type by day 10. After 17 days lipid-droplets become visible within both *Smarcad1*+/+ and -/- ASC-derived cultures. Images capture using 20x magnification, scale bars represent 10µm.

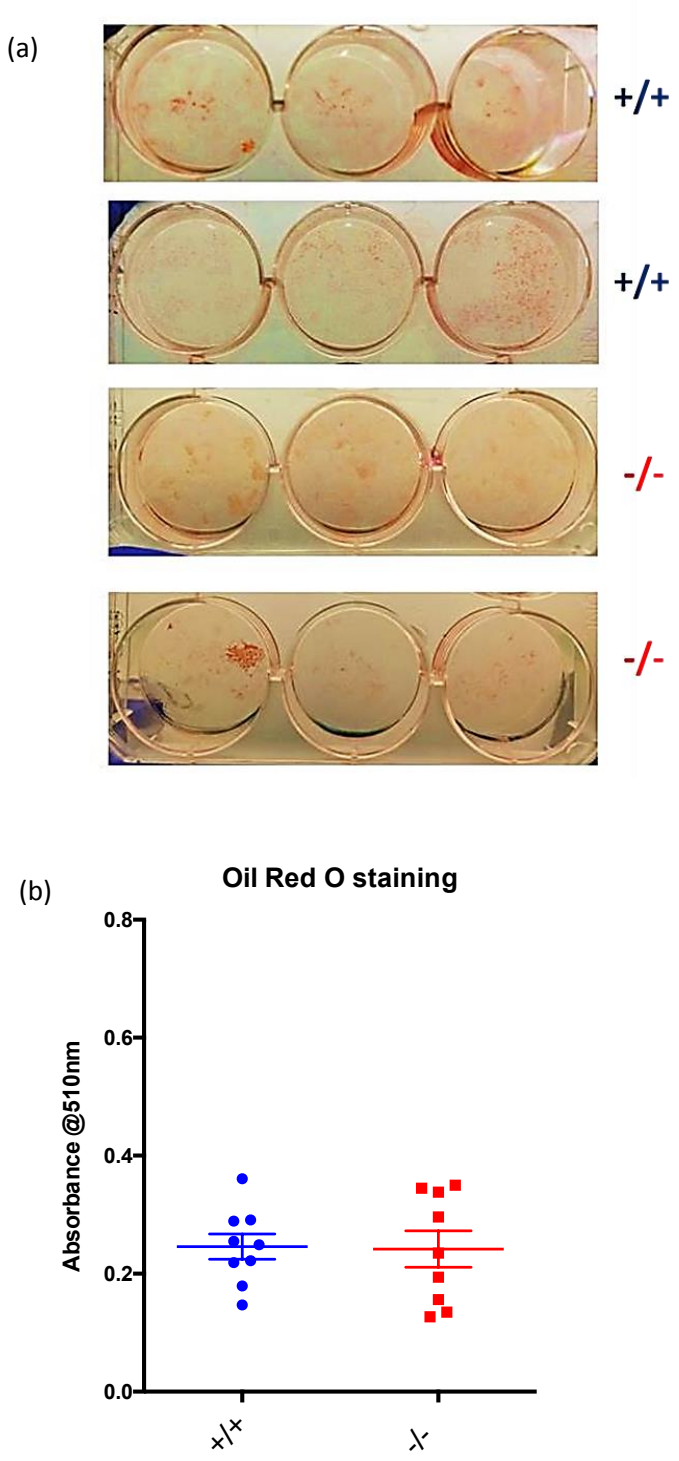

Figure 5.13. (a) Oil Red O staining of differentiated adipocyte stem cells confirms the adipogenic potential of sorted Lin-ve/CD29+ve/CD34+ve/Sca1+ve WAT-resident cells. (b) Quantitation of solublised Oil Red O reveals no significant difference in adipogenesis between *Smarcad1*+/+ and -/- mice.

5.4 Mice challenged with a high-fat diet show increased weight-gain in the absence of SMARCAD1.

Eight *Smarcad1*+/+ and eight *Smarcad1*-/- mice were individually caged and fed a 60% high fat diet for 6 weeks, with weekly recording of body mass for each mouse. At the end of high-fat diet challenge, mice were euthanized and white adipose tissue analysed for mass, stem cell number and number of adipose-tissue resident macrophages, alongside measurement of adipocyte size (i.e. area) using fixed WAT sections from both groups. In parallel, intestinal sections were taken from each mouse and used for microbiota population analysis using qPCR, alongside small intestinal iIEL counts (see appendix for results).

5.4.1 Changes in Smarcad1-/- vs +/+ mice after 6 week high-fat diet.

All mice challenged with a 60% high fat diet increased weight as expected, and showed an increase in the size of white adiocytes compared to normal chow-fed mice but no significant difference was seen in adipocyte size between *Smarcad1*+/+ and -/- groups. (Figure 5.14). Mice lacking SMARCAD1 showed a significant increase in body mass by week 2, which continued to increase compared to *Smarcad1*+/+ mice over the 6 weeks (Figure 5.15a). Furthermore, this increase was accompanied by a significant increase in the mass of subcutaneous WAT in -/- mice over +/+ mice (Figure 5.15b). Although both triglyceride and free fatty acid serum concentrations increased in comparison to chow-fed mice, there was no significant difference between +/+ and -/- groups (Figure 5.16). In addition, while the numerical value of mean adipocyte stem cells increased after high fat diet (compared to previous normal chow-fed mice) there was no significant difference between +/+ and -/- mice in ASC numbers (Figure 5.17).

Alongside the significant increase in subcutaneous WAT mass, *Smarcad1*-/- mice also show a significant increase in the number of tissue-resident macrophages after high fat diet. While normal chow-fed mice show a significant increase in macrophages numbers in the epididymal fat of *Smarcad1*-/- mice, this was not seen after high fat diet (Figure 5.18).

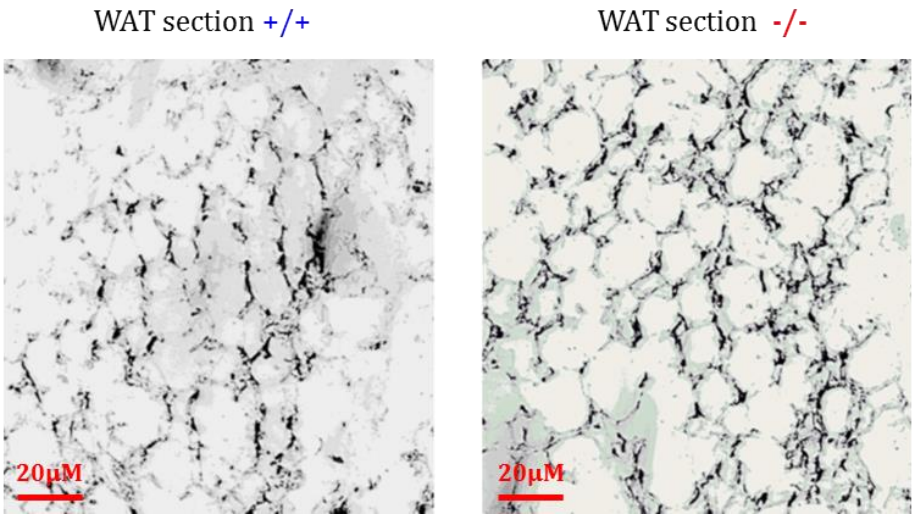

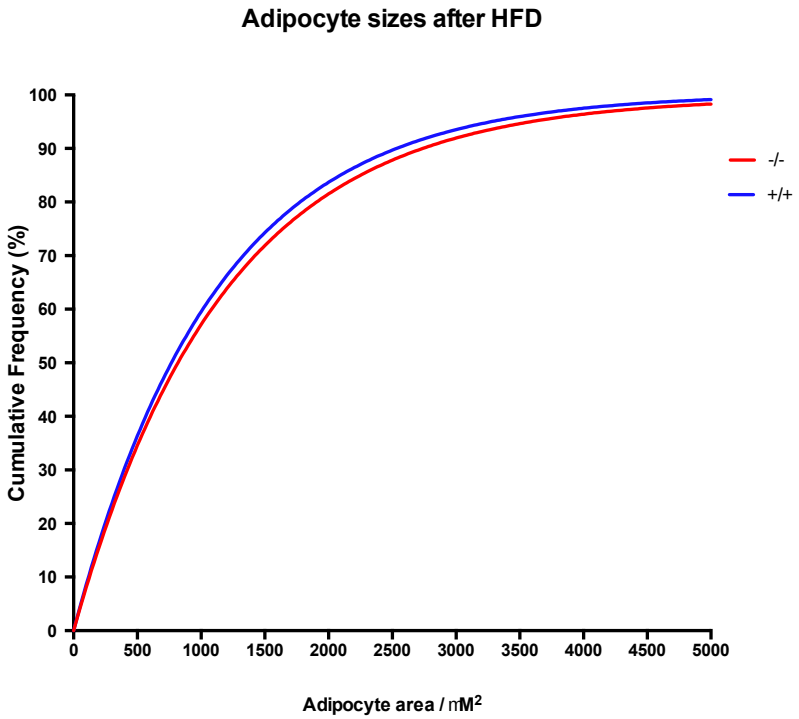

Figure 5.14. The size of adipocytes in subcutaneous WAT is not significantly increased after 6 weeks of high fat diet between *Smarcad1*+/+ and -/- mice. Subcutaneous WAT sections were fixed and quantified as in Figure 5.2. Images were captured at 10x magnification, and the scale bars represent 20µM.

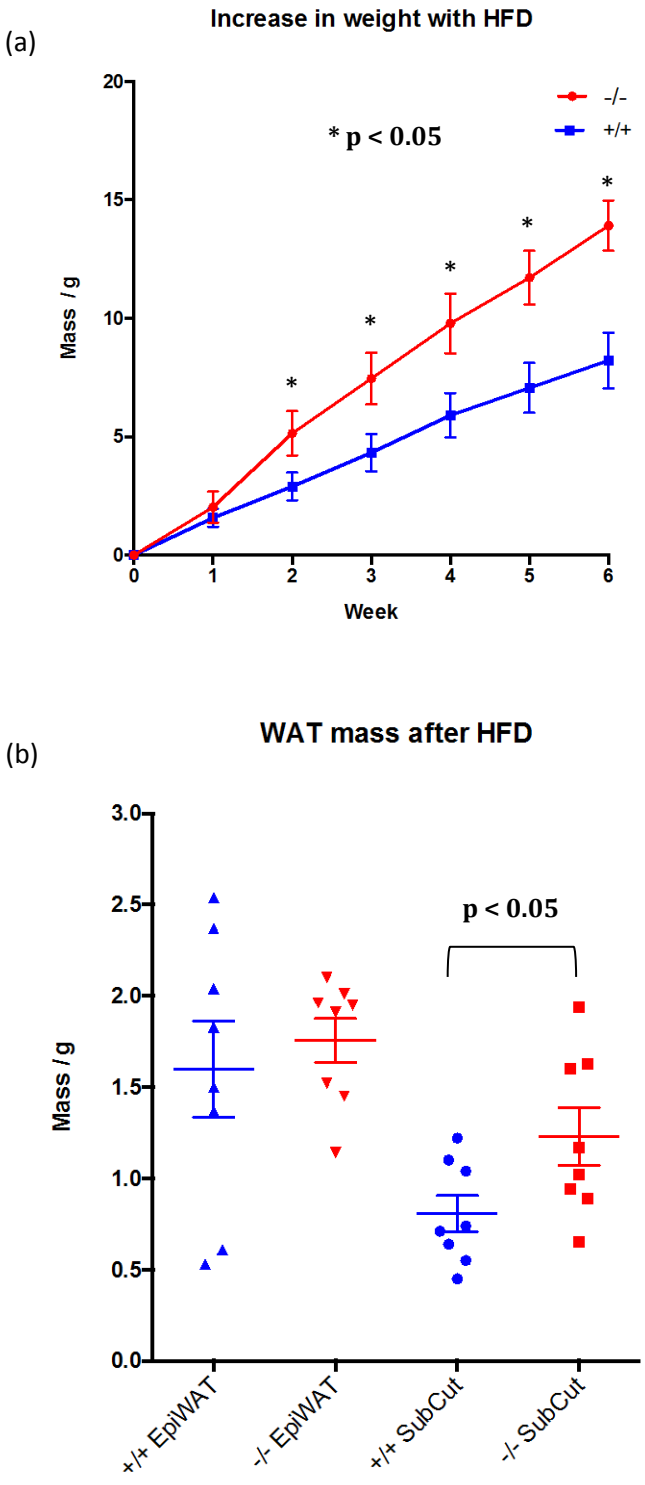

Figure 5.15 (a) High fat diet challenged *Smarcad1*-/- mice gain significantly more body weight than +/+ mice by week 2 of challenge, increasing over 6 weeks (p<0.05, students t-test). (b) Increase in body weight is associated with a significant increase in the mass of subcutaneous WAT, but not epididymal WAT.

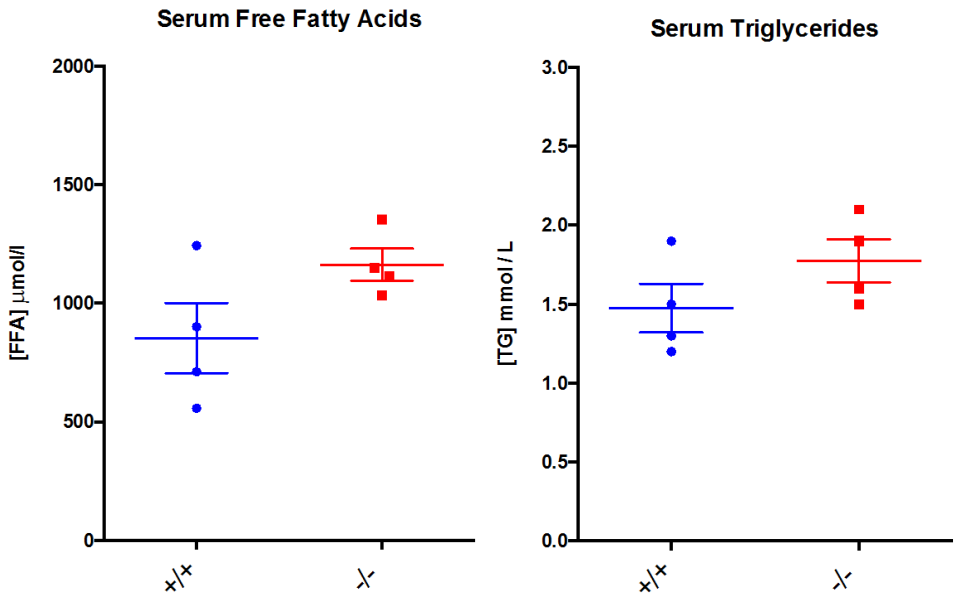

Figure 5.16. No significant difference was seen between *Smarcad1*+/+ and -/- mice in the serum free fatty acid and triglyceride concentrations after 6 weeks of high fat diet.

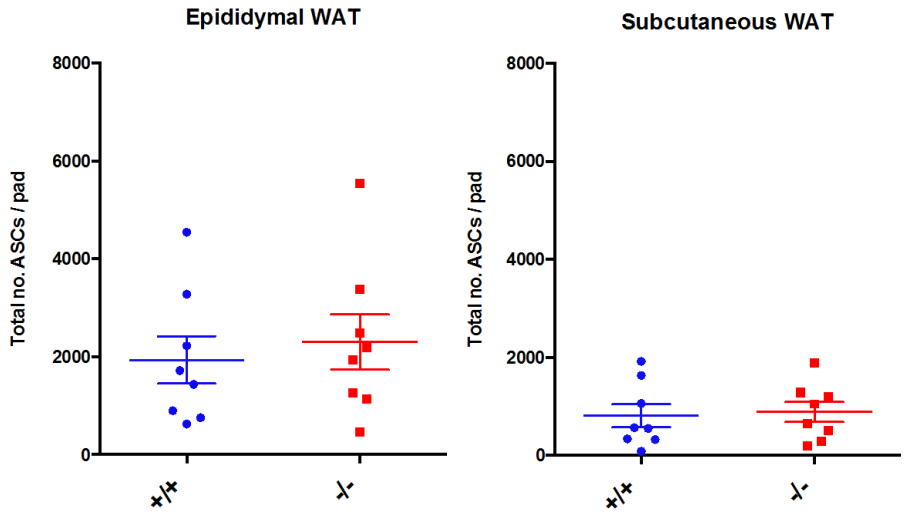

Figure 5.17. No significant difference was seen in the number of adipocyte stem cells resident in epididymal or subcutaneous WAT between *Smarcad1*+/+ and -/- mice after 6 weeks of high fat diet.

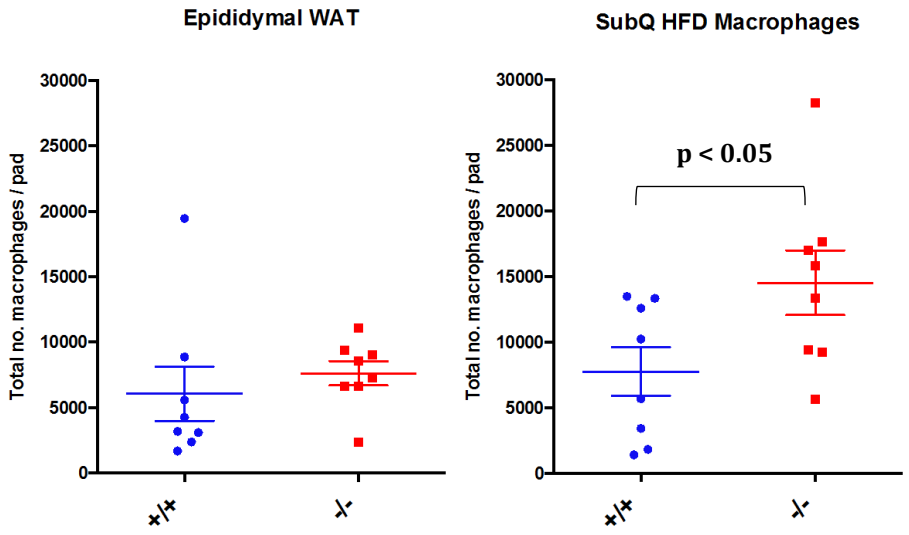

Figure 5.18. Tissue resident macrophages are significantly increased in the subcutaneous WAT of *Smarcad1*-/- over +/+ mice after 6 weeks of high fat diet (p<0.05, studens t-test), but not in epididymal WAT.

5.4.2 Changes in microbiota after high-fat-diet.

Sections of small intestine (ileum) and colon were taken from mice euthanized after 6 week high fat diet challenge, and analysed for microbial content. The proportional microbial subpopulations present can be quantified using a qPCR-based method with primers specific for the 16S rRNA genes of each subgroup. Relative proportions for each subpopulation are calculated by comparison with the total microbial content using primers common to all microbial groups known to inhabit the murine gut.

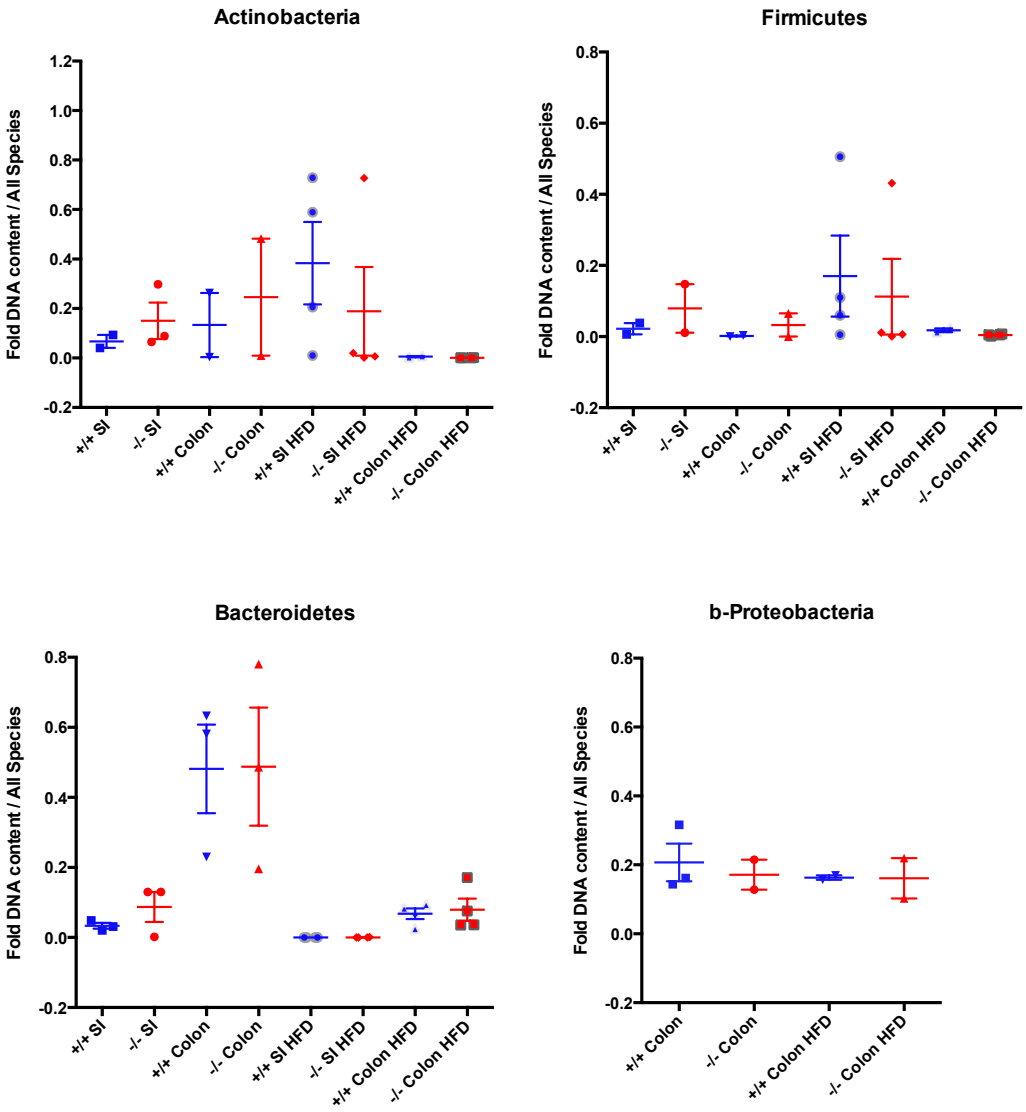

Figure 5.19. No significant difference is seen in the microbial subpopulations in the small or large intestine of *Smarcad1*+/+ and -/- mice fed on normal chow diet. After a 6 week high-fat diet challenge numerical changes in the proportion of actinobacteria and firmicutes are seen in the small intestine (a) and (b) of HFD v chow diet mice, but not between *Smarcad1*+/+ vs -/- mice. Similarly after 6 weeks of high fat diet the proportion of colonic bacteroidetes is significantly reduced between HFD and chow mice, but not between *Smarcad1*+/+ and -/- mice (c). No proteobacteria were detected in the small intestine, and no significant difference was found between any groups in the colon. No difference in microbial populations were observed between *Smarcad1*+/+ and -/- mice.

5.5 Investigation of SMARCAD1 impact on adipogenesis using Mouse embryonic fibroblasts.

As the availability of adipocyte stem cells from mice is limited, an alternative source of cells with adipogenic potential was used to study the effects of SMARCAD1 on adipogenesis. Mouse embryonic fibroblasts are capable of differentiation into mature adipocytes using the same differentiation cocktail and conditions as used to differentiate purified murine ASCs or pre-adipocyte cell lines (such as 3T3-L1 cells) into mature adipocytes. As MEFs are readily expanded *in vitro*, these also lend utility to experiments where cell numbers can be limiting (such as western blots).

MEFs previously isolated from *Smarcad1*+/- and -/- mice were used to assay for differences in epigenetic-related factors previously associated with SMARCAD1, in addition to the effect of SMARCAD1 on cell proliferation, adipogenesis and the cell cycle.

5.5.1 Adipogenesis assay of +/- vs -/- MEFs.

Mouse embryonic fibroblasts were grown until confluence and adipogenic differentiation was induced two days post-confluence. After 10 days cells were fixed and stained with Oil Red O, before dye re-solubilisation and optical density measurement at 510nm. (Figure 5.20a) Three wells each of four +/- and four -/-MEF lines were differentiated and adipogenesis quantified. In agreement with the in vitro studies on differentiated ASCs, no significant difference was found between *Smarcad1*+/- and -/- groups after differentiation (Figure 5.20b).

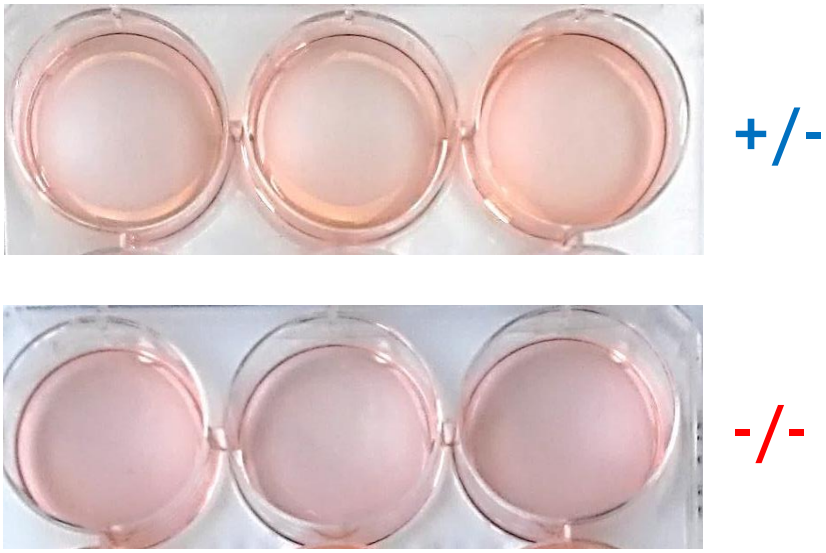

Figure 5.20 (a) Oil Red O staining of differentiated mouse embryonic fibroblasts and re-solublisation in 60% isopropanol. (b) Optical density read at 510nm of Oil Red O reveals no significant difference in adipogenesis between MEFs from *Smarcad1*+/- and -/- mice.

5.5.2 Growth curves of MEFS from +/- vs -/-.

To understand further whether SMARCAD1 impacts cell proliferation, mouse embryonic fibroblasts from four +/- and four -/- MEF lines were cultured until regularly dividing (i.e. cultured cells would need to be split every 2 days to avoid confluency) and then 10,000 cells/well were seeded into 12 wells of a 12 well plate. Four wells of each MEF line were then harvested and counted after 24 hours, another four wells after 48 hours and the final four wells from each plate counted after 72 hours. Counts from each genotype were combined for each time point and plotted to construct growth curve for both genotypes.

After 72 hours there were significantly more viable (phase bright) *Smarcad1*+/- cells, suggesting that either proliferation is increased or fewer cells perish during the growth of *Smarcad1*+/- MEFs (Figure 5.21).

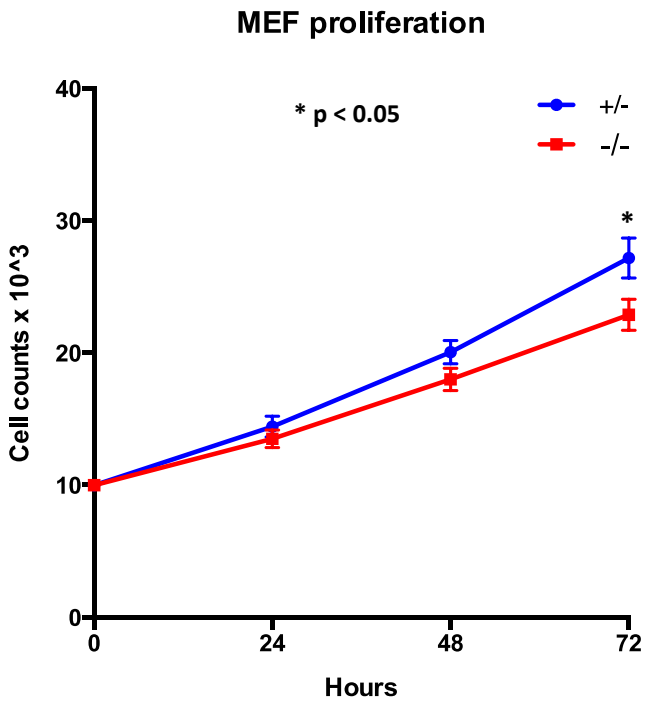

Figure 5.21. Growth curves of *Smarcad1*+/- and -/- MEFs indicate that cell proliferation is significantly reduced in *Smarcad1*-/- MEFs after 72 hours compared to *Snarcad1*+/- MEFs (* p < 0.05 students t-test).

5.5.3 Cell cycle analysis.

As MEFs lacking SMARCAD1 show a statistically significant reduction in the number of successfully proliferated cells after 72 hours of culture, the cell cycle was analysed in each MEF line by FACS using Propidium Iodide incorporation measurement. In brief, as cells begin the process of division and the genome is replicated, the net amount of DNA within a cell increases from G1 (Gap-1) phase with a ploidy number of n=2, increasing through in S-phase (Synthesis phase) until G2-phase (Gap-2) before division to 2 daughter cells (ploidy number 4) (Figure 5.22). Interestingly, while no difference was seen in the proportion of cells in G1 phase, there was a significant increase in the proportion of MEFs lacking SMARCAD1 in S-phase, and a decrease in the proportion of *Smarcad1*-/- MEFS in G2 phase (Figure 5.23). This is consistent with a model where impaired histone supply leads to a delay in the transition of cells through S-phase and reduced cell proliferation (Günesdogan, Jäckle, & Herzig, 2014).

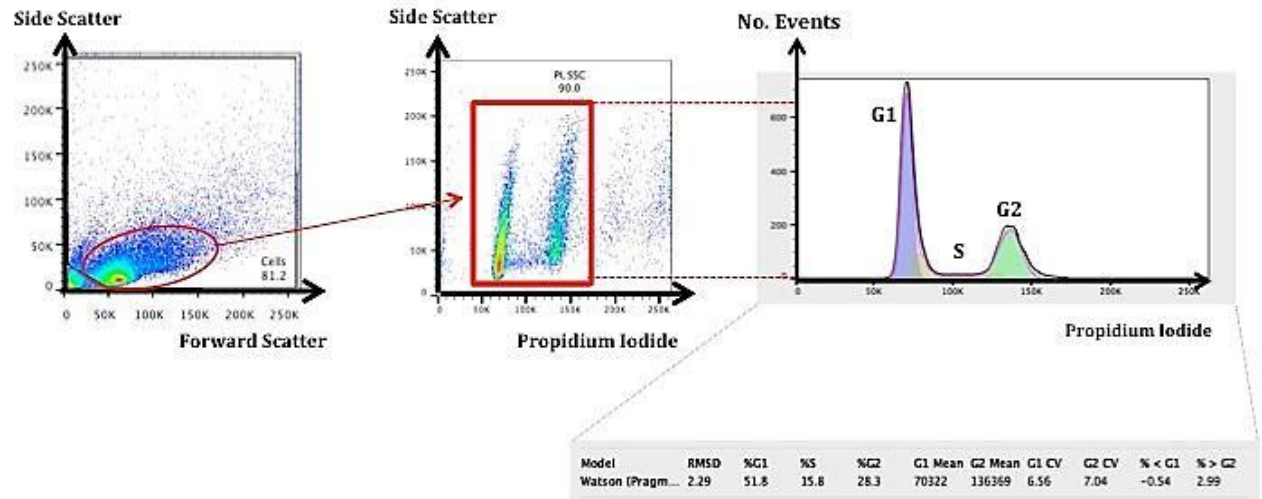

Figure 5.22. Flow cytometric gating scheme for cell cycle analysis of fixed, Propridium Iodide stained mouse embryonic fibroblasts. Quantitation of each phase of the cell cycle (G1, S, G2) is performed using FlowJo cytometry software (www.flowjo.com).

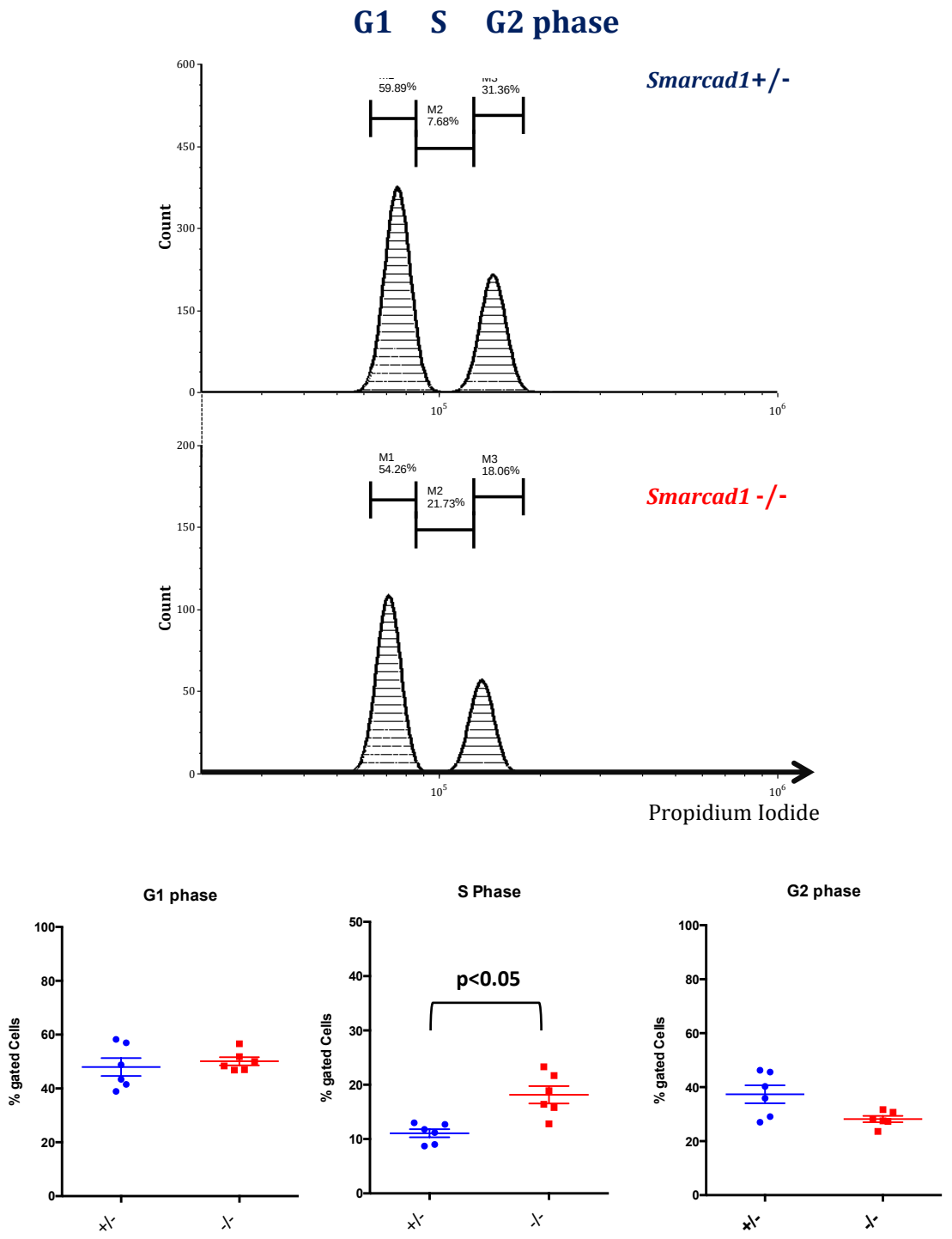

Figure 5.23. Significant differences are found in the proportion of cells in S and G2 phases between *Smarcad1*+/- and -/- MEFs. (a) Flow cytometry plots of PI stained MEFs, showing peaks at G1 and G2 phases of the cell cycle. (b) A significant increase in the number of cells in S-phase ($p<0.05$, students t-test) and decreased number in G2 phase are observed in *Smarcad1*-/- MEFs. Six replicates per genotype were used for each plot.

5.5.4 Western blotting of mouse embryonic fibroblasts reveals no difference in heterochromatic marker expression.

As human SMARCAD1 has been previously reported to impact the level of heterochromatic markers such as H3K9me3 and HP1γ, these marks were assessed by western blot to give insight into whether disruptions to the level of heterochromatin could underpin differences in the cell cycle or proliferation that were seen.

MEFs cultured as previously described were harvested and 100,000 cells per well were loaded and resolved by PAGE on a 16% gel. Four *Smarcad1*+/- and four *Smarcad1*-/- MEF lines were analysed for the presence of H3K9me3 and HP1γ signal (Figure 5.24). No binary difference was seen in the presence/absence of these marks, suggesting that different mechanisms may be responsible for differences seen in mouse cells that lack SMARCAD1. Furthermore, densitometry of these blots revealed no significant difference between the levels of H3K9me3 and HP1γ expressed in *Smarcad1*+/- and *Smarcad1*-/- MEFs (Figure 5.25).

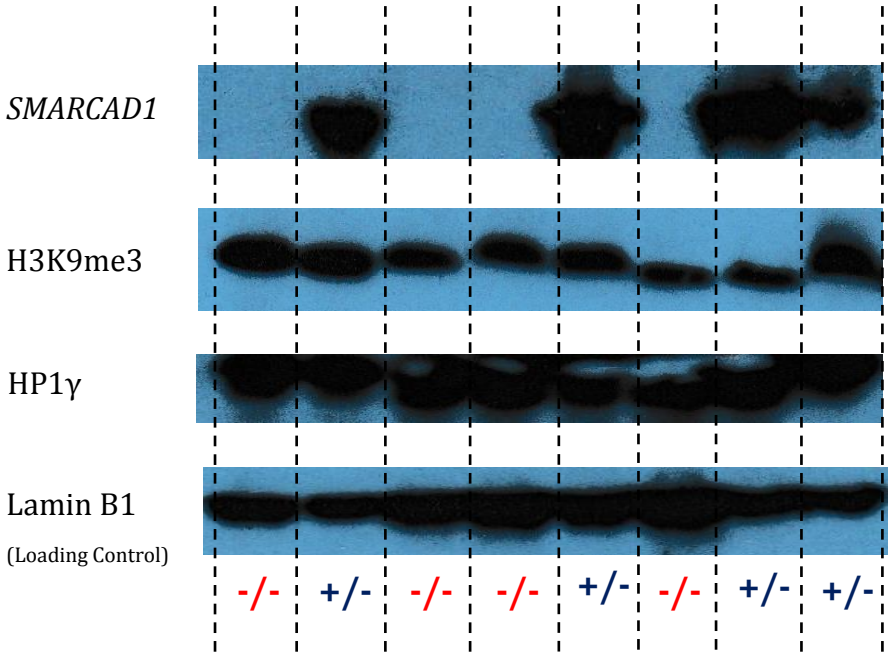

Figure 5.24. Western blotting of MEFs generated from *Smarcad1*+/- and -/- mice show that there is no difference in the levels of two markers of heterochromatin (H3K9me3 and HP1γ) in the absence of SMARCAD1.

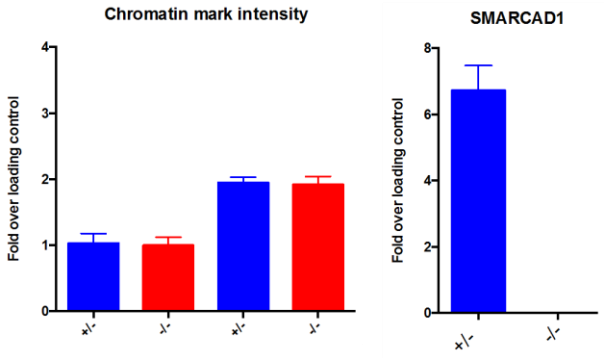

Figure 5.25. Densitometric analysis of MEF western blots (from figure 5.23). (a) Each of the probe intensities was calculated as fold intensity over loading control (Lamin B1) intensity for each MEF line. (b) Mean fold over loading control was calculated for each genotype. No significant difference is found in levels of H3K9me3 or HP1γ in the absence of SMARCAD1. Each bar represents the mean of n=4 MEFs (with S.E.M.) for each genotype.

5.6 Perspectives.

In spite of initial observations, mice lacking SMARCAD1 do not have smaller epididymal or subcutaneous white adipose tissue fat pads. However, in the absence of SMARCAD1 mice show elevated serum triglyceride and free fatty acid concentration. Closer examination of the size of adipocytes within white adipose tissue suggests that excess serum fat is not absorbed within the tissue itself as no difference was seen in adipocyte size between *Smarcad1*+/+ and -/- mice . This may explain the increase in liver size also seen in *Smarcad1*-/- mice and it is therefore likely these mice have fatty livers.

Transcriptomic analysis also negated a direct impact on adipogenesis of SMARCAD1 as none of the well-characterised adipogenic factors reported differential expression between experimental and control groups. However, *Smarcad1*-/- mice show an increase in the number of tissue-resident macrophages within white adipose tissue, possibly indicative of adipocyte dysfunction and death within the tissue.

Interestingly, during high fat diet challenge, *Smarcad1*-/- mice demonstrate an increased weight-gain when compared to wild-type (*Smarcad1*+/+) mice, which is accompanied by an increase in the size of subcutaneous white-adipose tissue. Measurement of the size of adipocytes suggests that the increase in tissue mass is driven by an increase in the number of adipocytes present (hyperplasia) rather than an increase in the size of the adipocytes itself. These observations are further supported by experiments using mouse embryonic fibroblasts, where again no difference in adipogenesis was observed, although a difference in proliferation and the proportion of cells within the S and G2 phase of the cell cycle were present.

Taken together these data suggest that responses of SMARCAD1-deficient mice to metabolic challenges are influenced more by cell turnover and proliferation, rather than direct metabolic-signalling based responses.

Chapter 6 –General Discussion.

6.1 General Discussion.

6.1.1 Biological impact of murine SMARCAD1 loss.

Mice lacking SMARCAD1 demonstrate a number of phenotypic features compared to control mice: fewer viable female -/- offspring are produced than males; in males, there is a difference in body mass over time, an increase in serum triglycerides and free fatty acids, increasing liver size over time, an increase in the number of adipose-tissue resident macrophages and a loss in intestinal intraepithelial lymphocytes with age. Some of these observations are in agreement with a previous knockout model of *Smarcad1* (Schoor et al 1999), in which the numbers of viable -/- offspring were reduced and surviving -/- mice weighed less than +/+ or +/- littermates. Indeed, the phenotype of +/+ and +/- mice were reported to be similar, and results from this thesis suggest that the level of SMARCAD1 peptide produced or resident in murine tissues is equivalent between heterozygous +/- and homozygous +/+ mice.

While the cause of the reduced number of *Smarcad1*-/- offspring was not investigated during this study, it is possible that other factors linked to peri- or pre-natal mortality from other mouse models can provide clues as to what underlies this loss. For example, genes on the X-chromosome are normally dosage controlled in females, whereby a number of genes are epigenetically silenced during widespread heterochromatin formation across one of the X-chromosomes (known as X-inactivation) (Lyon, 1961; Sidhu, Minks, Chang, Cotton, & Brown, 2008). Loss of this control can be lethal during embryonic development; indeed, mice generated that produced offspring unable to inactivate the X-chromosome were also unable to produce viable female offspring (which died early in embryonic development) (Marahrens, Panning, Dausman, Strauss, & Jaenisch, 1997). Given the link to heterochromatin with SMARCAD1 – and furthermore the binding of SMARCAD1 to PARP1 (Rowbotham et al 2011) which itself has been shown as an important factor in X-inactivation (Menissier de Murcia et al., 2003) – it is possible that the loss of SMARCAD1 impacts X-inactivation, thereby reducing the number of viable female offspring.

In the absence of a mechanistic link to X-inactivation, other factors (e.g. metabolic factors) may underpin perinatal lethality. As an example, non-shivering thermogenesis generated by brown adipose tissue (BAT) is critical to neonatal survival. Mice with

defects in BAT function are prone to neonatal hypothermia and mortality (Charalambous et al., 2012). As differences in white adipose tissue-related metabolism are apparent in *Smarcad1*-/-mice, it is possible that BAT-related function is also abnormal. Investigation of BAT in *Smarcad1*-/- mice vs controls would provide insight into this as a possible mechanism for perinatal mortality and later onset characteristics.

Other phenotypic features of this *Smarcad1* knockout model were noted but not investigated within this study, for example *Smarcad1*-/- males have smaller testes than control male mice. It should not be discounted that this may influence aspects of the phenotype reported in this study, i.e. it is likely that *Smarcad1*-/- males have lower serum levels of testosterone than +/+ mice, which is known to impact fat metabolism and the immune system. A number of studies have shown that reduced testosterone levels are linked to obesity (Fui, Dupuis, & Grossmann, 2014), and there is evidence that testosterone itself antagonizes adipogenesis (Zerradi, Dereumetz, Boulet, & Tchernof, 2014). A number of other studies have linked androgens (such as testosterone) to immune suppression - including suppressed antibody responses, inflammatory responses and B- and T-cell development (Trigunaite et al 2015). However, as lower testosterone levels in *Smarcad1*-/- mice is likely, this would more likely increase numbers of immune cells/immune cell subsets, which was not observed. In either case, future experiments using testosterone supplementation would help to address the role of testosterone in the phenotype of these knockout mice.

6.1.2 Logistical limitations and *Smarcad1*-/- mice experimental groups.

With the large number of mice required in each experimental group e.g. for iIEL studies, the development of a new genotyping method to allow increased sample turnover was essential for efficient colony management. The design of a new genotyping PCR strategy with primer pairs designed for a <700bp amplicon provided a robust assay applicable to crude DNA extracts (such as NaOH extracted DNA from neonatal ear-punches). However, as fewer *Smarcad1*-/- offspring were produced cf. *Smarcad1*+/+ or +/- mice, the production of large experimental groups and subsequent aging up to 1 year limited the number of experiments possible within the time and financial constraints of this project.

Interestingly, western blot analysis of *Smarcad1*+/+ and +/- mice suggested that peptide expression in muscle was equivalent irrespective of the gene copy number, although

expression in WAT, BAT and Pancreas mirrored the levels of cellular mRNA seen in the duodenum. A recent study investigating how far cellular mRNA levels influence peptide abundance within the cell (Liu et al 2016) noted that mRNA levels alone do not always predict protein levels, and additional factors (such as protein turnover) must be taken into account. Given the relative levels of SMARCAD1 peptide in +/+ vs +/- mice, future breeding strategies aimed at producing +/- and -/- litter mates may facilitate increased numbers of appropriate experimental groups.

6.1.3 Impact of SMARCAD1 loss on murine intestine IELs.

As mentioned, all areas studied within this thesis would have benefitted from increased sample numbers, especially for the study of gamma delta T-cell iIEL numbers. A shift in the number of γδ T-cells found in the spleen suggests that a systemic loss of γδ T-cells may occur with age in these mice. To understand better the origin of such loss, investigation of the thymus (in which key stages of T-cell development takes place) would provide insight into this source. The identification of SMARCAD1 expression in the thymus by western blot lends weight to the possibility that age-related changes in the thymus underpin any T-cell phenotype seen, although influences beyond the thymus should not be discounted.

The loss of intestinal IELs has been reported under a number of conditions, such as loss of an IEL survival factor (e.g. in *Ahr-/-* mice (Y. Li et al., 2011b)), metabolic challenge (e.g. high-fat diet, (Soares et al., 2015) dietary modification (da Silva Menezes et al., 2003) and a lack of interaction with the gut microbiota (Jiang et al., 2013). Although the thymus is key to development of the majority of T-cells, this may not be the case with iIELs, as athymic mice still harbour intestinal IEL T-cells (of which the majority are γδ T-cells ((Emoto, Emoto, Miyamoto, Yoshizawa, & Kaufmann, 2004; Hayday & Gibbons, 2008). Hence, while SMARCAD1 is highly expressed in the thymus, aberrations in thymic function may not be the cause of age-related IEL loss in *Smarcad1-/-* mice. Furthermore, as no significant difference was found in iIEL numbers after lymphocyte-intrinsic (CD2-Cre) loss of SMARCAD1, this would point toward any iIEL loss not being driven by cell intrinsic loss of SMARCAD1. On top of these results, as no clear cellular or microbiome-related differences were observed in the small intestine of SMARCAD1 mice, the underlying cause of age-related iIEL loss is not likely due to direct T-cell intrinsic or intestinal influences.

In this study no microbiome-related differences were found between the small intestines of *Smarcad1*+/+ and -/- mice; however, the approach used to quantify the microbial phyla (qPCR) was one of limited resolution, and therefore provides only a gross overview of the populations present (Fierer, Jackson, Vilgalys, & Jackson, 2005). More subtle population changes cannot be ruled out, and hence deeper investigation of gut microbiota using next generation sequencing based strategies may unveil such differences previously overlooked (see Jovel et al., (2016) for a recent review). These could in themselves give clues as to the potential mechanism behind iIEL loss.

Another potential driving factor in the loss of iIELs is constant stimulation through the T-cell receptor, leading to activation induced cell-death (AICD). Upon activation (*via* T-cell receptor or CD3 co-receptor stimulation) γδ T-cells in the intestine undergo degranulation and cell death within 2-3 days (Ogata & Itoh, 2016). While AICD ensures clonal deletion of activated T-cells (and therefore prevents excessive immune-cell proliferation and inflammation), within the intestinal T-cell compartment this confers a "one-shot" response to immune challenge, as γδ T-cell iIELs do not undergo proliferation after stimulation and hence degranulate then die (Ogata, Ota, Nanno, Suzuki, & Itoh, 2014). As it was recently discovered that T-cells can be activated by self-lipids (de Jong, 2015), the potential exists that elevated serum lipids (such as those found in *Smarcad1*-/- mice) activate T-cells and lead to AICD in γδ T-cell iIELs.

The results from this study suggest that elevated serum lipids may contribute to iIEL loss in (aging) mice, hence it is clear that any future study must assess both the level of serum lipids in the context of age (and how these correlate to iIEL numbers), in addition to whether increased thymic atrophy also contributes to a natural drop in iIEL numbers at the same time. It is possible that an inability to replace lost/activated iIELs in *Smarcad1*-/- mice ultimately drives the observed phenotype.

6.1.4 Impact of SMARCAD1 loss on murine WAT biology.

Closer examination of physical characteristics such as body weight of *Smarcad1*-/- mice revealed little difference in weight up to the age of 16 weeks, and no difference was present at birth. However, the male *Smarcad1*-/- mice weighed significantly less five weeks after birth than +/+ counterparts, which reflects the difference seen in the

original *Etl1* knockout study (Schoor et al 1999), although the magnitude was ostensibly greater in the original study. However, other characteristics mark the metabolism of *Smarcad1*-/- mice; serum levels of triglycerides and free fatty acids are elevated, and there is an increase in the number of adipose tissue macrophages present. Together these data suggest that there is some white adipose tissue dysfunction in the absence of SMARCAD1, as the presence of macrophages is associated with adipocyte death and lipolysis. Isolation and enumeration of adipocyte stem cells revealed that there were no significant differences in the number of adipocyte stem cells present in this tissue, and analysis of flow-sorted fractions by western blot demonstrated that SMARCAD1 is expressed in putative ASC (Lin-ve/ CD29+ve/CD34+ve/Sca1+ve) cells, with higher expression in the Lineage +ve fraction (likely from leukocytes). Subsequent culture and differentiation produced no significant difference in the adipogenic potential of these ASCs between *Smarcad1*+/+ and -/- mice. Any differences observed in white adipose tissue between *Smarcad1*+/+ and -/- mice are likely to either arise from the non-adipocyte stem cell fraction (i.e. the stem cell niche) or other mechanisms aside of differentiation (e.g. proliferation or loss of potency).

Interestingly, mice lacking SMARCAD1 challenged with a 60% high fat diet mice showed an increase in weight gain compared to +/+ counterparts, associated with a significant increase in the size of subcutaneous WAT. Examination of the size of adipocytes from high fat diet fed and normal chow mice suggest that there are no differences in the size of adipocytes (and hence adipogenesis) between +/+ and -/- mice. This implies that any differences observed are due to increased numbers of adipocytes within the tissue (cell hyperplasia) and again suggests that mechanisms outside of differentiation are responsible for phenotypic differences observed.

To try to shed further light on the cellular changes brought about by the absence of SMARCAD1, mouse embryonic fibroblasts derived from *Smarcad1*+/- and -/- mice were assayed for differentiation and proliferation. In agreement with ASC studies, no significant difference was observed in adipogenic potential between *Smarcad1*+/- and -/- MEFs. However, there was a decrease in proliferation seen between *Smarcad1*-/- derived MEFs over 72 hours, and examination of the cell cycle by FACS suggested that this was associated with an increase in -/- MEFS present (or retained) in S-phase. This could suggest that the supply of histones for newly synthesized/replicating DNA is affected in the absence of SMARCAD1, as a recent study revealed that histone supply

regulates transition through S-phase (Günesdogan et al., 2014). It should not be forgotten that SMARCAD1 is known to play a role in DNA-repair, and accumulation of DNA damage (in the absence of SMARCAD1) could also impact the cell cycle, as has been shown under other conditions of DNA damage (Barnum & O'Connell, 2014).

6.1.5 Molecular impact of SMARCAD1 loss.

Although the molecular impact of SMARCAD1 loss was not investigated in this study, a number of avenues remain available for future investigation. For example, the presence of the short isoform of SMARCAD1 in mice is yet to be confirmed, although it seems likely to be expressed in mouse given the conservation across species (Figure 16). In addition, the knockout approach used for this mouse model - targeting the catalytic ATPase domain of *Smarcad1* – may still leave a shorter, truncated isoform of *Smarcad1* retaining exons 1 to 11. Whether this truncated isoform is indeed produced and can still bind to the proteins known to form a complex with SMARCAD1 (such as HDAC1/2, KAP1, G9a) was not investigated within this study.

A number of other questions remains unanswered about SMARCAD1, for instance whether different complexes are formed with SMARCAD1 in different murine tissues such as the intestine and white adipose tissue. It is also possible that mutations in SMARCAD1 (or components that bind to SMARCAD1) drive inappropriate complex formation e.g. in cancer cells. Likewise, mutations in other factors present within a complex may drive the inappropriate sequestration of chromatin remodellers, leading to atypical remodelling of genomic loci within that cell type. Confirmation of remodelling complex components and related gene sequences would therefore address these possibilities.

The lack of reduction of H3K9me3 levels in *Smarcad1*-/- MEFs observed in this study follows the observation in mESCs also lacking functional SMARCAD1 (Xiao et al 2017). As noted by the authors, this may reflect a cell-type specific effect, and further investigation of the different complexes formed with SMARCAD1 in different cell types would confirm this point. It is highly possible that – given the spectrum of cellular/functional impact reported for SMARCAD1 – the exact molecular impact of SMARCAD1 is determined to a large degree by the subunits to which it is associated, and therefore what cell type and at what time-point this complex is formed.

6.1.6 Concluding points

The results described in this study point towards a WAT-metabolism phenotype of *Smarcad1-/-* mice, not related to changes in the microbiota. Furthermore, distal effects of this WAT-related phenotype may impact other factors such as γδ-T-cells, which can become activated by self-lipid. Of the γδ-T-cell types present in mouse, iIEL γδ-T-cells do not proliferate upon activation, and indeed apoptose within 3 days of activation - hence the loss observed in *Smarcad1-/-* mice may reflect a net loss with increasing serum fat content and reduced T-cell turnover/replacement during aging (e.g. due to thymic atrophy).

With respect to the mechanism underlying the WAT-related phenotype in *Smarcad1-/-* mice, the data presented in this study suggest a model where the loss of SMARCAD1 impacts cell turnover/proliferation rather than differentiation. The presence of elevated macrophage numbers in white adipose tissue implicate an increase in (adipocyte) cell death, white the reported expression of SMARCAD1 in stem cells would suggest that dysregulation of stem cell potency may underpin any tissue-related phenotype(s) seen. Further investigation (e.g. of adipocyte/mesenchymal stem cell) would clarify this point.

6.1.7 Proposed model for loss of SMARCAD1 impact.

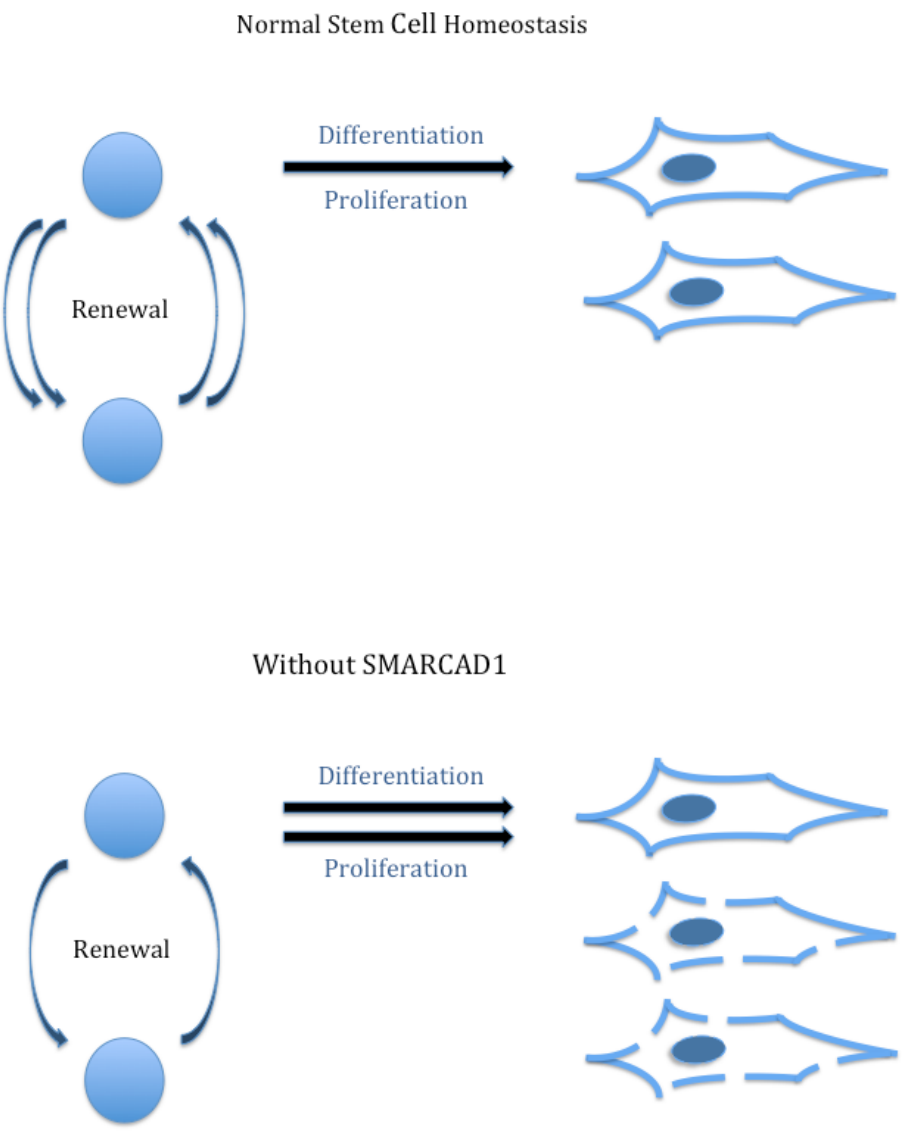

Figure 6.1. Proposed model for mechanisms underlying SMARCAD1 impact. In the absence of SMARCAD1, tissue stem cells do not retail potency or self-renew as efficiently, and instead will prematurely differentiate or proliferate. It would be possible that excess differentiated or prematurely proliferative cells apoptose and are cleared by resident macrophages. Tissue resident stem cell numbers would be maintained by the influx of new pluripotent stem cells to maintain the homeostasis.

6.2 Future studies.

A number of questions remain about the impact of SMARCAD1 on murine intestinal intraepithelial lymphocytes and white adipose tissue biology. Future studies could provide invaluable insight into these:-

- Confirmation of the expression of the short isoform of *Smarcad1* in mouse would provide more evidence for a conserved function of *Smarcad1* across species. Isolation of RNA from murine skin and cloning/PCR based methods would potentially confirm this.

- The expression of a truncated form of *Smarcad1* (from the ATPase domain deleted mouse model) and subsequent interaction with known binding partners should be investigated. Bands of a similar size to the potential truncated form of SMARCAD1 (~100kDa) are regularly visible on α-SMARCAD1 probed western blots. Immunoprecipitation of SMARCAD1 (using available antibodies to the N-terminal domain) and subsequent western blot for known binding partners (such as HDAC1/2, G9a and KAP1) using murine k/o cells would confirm these interactions are truly ablated.

- To investigate further the age-related loss of iIELs, a large cohort of mice aged >1 year would allow investigation of any thymus phenotype at this time point, such cell death/turnover. EdU incorporation would allow investigation of cell proliferation within the aged thymus, and simple measures of thymic size would show whether premature thymic atrophy occurs in *Smarcad1*-/- mice. The relative proportions of αβ to γδ T-cells by FACS would give some insight into whether thymic selection is affected at this age.

  (It should be noted that athymic mice still harbour iIELs, and the developmental routes and origin of iIELs is unclear, although it is likely that the thymus is still largely influential in iIEL development).

- Investigation of cell death in *ex-vivo* cells and cell cultures lacking SMARCAD1 may give insight into whether cell turnover and/or stem cell survival is affected. This could be done rapidly with a fluorescein-labelled dUTP FACS application to the TUNEL reaction (Terminal deoxynucleotidyl transferase (TdT) dUTP Nick-End Labeling).

- The loss of potency of adipocyte stem cells could be investigate by *ex-vivo* culture and simple qPCR screening for a known preadipocyte marker (such as *Dlk-1*)

- Any transcriptomic impact of the lack of SMARCAD1 on murine ASCs should be investigated, although large numbers of mice are required to provide enough material RNA-seq (typically <5000 ASCs are isolated from each fat pad).

- Co-culture experiments by combining different flow-sorted cell types from the stromal vascular fraction of white adipose tissue would give insight into how influential the niche is in adipocyte differentiation /adipogenesis.

- Longer term aging studies on *Smarcad1*-/- mice would give insight into the impact of SMARCAD1 on mortality (e.g. do *Smarcad1*-/- mice die younger than +/+ counterparts?) and whether numbers of tissue-resident stem cells decline earlier in these knockout mice.

- IP:Mass spectrometry to determine the subunit makeup of any SMARCAD1 complex in specific cell types.

References.

Adra, C. N., Donato, J.-L., Badovinac, R., Syed, F., Kheraj, R., Cai, H., … Drews, R. (2000). SMARCAD1, a Novel Human Helicase Family-Defining Member Associated with Genetic Instability: Cloning, Expression, and Mapping to 4q22–q23, a Band Rich in Breakpoints and Deletion Mutants Involved in Several Human Diseases. *Genomics*, *69*(2), 162–173. https://doi.org/10.1006/geno.2000.6281

Aihara, H., Nakagawa, T., Yasui, K., Ohta, T., Hirose, S., Dhomae, N., … Ito, T. (2004). Nucleosomal histone kinase-1 phosphorylates H2A Thr 119 during mitosis in the early Drosophila embryo. *Genes & Development*, *18*(8), 877–888. https://doi.org/10.1101/gad.1184604

Al Kubaisy, E., Arafat, K., De Wever, O., Hassan, A. H., & Attoub, S. (2016). SMARCAD1 knockdown uncovers its role in breast cancer cell migration, invasion, and metastasis. *Expert Opinion on Therapeutic Targets*, *20*(9), 1035–1043. https://doi.org/10.1080/14728222.2016.1195059

ALLFREY, V. G., FAULKNER, R., & MIRSKY, A. E. (1964). ACETYLATION AND METHYLATION OF HISTONES AND THEIR POSSIBLE ROLE IN THE REGULATION OF RNA SYNTHESIS. *Proceedings of the National Academy of Sciences of the United States of America*, *51*, 786–94. Retrieved from http://www.ncbi.nlm.nih.gov/pubmed/14172992

Apidianakis, Y., & Rahme, L. G. (2011). Drosophila melanogaster as a model for human intestinal infection and pathology. *Disease Models & Mechanisms*, *4*(1), 21–30. https://doi.org/10.1242/dmm.003970

Bäckhed, F., Manchester, J. K., Semenkovich, C. F., & Gordon, J. I. (2007). Mechanisms underlying the resistance to diet-induced obesity in germ-free mice. *Proceedings of the National Academy of Sciences*, *104*(3), 979–984. https://doi.org/10.1073/pnas.0605374104

Balachandran, S., Thomas, E., & Barber, G. N. (2004). A FADD-dependent innate immune mechanism in mammalian cells. *Nature*, *432*(7015), 401–405. https://doi.org/10.1038/nature03124

Bannister, A. J., & Kouzarides, T. (2011). Regulation of chromatin by histone modifications. *Cell Research*, *21*(3), 381–95. https://doi.org/10.1038/cr.2011.22

Bansal, S. K., Gupta, N., Sankhwar, S. N., & Rajender, S. (2015). Differential Genes Expression between Fertile and Infertile Spermatozoa Revealed by Transcriptome Analysis. *PloS One*, *10*(5), e0127007. https://doi.org/10.1371/journal.pone.0127007

Bao, X., Tang, J., Lopez-Pajares, V., Tao, S., Qu, K., Crabtree, G. R., & Khavari, P. A. (2013). ACTL6a Enforces the Epidermal Progenitor State by Suppressing SWI/SNF-Dependent Induction of KLF4. *Cell Stem Cell*, *12*(2), 193–203. https://doi.org/10.1016/j.stem.2012.12.014

Bao, Y., & Shen, X. (2007). INO80 subfamily of chromatin remodeling complexes. *Mutation Research*, *618*(1–2), 18–29. https://doi.org/10.1016/j.mrfmmm.2006.10.006

Barker, N., van Es, J. H., Kuipers, J., Kujala, P., van den Born, M., Cozijnsen, M., … Clevers, H. (2007). Identification of stem cells in small intestine and colon by marker gene Lgr5. *Nature*, *449*(7165), 1003–1007. https://doi.org/10.1038/nature06196

Barnum, K. J., & O'Connell, M. J. (2014). Cell cycle regulation by checkpoints. *Methods in Molecular Biology (Clifton, N.J.)*, *1170*, 29–40. https://doi.org/10.1007/978-1-4939-0888-2_2

Benoit, Y. D., Lepage, M. B., Khalfaoui, T., Tremblay, É., Basora, N., Carrier, J. C., … Beaulieu, J.-F. (2012). Polycomb repressive complex 2 impedes intestinal cell terminal differentiation. *Journal of Cell Science*, *125*(14). Retrieved from http://jcs.biologists.org/content/125/14/3454.short

Berry, D. C., Stenesen, D., Zeve, D., & Graff, J. M. (2013). The developmental origins of adipose tissue. *Development*, *140*(19), 3939–3949. https://doi.org/10.1242/dev.080549

Bevilacqua, A., Willis, M. S., & Bultman, S. J. (2014). SWI/SNF chromatin-remodeling complexes in cardiovascular development and disease. *Cardiovascular Pathology : The Official Journal of the Society for Cardiovascular Pathology*, *23*(2), 85–91. https://doi.org/10.1016/j.carpath.2013.09.003

Boismenu, R., & Havran, W. L. (1994). Modulation of epithelial cell growth by intraepithelial gamma delta T cells. *Science (New York, N.Y.)*, *266*(5188), 1253–5. Retrieved from http://www.ncbi.nlm.nih.gov/pubmed/7973709

Boyer, L. A., Latek, R. R., & Peterson, C. L. (2004). Opinion: The SANT domain: a unique histone-tail-binding module? *Nature Reviews Molecular Cell Biology*, *5*(2), 158–163. https://doi.org/10.1038/nrm1314

Boyer, L. A., Lee, T. I., Cole, M. F., Johnstone, S. E., Levine, S. S., Zucker, J. P., … Young, R. A. (2005). Core Transcriptional Regulatory Circuitry in Human Embryonic Stem Cells. *Cell*, *122*(6), 947–956. https://doi.org/10.1016/j.cell.2005.08.020

Brown, K., DeCoffe, D., Molcan, E., & Gibson, D. L. (2012). Diet-Induced Dysbiosis of the Intestinal Microbiota and the Effects on Immunity and Disease. *Nutrients*, *4*(12), 1095–1119. https://doi.org/10.3390/nu4081095

Buenrostro, J. D., Wu, B., Chang, H. Y., Greenleaf, W. J., Buenrostro, J. D., Wu, B., … Greenleaf, W. J. (2015). ATAC-seq: A Method for Assaying Chromatin Accessibility Genome-Wide. In *Current Protocols in Molecular Biology* (p. 21.29.1-21.29.9). Hoboken, NJ, USA: John Wiley & Sons, Inc. https://doi.org/10.1002/0471142727.mb2129s109

Bultman, S., Gebuhr, T., Yee, D., La Mantia, C., Nicholson, J., Gilliam, A., … Magnuson, T. (2000). A Brg1 null mutation in the mouse reveals functional differences among mammalian SWI/SNF complexes. *Molecular Cell*, *6*(6), 1287–95. Retrieved from http://www.ncbi.nlm.nih.gov/pubmed/11163203

Cai, Y., Jin, J., Yao, T., Gottschalk, A. J., Swanson, S. K., Wu, S., … Conaway, J. W. (2007). YY1 functions with INO80 to activate transcription. *Nature Structural & Molecular Biology*, *14*(9), 872–874. https://doi.org/10.1038/nsmb1276

Camp, J. G., Frank, C. L., Lickwar, C. R., Guturu, H., Rube, T., Wenger, A. M., … Rawls, J. F. (2014). Microbiota modulate transcription in the intestinal epithelium without remodeling the accessible chromatin landscape. *Genome Research*, *24*(9), 1504–16. https://doi.org/10.1101/gr.165845.113

Cawthorn, W. P., Scheller, E. L., & MacDougald, O. A. (2012). Adipose tissue stem cells meet preadipocyte commitment: going back to the future. *Journal of Lipid Research*, *53*(2), 227–246. https://doi.org/10.1194/jlr.R021089

Cetin, E., Cengiz, B., Gunduz, E., Gunduz, M., Nagatsuka, H., Bekir-Beder, L., … Nagai, N. (2008). Deletion mapping of chromosome 4q22-35 and identification of four frequently deleted regions in head and neck cancers. *Neoplasma*, *55*(4), 299–304. Retrieved from http://www.ncbi.nlm.nih.gov/pubmed/18505340

Charalambous, M., Ferron, S. R., da Rocha, S. T., Murray, A. J., Rowland, T., Ito, M., … Ferguson-Smith, A. C. (2012). Imprinted gene dosage is critical for the transition to independent life. *Cell Metabolism*, *15*(2), 209–21. https://doi.org/10.1016/j.cmet.2012.01.006

Cheroutre, H., Lambolez, F., & Mucida, D. (2011). The light and dark sides of intestinal intraepithelial lymphocytes. *Nature Reviews. Immunology*, *11*(7), 445–56. https://doi.org/10.1038/nri3007

Chi, T. H., Wan, M., Lee, P. P., Akashi, K., Metzger, D., Chambon, P., … Crabtree, G. R. (2003). Sequential Roles of Brg, the ATPase Subunit of BAF Chromatin Remodeling Complexes, in Thymocyte Development. *Immunity*, *19*(2), 169–182. https://doi.org/10.1016/S1074-7613(03)00199-7

Chi, T. H., Wan, M., Zhao, K., Taniuchi, I., Chen, L., Littman, D. R., & Crabtree, G. R. (2002). Reciprocal regulation of CD4/CD8 expression by SWI/SNF-like BAF complexes. *Nature*, *418*(6894), 195–199. https://doi.org/10.1038/nature00876

Chiba, T., Saito, T., Yuki, K., Zen, Y., Koide, S., Kanogawa, N., … Yokosuka, O. (2015). Histone lysine methyltransferase SUV39H1 is a potent target for epigenetic therapy of hepatocellular carcinoma. *International Journal of Cancer*, *136*(2), 289–298. https://doi.org/10.1002/ijc.28985

Choi, J., Ko, M., Jeon, S., Jeon, Y., Park, K., Lee, C., … Seong, R. H. (2012). The SWI/SNF-like BAF Complex Is Essential for Early B Cell Development. *The Journal of Immunology*, *188*(8), 3791–3803. https://doi.org/10.4049/jimmunol.1103390

Christophorou, M. A., Castelo-Branco, G., Halley-Stott, R. P., Oliveira, C. S., Loos, R., Radzisheuskaya, A., … Kouzarides, T. (2014). Citrullination regulates pluripotency and histone H1 binding to chromatin. *Nature*, *507*(7490), 104–108. https://doi.org/10.1038/nature12942

Chung, C. C., Kanetsky, P. A., Wang, Z., Hildebrandt, M. A. T., Koster, R., Skotheim, R. I., … Nathanson, K. L. (2013). Meta-analysis identifies four new loci associated with testicular germ cell tumor. *Nature Genetics*, *45*(6), 680–5. https://doi.org/10.1038/ng.2634

Chung, H., Pamp, S. J., Hill, J. A., Surana, N. K., Edelman, S. M., Troy, E. B., … Kasper, D. L. (2012). Gut Immune Maturation Depends on Colonization with a Host-Specific Microbiota. *Cell*, *149*(7), 1578–1593. https://doi.org/10.1016/j.cell.2012.04.037

Church, C. D., Berry, R., & Rodeheffer, M. S. (2014). Isolation and study of adipocyte precursors. *Methods in Enzymology*, *537*, 31–46. https://doi.org/10.1016/B978-0-12-411619-1.00003-3

Clapier, C. R., Kasten, M. M., Parnell, T. J., Sirinakis, G., Zhang, Y., Cairns Correspondence, B. R., … Cairns, B. R. (2016). Regulation of DNA Translocation Efficiency within the Chromatin Remodeler RSC/Sth1 Potentiates Nucleosome Sliding and Ejection. *Molecular Cell*, *62*, 453–461. https://doi.org/10.1016/j.molcel.2016.03.032

Clevers, H., & Batlle, E. (2013). SnapShot: the intestinal crypt. *Cell*, *152*(5), 1198–1198.e2. https://doi.org/10.1016/j.cell.2013.02.030

Costelloe, T., Louge, R., Tomimatsu, N., Mukherjee, B., Martini, E., Khadaroo, B., … Llorente, B. (2012a). The yeast Fun30 and human SMARCAD1 chromatin remodellers promote DNA end resection. *Nature*, *489*(7417), 581–584. https://doi.org/10.1038/nature11353

Costelloe, T., Louge, R., Tomimatsu, N., Mukherjee, B., Martini, E., Khadaroo, B., … Llorente, B. (2012b). The yeast Fun30 and human SMARCAD1 chromatin remodellers promote DNA end resection. *Nature*, *489*(7417), 581–4. https://doi.org/10.1038/nature11353

Cronin, S. J. F., Nehme, N. T., Limmer, S., Liegeois, S., Pospisilik, J. A., Schramek, D., … Penninger, J. M. (2009). Genome-wide RNAi screen identifies genes involved in intestinal pathogenic bacterial infection. *Science (New York, N.Y.)*, *325*(5938), 340–3. https://doi.org/10.1126/science.1173164

Cuaranta-Monroy, I., Simandi, Z., Kolostyak, Z., Doan-Xuan, Q.-M., Poliska, S., Horvath, A., … Nagy, L. (2014). Highly efficient differentiation of embryonic stem cells into adipocytes by ascorbic acid. *Stem Cell Research*, *13*(1), 88–97. https://doi.org/10.1016/j.scr.2014.04.015

da Silva Menezes, J., de Sousa Mucida, D., Cara, D. C., Alvarez-Leite, J. I., Russo, M., Vaz, N. M., & de Faria, A. M. C. (2003). Stimulation by food proteins plays a critical role in the maturation of the immune system. *International Immunology*, *15*(3), 447–455. https://doi.org/10.1093/intimm/dxg043

Dang, W., & Bartholomew, B. (2007). Domain architecture of the catalytic subunit in the ISW2-nucleosome complex. *Molecular and Cellular Biology*, *27*(23), 8306–17. https://doi.org/10.1128/MCB.01351-07

Dastagir, K., Reimers, K., Lazaridis, A., Jahn, S., Maurer, V., Strauß, S., … Vogt, P. M. (2014). Murine embryonic fibroblast cell lines differentiate into three mesenchymal lineages to different extents: new models to investigate differentiation processes. *Cellular Reprogramming*, *16*(4), 241–52. https://doi.org/10.1089/cell.2014.0005

Davie, J. R. (2003). Inhibition of histone deacetylase activity by butyrate. *The Journal of Nutrition*, *133*(7 Suppl), 2485S–2493S. Retrieved from http://www.ncbi.nlm.nih.gov/pubmed/12840228

de Jong, A. (2015). Activation of human T cells by CD1 and self-lipids. *Immunological Reviews*, *267*(1), 16–29. https://doi.org/10.1111/imr.12322

de la Serna, I. L., Ohkawa, Y., & Imbalzano, A. N. (2006). Chromatin remodelling in mammalian differentiation: lessons from ATP-dependent remodellers. *Nature Reviews Genetics*, *7*(6), 461–473. https://doi.org/10.1038/nrg1882

de Santa Barbara, P., van den Brink, G. R., & Roberts, D. J. (2003). Development and differentiation of the intestinal epithelium. *Cellular and Molecular Life Sciences : CMLS*, *60*(7), 1322–32. https://doi.org/10.1007/s00018-003-2289-3

den Besten, G., van Eunen, K., Groen, A. K., Venema, K., Reijngoud, D.-J., & Bakker, B. M. (2013). The role of short-chain fatty acids in the interplay between diet, gut microbiota, and host energy metabolism. *Journal of Lipid Research*, *54*(9), 2325–40. https://doi.org/10.1194/jlr.R036012

Densham, R. M., Garvin, A. J., Stone, H. R., Strachan, J., Baldock, R. A., Daza-Martin, M., … Morris, J. R. (2016). Human BRCA1–BARD1 ubiquitin ligase activity counteracts chromatin barriers to DNA resection. *Nature Structural & Molecular Biology*, *23*(7), 647–655. https://doi.org/10.1038/nsmb.3236

Denslow, S. A., & Wade, P. A. (2007). The human Mi-2/NuRD complex and gene regulation. *Oncogene*, *26*(37), 5433–5438. https://doi.org/10.1038/sj.onc.1210611

Devine, W. P., Wythe, J. D., George, M., Koshiba-Takeuchi, K., & Bruneau, B. G. (2014). Early patterning and specification of cardiac progenitors in gastrulating mesoderm. *eLife*, *3*. https://doi.org/10.7554/eLife.03848

Dheer, R., Santaolalla, R., Davies, J. M., Lang, J. K., Phillips, M. C., Pastorini, C., … Abreu, M. T.

(2016). Intestinal Epithelial Toll-Like Receptor 4 Signaling Affects Epithelial Function and Colonic Microbiota and Promotes a Risk for Transmissible Colitis. *Infection and Immunity*, *84*(3), 798–810. https://doi.org/10.1128/IAI.01374-15

do Valle, T. Z., Billecocq, A., Guillemot, L., Alberts, R., Gommet, C., Geffers, R., … Panthier, J.-J. (2010). A New Mouse Model Reveals a Critical Role for Host Innate Immunity in Resistance to Rift Valley Fever. *The Journal of Immunology*, *185*(10), 6146–6156. https://doi.org/10.4049/jimmunol.1000949

Doiguchi, M., Nakagawa, T., Imamura, Y., Yoneda, M., Higashi, M., Kubota, K., … Ito, T. (2016). SMARCAD1 is an ATP-dependent stimulator of nucleosomal H2A acetylation via CBP, resulting in transcriptional regulation. *Scientific Reports*, *6*, 20179. https://doi.org/10.1038/srep20179

Edwards, C. A., Mungall, A. J., Matthews, L., Ryder, E., Gray, D. J., Pask, A. J., … Ferguson-Smith, A. C. (2008). The Evolution of the DLK1-DIO3 Imprinted Domain in Mammals. *PLoS Biology*, *6*(6), e135. https://doi.org/10.1371/journal.pbio.0060135

Emoto, Y., Emoto, M., Miyamoto, M., Yoshizawa, I., & Kaufmann, S. H. E. (2004). Functionally active CD8alphabeta+ TCRgammadelta intestinal intraepithelial lymphocytes in athymic nu/nu mice. *International Immunology*, *16*(1), 111–7. Retrieved from http://www.ncbi.nlm.nih.gov/pubmed/14688066

Fava, S. (2014). Glucagon-like peptide 1 and the cardiovascular system. *Current Diabetes Reviews*, *10*(5), 302–10. Retrieved from http://www.ncbi.nlm.nih.gov/pubmed/25360712

Ferreira, C., & Veldhoen, M. (2012a). Host and Microbes Date Exclusively. *Cell*, *149*(7), 1428–1430. https://doi.org/10.1016/j.cell.2012.06.005

Ferreira, C., & Veldhoen, M. (2012b). Host and microbes date exclusively. *Cell*, *149*(7), 1428–30. https://doi.org/10.1016/j.cell.2012.06.005

Fierer, N., Jackson, J. A., Vilgalys, R., & Jackson, R. B. (2005). Assessment of Soil Microbial Community Structure by Use of Taxon-Specific Quantitative PCR Assays. *Applied and Environmental Microbiology*, *71*(7), 4117–4120. https://doi.org/10.1128/AEM.71.7.4117-4120.2005

Filippakopoulos, P., & Knapp, S. (2012). The bromodomain interaction module. *FEBS Letters*, *586*(17), 2692–2704. https://doi.org/10.1016/j.febslet.2012.04.045

Fong, A. P., Yao, Z., Zhong, J. W., Cao, Y., Ruzzo, W. L., Gentleman, R. C., & Tapscott, S. J. (2012). Genetic and epigenetic determinants of neurogenesis and myogenesis. *Developmental Cell*, *22*(4), 721–35. https://doi.org/10.1016/j.devcel.2012.01.015

Fui, M. N. T., Dupuis, P., & Grossmann, M. (2014). Lowered testosterone in male obesity: mechanisms, morbidity and management. *Asian Journal of Andrology*, *16*(2), 223–31. https://doi.org/10.4103/1008-682X.122365

Funicello, M., Novelli, M., Ragni, M., Vottari, T., Cocuzza, C., Soriano-Lopez, J., … Maffei, M. (2007). Cathepsin K null mice show reduced adiposity during the rapid accumulation of fat stores. *PloS One*, *2*(8), e683. https://doi.org/10.1371/journal.pone.0000683

Furuse, M., Hata, M., Furuse, K., Yoshida, Y., Haratake, A., Sugitani, Y., … Tsukita, S. (2002). Claudin-based tight junctions are crucial for the mammalian epidermal barrier. *The Journal of Cell Biology*, *156*(6). Retrieved from http://jcb.rupress.org/content/156/6/1099?ijkey=64962c95d740e72c0b437ab233cf530db5b646d3&keytype2=tf_ipsecsha

Gicquel, C., Weiss, J., Amiel, J., Gaston, V., Le Bouc, Y., & Scott, C. D. (2004). Epigenetic abnormalities of the mannose-6-phosphate/ IGF2 receptor gene are uncommon in human overgrowth syndromes. *J Med Genet*, *41*. Retrieved from http://www.jmedgenet.com/cgi/content/full/41/1/e4

Günesdogan, U., Jäckle, H., & Herzig, A. (2014). Histone supply regulates S phase timing and cell cycle progression. *eLife*, *3*, e02443. https://doi.org/10.7554/eLife.02443

Haig, D. (2014). Frugal fat or munificent muscle: genomic imprinting and metabolism. *BMC Biology*, *12*, 772. https://doi.org/10.1186/s12915-014-0104-2

Hauge, S., Madhun, A. S., Cox, R. J., Brokstad, K. A., & Haaheim, L. R. (2007). A comparison of the humoral and cellular immune responses at different immunological sites after split influenza virus vaccination of mice. *Scandinavian Journal of Immunology*, *65*(1), 14–21. https://doi.org/10.1111/j.1365-3083.2006.01862.x

Hayday, A. Findly, R.C. Plehn-Dujowich, D. Viney, J.L. Owen, M.J. Roberts, S. J. (1994). Intraepithelial T cells in natural infection and in coeliac disease: protectors of epithelial

integrity and mediators of immune regulation. In *6th International Proceedings on Coeliac Disease.* (pp. 46–57).

Hayday, A., & Gibbons, D. (2008). Brokering the peace: the origin of intestinal T cells. *Mucosal Immunology*, *1*(3), 172–174. https://doi.org/10.1038/mi.2008.8

Hayday, A., Theodoridis, E., Ramsburg, E., & Shires, J. (2001). Intraepithelial lymphocytes: exploring the Third Way in immunology. *Nature Immunology*, *2*(11), 997–1003. https://doi.org/10.1038/ni1101-997

Ho, L., Jothi, R., Ronan, J. L., Cui, K., Zhao, K., & Crabtree, G. R. (2009). An embryonic stem cell chromatin remodeling complex, esBAF, is an essential component of the core pluripotency transcriptional network. *Proceedings of the National Academy of Sciences*, *106*(13), 5187–5191. https://doi.org/10.1073/pnas.0812888106

Ho, L., Ronan, J. L., Wu, J., Staahl, B. T., Chen, L., Kuo, A., … Crabtree, G. R. (2009). An embryonic stem cell chromatin remodeling complex, esBAF, is essential for embryonic stem cell self-renewal and pluripotency. *Proceedings of the National Academy of Sciences*, *106*(13), 5181–5186. https://doi.org/10.1073/pnas.0812889106

Holik, A. Z., Krzystyniak, J., Young, M., Richardson, K., Jardé, T., Chambon, P., … Clarke, A. R. (2013). Brg1 is required for stem cell maintenance in the murine intestinal epithelium in a tissue-specific manner. *STEM CELLS*, *31*(11), 2457–2466. https://doi.org/10.1002/stem.1498

Hong, F., Fang, F., He, X., Cao, X., Chipperfield, H., Xie, D., … Zhong, S. (2009). Dissecting Early Differentially Expressed Genes in a Mixture of Differentiating Embryonic Stem Cells. *PLoS Computational Biology*, *5*(12), e1000607. https://doi.org/10.1371/journal.pcbi.1000607

Hota, S. K., & Bruneau, B. G. (2016). ATP-dependent chromatin remodeling during mammalian development. *Development*, *143*(16). Retrieved from http://dev.biologists.org/content/143/16/2882

Huen, J., Kakihara, Y., Ugwu, F., Cheung, K. L. Y., Ortega, J., & Houry, W. A. (2010). Rvb1–Rvb2: essential ATP-dependent helicases for critical complexesThis paper is one of a selection of papers published in this special issue entitled 8th International Conference on AAA Proteins and has undergone the Journal's usual peer review process. *Biochemistry and Cell Biology*, *88*(1), 29–40. https://doi.org/10.1139/O09-122

Indra, A. K., Dupé, V., Bornert, J.-M., Messaddeq, N., Yaniv, M., Mark, M., … Metzger, D. (2005). Temporally controlled targeted somatic mutagenesis in embryonic surface ectoderm and fetal epidermal keratinocytes unveils two distinct developmental functions of BRG1 in limb morphogenesis and skin barrier formation. *Development*, *132*(20). Retrieved from http://dev.biologists.org/content/132/20/4533?ijkey=5c21e747fa1a6b5c5e79083902cf79a063dc7dc0&keytype2=tf_ipsecsha

Ito, T., Levenstein, M. E., Fyodorov, D. V., Kutach, A. K., Kobayashi, R., & Kadonaga, J. T. (1999). ACF consists of two subunits, Acf1 and ISWI, that function cooperatively in the ATP-dependent catalysis of chromatin assembly. *Genes and Development*, *13*(12), 1529–1539. https://doi.org/10.1101/gad.13.12.1529

Ivkovic, S., Yoon, B. S., Popoff, S. N., Safadi, F. F., Libuda, D. E., Stephenson, R. C., … Lyons, K. M. (2003). Connective tissue growth factor coordinates chondrogenesis and angiogenesis during skeletal development. *Development*, *130*(12). Retrieved from http://dev.biologists.org/content/130/12/2779?ijkey=735d4da5e36f35154daa2918f2268d8312b28d98&keytype2=tf_ipsecsha

Janeway, C. (2001). *Immunobiology 5 : the immune system in health and disease*. Garland Pub. Retrieved from https://www.ncbi.nlm.nih.gov/books/NBK10757/

Jiang, W., Wang, X., Zeng, B., Liu, L., Tardivel, A., Wei, H., … Zhou, R. (2013). Recognition of gut microbiota by NOD2 is essential for the homeostasis of intestinal intraepithelial lymphocytes. *The Journal of Experimental Medicine*, *210*(11), 2465–2476. https://doi.org/10.1084/jem.20122490

Jovel, J., Patterson, J., Wang, W., Hotte, N., O'Keefe, S., Mitchel, T., … Wong, G. K.-S. (2016). Characterization of the Gut Microbiome Using 16S or Shotgun Metagenomics. *Frontiers in Microbiology*, *7*, 459. https://doi.org/10.3389/fmicb.2016.00459

Kadam, S., & Emerson, B. M. (2003). Transcriptional Specificity of Human SWI/SNF BRG1 and BRM Chromatin Remodeling Complexes. *Molecular Cell*, *11*(2), 377–389. https://doi.org/10.1016/S1097-2765(03)00034-0

Kadoch, C., Copeland, R. A., & Keilhack, H. (2016). PRC2 and SWI/SNF Chromatin Remodeling

Complexes in Health and Disease. *Biochemistry*, *55*(11), 1600–1614. https://doi.org/10.1021/acs.biochem.5b01191

Kidder, B. L., Palmer, S., & Knott, J. G. (2009). SWI/SNF-Brg1 Regulates Self-Renewal and Occupies Core Pluripotency-Related Genes in Embryonic Stem Cells. *Stem Cells*, *27*(2), 317–328. https://doi.org/10.1634/stemcells.2008-0710

Kim, K. H., & Roberts, C. W. M. (2016). Targeting EZH2 in cancer. *Nature Medicine*, *22*(2), 128–134. https://doi.org/10.1038/nm.4036

Kim, Y. Z. (2014). Altered Histone Modifications in Gliomas. *Brain Tumor Research and Treatment*, *2*(1), 7. https://doi.org/10.14791/btrt.2014.2.1.7

Klose, R. J., Kallin, E. M., & Zhang, Y. (2006). JmjC-domain-containing proteins and histone demethylation. *Nature Reviews Genetics*, *7*(9), 715–727. https://doi.org/10.1038/nrg1945

Konev, A. Y., Tribus, M., Park, S. Y., Podhraski, V., Lim, C. Y., Emelyanov, A. V., … Fyodorov, D. V. (2007). CHD1 Motor Protein Is Required for Deposition of Histone Variant H3.3 into Chromatin in Vivo. *Science*, *317*(5841), 1087–1090. https://doi.org/10.1126/science.1145339

Kooistra, S. M., & Helin, K. (2012). Molecular mechanisms and potential functions of histone demethylases. *Nature Reviews Molecular Cell Biology*, *13*(5), 297–311. https://doi.org/10.1038/nrm3327

Kouzarides, T. (2007). Chromatin Modifications and Their Function. *Cell*, *128*(4), 693–705. https://doi.org/10.1016/j.cell.2007.02.005

Krasteva, V., Buscarlet, M., Diaz-Tellez, A., Bernard, M.-A., Crabtree, G. R., & Lessard, J. A. (2012). The BAF53a subunit of SWI/SNF-like BAF complexes is essential for hemopoietic stem cell function. *Blood*, *120*(24), 4720–4732. https://doi.org/10.1182/blood-2012-04-427047

Krautkramer, K. A., Kreznar, J. H., Romano, K. A., Vivas, E. I., Barrett-Wilt, G. A., Rabaglia, M. E., … al., et. (2016). Diet-Microbiota Interactions Mediate Global Epigenetic Programming in Multiple Host Tissues. *Molecular Cell*, *64*(5), 982–992. https://doi.org/10.1016/j.molcel.2016.10.025

Ku, S. K., Sung, S. H., Choung, J. J., Choi, J.-S., Shin, Y. K., & Kim, J. W. (2016). Anti-obesity and anti-diabetic effects of a standardized potato extract in ob/ob mice. *Experimental and Therapeutic Medicine*, *12*(1), 354–364. https://doi.org/10.3892/etm.2016.3256

Kurisaki, A., Hamazaki, T. S., Okabayashi, K., Iida, T., Nishine, T., Chonan, R., … Sugino, H. (2005). Chromatin-related proteins in pluripotent mouse embryonic stem cells are downregulated after removal of leukemia inhibitory factor. *Biochemical and Biophysical Research Communications*, *335*(3), 667–675. https://doi.org/10.1016/j.bbrc.2005.07.128

Lalani, S. R., Safiullah, A. M., Fernbach, S. D., Harutyunyan, K. G., Thaller, C., Peterson, L. E., … Belmont, J. W. (2006). Spectrum of CHD7 Mutations in 110 Individuals with CHARGE Syndrome and Genotype-Phenotype Correlation. *The American Journal of Human Genetics*, *78*(2), 303–314. https://doi.org/10.1086/500273

Landschoot, L. (2014). Regulation of the Kcnq1ot1 Imprinting Domain in Mouse. *Electronic Thesis and Dissertation Repository*. Retrieved from http://ir.lib.uwo.ca/etd/2382

Längst, G., & Manelyte, L. (2015). Chromatin Remodelers: From Function to Dysfunction. *Genes*, *6*(2), 299–324. https://doi.org/10.3390/genes6020299

LeBlanc, S. E., Wu, Q., Lamba, P., Sif, S., & Imbalzano, A. N. (2016). Promoter-enhancer looping at the PPARγ2 locus during adipogenic differentiation requires the Prmt5 methyltransferase. *Nucleic Acids Research*, *44*(11), 5133–47. https://doi.org/10.1093/nar/gkw129

Lee, K., Villena, J. A., Moon, Y. S., Kim, K.-H., Lee, S., Kang, C., & Sul, H. S. (2003). Inhibition of adipogenesis and development of glucose intolerance by soluble preadipocyte factor–1 (Pref-1). *Journal of Clinical Investigation*, *111*(4), 453–461. https://doi.org/10.1172/JCI15924

Lei, Y. (2013). Generation and Culture of Mouse Embryonic Fibroblasts. In *Methods in molecular biology (Clifton, N.J.)* (Vol. 1031, pp. 59–64). https://doi.org/10.1007/978-1-62703-481-4_7

Lessard, J., Wu, J. I., Ranish, J. A., Wan, M., Winslow, M. M., Staahl, B. T., … Crabtree, G. R. (2007). An essential switch in subunit composition of a chromatin remodeling complex during neural development. *Neuron*, *55*(2), 201–15. https://doi.org/10.1016/j.neuron.2007.06.019

Li, M., Wang, J., Li, Z., Zhang, J., Ni, C., Cheng, R., & Yao, Z. (2016). Genome-wide linkage analysis and whole-genome sequencing identify a recurrent SMARCAD1 variant in a unique Chinese family with Basan syndrome. *European Journal of Human Genetics*, *24*(9), 1367–1370. https://doi.org/10.1038/ejhg.2016.15

Li, Y., Innocentin, S., Withers, D. R., Roberts, N. A., Gallagher, A. R., Grigorieva, E. F., … Veldhoen, M. (2011a). Exogenous Stimuli Maintain Intraepithelial Lymphocytes via Aryl Hydrocarbon Receptor Activation. *Cell*, *147*(3), 629–640. https://doi.org/10.1016/j.cell.2011.09.025

Li, Y., Innocentin, S., Withers, D. R., Roberts, N. A., Gallagher, A. R., Grigorieva, E. F., … Veldhoen, M. (2011b). Exogenous stimuli maintain intraepithelial lymphocytes via aryl hydrocarbon receptor activation. *Cell*, *147*(3), 629–40. https://doi.org/10.1016/j.cell.2011.09.025

Llames, S., García-Pérez, E., Meana, Á., Larcher, F., & del Río, M. (2015). Feeder Layer Cell Actions and Applications. *Tissue Engineering. Part B, Reviews*, *21*(4), 345–53. https://doi.org/10.1089/ten.TEB.2014.0547

Luger, K., Mä, A. W., Richmond, R. K., Sargent, D. F., & Richmond, T. J. (1997). Crystal structure of the nucleosome core particle at 2.8 Å resolution. *NATURE*, *389*. Retrieved from https://www.nature.com/nature/journal/v389/n6648/pdf/389251a0.pdf

Lumeng, C. N., Bodzin, J. L., & Saltiel, A. R. (2007). Obesity induces a phenotypic switch in adipose tissue macrophage polarization. *Journal of Clinical Investigation*, *117*(1), 175–184. https://doi.org/10.1172/JCI29881

Lusser, A., Urwin, D. L., & Kadonaga, J. T. (2005). Distinct activities of CHD1 and ACF in ATP-dependent chromatin assembly. *Nature Structural & Molecular Biology*, *12*(2), 160–166. https://doi.org/10.1038/nsmb884

LYON, M. F. (1961). Gene action in the X-chromosome of the mouse (Mus musculus L.). *Nature*, *190*, 372–3. Retrieved from http://www.ncbi.nlm.nih.gov/pubmed/13764598

Marahrens, Y., Panning, B., Dausman, J., Strauss, W., & Jaenisch, R. (1997). Xist-deficient mice are defective in dosage compensation but not spermatogenesis. *Genes & Development*, *11*(2), 156–66. Retrieved from http://www.ncbi.nlm.nih.gov/pubmed/9009199

Marathe, H. G., Mehta, G., Zhang, X., Datar, I., Mehrotra, A., Yeung, K. C., & de la Serna, I. L. (2013). SWI/SNF Enzymes Promote SOX10- Mediated Activation of Myelin Gene Expression. *PLoS ONE*, *8*(7), e69037. https://doi.org/10.1371/journal.pone.0069037

Marenda, D. R., Zraly, C. B., Feng, Y., Egan, S., & Dingwall, A. K. (2003). The Drosophila SNR1 (SNF5/INI1) Subunit Directs Essential Developmental Functions of the Brahma Chromatin Remodeling Complex. *Molecular and Cellular Biology*, *23*(1), 289–305. https://doi.org/10.1128/MCB.23.1.289-305.2003

Marks, K. C., Banks, W. R., Cunningham, D., Witman, P. M., & Herman, G. E. (2014). Analysis of two candidate genes for Basan syndrome. *American Journal of Medical Genetics Part A*, *164*(5), 1188–1191. https://doi.org/10.1002/ajmg.a.36438

Martinez-Santibañez, G., & Nien-Kai Lumeng, C. (2014). Macrophages and the Regulation of Adipose Tissue Remodeling. *Annual Review of Nutrition*, *34*(1), 57–76. https://doi.org/10.1146/annurev-nutr-071812-161113

Menissier de Murcia, J., Ricoul, M., Tartier, L., Niedergang, C., Huber, A., Dantzer, F., … de Murcia, G. (2003). Functional interaction between PARP-1 and PARP-2 in chromosome stability and embryonic development in mouse. *The EMBO Journal*, *22*(9), 2255–2263. https://doi.org/10.1093/emboj/cdg206

Mermoud, J. E., Rowbotham, S. P., & Varga-Weisz, P. D. (2011). Keeping chromatin quiet. *Cell Cycle*, *10*(23), 4017–4025. https://doi.org/10.4161/cc.10.23.18558

Montufar-Solis, D., & Klein, J. R. (2006). An improved method for isolating intraepithelial lymphocytes (IELs) from the murine small intestine with consistently high purity. *Journal of Immunological Methods*, *308*(1–2), 251–4. https://doi.org/10.1016/j.jim.2005.10.008

Moon, Y. S., Smas, C. M., Lee, K., Villena, J. A., Kim, K.-H., Yun, E. J., & Sul, H. S. (2002). Mice lacking paternally expressed Pref-1/Dlk1 display growth retardation and accelerated adiposity. *Molecular and Cellular Biology*, *22*(15), 5585–92. https://doi.org/10.1128/mcb.22.15.5585-5592.2002

Murawska, M., & Brehm, A. (2011). CHD chromatin remodelers and the transcription cycle. *Transcription*, *2*(6), 244–53. https://doi.org/10.4161/trns.2.6.17840

Nathan, D., Ingvarsdottir, K., Sterner, D. E., Bylebyl, G. R., Dokmanovic, M., Dorsey, J. A., … Berger, S. L. (2006). Histone sumoylation is a negative regulator in Saccharomyces cerevisiae and shows dynamic interplay with positive-acting histone modifications. *Genes & Development*, *20*(8), 966–976. https://doi.org/10.1101/gad.1404206

Neves-Costa, A., Will, W. R., Vetter, A. T., Miller, J. R., & Varga-Weisz, P. (2009). The SNF2-Family Member Fun30 Promotes Gene Silencing in Heterochromatic Loci. *PLoS ONE*, *4*(12), e8111. https://doi.org/10.1371/journal.pone.0008111

Nguyen, K. H., Xu, F., Flowers, S., Williams, E. A. J., Fritton, J. C., & Moran, E. (2015). SWI/SNF-Mediated Lineage Determination in Mesenchymal Stem Cells Confers Resistance to Osteoporosis. *Stem Cells (Dayton, Ohio)*, *33*(10), 3028–38. https://doi.org/10.1002/stem.2064

Nousbeck, J., Burger, B., Fuchs-Telem, D., Pavlovsky, M., Fenig, S., Sarig, O., … Sprecher, E. (2011). A Mutation in a Skin-Specific Isoform of SMARCAD1 Causes Autosomal-Dominant Adermatoglyphia. *The American Journal of Human Genetics*, *89*(2), 302–307. https://doi.org/10.1016/j.ajhg.2011.07.004

O'Donnell, P. H., Stark, A. L., Gamazon, E. R., Wheeler, H. E., McIlwee, B. E., Gorsic, L., … Dolan, M. E. (2012). Identification of novel germline polymorphisms governing capecitabine sensitivity. *Cancer*, *118*(16), 4063–4073. https://doi.org/10.1002/cncr.26737

Ogata, M., & Itoh, T. (2016). Gamma/delta intraepithelial lymphocytes in the mouse small intestine. *Anatomical Science International*, *91*(4), 301–312. https://doi.org/10.1007/s12565-016-0341-2

Ogata, M., Ota, Y., Nanno, M., Suzuki, R., & Itoh, T. (2014). Activation of intra-epithelial lymphocytes; their morphology, marker expression and ultimate fate. *Cell and Tissue Research*, *356*(1), 217–230. https://doi.org/10.1007/s00441-013-1786-4

Okazaki, N., Ikeda, S., Ohara, R., Shimada, K., Yanagawa, T., Nagase, T., … Koga, H. (2008). *The Novel Protein Complex with SMARCAD1/KIAA1122 Binds to the Vicinity of TSS*. *Journal of Molecular Biology* (Vol. 382). https://doi.org/10.1016/j.jmb.2008.07.031

Ozturk, N., Singh, I., Mehta, A., Braun, T., & Barreto, G. (2014). HMGA proteins as modulators of chromatin structure during transcriptional activation. *Frontiers in Cell and Developmental Biology*, *2*, 5. https://doi.org/10.3389/fcell.2014.00005

Panamarova, M., Cox, A., Wicher, K. B., Butler, R., Bulgakova, N., Jeon, S., … Zernicka-Goetz, M. (2016). The BAF chromatin remodelling complex is an epigenetic regulator of lineage specification in the early mouse embryo. *Development (Cambridge, England)*, *143*(8), 1271–83. https://doi.org/10.1242/dev.131961

Papamichos-Chronakis, M., Watanabe, S., Rando, O. J., & Peterson, C. L. (2011). Global Regulation of H2A.Z Localization by the INO80 Chromatin-Remodeling Enzyme Is Essential for Genome Integrity. *Cell*, *144*(2), 200–213. https://doi.org/10.1016/j.cell.2010.12.021

Park, J.-H., Kotani, T., Konno, T., Setiawan, J., Kitamura, Y., Imada, S., … Matozaki, T. (2016). Promotion of Intestinal Epithelial Cell Turnover by Commensal Bacteria: Role of Short-Chain Fatty Acids. *PloS One*, *11*(5), e0156334. https://doi.org/10.1371/journal.pone.0156334

Park, M., Yi, J.-W., Kim, E.-M., Yoon, I.-J., Lee, E.-H., Lee, H.-Y., … Kang, H.-S. (2015). Triggering Receptor Expressed on Myeloid Cells 2 (TREM2) Promotes Adipogenesis and Diet-Induced Obesity. *Diabetes*, *64*(1), 117–127. https://doi.org/10.2337/db13-1869

Paul, C., Sardet, C., & Fabbrizio, E. (2015). The Wnt-target gene Dlk-1 is regulated by the Prmt5-associated factor Copr5 during adipogenic conversion. *Biology Open*, *4*(3), 312–316. https://doi.org/10.1242/bio.201411247

Peters, J. (2014). The role of genomic imprinting in biology and disease: an expanding view. *Nature Reviews Genetics*, *15*(8), 517–530. https://doi.org/10.1038/nrg3766

Pradhan, S. K., Su, T., Yen, L., Jacquet, K., Huang, C., Côté, J., … Carey, M. F. (2016). EP400 Deposits H3.3 into Promoters and Enhancers during Gene Activation. *Molecular Cell*, *61*(1), 27–38. https://doi.org/10.1016/j.molcel.2015.10.039

Reznikoff, C. A., Bertram, J. S., Brankow, D. W., & Heidelberger, C. (1973). Quantitative and qualitative studies of chemical transformation of cloned C3H mouse embryo cells sensitive to postconfluence inhibition of cell division. *Cancer Research*, *33*(12), 3239–49. Retrieved from http://www.ncbi.nlm.nih.gov/pubmed/4796800

Rosen, E. D., & MacDougald, O. A. (2006). Adipocyte differentiation from the inside out. *Nature Reviews Molecular Cell Biology*, *7*(12), 885–896. https://doi.org/10.1038/nrm2066

Rowbotham, S. P., Barki, L., Neves-Costa, A., Santos, F., Dean, W., Hawkes, N., … Mermoud, J. E. (2011a). Maintenance of Silent Chromatin through Replication Requires SWI/SNF-like Chromatin Remodeler SMARCAD1. *Molecular Cell*, *42*(3), 285–296. https://doi.org/10.1016/j.molcel.2011.02.036

Rowbotham, S. P., Barki, L., Neves-Costa, A., Santos, F., Dean, W., Hawkes, N., … Mermoud, J. E. (2011b). Maintenance of silent chromatin through replication requires SWI/SNF-like chromatin remodeler SMARCAD1. *Molecular Cell*, *42*(3), 285–96.

https://doi.org/10.1016/j.molcel.2011.02.036
Ryan, D. P., Sundaramoorthy, R., Martin, D., Singh, V., & Owen-Hughes, T. (2011). The DNA-binding domain of the Chd1 chromatin-remodelling enzyme contains SANT and SLIDE domains. *The EMBO Journal*, *30*(13), 2596–2609. https://doi.org/10.1038/emboj.2011.166
Sabari, B. R., Zhang, D., Allis, C. D., & Zhao, Y. (2016). Metabolic regulation of gene expression through histone acylations. *Nature Reviews Molecular Cell Biology*, *18*(2), 90–101. https://doi.org/10.1038/nrm.2016.140
Saeed, H., Taipaleenmäki, H., Aldahmash, A. M., Abdallah, B. M., & Kassem, M. (2012). Mouse Embryonic Fibroblasts (MEF) Exhibit a Similar but not Identical Phenotype to Bone Marrow Stromal Stem Cells (BMSC). *Stem Cell Reviews and Reports*, *8*(2), 318–328. https://doi.org/10.1007/s12015-011-9315-x
Sato, T., Vries, R. G., Snippert, H. J., van de Wetering, M., Barker, N., Stange, D. E., … Clevers, H. (2009). Single Lgr5 stem cells build crypt-villus structures in vitro without a mesenchymal niche. *Nature*, *459*(7244), 262–5. https://doi.org/10.1038/nature07935
Schoor, M., Schuster-Gossler, K., Roopenian, D., & Gossler, A. (1999). Skeletal dysplasias, growth retardation, reduced postnatal survival, and impaired fertility in mice lacking the SNF2/SWI2 family member ETL1. *Mechanisms of Development*, *85*(1–2), 73–83. https://doi.org/10.1016/S0925-4773(99)00090-8
Schroeder, B. O., & Bäckhed, F. (2016). Signals from the gut microbiota to distant organs in physiology and disease. *Nature Medicine*, *22*(10), 1079–1089. https://doi.org/10.1038/nm.4185
Sebald, J., Willi, M., Schoberleitner, I., Krogsdam, A., Orth-Höller, D., Trajanoski, Z., & Lusser, A. (2016). Impact of the Chromatin Remodeling Factor CHD1 on Gut Microbiome Composition of Drosophila melanogaster. *PLOS ONE*, *11*(4), e0153476. https://doi.org/10.1371/journal.pone.0153476
Seki, Y., Kurisaki, A., Watanabe-Susaki, K., Nakajima, Y., Nakanishi, M., Arai, Y., … Asashima, M. (2010). TIF1beta regulates the pluripotency of embryonic stem cells in a phosphorylation-dependent manner. *Proceedings of the National Academy of Sciences of the United States of America*, *107*(24), 10926–31. https://doi.org/10.1073/pnas.0907601107
Semenkovich, N. P., Planer, J. D., Ahern, P. P., Griffin, N. W., Lin, C. Y., & Gordon, J. I. (2016). Impact of the gut microbiota on enhancer accessibility in gut intraepithelial lymphocytes. *Proceedings of the National Academy of Sciences of the United States of America*, *113*(51), 14805–14810. https://doi.org/10.1073/pnas.1617793113
Seo, E., Basu-Roy, U., Zavadil, J., Basilico, C., & Mansukhani, A. (2011). Distinct functions of Sox2 control self-renewal and differentiation in the osteoblast lineage. *Molecular and Cellular Biology*, *31*(22), 4593–608. https://doi.org/10.1128/MCB.05798-11
Sheridan, B. S., & Lefrançois, L. (2010). Intraepithelial lymphocytes: to serve and protect. *Current Gastroenterology Reports*, *12*(6), 513–21. https://doi.org/10.1007/s11894-010-0148-6
Shi, Y., Lan, F., Matson, C., Mulligan, P., Whetstine, J. R., Cole, P. A., … Shi, Y. (2004). Histone Demethylation Mediated by the Nuclear Amine Oxidase Homolog LSD1. *Cell*, *119*(7), 941–953. https://doi.org/10.1016/j.cell.2004.12.012
Shieh, S.-J., Varkey, P., Chen, P.-Y., Chang, S.-Y., & Huang, L. L. H. (2014). Counting CD4(+) and CD8(+) T cells in the spleen: a novel in vivo method for assessing biomaterial immunotoxicity. *Regenerative Biomaterials*, *1*(1), 11–6. https://doi.org/10.1093/rb/rbu003
Sidhu, S. K., Minks, J., Chang, S. C., Cotton, A. M., & Brown, C. J. (2008). X chromosome inactivation: heterogeneity of heterochromatin. *Biochemistry and Cell Biology = Biochimie et Biologie Cellulaire*, *86*(5), 370–9. https://doi.org/10.1139/o08-100
Siersbæk, R., Nielsen, R., & Mandrup, S. (2012). Transcriptional networks and chromatin remodeling controlling adipogenesis. *Trends in Endocrinology & Metabolism*, *23*(2), 56–64. https://doi.org/10.1016/j.tem.2011.10.001
Singhal, P. K., Sassi, S., Lan, L., Au, P., Halvorsen, S. C., Fukumura, D., … Seed, B. (2016). Mouse embryonic fibroblasts exhibit extensive developmental and phenotypic diversity. *Proceedings of the National Academy of Sciences of the United States of America*, *113*(1), 122–7. https://doi.org/10.1073/pnas.1522401112
Smith-Roe, S. L., Nakamura, J., Holley, D., Chastain, P. D., Rosson, G. B., Simpson, D. A., … Bultman, S. J. (2015). SWI/SNF complexes are required for full activation of the DNA-damage response. *Oncotarget*, *6*(2), 732–745. https://doi.org/10.18632/oncotarget.2715

Soares, A., Beraldi, E. J., Ferreira, P. E. B., Bazotte, R. B., & Buttow, N. C. (2015). Intestinal and neuronal myenteric adaptations in the small intestine induced by a high-fat diet in mice. *BMC Gastroenterology*, *15*(1), 3. https://doi.org/10.1186/s12876-015-0228-z

Soininen, R., Schoor, M., Henseling, U., Tepe, C., Kisters-Woike, B., Rossant, J., & Gossler, A. (1992). The mouse Enhancer trap locus 1 (Etl-1): a novel mammalian gene related to Drosophila and yeast transcriptional regulator genes. *Mechanisms of Development*, *39*(1–2), 111–23. Retrieved from http://www.ncbi.nlm.nih.gov/pubmed/1489724

Song, L., & Crawford, G. E. (2010). DNase-seq: a high-resolution technique for mapping active gene regulatory elements across the genome from mammalian cells. *Cold Spring Harbor Protocols*, *2010*(2), pdb.prot5384. https://doi.org/10.1101/pdb.prot5384

Sterner, D. E., & Berger, S. L. (2000). Acetylation of histones and transcription-related factors. *Microbiology and Molecular Biology Reviews : MMBR*, *64*(2), 435–59. Retrieved from http://www.ncbi.nlm.nih.gov/pubmed/10839822

Steshina, E. Y., Carr, M. S., Glick, E. A., Yevtodiyenko, A., Appelbe, O. K., & Schmidt, J. V. (2006). Loss of imprinting at the Dlk1-Gtl2 locus caused by insertional mutagenesis in the Gtl2 5' region. *BMC Genetics*, *7*(1), 44. https://doi.org/10.1186/1471-2156-7-44

Stokes, D. G., & Perry, R. P. (1995). DNA-binding and chromatin localization properties of CHD1. *Molecular and Cellular Biology*, *15*(5), 2745–53. Retrieved from http://www.ncbi.nlm.nih.gov/pubmed/7739555

Strohner, R., Németh, A., Nightingale, K. P., Grummt, I., Becker, P. B., & Längst, G. (2004). Recruitment of the nucleolar remodeling complex NoRC establishes ribosomal DNA silencing in chromatin. *Molecular and Cellular Biology*, *24*(4), 1791–8. https://doi.org/10.1128/MCB.24.4.1791-1798.2004

Surmi, B. K., & Hasty, A. H. (2008). Macrophage infiltration into adipose tissue: initiation, propagation and remodeling. *Future Lipidology*, *3*(5), 545–556. https://doi.org/10.2217/17460875.3.5.545

Suzuki, H. (2012). Age-dependent changes in intraepithelial lymphocytes (IELs) of the small intestine, cecum, and colon from young adult to aged mice. *Archives of Gerontology and Geriatrics*, *55*(2), 261–70. https://doi.org/10.1016/j.archger.2011.07.009

Takahashi, K., Sugi, Y., Hosono, A., & Kaminogawa, S. (2009). Epigenetic regulation of TLR4 gene expression in intestinal epithelial cells for the maintenance of intestinal homeostasis. *Journal of Immunology (Baltimore, Md. : 1950)*, *183*(10), 6522–9. https://doi.org/10.4049/jimmunol.0901271

Takahashi, K., & Yamanaka, S. (2006). Induction of Pluripotent Stem Cells from Mouse Embryonic and Adult Fibroblast Cultures by Defined Factors. *Cell*, *126*(4), 663–676. https://doi.org/10.1016/j.cell.2006.07.024

Takeuchi, J. K., & Bruneau, B. G. (2009). Directed transdifferentiation of mouse mesoderm to heart tissue by defined factors. *Nature*, *459*(7247), 708–711. https://doi.org/10.1038/nature08039

Takeuchi, J. K., Lou, X., Alexander, J. M., Sugizaki, H., Delgado-Olguín, P., Holloway, A. K., … Bruneau, B. G. (2011). Chromatin remodelling complex dosage modulates transcription factor function in heart development. *Nature Communications*, *2*, 187. https://doi.org/10.1038/ncomms1187

Tapak, L., Saidijam, M., Sadeghifar, M., Poorolajal, J., & Mahjub, H. (2015). Competing Risks Data Analysis with High-dimensional Covariates: An Application in Bladder Cancer. *Genomics, Proteomics & Bioinformatics*, *13*(3), 169–176. https://doi.org/10.1016/j.gpb.2015.04.001

Teixeira da Rocha, S., Charalambous, M., Lin, S.-P., Gutteridge, I., Ito, Y., Gray, D., … Ferguson-Smith, A. C. (2009). Gene Dosage Effects of the Imprinted Delta-Like Homologue 1 (Dlk1/Pref1) in Development: Implications for the Evolution of Imprinting. *PLoS Genetics*, *5*(2), e1000392. https://doi.org/10.1371/journal.pgen.1000392

Thiru, A., Nietlispach, D., Mott, H. R., Okuwaki, M., Lyon, D., Nielsen, P. R., … Laue, E. D. (2004). Structural basis of HP1/PXVXL motif peptide interactions and HP1 localisation to heterochromatin. *The EMBO Journal*, *23*(3), 489–99. https://doi.org/10.1038/sj.emboj.7600088

Turgeon, B., & Meloche, S. (2009). Interpreting Neonatal Lethal Phenotypes in Mouse Mutants: Insights Into Gene Function and Human Diseases. *Physiological Reviews*, *89*(1). Retrieved from http://physrev.physiology.org/content/89/1/1.long

Turnbaugh, P. J., Ley, R. E., Mahowald, M. A., Magrini, V., Mardis, E. R., & Gordon, J. I. (2006). An

obesity-associated gut microbiome with increased capacity for energy harvest. *Nature*, *444*(7122), 1027–131. https://doi.org/10.1038/nature05414

Udugama, M., Sabri, A., & Bartholomew, B. (2011). The INO80 ATP-Dependent Chromatin Remodeling Complex Is a Nucleosome Spacing Factor. *Molecular and Cellular Biology*, *31*(4), 662–673. https://doi.org/10.1128/MCB.01035-10

van Attikum, H., Fritsch, O., & Gasser, S. M. (2007). Distinct roles for SWR1 and INO80 chromatin remodeling complexes at chromosomal double-strand breaks. *The EMBO Journal*, *26*(18), 4113–4125. https://doi.org/10.1038/sj.emboj.7601835

van der Heyde, H. C., Batchelder, J. M., Sandor, M., & Weidanz, W. P. (2006). Splenic gammadelta T cells regulated by CD4+ T cells are required to control chronic Plasmodium chabaudi malaria in the B-cell-deficient mouse. *Infection and Immunity*, *74*(5), 2717–25. https://doi.org/10.1128/IAI.74.5.2717-2725.2006

Vermeulen, L., & Snippert, H. J. (2014). Stem cell dynamics in homeostasis and cancer of the intestine. *Nature Reviews Cancer*, *14*(7), 468–480. https://doi.org/10.1038/nrc3744

Vierbuchen, T., Ostermeier, A., Pang, Z. P., Kokubu, Y., Südhof, T. C., & Wernig, M. (2010). Direct conversion of fibroblasts to functional neurons by defined factors. *Nature*, *463*(7284), 1035–1041. https://doi.org/10.1038/nature08797

Wan, M., Zhang, J., Lai, D., Jani, A., Prestone-Hurlburt, P., Zhao, L., … Chi, T. (2009). Molecular basis of CD4 repression by the Swi/Snf-like BAF chromatin remodeling complex. *European Journal of Immunology*, *39*(2), 580–588. https://doi.org/10.1002/eji.200838909

Wang, H., Wang, L., Erdjument-Bromage, H., Vidal, M., Tempst, P., Jones, R. S., & Zhang, Y. (2004). Role of histone H2A ubiquitination in Polycomb silencing. *Nature*, *431*(7010), 873–878. https://doi.org/10.1038/nature02985

Wang, X., Sumida, H., & Cyster, J. G. (2014). GPR18 is required for a normal CD8αα intestinal intraepithelial lymphocyte compartment. *The Journal of Experimental Medicine*, *211*(12), 2351–2359. https://doi.org/10.1084/jem.20140646

Wu, J. I. (2012). Diverse functions of ATP-dependent chromatin remodeling complexes in development and cancer. *Acta Biochimica et Biophysica Sinica*, *44*(1), 54–69. https://doi.org/10.1093/abbs/gmr099

Wu, J. I., Lessard, J., Olave, I. A., Qiu, Z., Ghosh, A., Graef, I. A., & Crabtree, G. R. (2007). Regulation of Dendritic Development by Neuron-Specific Chromatin Remodeling Complexes. *Neuron*, *56*(1), 94–108. https://doi.org/10.1016/j.neuron.2007.08.021

Wu, S., Shi, Y., Mulligan, P., Gay, F., Landry, J., Liu, H., … Shi, Y. (2007). A YY1-INO80 complex regulates genomic stability through homologous recombination-based repair. *Nature Structural & Molecular Biology*, *14*(12), 1165–72. https://doi.org/10.1038/nsmb1332

Xian, L., Georgess, D., Huso, T., Cope, L., Belton, A., Chang, Y.-T., … Resar, L. M. S. (2017). HMGA1 amplifies Wnt signalling and expands the intestinal stem cell compartment and Paneth cell niche. *Nature Communications*, *8*, 15008. https://doi.org/10.1038/ncomms15008

Xiao, B., Jing, C., Wilson, J. R., Walker, P. A., Vasisht, N., Kelly, G., … Gamblin, S. J. (2003). Structure and catalytic mechanism of the human histone methyltransferase SET7/9. *Nature*, *421*(6923), 652–656. https://doi.org/10.1038/nature01378

Xiao, H., Sandaltzopoulos, R., Wang, H. M., Hamiche, A., Ranallo, R., Lee, K. M., … Wu, C. (2001). Dual functions of largest NURF subunit NURF301 in nucleosome sliding and transcription factor interactions. *Molecular Cell*, *8*(3), 531–43. Retrieved from http://www.ncbi.nlm.nih.gov/pubmed/11583616

Xiao, S., Lu, J., Sridhar, B., Tanaka, T. S., Stormo, G., Zhong Correspondence, S., … Zhong, S. (2017). SMARCAD1 Contributes to the Regulation of Naive Pluripotency by Interacting with Histone Citrullination. *Cell Reports*, *18*, 3117–3128. https://doi.org/10.1016/j.celrep.2017.02.070

Yang, M., Sun, J., Zhang, T., Liu, J., Zhang, J., Shi, M. A., … Shi, G.-P. (2008). Deficiency and inhibition of cathepsin K reduce body weight gain and increase glucose metabolism in mice. *Arteriosclerosis, Thrombosis, and Vascular Biology*, *28*(12), 2202–8. https://doi.org/10.1161/ATVBAHA.108.172320

Yu, Y., Chen, Y., Kim, B., Wang, H., Zhao, C., He, X., … Lu, Q. R. (2013). Olig2 Targets Chromatin Remodelers to Enhancers to Initiate Oligodendrocyte Differentiation. *Cell*, *152*(1–2), 248–261. https://doi.org/10.1016/j.cell.2012.12.006

Yusuf, B., Gopurappilly, R., Dadheech, N., Gupta, S., Bhonde, R., & Pal, R. (2013). Embryonic fibroblasts represent a connecting link between mesenchymal and embryonic stem cells. *Development, Growth & Differentiation*, *55*(3), 330–340.

https://doi.org/10.1111/dgd.12043
Zelante, T., Iannitti, R. G., Cunha, C., De Luca, A., Giovannini, G., Pieraccini, G., … Romani, L. (2013). Tryptophan Catabolites from Microbiota Engage Aryl Hydrocarbon Receptor and Balance Mucosal Reactivity via Interleukin-22. *Immunity*, *39*(2), 372–385. https://doi.org/10.1016/j.immuni.2013.08.003
Zeng, X., Lin, X., & Hou, S. X. (2013). The Osa-containing SWI/SNF chromatin-remodeling complex regulates stem cell commitment in the adult Drosophila intestine. *Development (Cambridge, England)*, *140*(17), 3532–40. https://doi.org/10.1242/dev.096891
Zerradi, M., Dereumetz, J., Boulet, M.-M., & Tchernof, A. (2014). Androgens, body fat Distribution and Adipogenesis. *Current Obesity Reports*, *3*(4), 396–403. https://doi.org/10.1007/s13679-014-0119-6
Zhang, P., Li, L., Bao, Z., & Huang, F. (2016). Role of BAF60a/BAF60c in chromatin remodeling and hepatic lipid metabolism. *Nutrition & Metabolism*, *13*, 30. https://doi.org/10.1186/s12986-016-0090-1
Zheng, C., Yang, Q., Xu, C., Shou, P., Cao, J., Jiang, M., … Wang, Y. (2015). CD11b regulates obesity-induced insulin resistance via limiting alternative activation and proliferation of adipose tissue macrophages. *Proceedings of the National Academy of Sciences of the United States of America*, *112*(52), E7239-48. https://doi.org/10.1073/pnas.1500396113
Zimmermann, S., Kiefer, F., Prudenziati, M., Spiller, C., Hansen, J., Floss, T., … Göttlicher, M. (2007). Reduced body size and decreased intestinal tumor rates in HDAC2-mutant mice. *Cancer Research*, *67*(19), 9047–54. https://doi.org/10.1158/0008-5472.CAN-07-0312

7 Appendices.

APPENDIX 1: Quantification of protein from western blot band signal intensity using GelQuantNET.

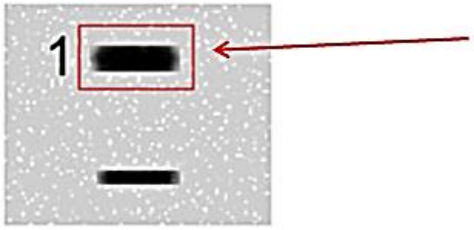

1. An area is drawn around first band of interest, which includes some surrounding (background area).

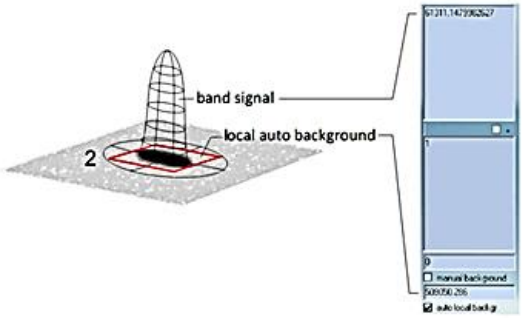

2. The average intensity of the band area and the background area is calculated / assigned a numerical value, along with the surrounding background signal.

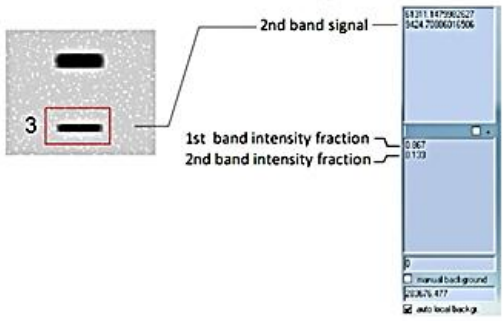

3. The process is repeated for a each band of interest. A list of background-subtracted values is shown on the top right-hand-side, along with the intensity fraction for each band (i.e. area of quantified region covered by the actual band signal).

Appendix 1: Measurement and quantitation of peptide following western blot using GelQuantNet software (see http://biochemlabsolutions.com/GelQuantNET.html). Regions of interest are specified by the user, which should include a surrounding region of background signal. Numerical values based on band size and intensity are generated by the software, allowing the user to perform subsequent quantitative analysis.

APPENDIX 2: Detailed gating scheme for flow cytometric analysis of iIEL cell counts.

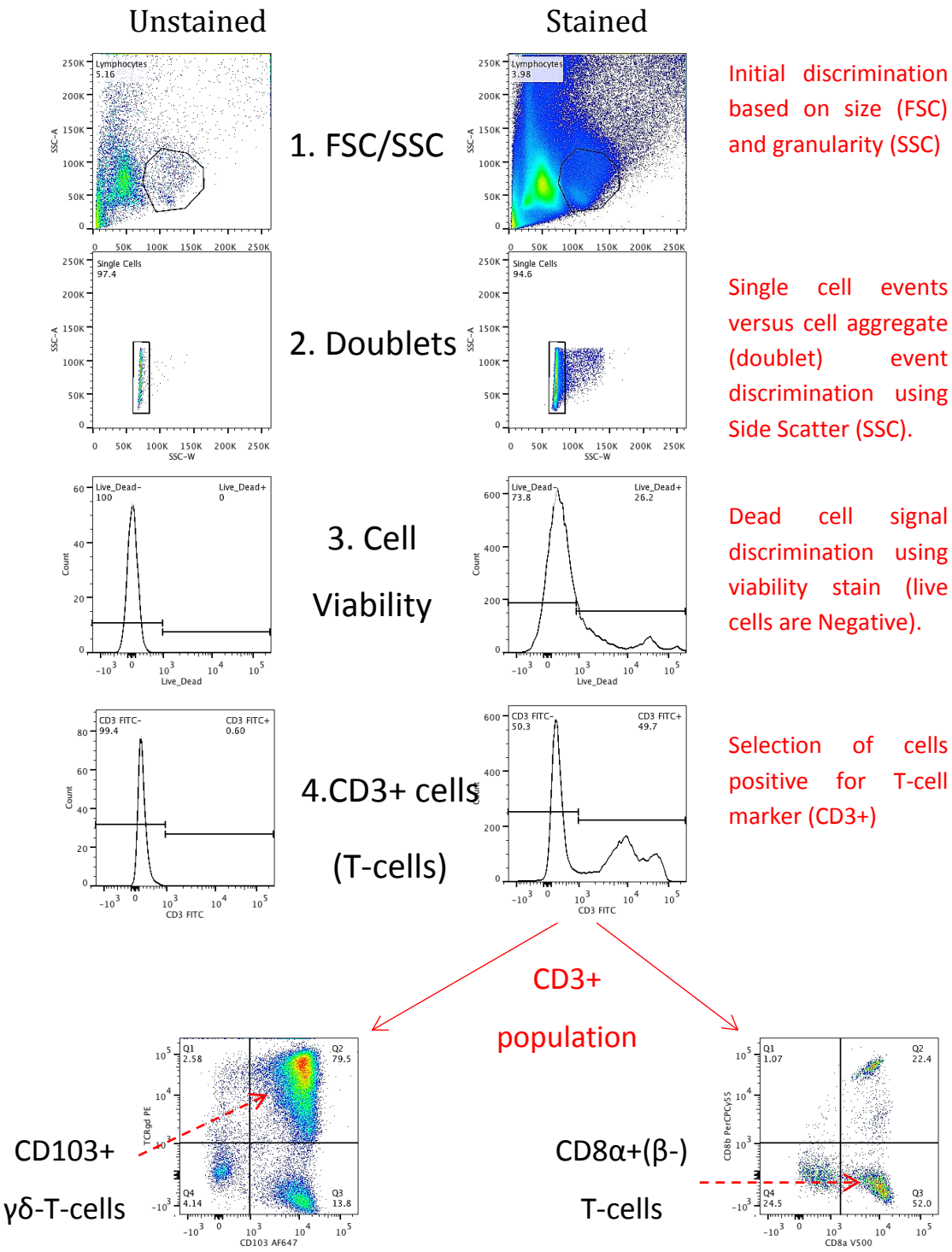

Appendix 2: Gating scheme for iIEL FACS. Cells of appropriate size/granularity are selected using FSC/SSC gating, and clumped cells ("doublets") along with dead cells are removed before subsequent analysis of cell surface markers using additional fluorescence channels.

APPENDIX 3: FACS of iIELs from HFD challenged *Smarcad1* +/+ and -/- mice, and control (*Smarcad1* +/+ normal chow diet) mice.

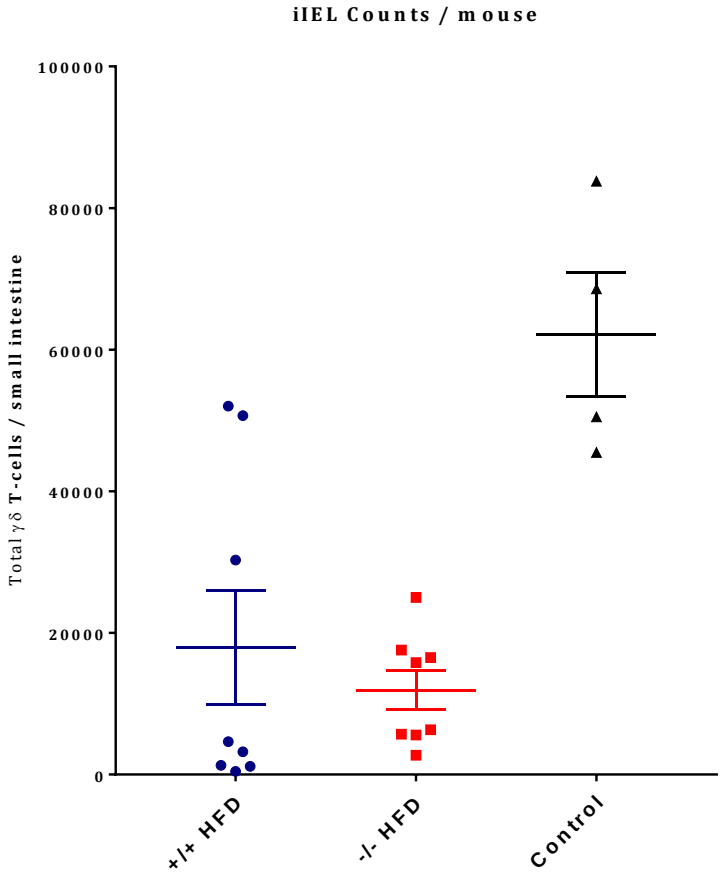

Appendix 3: Preliminary data suggest that mice challenged with a high fat diet for 6 weeks lose intestinal (γδ-T-cell) IELs compared to control chow fed mice. Both *SMARCAD1*+/+ and *SMARCAD1*-/- HFD mice reported a reduction in iIEL numbers compared to controls, although further investigation using higher samples numbers from repeat experiment(s) would clarify any significant difference(s) between the groups.

APPENDIX 4: Measurement of adipocyte sizes using Image J and a Watershed algorithm.

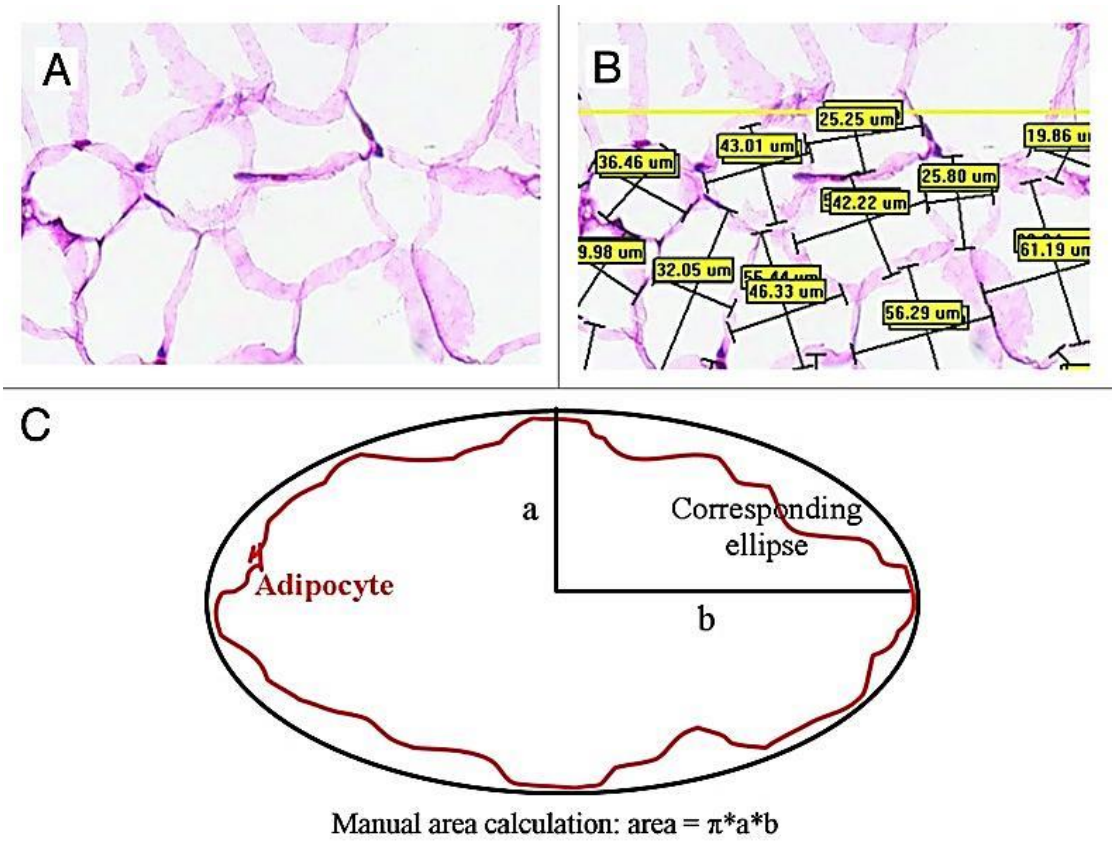

Appendix 4: Adipocyte areas measured using images obtained from Image J software (post capture at 10x magnification). Initial identification of cell boundaries allows the Watershed algorithm to estimate adipocyte size based on a best-fit ellipse. Regions within the image without clear (cell) boundaries or presenting an area greater than pre-set thresholds are excluded.

APPENDIX 5: BioAnalyzer spectrometry of (whole-WAT) RNA-seq libraries.

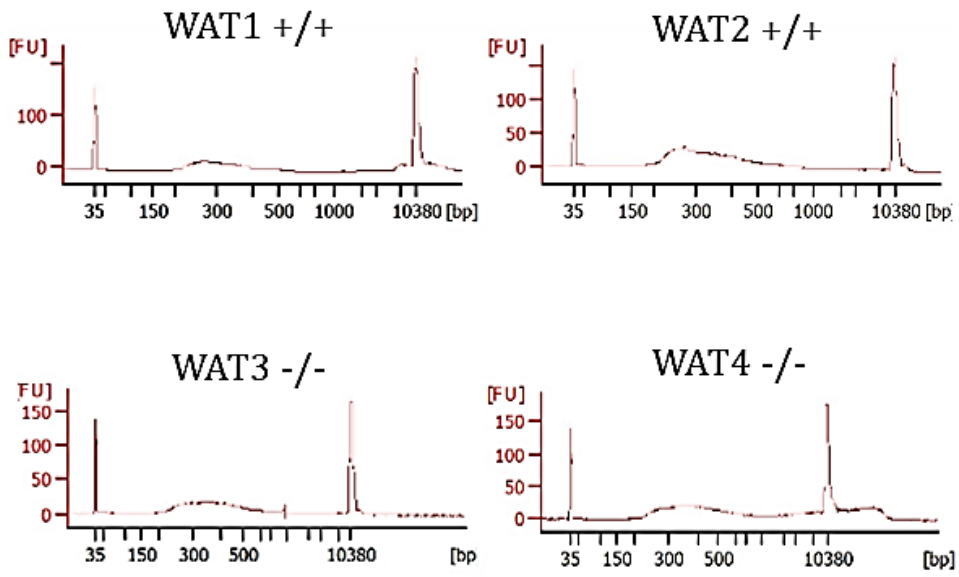

Appendix 5. BioAnalyzer electrophoregram analysis of RNA-seq library content size and concentration. Samples had the following size peaks and concentrations: WAT1+/+ peak 277bp, 445 [pg/µl], WAT2+/+ peak 276bp, 359 [pg/µl], WAT3 peak 343bp, 396 [pg/µl] and WAT4-/- peak 352bp, 340[pg/µl].